Non-dispersive wave packets in periodically driven quantum systems

Andreas Buchleitner[1], Dominique Delande [1,2], and Jakub Zakrzewski[3]

[1] *Max-Planck-Institut für Physik komplexer Systeme, Dresden, Germany*

[2] *Laboratoire Kastler-Brossel, Tour 12, Étage 1, Université Pierre et Marie Curie, 4 Place Jussieu, 75005 Paris, France*

[3] *Instytut Fizyki imienia Mariana Smoluchowskiego, Uniwersytet Jagielloński, Reymonta 4, PL-30-059 Kraków, Poland*

Contents

Preprint submitted to Elsevier Science

Abstract

With the exception of the harmonic oscillator, quantum wave-packets usually spread as time evolves. This is due to the non-linear character of the classical equations of motion which makes the various components of the wave-packet evolve at various frequencies. We show here that, using the nonlinear resonance between an internal frequency of a system and an external periodic driving, it is possible to overcome this spreading and build non-dispersive (or non-spreading) wave-packets which are well localized and follow a classical periodic orbit without spreading. From the quantum mechanical point of view, the non-dispersive wave-packets are time periodic eigenstates of the Floquet Hamiltonian, localized in the nonlinear resonance island.

We discuss the general mechanism which produces the non-dispersive wave-packets, with emphasis on simple realization in the electronic motion of a Rydberg electron driven by a microwave field. We show the robustness of such wavepackets for a model one-dimensional as well as for realistic three dimensional atoms. We consider their essential properties such as the stability versus ionization, the characteristic energy spectrum and long lifetimes. The requirements for experiments aimed at observing such non-dispersive wave-packets are also considered.

The analysis is extended to situations in which the driving frequency is a multiple of the internal atomic frequency. Such a case allows us to discuss non-dispersive states composed of several, macroscopically separated wave-packets communicating among themselves by tunneling. Similarly we briefly discuss other closely related phenomena in atomic and molecular physics as well as possible further extensions of the theory.

Keywords: wave-packet, dispersion, spreading, coherent states, Rydberg atoms, non-linear resonance, atom-field interaction
PACS: 05.45.Mt, 03.65.Sq, 32.80.Qk, 32.80.Rm, 42.50.Hz

1 Introduction

1.1 What is a wave packet?

It is commonly accepted that, for macroscopic systems like comets, cars, cats, and dogs [1], quantum objects behave like classical ones. Throughout this report, we will understand by "quantum objects" physical systems governed by the Schrödinger equation: the system can then be entirely described by its state $|\psi\rangle$, which, mathematically speaking, is just a vector in Hilbert space. We will furthermore restrict ourselves to the dynamics of a single, spin-less particle, such as to have an immediate representation of $|\psi\rangle$ in configuration and momentum space by the wave functions $\langle\vec{r}|\psi\rangle = \psi(\vec{r})$ and $\langle\vec{p}|\psi\rangle = \psi(\vec{p})$,

respectively. The same object is in classical mechanics described by its phase space coordinates $\vec{r}$ and $\vec{p}$ (or variants thereof), and our central concern will be to understand how faithfully we can mimic the classical time evolution of $\vec{r}$ and $\vec{p}$ by a *single* quantum state $|\psi\rangle$, in the *microscopic* realm.

Whereas classical dynamics are described by Hamilton's equations of motion, which determine the values of $\vec{r}$ and $\vec{p}$ at any time, given some initial condition $(\vec{r_0}, \vec{p_0})$, the quantum evolution is described by the Schrödinger equation, which propagates the wave function. Hence, it is suggestive to associate a classical particle with a quantum state $|\psi\rangle$ which is optimally localized around the classical particle's phase space position, at any time t. However, quantum mechanics imposes a fundamental limit on localization, expressed by Heisenberg's uncertainty relation

$$\Delta z \; . \; \Delta p \geq \frac{\hbar}{2}, \tag{1}$$

where Δz and Δp are the uncertainties (i.e., square roots of the variances) of the probability distributions of z and its conjugate momentum p in state $|\psi\rangle$, respectively (similar relations hold for other choices of canonically conjugate coordinates). Consequently, the best we can hope for is a quantum state localized with a finite width $(\Delta z, \Delta p)$ around the particle's classical position (z, p), with Δz and Δp much smaller than the typical scales of the classical trajectory. This, however, would satisfy our aim of constructing a quantum state that mimics the classical motion, provided $|\psi\rangle$ keeps track of the classical time evolution of z and p, and Δz and Δp remain small as time proceeds. After all, also classical bodies follow their center of mass trajectory even if they have a finite volume. Quantum states which exhibit these properties at least on a finite time scale are called "wave-packets", simply due to their localization properties in phase space [2].

More formally, a localized solution of a wave equation like the Schrödinger equation can be conceived as a linear superposition of plane waves (eigenstates of the momentum operator) or of any other suitable basis states. From a purely technical point of view, such a superposition may be seen as a *packet of waves*, hence, a wave-packet. Note, however, that any strongly localized object is a wave-packet in this formal sense, though not all superpositions of plane waves qualify as localized objects. In addition, this formal definition quite obviously depends on the basis used for the decomposition. Therefore, the only sensible definition of a wave-packet can be through its localization properties in phase space, as outlined above.

What can we say about the localization properties of a quantum state $|\psi\rangle$ as time evolves? For simplicity, let us assume that the Hamiltonian describing

the dynamics has the time-independent form

$$H = \frac{\vec{p}^2}{2m} + V(\vec{r}), \tag{2}$$

with $V(\vec{r})$ some potential. The time evolution of $|\psi\rangle$ is then described by the Schrödinger equation

$$\left[-\frac{\hbar^2}{2m}\Delta + V(\vec{r})\right]\psi(\vec{r},t) = i\hbar\frac{\partial\psi(\vec{r},t)}{\partial t}. \tag{3}$$

The expectation values of position and momentum in this state are given by

$$< \vec{r}(t) >= \langle\psi(t)|\ \vec{r}\ |\psi(t)\rangle, \tag{4}$$
$$< \vec{p}(t) >= \langle\psi(t)|\ \vec{p}\ |\psi(t)\rangle, \tag{5}$$

with time evolution

$$\frac{d < \vec{r} >}{dt} = \frac{1}{i\hbar}\ < [\vec{r}, H] >= \frac{< \vec{p} >}{m}, \tag{6}$$
$$\frac{d < \vec{p} >}{dt} = \frac{1}{i\hbar}\ < [\vec{p}, H] >= - < \nabla V(\vec{r}) >, \tag{7}$$

and $[.,.]$ the commutator. These are almost the classical equations of motion generated by H, apart from the right hand side of eq. (7), and apply for *any* $|\psi\rangle$, irrespective of its localization properties. If we additionally assume $|\psi\rangle$ to be localized within a spatial region where $\nabla V(\vec{r})$ is essentially constant, we have $< \nabla V(\vec{r}) > \simeq \nabla V(< \vec{r} >)$, and therefore

$$\frac{d < \vec{r} >}{dt} = \frac{< \vec{p} >}{m}, \tag{8}$$
$$\frac{d < \vec{p} >}{dt} \simeq -\nabla V(< \vec{r} >), \tag{9}$$

precisely identical to the classical equations of motion. This is nothing but Ehrenfest's theorem and tells us that the quantum expectation values of $\vec{r}$ and $\vec{p}$ of an initially localized wave-packet evolve according to the classical dynamics, as long as $|\psi\rangle$ remains localized within a range where $\nabla V(\vec{r})$ is approximately constant. However, these equations do not yet give us any clue on the time evolution of the uncertainties $(\Delta z, \Delta p)$ (and of those in the remaining degrees of freedom), and, consequently, neither on the time scales on which they are reliable.

On the other hand, given a localized wave-packet at time $t = 0$, a decomposition

$$|\psi(t=0)\rangle = \sum_n c_n\ |\phi_n\rangle \tag{10}$$

with coefficients

$$c_n = \langle \phi_n | \psi(t=0) \rangle \tag{11}$$

in unperturbed energy eigenstates

$$H|\phi_n\rangle = E_n|\phi_n\rangle,\ n = 1, 2, \ldots, \tag{12}$$

tells us immediately that

$$|\psi(t)\rangle = \sum_n c_n \exp\left(-i\frac{E_n t}{\hbar}\right)\ |\phi_n\rangle \tag{13}$$

cannot be stationary, *except* for

$$|\psi(t=0)\rangle = |\phi_j\rangle, \tag{14}$$

for some suitable j.

The eigenstates $|\phi_j\rangle$ are typically delocalized over a large part of phase space (for example, over a classical trajectory, see section 2), and thus are not wave-packets. There is however, an exception: in the vicinity of a (stable) fixed point of the classical dynamics (defined [3] as a point in phase space where the time derivatives of positions and momenta vanish simultaneously), there exist localized eigenstates, see section 3.1.

For a particle moving in a one-dimensional, binding potential bounded from below, there is a stable fixed point at any potential minimum. The quantum mechanical ground state of this system is localized near the fixed point at the global minimum of the potential and is a wave-packet, though a very special one: it does not evolve in time. Note that there is no need for the potential to be harmonic, any potential minimum will do. The same argument can be used for a one-dimensional binding potential whose origin moves with uniform velocity. The problem can be reduced to the previous one by transforming to the moving frame where the potential is stationary. Back in the laboratory frame, the ground state of the particle in the moving frame will appear as a wave-packet which moves at uniform velocity. Obviously, expanding the wave-packet in a stationary basis in the laboratory frame will result in an awfully complicated decomposition, with time-dependent coefficients, and this example clearly illustrates the importance of the proper choice of the referential. [1]

If eq. (14) is not fulfilled, the initial localization of $|\psi(t=0)\rangle$ (which is equivalent to an appropriate choice of the c_n in eq. (11)) will progressively deteriorate

[1] In passing, note that such a situation is actually realized in particle accelerators: electromagnetic fields are applied to the particles, such that these are trapped at some fixed point (preferably stable) in an accelerated frame [3].

as time evolves, the wave-packet will *spread*, due to the accumulation of relative phases of the different contributions to the sum in eq. (13). Whereas the classical dynamics in a one-dimensional binding potential $V(\vec{r})$ are described by periodic orbits (at any energy), the quantum dynamics are in general *not* periodic. A return to the initial state is *only* possible if *all* the phases $\exp(-iE_nt/\hbar)$ simultaneously take the same value. This implies that all the energy levels E_n (with $c_n \neq 0$) are equally spaced, or that all the level spacings are integer multiples of some quantity. In practice, this is realized only for the harmonic oscillator (in any dimension), and for tops or rotors where the Hamiltonian is proportional to some component of an angular momentum variable. Another possibility is to use the linear Stark effect in the hydrogen atom which produces manifolds of equally spaced energy levels. However, experimental imperfections (higher order Stark effect and effect of the ionic core on non-hydrogenic Rydberg atoms) break the equality of the spacings and consequently lead to dispersion [4].

The equality of consecutive spacings has a simple classical interpretation: since all classical trajectories are periodic with the *same* period, the system is exactly back in its initial state after an integer number of periods. In other words, in those special cases, there is no wave-packet spreading at long times.

However, for more generic systems, the energy levels are not equally spaced, neither are the spacings simply related, and a wave-packet *will* spread. For a one-dimensional, time-independent system, it is even possible to estimate the time after which the wave-packet has significantly spread (this phenomenon is also known as the "collapse" of the wave-packet [5,6]). This is done by expanding the various energies E_n around the "central" energy E_{n_0} of the wave-packet:

$$E_n \simeq E_{n_0} + (n-n_0)\frac{dE_n}{dn}(n_0) + \frac{(n-n_0)^2}{2}\frac{d^2E_n}{dn^2}(n_0). \tag{15}$$

The wave-packet being initially localized, its energy is more or less well defined and only a relatively small number $\Delta n \ll n_0$ of the coefficients c_n have significant values. At short times, the contribution of the second order term in eq. (15) to the evolution can be neglected. Within this approximation, the important energy levels can be considered as equally spaced, and one obtains a periodic motion of the wave-packet, with period:

$$T_{\text{recurrence}} = \frac{2\pi\hbar}{\frac{dE_n}{dn}(n_0)}. \tag{16}$$

In the standard semiclassical WKB approximation (discussed in section 2.1) [7], this is nothing but the classical period of the motion at energy E_{n_0}, and one recovers the similarity between the quantum motion of the wave-packet and the classical motion of a particle.

At longer times, the contributions of the various eigenstates to the dynamics of the wave-packet will come out of phase because of the second order term in eq. (15), resulting in spreading and collapse of the wave-packet. A rough estimate of the collapse time is thus when the relevant phases have changed by 2π. One obtains:

$$T_{\text{collapse}} \simeq \frac{1}{(\Delta n)^2} \, \frac{2\hbar}{\frac{d^2 E_n}{dn^2}(n_0)}. \tag{17}$$

Using the standard WKB approximation, one can show that this expression actually corresponds to the time needed for the corresponding classical phase space density to significantly spread under the influence of the *classical* evolution.

At still longer times, a pure quantum phenomenon appears, due to the discrete nature of the energy spectrum. Since the $(n - n_0)^2$ factors in eq. (15) are all integers, the second order contributions to the phase are all integer multiples of the phase of the $n - n_0 = 1$ term. If the latter is an integer multiple of 2π, *all* the second order contributions will rephase, inducing a revival of the wave-packet in its original shape. A refined estimation of the revival time actually shows that this analysis overestimates the revival time by a factor two. [2] The correct result is [8–11]:

$$T_{\text{revival}} = \frac{2\pi\hbar}{\frac{d^2 E_n}{dn^2}(n_0)}. \tag{18}$$

Based on the very elementary considerations above, we can so far draw the following conclusions:

- An initially localized wave-packet will follow the classical equations of motion for a finite time $t \sim T_{\text{recurrence}}$;
- its localization properties *cannot* be stationary as time evolves;
- in general, the initial quasi-classical motion is followed by collapse and revival, with the corresponding time scales $T_{\text{recurrence}} < T_{\text{collapse}} < T_{\text{revival}}$.

In the sequel of this report, we will show how under very general conditions it is indeed possible to create wave-packets as single eigenstates of quantum systems, i.e., as localized ground states in an appropriately defined reference frame. The most suitable framework is to consider quantum evolution in classical phase space, that provides a picture which is *independent* of the choice of

[2] It must also be noted that, at simple rational multiples (such as 1/3, 1/2, 2/3) of the revival time, one observes "fractional revivals" [8–11], where only part of the various amplitudes which contribute to eq. (13) rephase. This generates a wave-function split into several individual wave-packets, localized at different positions along the classical orbit.

the basis and allows for an immediate comparison with the classical Hamiltonian flow. In addition, such a picture motivates a semiclassical interpretation, which we will expand upon in sec. 2. The appropriate technical tool for a phase space description are quasiprobability distributions [12] as the Wigner representation of the state $|\psi(t)\rangle$,

$$W(\vec{r},\vec{p}) = \frac{1}{(2\pi\hbar)^f} \int \psi^*\left(\vec{r}+\frac{\vec{x}}{2}\right)\psi\left(\vec{r}-\frac{\vec{x}}{2}\right)\exp\left(i\frac{\vec{x}.\vec{p}}{\hbar}\right)\,\mathrm{d}^f\vec{x}, \tag{19}$$

where f is the number of degrees of freedom.

The Wigner density $W(\vec{r},\vec{p})$ is real, but not necessarily positive [12,13]. Its time-evolution follows from the Schrödinger equation [12]:

$$\hbar\frac{\partial W(\vec{r},\vec{p},t)}{\partial t} = -2H(\vec{r},\vec{p},t)\sin\left(\frac{\hbar\Lambda}{2}\right)\,W(\vec{r},\vec{p},t), \tag{20}$$

where

$$\Lambda = \overleftarrow{\nabla}_{\vec{p}}\overrightarrow{\nabla}_{\vec{r}} - \overleftarrow{\nabla}_{\vec{r}}\overrightarrow{\nabla}_{\vec{p}}, \tag{21}$$

and the arrows indicate in which direction the derivatives act. Eq. (20) can serve to motivate the semiclassical approach. Indeed, the sin function can be expanded in a Taylor series, i.e. a power expansion in $\hbar$. At lowest non–vanishing order, only terms linear in Λ contribute and one obtains:

$$\frac{\partial W(\vec{r},\vec{p},t)}{\partial t} = \{H, W(\vec{r},\vec{p},t)\}, \tag{22}$$

where $\{.,.\}$ denotes the classical Poisson bracket [3]: [3]

$$\{f,g\} = \sum_{i=1\ldots f}\frac{\partial f}{\partial r_i}\frac{\partial g}{\partial p_i} - \frac{\partial f}{\partial p_i}\frac{\partial g}{\partial r_i}. \tag{23}$$

Eq. (22) is nothing but the classical Liouville equation [3] which describes the classical evolution of a phase space density. Hence, in the "semiclassical limit" $\hbar \to 0$, the Wigner density evolves classically. Corrections of higher power in $\hbar$ can be calculated systematically. For example, the next order is $\hbar^3 H\Lambda^3 W/24$ in eq. (20), and generates terms which contain third order derivatives (in either position and/or momentum) of the Hamiltonian. Therefore, for a Hamiltonian of maximal degree two in position and/or momentum, all higher order terms in eq. (20) vanish and the Wigner distribution follows the classical evolution for an arbitrary initial phase space density, and for arbitrarily long times. The harmonic oscillator is an example of such a system [2,16], in agreement with our discussion of eq. (15) above.

[3] We choose here the most common definition of the Poisson bracket. Note, however, that some authors [14,15] use the opposite sign!

Now, once again, why does a wave-packet spread? At first sight, it could be thought that this is due to the higher order terms in eq. (20), and thus of quantum origin. This is not true and spreading of a wave-packet has a purely classical origin, as illustrated by the following example. Let us consider a one-dimensional, free particle (i.e. no potential), initially described by a Gaussian wave-function with average position z_0, average momentum $p_0 > 0$, and spatial width σ:

$$\psi(z, t = 0) = \frac{1}{\pi^{1/4}\sqrt{\sigma}} \exp\left(i\frac{p_0 z}{\hbar} - \frac{(z - z_0)^2}{2\sigma^2}\right). \tag{24}$$

The corresponding Wigner distribution is a Gaussian in phase space:

$$W(z, p, t = 0) = \frac{1}{\pi\hbar} \exp\left(-\frac{(z - z_0)^2}{\sigma^2} - \frac{\sigma^2(p - p_0)^2}{\hbar^2}\right). \tag{25}$$

As the Hamiltonian is quadratic in the momentum, without potential, this distribution evolves precisely alike the equivalent classical phase space density. Hence, the part of the wave-packet with $p > p_0$ will evolve with a larger velocity than the part with $p < p_0$. Even if both parts are initially localized close to z_0, the contribution of different velocity classes implies that their distance will increase without bound at long times. The wave-packet will therefore *spread*, because the various *classical* trajectories have different velocities. Spreading is thus a completely classical phenomenon.

This can be seen quantitatively by calculating the exact quantum evolution. One obtains

$$W(z, p, t) = \frac{1}{\pi\hbar} \exp\left(-\frac{(z - z_0 - pt/m)^2}{\sigma^2} - \frac{\sigma^2(p - p_0)^2}{\hbar^2}\right) \tag{26}$$

for the Wigner distribution, and

$$\psi(z, t) = \frac{1}{\pi^{1/4}} \frac{\mathrm{e}^{i\phi}}{\left(\sigma^2 + \frac{\hbar^2 t^2}{m^2\sigma^2}\right)^{1/4}} \exp\left\{i\frac{p_0 z}{\hbar} - \frac{\left(z - z_0 - \frac{p_0 t}{m}\right)^2}{2\sigma^2 + \frac{2i\hbar t}{m}}\right\} \tag{27}$$

for the wave-function ($\mathrm{e}^{i\phi}$ is an irrelevant, complicated phase factor). The former is represented in fig. 1, together with the evolution of a swarm of classical particles with an initial phase space density identical to the one of the initial quantum wave-packet. Since the quantum evolution follows exactly the classical one, the phase space volume of the wave-packet is preserved. However, the Wigner distribution is progressively stretched along the z axis.

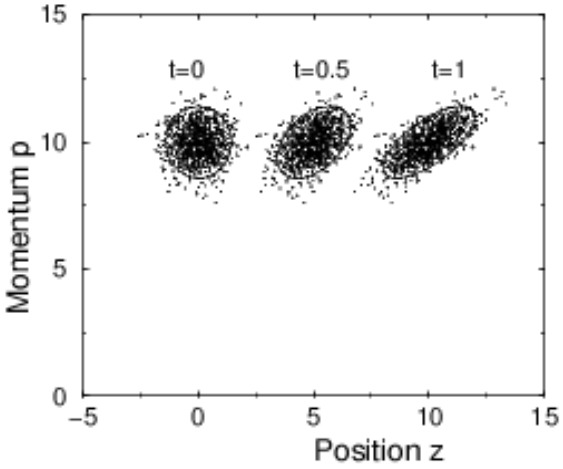

Fig. 1. Evolution of the Wigner density of a wave-packet for a free particle moving in a one-dimensional configuration space, compared to the classical evolution of a swarm of classical particles with the same initial probability density. While the uncertainty in momentum does not vary with time, the Wigner density stretches along the position coordinate and loses its initial minimum uncertainty character. This implies spreading of the wave-packet. This has a purely classical origin, as shown by the classical evolution of the swarm of particles, which closely follow the quantum evolution. The contour of the Wigner density is chosen to contain 86% of the probability.

This results in a less and less localized wave-packet, with

$$\begin{cases} \Delta z(t) = \dfrac{\sigma}{\sqrt{2}}\sqrt{1+\dfrac{\hbar^2 t^2}{m^2\sigma^4}}, \\ \Delta p(t) = \dfrac{\hbar}{\sigma\sqrt{2}}. \end{cases} \tag{28}$$

The product $\Delta z \Delta p$, initially minimum $(\hbar/2)$, continuously increases and localization is eventually lost.

1.2 Gaussian wave-packets – Coherent states

We have already realized above that, for the harmonic oscillator, the second derivative d^2E_n/dn^2 in eq. (15) vanishes identically, and a wave-packet does not spread, undergoing periodic motion. For this specific system, one can define a restricted class of wave-packets, which are minimum uncertainty states (i.e., $\Delta z \Delta p = \hbar/2$), and remain minimal under time-evolution [2]. Nowadays, these states are known as "coherent" states of the harmonic oscillator [16], and are frequently employed in the analysis of simple quantum systems such as the quantized electromagnetic field [17,18]. They have Gaussian wave-functions, see fig. 2(a), given by eq. (24), and characterized by an average position z_0,

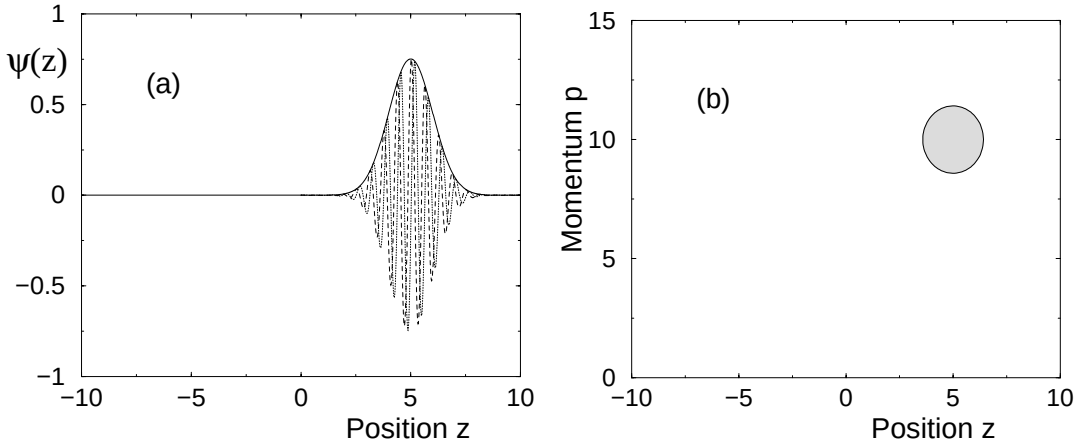

Fig. 2. (a): Coherent state of the harmonic oscillator [2]. The probability density and the modulus of the wave-function (solid line) have a Gaussian distribution. The real (dashed line) and the imaginary (dotted line) part of the wave-function show, in addition, oscillations which reflect the non-vanishing momentum. Whereas the envelope of the wave-function preserves its shape under time evolution, the frequency of the oscillations exhibits the same time dependence as the momentum of the corresponding classical particle. (b): Contour of the corresponding Wigner distribution which shows localization in both position and momentum. The isovalue for the contour is chosen to enclose 86% of the total probability.

an average momentum p_0, and a spatial width

$$\sigma = \sqrt{\frac{\hbar}{m\omega}}, \tag{29}$$

where ω is the classical eigenfrequency of the harmonic oscillator. The corresponding Wigner distribution, eq. (25), also has Gaussian shape. The properties of coherent states are widely discussed in the litterature, see [19,20].

In the "naturally scaled", dimensionless coordinates $z\sqrt{m\omega/\hbar}$ and $p/\sqrt{m\omega\hbar}$, the classical trajectories of the harmonic oscillator are circles, and the Wigner distribution is an isotropic Gaussian centered at (z_0, p_0), see fig. 2(b). Under time evolution, which follows precisely the classical dynamics, its isotropic Gaussian shape is preserved.

An important point when discussing wave-packets is to avoid the confusion between localized wave-packets (as defined above) and minimum uncertainty (coherent or squeezed [18]) states. The latter are just a very restricted class of localized states. They are the best ones in the sense that they have optimum localization. On the other hand, as soon as dynamics is considered, they have nice properties only for harmonic oscillators. In generic systems, they spread exactly like other wave-packets. Considering only coherent states as good semiclassical analogs of classical particles is in our opinion a too formal point of view. Whether the product $\Delta z \Delta p$ is exactly $\hbar/2$ or slightly larger is

certainly of secondary relevance for the semiclassical character of the wave-packet. What counts is that, in the semiclassical limit $\hbar \to 0$, the wave-packet is asymptotically perfectly localized in all directions of phase space. This was Schrödinger's original concern, without reference to the actual value of $\Delta z \Delta p$ [2].

Finally, for future applications, let us define the so called Husimi representation of the quantum wave-function [21]. It is the squared projection of a given quantum state over a set of coherent states. Let us denote the gaussian wavefunction of eq. (24) (with σ given by eq. (29)) as $|\mathrm{Coh}(z_0, p_0)\rangle$. Then the Husimi representation of $\psi(z)$ is defined as

$$\mathrm{Hus}(z,p) = \frac{1}{\pi} |\langle \mathrm{Coh}(z,p)|\psi\rangle|^2, \tag{30}$$

where the factor $1/\pi$ is due to the resolution of unity in the coherent states basis [19] and is often omitted (to confuse the reader). Alternatively, the Husimi function may be looked upon as a Wigner function convoluted with a Gaussian [12].

1.3 A simple example: the one-dimensional hydrogen atom

We now illustrate the ideas discussed in the preceding sections, using the specific example of a one-dimensional hydrogen atom. This object is both, representative of generic systems, and useful for atomic systems to be discussed later in this paper. We choose the simplest hydrogen atom: we neglect all relativistic, spin and QED effects, and assume that the nucleus is infinitely massive. The Hamiltonian reads:

$$H = \frac{p^2}{2m} - \frac{e^2}{z}, \tag{31}$$

where m is the mass of the electron, $e^2 = q^2/4\pi\epsilon_0$, with q the elementary charge, and z is restricted to the positive real axis. The validity of this model as compared to the real 3D atom will be discussed in sec. 3.3.

Here and in the rest of this paper, we will use atomic units, defined by m, e^2 and $\hbar$. The unit of length is the Bohr radius $a_0 = \hbar^2/me^2 = 5.2917 \times 10^{-11}$ m, the unit of time is $\hbar^3/me^4 = 2.4189 \times 10^{-17}$ s, the unit of energy is the Hartree $me^4/\hbar^2 = 27.2$ eV, *twice* the ionization energy of the hydrogen atom, and the unit of frequency is $me^4/2\pi\hbar^3 = 6.5796 \times 10^{16}$ Hz [22].

With these premises, the energy levels are: [4]

$$E_n = -\frac{1}{2n^2}, \qquad \text{for } n \geq 1. \tag{32}$$

Clearly, the levels are not equally spaced, and therefore (see eq. (15)) any wave-packet will spread.

Fig. 3 shows the evolution of a wave-packet built from a linear combination of eigenstates of H, using a Gaussian distribution of the coefficients c_n in eq. (13). The distribution is centered at $n_0 = 60$, with a width $\Delta n = 1.8$ for the $|c_n|^2$. The calculation is done numerically, but is simple in the hydrogen atom since all ingredients – energy levels and eigenstates – are known analytically. At time $t = 0$, the wave-packet is localized at the outer turning point (roughly at a distance $2n_0^2$ from the origin), and has zero initial momentum; its shape is roughly Gaussian. After a quarter of a classical Kepler period $T_{\text{recurrence}}$, it is significantly closer to the nucleus, with negative velocity, following the classical trajectory. After half a period, it has reached the nucleus (it is essentially localized near the origin). However, interference fringes are clearly visible: they originate from the interference between the head of the wave-packet, which has already been reflected off the nucleus, and its tail, which has not yet reached the nucleus. After 3/4 of a period, the interference fringes have disappeared, and the wave-packet propagates to the right. It has already spread significantly. After one period, it is close to its initial position, but no more as well localized as initially. This recurrence time is given by eqs. (16) and (32):

$$T_{\text{recurrence}} = 2\pi n_0^3. \tag{33}$$

After few periods, the wave-packet has considerably spread and is now completely delocalized along the classical trajectory. The time for the collapse of the wave-packet is well predicted by eq. (17):

$$\begin{aligned} T_{\text{collapse}} &\simeq \frac{2n_0^4}{3(\Delta n)^2} = \frac{n_0}{3\pi(\Delta n)^2} \times T_{\text{recurrence}} \\ &= 1.96 \times T_{\text{recurrence}}, \text{ for } n_0 = 60 \text{ and } \Delta n = 1.8. \end{aligned} \tag{34}$$

Finally, after 20 periods, the wave-packet revives with a shape similar to its initial state. Again, this revival time is in good agreement with the theoretical prediction, eq. (18):

$$T_{\text{revival}} = \frac{2\pi n_0^4}{3} = \frac{n_0}{3} \times T_{\text{recurrence}}$$

[4] The present analysis is restricted to bound states of the atom. Continuum (i.e., scattering) states also exist but usually do not significantly contribute to the wave-packet dynamics. If needed, they can be incorporated without any fundamental difficulty [23,24].

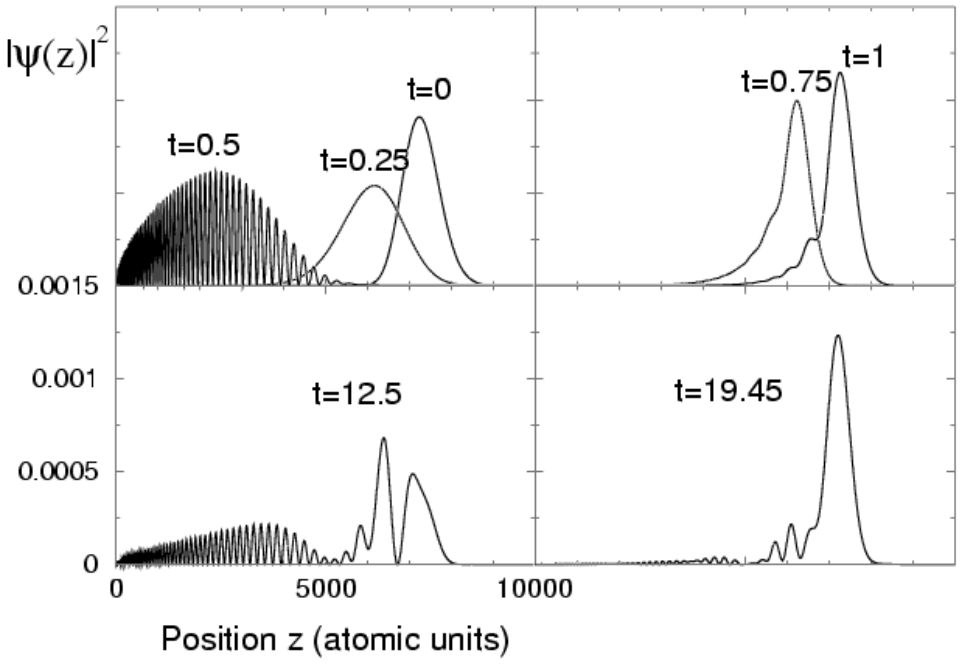

Fig. 3. Time evolution of an initially localized wave-packet in the one-dimensional hydrogen atom, eq. (31). The wave-packet is constructed as a linear superposition of energy eigenstates of H, with a Gaussian distribution (centered at $n_0 = 60$, with a width $\Delta n = 1.8$ of the $|c_n|^2$) of the coefficients c_n in eq. (10). Time t is measured in units of the classical Kepler period $T_{\rm recurrence}$, eq. (33). Note the quasiclassical approach of the wave-packet to the nucleus, during the first half period (top left), with the appearance of interference fringes as the particle is accelerated towards the Coulomb center. After one period (top right) the wave-packet almost resumes its initial shape at the outer turning point of the classical motion, but exhibits considerable dispersion (collapse) after few Kepler cycles (bottom left). Leaving a little more time to the quantum evolution, we observe a non-classical revival after approx. 20 Kepler cycles (bottom right). Recurrence, collapse and revival times are very well predicted by eqs. (33), (34) and (35).

$$= 20 \times T_{\rm recurrence}, \text{ for } n_0 = 60 \text{ and } \Delta n = 1.8. \tag{35}$$

At longer times, the wave-packet continues to alternate between collapses and revivals. In fig. 4, we show the temporal evolution of the product $\Delta z \Delta p$. It is initially close to the Heisenberg limit (minimum value) $\hbar/2$, and oscillates at the frequency of the classical motion with a global increase. When the wave-packet has completely spread, the uncertainty product is roughly constant, with apparently erratic fluctuations. At the revival time, the uncertainty undergoes again rather orderly oscillations of a relatively large magnitute reaching, at minima, values close to $\hbar$. That is a manifestation of its

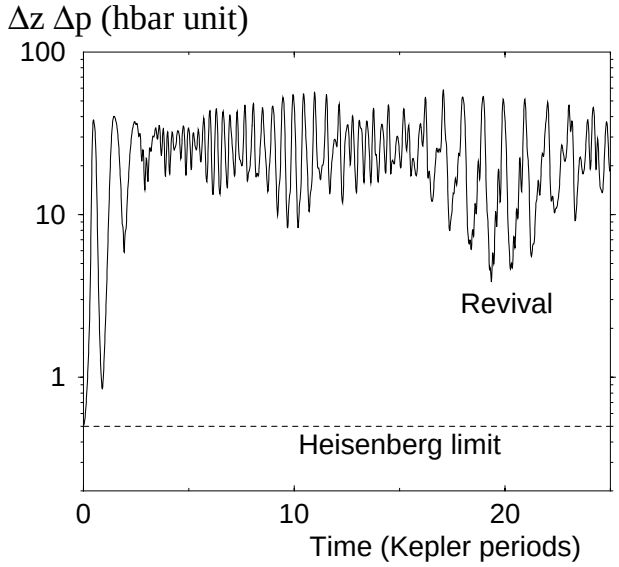

Fig. 4. Time evolution of the uncertainty product $\Delta z \Delta p$ (in units of $\hbar$) of the wave-packet shown in fig. 3. Starting out from minimum uncertainty, $\Delta z \Delta p \simeq \hbar/2$ (the Heisenberg limit, eq. (1)), the wave-packet exhibits some transient spreading on the time scale of a Kepler period $T_{\rm recurrence}$, thus reflecting the classical motion (compare top left of fig. 3), collapses on a time scale of few Kepler cycles (manifest in the damping of the oscillations of $\Delta z \Delta p$ during the first five classical periods), shows a fractional revival around $t \simeq 10 \times T_{\rm recurrence}$, and a full revival at $t \simeq 20 \times T_{\rm recurrence}$. Note that, nontheless, even at the full revival the contrast of the oscillations of the uncertainty product is reduced as compared to the initial stage of the evolution, as a consequence of higher-order corrections which are neglected in eq. (15).

partial relocalization.

For the three-dimensional hydrogen atom, the energy spectrum is exactly the same as in one dimension. This implies that the temporal dynamics is built from exactly the same frequencies; thus, the 3D dynamics is essentially the same as the 1D dynamics. [5] Indeed, collapses and revivals of the wave-packet were also observed, under various experimental conditions, in the laboratory [5,11,25,26]. Fig. 5 shows the evolution of a minimum uncertainty wave-packet of the 3D atom, initially localized on a circular Kepler orbit of the electron. It is built as a linear combination of circular hydrogenic states (i.e., states with maximum angular and magnetic quantum numbers $L = M = n - 1$), using the same Gaussian distribution of the coefficients as in fig. 3. As expected, the wave-packet spreads along the circular trajectory (but not transversally to it) and eventually re-establishes its initial shape after $T_{\rm revival}$. Figure 6 shows

[5] In a generic, multidimensional, integrable system, there are several different classical frequencies along the various degrees of freedom. Hence, only partial revivals of the wave-packet at various times are observed. The 3D hydrogen atom is *not* generic, because the three frequencies are degenerate, which opens the possibility of a *complete* revival, *simultaneously* along all three coordinates.

the corresponding evolution of a swarm of classical particles, for the same initial phase space density. The spreading of the classical distribution and of the quantum wave-packet proceeds very similarly, whereas the revival is completely absent in the classical evolution, which once more illustrates its purely quantum origin.

Finally, let us notice that collapse and revival of a 3D wave-packet depend on the principal quantum number n_0 only – see eqs. (34) and (35) – and are independent of other parameters which characterize the classical motion, such as the eccentricity and the orientation of the classical elliptical trajectory. This establishes that a 3D wave-packet with low average angular momentum (and, a fortiori, a 1D wave-packet as shown in fig. 3) – which deeply explores the non-linearity of the Coulomb force – does not disperse faster than a circular wave-packet which essentially feels a constant force. Hence, arguments on the non-linear character of the interaction should be used with some caution.

There have been several experimental realizations of electronic wave-packets in atoms [4,5,11,25,27,28], either along the pure radial coordinate or even along angular coordinates too. However, all these wave-packets dispersed rather quickly.

1.4 How to overcome dispersion

Soon after the discovery of quantum mechanics, the spreading of wave-packets was realized and attempts were made to overcome it [2]. From eq. (13), it is however clear that this is only possible if the populated energy levels are equally spaced. In practice, this condition is only met for the harmonic oscillator (or simple tops and rotors). In any other system, the anharmonicity of the energy ladder will induce dispersion. Hence, the situation seems hopeless.

Surprisingly, it is classical mechanics which provides us with a possible solution. Indeed, as discussed above, a quantum wave-packet spreads exactly as the corresponding swarm of classical particles. Hence, dispersion can be overcome if all classical trajectories behave similarly in the long time limit. In other words, if an initial volume of phase space remains well localized under time evolution, it is reasonable to expect that a wave-packet built on this initial volume will not spread either. The simplest example is to consider a stable fixed point: by definition [3], every initial condition in its vicinity will forever remain close to it. The corresponding wave-packet indeed does not spread at long times ... though this is of limited interest, as it is simply at rest!

Another possibility is to use a set of classical trajectories which all exhibit the same periodic motion, *with the same period for all trajectories*. This condition, however, is too restrictive, since it leads us back to the harmonic oscillator.

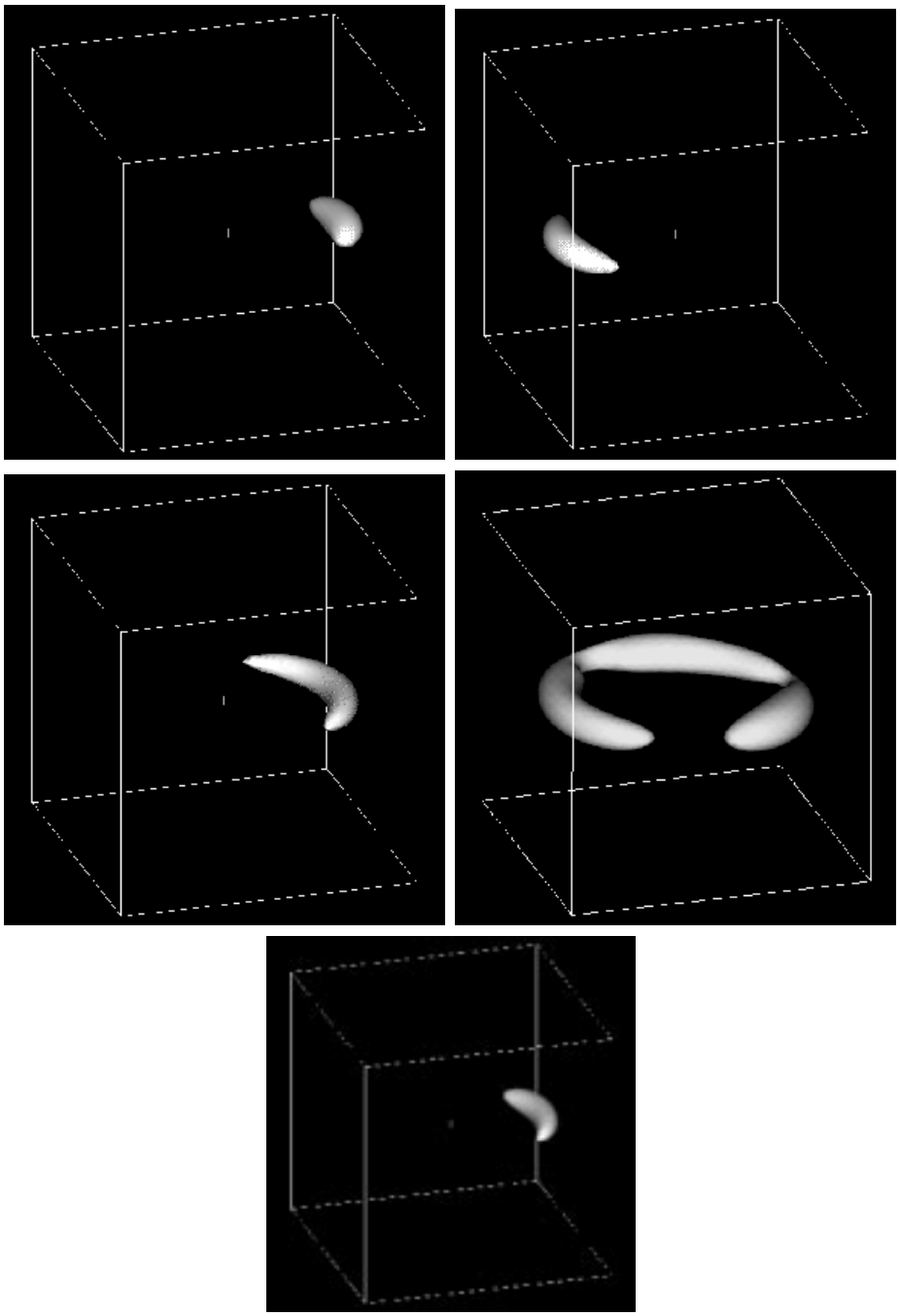

Fig. 5. Time evolution of a wave-packet launched along a circular Kepler trajectory, with the same Gaussian weights c_n, eq. (11), as employed for the one-dimensional example displayed in fig. 3, i.e., centered around the principal quantum number $n_0 = 60$. Since the relative phases accumulated during the time evolution only depend on n_0 – see eq. (13) – we observe precisely the same behaviour as in the one-dimensional case: classical propagation at short times (top), followed by spreading and collapse (middle), and revival (bottom). The snapshots of the wave function are taken at times (in units of $T_{\mathrm{recurrence}}$) $t = 0$ (top left), $t = 0.5$ (top right), $t = 1$ (middle left), $t = 12.5$ (middle right), and $t = 19.45$ (bottom). The cube size is 10000 Bohr radii, centered on the nucleus (marked with a cross). The radius of the circular wave-packet trajectory equals approx. 3600 Bohr radii.

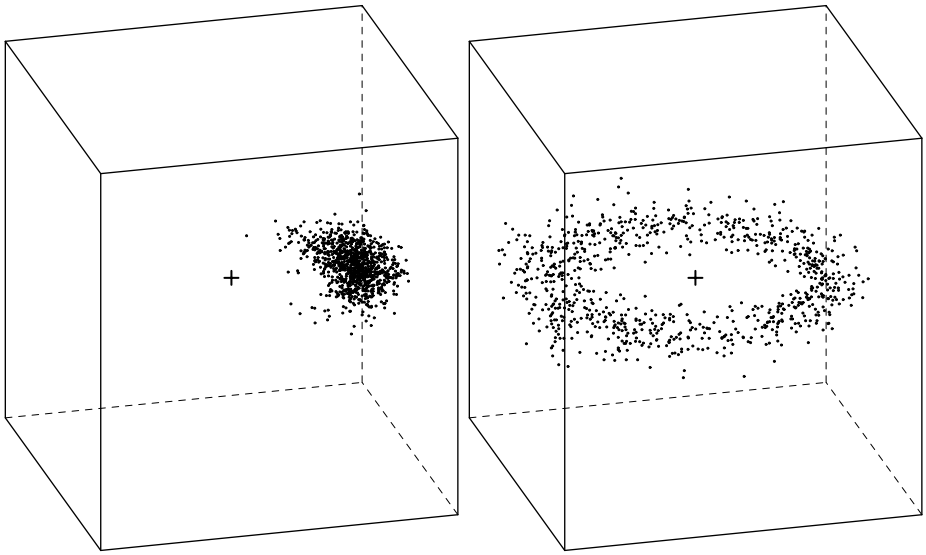

Fig. 6. Classical time evolution of a Gaussian (in spherical coordinates) phase space density fitted to the minimum uncertainty wave-packet of fig. 5 at time $t = 0$ (left). As time evolves, the classical phase space density spreads along the circular Kepler orbit ($t = 12.5$, right), but exhibits no revival. Hence, wave-packet spreading is of purely classical origin, only the revival is a quantum feature. The cube size is 10000 Bohr radii, centered on the nucleus (marked with a cross). The radius of the circular wave-packet trajectory equals approx. 3600 Bohr radii.

Though, we can slightly relax this constraint by allowing classical trajectories which are not strictly periodic but quasi-periodic and staying forever in the vicinity of a well defined periodic orbit: A wave-packet built on such orbits should evolve along the classical periodic orbit while keeping a finite dispersion around it.

It happens that there is a simple possibility to generate such classical trajectories *locked* on a periodic orbit, which is to drive the system by an external periodic driving. The general theory of nonlinear dynamical systems (described in section 3.1.1) [3,29] shows that when a nonlinear system (the internal frequency of which depends on the initial conditions) is subject to an external periodic driving, a *phase locking* phenomenon – known as a nonlinear resonance – takes place. For initial conditions where the internal frequency is close to the driving frequency (quasi-resonant trajectories), the effect of the coupling is to force the motion towards the external frequency. In other words, trajectories which, in the absence of the coupling, would oscillate at a frequency slightly lower than the driving are pushed forward by the nonlinear coupling, and trajectories with slightly larger frequency are pulled backward. In a certain region of phase space – termed "nonlinear resonance island" – all trajectories are trapped, and locked on the external driving. At the center of the resonance island, there is a stable periodic orbit which precisely evolves with the driving frequency. If the driving is a small perturbation, this periodic orbit is just the periodic orbit which, in the absence of driving, has exactly

the driving frequency. All the trajectories in the resonance island are winding around the central orbit with their phases locked on the external driving. The crucial point for our purposes is that the resonance island occupies a finite volume of phase space, i.e., it traps all trajectories in a window of internal frequencies centered around the driving frequency. The size of this frequency window *increases* with the amplitude of the system-driving coupling, and, as we shall see in section 3.1, can be made large enough to support wave-packet eigenstates of the corresponding quantum system.

The classical trapping mechanism is illustrated in fig. 7 which shows a swarm of classical particles launched along a circular Kepler orbit of a three-dimensional hydrogen atom exposed to a resonant, circularly polarized microwave field: the effect of the microwave field is to lock the particles in the vicinity of a circular trajectory. Note that also the phase along the classical circular trajectory is locked: the particles are grouped in the direction of the microwave field and follow its circular motion without any drift. There is a striking difference with the situation shown previously in fig. 6, where the cloud of particles rapidly spreads in the absence of the microwave field (the same swarm of initial conditions is used in the two figures). In figure 7, there are few particles (about 10%) in the swarm which are not phase locked with the microwave field. This is due to the finite subvolume of phase space which is effectively phase locked. Particles in the tail of the initial Gaussian distribution may not be trapped [30].

Although the microwave field applied in fig. 7 amounts to less than 5% of the Coulomb field along the classical trajectory, it is sufficient to synchronize the classical motion. The same phenomenon carries over to quantum mechanics, and allows the creation of non-dispersive wave-packets, as will be explained in detail in section 3.1.2.

1.5 The interest of non-dispersive wave-packets

Schrödinger dreamt of the possibility of building quantum wave-packets following classical trajectories [2]. He succeded for the harmonic oscillator, but failed for other systems [31]. It was then believed that wave-packets must spread if the system is nonlinear, and this is correct for time-independent systems. However, this is not true *in general*, and we have seen in the previous section that clever use of the non-linearity may, on the contrary, *stabilize* a wave-packet and preserve it from spreading. Such non-dispersive wave-packets are thus a realization of Schrödinger's dream.

One has to emphasize strongly that they are *not* some variant of the coherent states of the harmonic oscillator. They are of intrinsically completely differ-

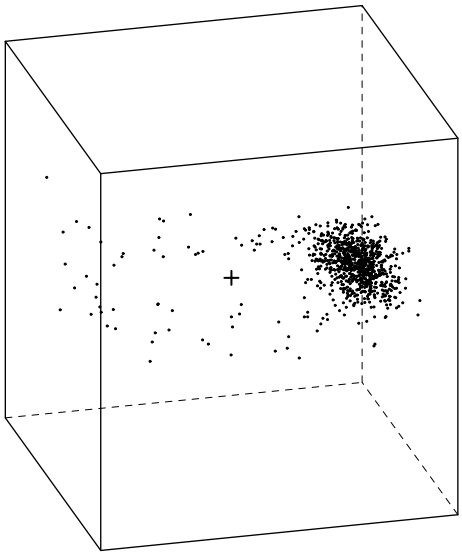

Fig. 7. The initially Gaussian distributed swarm of classical particles, shown in fig. 6, after evolution in the presence of the Coulomb field of the nucleus, with a resonant, circularly polarized microwave field in the plane of the circular Kepler trajectory added. The nonlinear resonance between the unperturbed Kepler motion and the driving field locks the phase of the particles on the phase of the driving field. As opposed to the free (classical) evolution depicted in fig. 6, the classical distribution does *not* exhibit dispersion along the orbit, except for few particles launched from the tail of the initial Gaussian distribution, which are not trapped by the principal resonance island.

ent origin. Paradoxically, they exist only if there is some non-linearity, i.e. some unharmonicity, in the classical system. They have some resemblance with classical solitons which are localized solutions of a non-linear equation that propagate without spreading. However, they are *not* solitons, as they are solutions of the *linear* Schrödinger equation. They are simply new objects.

Non-dispersive wave-packets in atomic systems were identified for the hydrogen atom exposed to a linearly polarized [32,33] and circularly polarized [34] microwave fields quite independently and using different physical pictures. The former approach associated the wave-packets with single Floquet states localized in the vicinity of the periodic orbit corresponding to atom-microwave nonlinear resonance. The latter treatment relied on the fact that a transformation to a frame corotating with the microwave field removes the explicit time-dependence of the Hamiltonian for the circular polarization (see section 3.4). The states localized near the equilibria of the rotating system were baptized "Trojan wave-packets" to stress the analogy of the stability mechanism with Trojan asteroids. Such an approach is, however, restricted to a narrow class of systems where the time-dependence can be removed and lacks the identification of the non-linear resonance as the relevant mechanism. We thus prefer to use in this review the more general term "non-dispersive wave-packets" noting also that in several other papers "non-spreading wave-packets" appear equally

often.

Apart from their possible practical applications (for example, for the purpose of quantum control of atomic or molecular fragmentation processes [28], or for information storage [35–38] in a confined volume of (phase) space for long times), they show the fruitful character of classical nonlinear dynamics. Indeed, here the nonlinearity is not a nuisance to be minimized, but rather the essential ingredient. From complex nonlinear dynamics, a simple object is born. The existence of such non-dispersive wave-packets it extremely difficult to understand (let alone to predict) from quantum mechanics and the Schrödinger equation alone. The classical nonlinear dynamics point of view is by far more illuminating and predictive. It is the classical mechanics inside which led Berman and Zaslavsky [39] to the pioneering discussion of states associated with the classical resonance island, the subsequent studies [40–42] further identified such states for driven one-dimensional systems using the Mathieu approach without, however, discussing the wave-packet aspects of the states. The best proof of the importance of the classical mechanics inside is that the non-dispersive wave-packets could have been discovered for a very long time (immediately after the formulation of the Schrödinger equation), but were actually identified only during the last ten years [43,32–34,44–75], after the recent major developments of nonlinear dynamics.

2 Semiclassical quantization

In this section, we briefly recall the basic results on the semiclassical quantization of Hamiltonian systems, which we will need for the construction of non-spreading wave-packets in classical phase space, as well as to understand their properties. This section does not contain any original material.

2.1 WKB quantization

For a one-dimensional, bounded, time-independent system, the Hamilton function (equivalent to the total energy) is a classical constant of motion, and the dynamics are periodic. It is possible to define canonically conjugate action-angle variables (I, θ), such that the Hamilton function depends on the action alone. The usual definition of the action along a periodic orbit (p.o.) writes:

$$I = \frac{1}{2\pi} \oint_{\text{p.o.}} p \, dz, \tag{36}$$

where p is the momentum along the trajectory.

The WKB (for Wentzel, Kramers, and Brillouin) method [76] allows to construct an approximate solution of the Schrödinger equation, in terms of the classical action-angle variables and of Planck's constant $\hbar$:

$$\psi(z) = \frac{1}{\sqrt{p}} \exp\left(\frac{i}{\hbar}\int p\, dz\right) \tag{37}$$

as an integral along the classical trajectory. This construction is possible if and only if the phase accumulated along a period of the orbit is an integer multiple of 2π. This means that the quantized states are those where the action variable I is an integer multiple of $\hbar$. This simple picture has to be slightly amended because the semiclassical WKB approximation for the wave-function breaks down at the turning points of the classical motion, where the velocity of the classical particle vanishes and, consequently, the expression (37) diverges. This failure can be repaired [76] by adding an additional phase $\pi/2$ for each turning point. This leads to the final quantization condition

$$I = \frac{1}{2\pi}\oint_{\text{p.o.}} p\, dz = \left(n + \frac{\mu}{4}\right)\hbar, \tag{38}$$

where n is a non-negative integer and μ – the "Maslov index" – counts the number of turning points along the periodic orbit ($\mu = 2$ for a simple 1D periodic orbit).

Thus, the WKB recipe is extremely simple: when the classical Hamilton function $H(I)$ is expressed in terms of the action I, the semiclassical energy levels are obtained by calculating $H(I)$ for the quantized values of I:

$$E_n = H\left(I = \left(n + \frac{\mu}{4}\right)\hbar\right). \tag{39}$$

Finally, as a consequence of eqs. (38),(39), the spacing between two consecutive semiclassical energy levels is simply related to the classical frequency Ω of the motion,

$$E_{n+1} - E_n \simeq \frac{dE_n}{dn} = \hbar\frac{dH}{dI} = \hbar\Omega(I), \tag{40}$$

a result which establishes the immediate correspondence between a resonant transition between two quantum mechanical eigenstates in the semiclassical regime, and resonant driving of the associated classical trajectory.

In the vicinity of a fixed (equilibrium) point, the Hamilton function can be expanded at second order (the first order terms are zero, by definition of the fixed point), leading to the "harmonic approximation". If the fixed point is stable, the semiclassical WKB quantization of the harmonic approximation gives exactly the quantum result, although the semiclassical wave-function, eq. (37), is incorrect. This remarkable feature is not true for an unstable fixed

point (where classical trajectories escape far from the fixed point), and the WKB approximation fails in this case.

2.2 EBK quantization

For a multi-dimensional system, it is a much more complicated task to extract the quantum mechanical eigenenergies from the classical dynamics of a Hamiltonian system. The problem can be solved for *integrable* systems, where there are as many constants of motion as degrees of freedom [77]. This is known as EBK (for Einstein, Brillouin, and Keller) quantization [78], and is a simple extension of the WKB quantization scheme. Let us choose two degrees of freedom for simplicity, the extension to higher dimensions being straightforward. If the system is integrable, the Liouville-Arnold theorem [3] assures the existence of two pairs of canonically conjugate action-angle variables, (I_1, θ_1) and (I_2, θ_2), such that the classical Hamilton function depends only on the actions:

$$H = H(I_1, I_2). \tag{41}$$

The classical motion is periodic along each angle (the actions being constants of the motion) with frequencies

$$\Omega_1 = \frac{\partial H}{\partial I_1}, \tag{42}$$

$$\Omega_2 = \frac{\partial H}{\partial I_2}. \tag{43}$$

In the generic case, these two frequencies are incommensurate, such that the full motion in the four-dimensional phase space is quasi-periodic, and densely fills the so-called "invariant torus" defined by the constant values I_1 and I_2. The semiclassical wave-function is constructed similarly to the WKB wave-function. Turning points are now replaced by caustics [29,78,79] of the classical motion (where the projection of the invariant torus on configuration space is singular), but the conclusions are essentially identical. The single-valued character of the wave-function requires the following quantization of the actions:

$$I_1 = \left(n_1 + \frac{\mu_1}{4}\right)\hbar, \tag{44}$$

$$I_2 = \left(n_2 + \frac{\mu_2}{4}\right)\hbar, \tag{45}$$

where n_1, n_2 are two non-negative integers, and μ_1, μ_2 the Maslov indices (counting the number of caustics encountered on the torus) along the θ_1, θ_2 directions. Once again, the semiclassical energy levels (which now depend on two quantum numbers) are obtained by substitution of these quantized values into the classical Hamilton function.

An alternative formulation of the EBK criterium is possible using the original position-momentum coordinates. Indeed, eq. (45) just expresses that, along any closed loop on the invariant torus, the phase accumulated by the wave-function is an integer multiple of 2π (modulo the Maslov contribution). Using the canonical invariance of the total action [77], the EBK quantization conditions can be written as:

$$\frac{1}{2\pi} \oint_{\text{closed path } \gamma_i} \vec{p}.\,\mathrm{d}\vec{\mathrm{r}} = \left(n_i + \frac{\mu_i}{4}\right)\hbar \tag{46}$$

where the integral has to be taken along two topologically independent closed paths (γ_1, γ_2) on the invariant torus.

Note that, as opposed to the WKB procedure in a 1D situation, the EBK quantization uses the invariant tori of the classical dynamics, *not* the trajectories themselves. When there is a stable periodic orbit, it is surrounded by invariant tori. The smallest quantized torus around the stable orbit is associated with a quantum number equal to zero for the motion transverse to the orbit: it defines a narrow tube around the orbit, whose projection on configuration space will be localized in the immediate vicinity of the orbit. Thus, the corresponding wave-function will also be localized close to this narrow tube, i.e., along the stable periodic orbit in configuration space. Transversely to the orbit, the wave-function (or the Wigner function) will essentially look like the ground state of an harmonic oscillator, i.e. like a Gaussian.

Finally, let us note that it is also possible to develop an analogous EBK scheme for periodically time dependent Hamiltonians [80] using the notion of an extended phase space [3]. Such an approach will be extensively used in the next section, so it is discussed in detail there.

2.3 Scars

When a periodic orbit is unstable, there is no torus closely surrounding it. However, it often happens that quantum eigenstates exhibit an increased probability density in the vicinity of unstable periodic orbits. This scarring phenomenon is nowadays relatively well understood, and the interested reader may consult references [81,82].

Similarly, some quantum states have an increased probability density in the vicinity of an unstable equilibrium point [33,83,84]. This localization is only partial. Indeed, since a quantum eigenstate is a stationary structure, some probability density *must* localize along the unstable directions of the classical Hamiltonian flow [77], and the localization cannot be perfect. This is in sharp contrast with stable equilibrium points and stable periodic orbits which – see

above – optimally support localized eigenstates.

Note that there is, however, a big difference between scarring and localization in the vicinity of an unstable fixed point. The latter phenomenon is of purely classical origin. Indeed, close to an equilibrium point, the velocity goes to zero and the particle consequently spends more time close to the equilibrium point than further away from it. The quantum eigenfunctions have the same property: the probability density is large near the equilibrium point. This trivial enhancement of the probability density is already well known for a one-dimensional system where the WKB wave-function, eq. (37), diverges when the momentum tends to zero. The localization effect near an unstable point is just the quantum manifestation of the critical slowing down of the classical particle [60].

3 Non-dispersive wave-packets and their realization in various atomic systems

3.1 General model – nonlinear resonances

In this section, we present the general theory of non-dispersive wave-packets. As explained in section 1.4, the basic ingredients for building a non-dispersive wave-packet are a non-linear dynamical system and an external periodic driving which is resonant with an internal frequency of the dynamical system. We present here a very general theory starting out from classical mechanics which provides us with the most suggestive approach to non-linear resonances. In a second step, we choose a pure quantum approach giving essentially the same physics.

We use a one-dimensional model, which displays all the interesting features of non-linear resonances. While the direct link between classical nonlinear resonances, the corresponding Floquet states, and non-dispersive wave-packets has been identified only recently [43,32,33,49,64] some aspects of the developments presented below may be found in earlier studies [39,85,40,42].

Several complications not included in the simple one-dimensional model are important features of "real systems". They are discussed at a later stage in this paper:

– the effect of additional degrees of freedom, in sections 3.3.2-3.5;
– higher nonlinear resonances (where the driving frequency is a multiple of the internal frequency), in section 5;
– an unbounded phase space, leading to the decay of non-dispersive wave-

packets (as "open quantum systems"), in section 7.1;
– sources of "decoherence", such as spontaneous emission of atomic wavepackets, in section 7.2;
– deviations from temporal periodicity, in section 8.3.

In particular cases, an apparently simpler approach is also possible (such as the use of the rotating frame for a Rydberg atom exposed to a circularly polarized electromagnetic field, see section 3.4). Despite all its advantages, it may be quite specific and too restricted to reveal nonlinear resonances as the actual cause of the phenomenon. Here, we seek the most general description.

3.1.1 Classical dynamics

Let us start from a time-independent, bounded, one-dimensional system described by the Hamilton function $H_0(p, z)$. Since energy is conserved, the motion is confined to a one-dimensional manifold in two-dimensional phase space. Except for energies which define a fixed point of the Hamiltonian dynamics (such that $\partial H_0/\partial z = 0$ and $\partial H_0/\partial p = 0$; these fixed points generically only exist at some isolated values of energy, for example at $E = 0$ for the harmonic oscillator), the motion is periodic in time, and the phase space trajectory is a simple closed loop.

It is always possible to find a set of canonically conjugate phase space coordinates adapted to the dynamics of the system. These are the action-angle coordinates (I, θ), whose existence is guaranteed by the Liouville-Arnold theorem [3], with:

$$0 \leq I, \tag{47}$$
$$0 \leq \theta \leq 2\pi, \tag{48}$$
$$\{\theta, I\} = 1, \tag{49}$$

and $\{.,.\}$ the usual Poisson brackets, eq. (23).

A fundamental property is that the Hamilton function in these coordinates depends on I alone, not on θ :

$$H_0 = H_0(I). \tag{50}$$

As a consequence of Hamilton's equations of motion, I is a constant of motion, and

$$\theta = \Omega t + \theta_0 \tag{51}$$

evolves linearly in time, with the angular velocity

$$\Omega(I) = \frac{\partial H_0}{\partial I}(I), \tag{52}$$

which depends on the action I. The period of the motion at a given value of I reads

$$T = \frac{2\pi}{\Omega(I)}. \tag{53}$$

In simple words, the action I is nothing but the properly "rescaled" total energy, and the angle θ just measures how time evolves along the (periodic) orbits. In a one-dimensional system, the action variable can be expressed as an integral along the orbit, see eq. (36).

Suppose now that the system is exposed to a periodic driving force, such that the Hamilton function, in the original coordinates, writes

$$H = H_0(p, z) + \lambda V(p, z) \cos \omega t, \tag{54}$$

with ω the frequency of the periodic drive and λ some small parameter which determines the strength of the perturbation. For simplicity, we choose a single cosine function to define the periodic driving. For a more complicated dependence on time [86], it is enough to expand it in a Fourier series, see section 3.5. The equations become slightly more complicated, but the physics is essentially identical.

We now express the perturbation $V(p, z)$ in action-angle coordinates. Since θ is $2\pi-$periodic, eq. (48), we obtain a Fourier series:

$$V(I, \theta) = \sum_{m=-\infty}^{+\infty} V_m(I) \ \exp(im\theta). \tag{55}$$

Note that, as θ evolves linearly with time t for the unperturbed motion (and therefore parametrizes an unperturbed periodic orbit), the V_m can also be seen as the Fourier components of $V(t)$ evaluated along the classical, unperturbed trajectory. Furthermore, since the Hamilton function is real, $V_{-m} = V_m^*$. Again for the sake of simplicity, we will assume that both are real and thus equal. The general case can be studied as well, at the price of slightly more complicated formulas.

Plugging eq. (55) in eq. (54) results in the following Hamilton function in action-angle coordinates,

$$H = H_0(I) + \lambda \sum_{m=-\infty}^{+\infty} V_m(I) \ \exp(im\theta) \cos \omega t, \tag{56}$$

which (assuming $V_{-m} = V_m$ – see above) can be rewritten as

$$H = H_0(I) + \lambda \sum_{m=-\infty}^{+\infty} V_m(I) \ \cos(m\theta - \omega t). \tag{57}$$

For λ sufficiently small, the phase space trajectories of the perturbed dynamics will remain close to the unperturbed ones (for short times). This means that $m\theta - \omega t$ evolves approximately linearly in time as $(m\Omega - \omega)t$ (see eq. (51)), while I is slowly varying. It is therefore reasonable to expect that all the terms $V_m(I)\ \cos(m\theta - \omega t)$ will oscillate rapidly and average out to zero, leading to an effective approximate Hamiltonian identical to the unperturbed one. Of course, this approach is too simple. Indeed, close to a "resonance", where $(s\Omega - \omega)$ is small, the various terms $V_m\ \cos(m\theta - \omega t)$ oscillate, except for the $m = s$ term which may evolve very *slowly* and affect the dynamics considerably. For simplicity, we restrict the present analysis to the principal resonance such that $\Omega \simeq \omega$. The extension to higher resonances (with $s\Omega \simeq \omega$) is discussed in section 5.

Our preceding remark is the basis of the "secular approximation" [3,18]. The guiding idea is to perform a canonical change of coordinates involving the slowly varying variable $\theta - \omega t$. Because of the explicit time dependence, this requires first the passage to an extended phase space, which comprises time as an additional coordinate. The Hamilton function in extended phase space is defined by

$$\mathcal{H} = P_t + H, \tag{58}$$

with P_t the momentum canonically conjugate to the new coordinate - time t. The physical time t is now parametrized by some fictitious time, say ξ. However,

$$\frac{\partial \mathcal{H}}{\partial P_t} = \frac{dt}{d\xi} = 1, \tag{59}$$

i.e., t and ξ are essentially identical. $\mathcal{H}$, being independent of ξ, is conserved as ξ evolves. The requested transformation to slowly varying variables $\theta - \omega t$ reads: [6]

$$\hat{\theta} = \theta - \omega t, \tag{60}$$

$$\hat{I} = I, \tag{61}$$

$$\hat{P}_t = P_t + \omega I, \tag{62}$$

which transforms $\mathcal{H}$ into

$$\hat{\mathcal{H}} = \hat{P}_t + H_0(\hat{I}) - \omega \hat{I} + \lambda \sum_{m=-\infty}^{+\infty} V_m(\hat{I})\ \cos(m\hat{\theta} + (m-1)\omega t). \tag{63}$$

[6] This *canonical* change of coordinates is often refered to as "passing to the rotating frame". It should however be emphasized that this suggests the correct picture *only* in phase space spanned by the action-angle coordinates (I, θ). In the original coordinates (p, z), the transformation is usually very complicated, and only rarely a standard rotation in configuration space (see also section 3.4).

This Hamilton function does not involve any approximation yet. Only in the next step we average $\hat{\mathcal{H}}$ over the fast variable t, i.e., over one period of the external driving. This has the effect of canceling all oscillating terms in the sum, except the resonant one, defined by $m = 1$. Consequently, we are left with the approximate, "secular" Hamilton function:

$$\mathcal{H}_{\rm sec} = \hat{P}_t + H_0(\hat{I}) - \omega\hat{I} + \lambda V_1(\hat{I})\cos\hat{\theta}. \tag{64}$$

The secular Hamilton function no longer depends on time. Hence, $\hat{P}_t$ is a constant of motion and we are left with an integrable Hamiltonian system living in a two-dimensional phase space, spanned by $(\hat{I}, \hat{\theta})$. The above averaging procedure is valid at first order in λ. Higher order expansions, using, e.g., the Lie algebraic transformation method [3], are possible.[7] Basically, the interesting physical phenomena are already present at lowest non-vanishing order, to which we will restrain in the following.

The dynamics generated by the secular Hamilton function is rather simple. At order zero in λ, $\hat{I}$ is constant and $\hat{\theta}$ evolves linearly with time. As we can read from eq. (64), a continuous family (parametrized by the value of $0 \leq \hat{\theta} < 2\pi$) of fixed points exists if $d\hat{\theta}/dt = \partial\mathcal{H}_{\rm sec}/\partial\hat{I}$ vanishes, i.e., at actions $\hat{I}_1$ such that

$$\Omega(\hat{I}_1) = \frac{\partial H_0}{\partial I}(\hat{I}_1) = \omega. \tag{65}$$

Thus, unperturbed trajectories that are *resonant* with the external drive are fixed points of the unperturbed secular dynamics. This is precisely why slowly varying variables are introduced.

Typically, eq. (65) has only isolated solutions – we will assume that in the following. Such is the case when $\partial^2 H_0/\partial I^2$ does not vanish – excluding the pathological situation of the harmonic oscillator, where all trajectories are simultaneously resonant. Hence, if $\partial^2 H_0/\partial I^2$ is positive, the line $(\hat{I} = \hat{I}_1, 0 \leq \hat{\theta} < 2\pi$, parametrized by $\hat{\theta})$ is a minimum of the unperturbed secular Hamilton function $\mathcal{H}_{\rm sec}$; if $\partial^2 H_0/\partial I^2$ is negative, it is a maximum.

At first order in λ, the fixed points of the secular Hamiltonian should have an action close to $\hat{I}_1$. Hence, it is reasonable to perform a power expansion of the unperturbed Hamiltonian in the vicinity of $\hat{I} = \hat{I}_1$. We obtain the following approximate Hamiltonian:

$$\mathcal{H}_{\rm pend} = \hat{P}_t + H_0(\hat{I}_1) - \omega\hat{I}_1 + \frac{1}{2}H_0''(\hat{I}_1)\ (\hat{I} - \hat{I}_1)^2 + \lambda V_1(\hat{I}_1)\cos\hat{\theta}, \tag{66}$$

[7] An example is given in [87], in a slightly different situation, where the perturbation is not resonant with the internal frequency.

with:

$$H_0^{''} = \frac{\partial^2 H_0}{\partial I^2}. \tag{67}$$

Consistently at lowest order in λ, it is not necessary to take into account the dependence of V_1 on $\hat{I}$.

As already anticipated by the label, $\mathcal{H}_{\rm pend}$ defined in eq. (66) describes a usual, one-dimensional pendulum: $\hat{\theta}$ represents the angle of the pendulum with the vertical axis, $\hat{I} - \hat{I}_1$ its angular velocity, $1/H_0^{''}(\hat{I}_1)$ its momentum of inertia and $\lambda V_1(\hat{I}_1)$ the gravitational field. This equivalence of the secular Hamilton function with that of a pendulum, in the vicinity of the resonant action $\hat{I}_1$, is extremely useful to gain some physical insight in the dynamics of any Hamiltonian system close to a resonance. In particular, it will render our analysis of non-dispersive wave-packets rather simple.

Figure 8 shows the isovalue lines of $\mathcal{H}_{\rm pend}$ in the $(\hat{I}, \hat{\theta})$ plane, i.e. the classical phase space trajectories in the presence of the resonant perturbation. In the absence of the resonant perturbation, these should be horizontal straight lines at constant $\hat{I}$. We observe that the effect of the resonant perturbation is mainly to create a new structure, called the "resonance island", located around the resonant action $\hat{I}_1$.

To characterize this structure, let us examine the fixed points of the Hamiltonian (66). They are easily calculated (imposing $\partial\mathcal{H}_{\rm pend}/\partial\hat{I} = \partial\mathcal{H}_{\rm pend}/\partial\hat{\theta} = 0$), and located at

$$\hat{I} = \hat{I}_1, \quad \hat{\theta} = 0, \quad \text{with energy } H_0(\hat{I}_1) - \omega\hat{I}_1 + \lambda V_1(\hat{I}_1), \tag{68}$$

and

$$\hat{I} = \hat{I}_1, \quad \hat{\theta} = \pi, \quad \text{with energy } H_0(\hat{I}_1) - \omega\hat{I}_1 - \lambda V_1(\hat{I}_1), \tag{69}$$

respectively.

If $H_0^{''}(\hat{I}_1)$ (and thus the "kinetic energy" part in $\mathcal{H}_{\rm pend}$) is positive, the minimum of the potential $\lambda V_1(\hat{I}_1)\cos\hat{\theta}$ corresponds to a global minimum of $\mathcal{H}_{\rm pend}$, and thus to a stable equilibrium point. The maximum of $\lambda V_1(\hat{I}_1)\cos\hat{\theta}$ is a saddle point of $\mathcal{H}_{\rm pend}$, and thus represents an unstable equilibrium point, as the standard intuition suggests. For $H_0^{''}(\hat{I}_1) < 0$ the situation is reversed – and less intuitive since the "kinetic energy" is negative – and the *maximum* of $\mathcal{H}_{\rm pend}$ is now a stable equilibrium point, as the reader may easily check by standard linear stability analysis in the vicinity of the fixed point. Thus, in compact form, if $\lambda V_1(\hat{I}_1)H_0^{''}(\hat{I}_1)$ is positive, $\hat{\theta} = \pi$ is a stable equilibrium point, while $\hat{\theta} = 0$ is unstable. If $\lambda V_1(\hat{I}_1)H_0^{''}(\hat{I}_1)$ is negative, the stable and unstable points are interchanged.

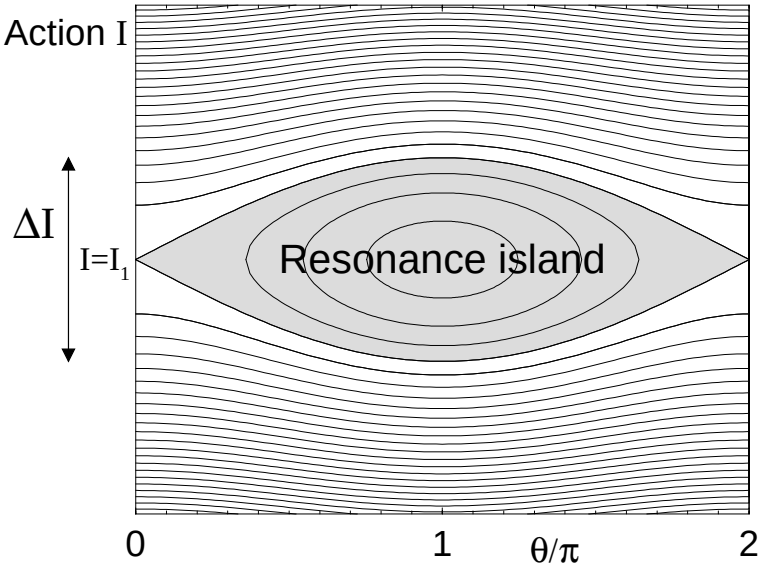

Fig. 8. Isovalues of the Hamiltonian $\mathcal{H}_{\rm pend}$ of a pendulum in a gravitational field. This Hamiltonian is a good approximation for the motion of a periodically driven system when the driving frequency is resonant with the internal frequency of the system. The stable equilibrium point of the pendulum is surrounded by an island of librational motion (shaded region). This defines the resonance island of the periodically driven system, where the internal motion is *locked* on the external driving. This nonlinear phase-locking phenomenon is essential for the existence of non-dispersive wave-packets.

There are two qualitatively different types of motion:

– Close to the stable equilibrium point of the pendulum, $\hat{\theta}$ oscillates periodically, with an amplitude smaller than π. This is the "librational motion" of the pendulum inside the resonance island. Any trajectory started within this region of phase space (the shaded area in fig. 8) exhibits librational motion. It should be realized that the resonance island confines the motion to finite intervals in $\hat{I}$ and $\hat{\theta}$, and thereby strongly affects all trajectories with action close to the resonant action. According to eqs. (68,69), the resonance island is associated with the energy range $[H_0(\hat{I}_1) - \omega\hat{I}_1 - |\lambda V_1(\hat{I}_1)|, H_0(\hat{I}_1) - \omega\hat{I}_1 + |\lambda V_1(\hat{I}_1)|]$.
– For any initial energy outside that energy range the pendulum has sufficient kinetic energy to rotate. This is the "rotational motion" of the pendulum outside the resonance island, where $\hat{\theta}$ is an unbounded and monotonous function of time. Far from the center of the island, the motion occurs at almost constant unperturbed action $\hat{I}$, with an almost constant angular velocity in $\hat{\theta}$, tending to the unperturbed motion. This illustrates that the effect of the perturbation is important for initial conditions close to the resonance island, but negligible for non-resonant trajectories.

The size of the resonance island can be simply estimated from eq. (66) and

fig. 8. The extension in $\hat{\theta}$ is 2π, its width in $\hat{I}$ (which depends on $\hat{\theta}$) is:

$$\Delta\hat{I} = 4\sqrt{\left|\frac{\lambda V_1(\hat{I}_1)}{H_0''(\hat{I}_1)}\right|}, \tag{70}$$

and the total area [3]:

$$A(\lambda) = 16\sqrt{\left|\frac{\lambda V_1(\hat{I}_1)}{H_0''(\hat{I}_1)}\right|}. \tag{71}$$

The dependence of $A(\lambda)$ on $\sqrt{|\lambda|}$ implies that even a small perturbation may induce significant changes in the phase space structure, provided the pertubation is resonant.

The above picture is valid in the rotating frame defined by eqs. (60-62). If we go back to the original action-angle coordinates (I, θ), the stable (resp. unstable) fixed point of the secular Hamiltonian is mapped on a stable (resp. unstable) periodic orbit whose period is *exactly* equal to the period of the driving perturbation, as a consequence of eq. (65). Any trajectory started in the vicinity of the stable periodic orbit will correspond to an initial point close to the fixed point in the rotating frame, and thus will remain trapped within the resonance island. In the original coordinate frame, it will appear as a trajectory evolving close to the stable periodic orbit forever. In particular, the difference in θ between the stable periodic orbit and any orbit trapped in the resonance island remains bounded within $(-\pi, +\pi)$, for arbitrarily long times. This means that the phase of any trapped trajectory cannot drift with respect to the phase of the periodic orbit. As the latter evolves at the driving frequency, we reach the conclusion that the phase of any trajectory started in the resonance island will be *locked* on the phase of the driving field. This is the very origin of the phase locking phenomenon discussed in section 1.4 above. A crucial point herein is that the resonance island covers a significant part of phase space with finite volume: it is the whole structure, not few trajectories, which is phase locked. This is why, further down, we will be able to build quantum wave-packets on this structure, which will be phase locked to the classical orbit and will not spread. The classical version of a non-spreading wave-packet thus consists of a family of trajectories, trapped within the resonance island, such that this family is invariant under the evolution generated by the pendulum Hamiltonian. The simplest possibility is to sample all trajectories within the "energy" range $[H_0(\hat{I}_1) - \omega\hat{I}_1 - |\lambda V_1(\hat{I}_1)|, H_0(\hat{I}_1) - \omega\hat{I}_1 + |\lambda V_1(\hat{I}_1)|]$ of the pendulum. In real space, this will appear as a localized probability density following the classical stable periodic orbit, reproducing its shape exactly after each period of the drive.

So far, to derive the characteristics of the resonance island, we have consistently used first order perturbation theory, which is valid for small λ. At higher

values of λ, higher order terms come into play and modify the shape and the precise location of the resonance island. However, it is crucial to note that the island itself considered as a structure is robust, and will survive up to rather high values of λ (as a consequence of the KAM theorem [3]). Since the size of the resonance island grows with $|\lambda|$, eq. (71), the island may occupy a significant area in phase space and eventually interact with islands associated with other resonances, for sufficiently large $|\lambda|$. The mechanism of this "resonance overlap" is rather well understood [88,89]: in general, the motion close to the separatrix (where the period of the classical motion of the pendulum tends to infinity) is most sensitive to higher order corrections. The general scenario is thus the nonintegrable perturbation of the separatrix and the emergence of a "stochastic" layer of chaotic motion in phase space, as $|\lambda|$ is increased. At still larger values of $|\lambda|$, chaos may invade large parts of phase space, and the resonance island may shrink and finally disappear. While considering realistic examples later-on, we shall enter the non-perturbative regime. Let us, however, consider first the quantum perturbative picture.

3.1.2 Quantum dynamics

As shown in the previous section, the dynamics of a one-dimensional system exposed to a weak, resonant, periodic driving is essentially regular and analogous to the one of a pendulum, eq. (67) (in the rotating frame, eqs. (60-62)). In the present section, we will show that the same physical picture can be employed in quantum mechanics, to construct non-dispersive wave-packets. They will follow the stable classical trajectory locked on the external drive, and exactly reproduce their initial shape after each period.

Our starting point is the time-dependent Schrödinger equation associated with the Hamiltonian (54): [8]

$$i\hbar \frac{d|\psi(t)\rangle}{dt} = (H_0 + \lambda V \cos\omega t)|\psi(t)\rangle. \tag{72}$$

Since the Hamiltonian (54) is periodic in time, the Floquet theorem [9] guarantees that the general solution of eq. (72) is given by a linear combination of elementary, time-periodic states – the so-called "Floquet eigenstates" of the system – multiplied by oscillatory functions:

$$|\psi(t)\rangle = \sum_j c_j \exp\left(-i\frac{\mathcal{E}_j t}{\hbar}\right)|\mathcal{E}_j(t)\rangle, \tag{73}$$

[8] For simplicity, we use the same notation for classical and quantum quantities, the distinction between them will become clear from the context.

[9] The Floquet theorem [90] in the time domain is strictly equivalent to the Bloch theorem for potentials periodic in space [91].

with

$$|\mathcal{E}_j(t+T)\rangle = |\mathcal{E}_j(t)\rangle. \tag{74}$$

The $\mathcal{E}_j$ are the "quasi-energies" of the system. Floquet states and quasi-energies are eigenstates and eigenenergies of the Floquet Hamiltonian

$$\mathcal{H} = H_0 + \lambda V \cos\omega t - i\hbar\frac{\partial}{\partial t}. \tag{75}$$

Note that, because of the time-periodicity with period $T = 2\pi/\omega$, the quasi-energies are defined modulo $\hbar\omega$ [92].

The Floquet Hamiltonian (75) is nothing but the quantum analog of the classical Hamiltonian (58) in extended phase space. Indeed, $-i\hbar\partial/\partial t$ is the quantum version of the canonical momentum P_t conjugate to time t. In strict analogy with the classical discussion of the previous section, it is the Floquet Hamiltonian in extended phase space which will be the central object of our discussion. It contains all the relevant information on the system, encoded in its eigenstates.

In a quantum optics or atomic physics context – with the external perturbation given by quantized modes of the electromagnetic field – the concept of "dressed atom" is widely used [18]. There, a given field mode and the atom are treated on an equal footing, as a composite quantum system, leading to a time-independent Hamiltonian (energy is conserved for the entire system comprising atom *and* field). This picture is indeed very close to the Floquet picture. If the field mode is in a coherent state [18] with a large average number of photons, the electromagnetic field can be treated (semi)classically – i.e., replaced by a cos time dependence and a fixed amplitude F – and the energy spectrum of the dressed atom exactly coincides with the spectrum of the Floquet Hamiltonian [92].

By its mere definition, eq. (74), each Floquet eigenstate is associated with a strictly time-periodic probability density in configuration space. Due to this periodicity with the period of the driving field, the probability density of a Floquet eigenstate in general changes its shape as time evolves, but recovers its initial shape after each period. Hence, the Floquet picture provides clearly the simplest approach to non-dispersive wave-packets. Given the ability to build a Floquet state which is well localized at a given phase of the driving field, it will *automatically* represent a non-dispersive wave-packet. In our opinion, this is a much simpler approach than the attempt to build an *a priori* localized wave-packet and try to minimize its spreading during the subsequent evolution [44,45,34,47].

Note that also the reverse property holds true. Any state with T-periodic probability density (and, in particular, any localized wave-packet propagat-

ing along a T-periodic classical orbit) has to be a single Floquet eigenstate: Such a state can be expanded into the Floquet eigenbasis, and during one period, the various components of the expansion accumulate phase factors $\exp(-i\mathcal{E}_i T/\hbar)$. Hence, the only solution which allows for a T-periodic density is a one-component expansion, i.e., a single Floquet eigenstate [10].

To summarize, the construction of non-dispersive wave-packets in a time-periodic system is equivalent to finding localized Floquet eigenstates. The existence of such states is far from obvious, as the Floquet spectrum is usually very complex, composed of quasi-bound states, resonances and continua. This is why a semiclassical analysis can be very helpful in finding these objects.

3.1.3 Semiclassical approximation

Dealing with highly excited states, a semiclassical approximation can be used to determine quasi-energies and Floquet eigenstates [80]. If the driving perturbation is sufficiently weak, we have shown in section 3.1.1 that the classical dynamics close to a nonlinear resonance is essentially regular and accurately described by the pendulum Hamiltonian (66). It describes a system with two degrees of freedom (along t and $\hat{\theta}$, with their conjugate momenta $\hat{P}_t$ and $\hat{I}$, respectively) which is essentially regular. For semiclassical quantization, we may then use the standard EBK rules, eq. (45), introduced in section 2.

The momentum $\hat{P}_t$ is a constant of the motion, and the isovalue curves of $\hat{P}_t, \hat{I}, \hat{\theta}$ lying on the invariant tori can be used for the EBK quantization scheme. Along such a curve, t evolves from 0 to $2\pi/\omega$, with $\hat{\theta} = \theta - \omega t$ kept constant. Thus, θ itself is changed by 2π, what implies that the Maslov index μ of the unperturbed (I, θ) motion has to be included, leading to the following quantization condition for $\hat{P}_t$,

$$\frac{1}{2\pi}\int_0^T \hat{P}_t dt = \frac{\hat{P}_t T}{2\pi} = \left(k + \frac{\mu}{4}\right)\hbar, \tag{76}$$

with integer k. Since $T = 2\pi/\omega$ is just the period of the resonant driving, we get the quantized values of $\hat{P}_t$:

$$\hat{P}_t = \left(k + \frac{\mu}{4}\right)\ \hbar\omega \tag{77}$$

which are equally spaced by $\hbar\omega$. Thus, we recover semiclassically the ω-periodicity of the Floquet spectrum.

[10] One might argue that Floquet states differing in energy by an integer multiple of $\hbar\omega$ could be used. However, the Floquet spectrum is $\hbar\omega$-periodic by construction [92], and two such states represent the same physical state.

For the motion in the $(\hat{I}, \hat{\theta})$ plane, we can use the isocontour lines of the pendulum Hamiltonian $H_{\rm pend}$, eq. (66), as closed paths, keeping $\hat{P}_t$ and t constant. Depending on the nature of the pendulum motion (librational or rotational), the topology of the closed paths is different, leading to distinct expressions:

– For trapped librational motion, inside the resonance island, the path is isomorphic to a circle in the $(\hat{I}, \hat{\theta})$ plane, with a Maslov index equal to two. The quantization condition is:

$$\frac{1}{2\pi} \oint \hat{I} d\hat{\theta} = \left(N + \frac{1}{2} \right) \hbar, \text{ (librational motion)} \tag{78}$$

with N a non-negative integer. Of special interest is the "fundamental" state, $N = 0$, which exhibits maximum localization within the resonance island and is therefore expected to represent the optimal non-dispersive wave-packet.

– For unbounded rotational motion, outside the resonance island, the path includes a 2π phase change for θ and acquires the Maslov index of the unperturbed motion:

$$\frac{1}{2\pi} \int_0^{2\pi} \hat{I} d\hat{\theta} = \left(N + \frac{\mu}{4} \right) \hbar, \text{ (rotational motion)}. \tag{79}$$

This semiclassical quantization scheme is expected to work provided the classical phase space velocity is sufficiently large, see section 2. This may fail close to the stable and unstable fixed points where the velocity vanishes. Near the stable equilibrium point, the expansion of the Hamiltonian at second order leads to an approximate harmonic Hamiltonian with frequency:

$$\omega_{\rm harm} = \sqrt{|\lambda V_1(\hat{I}_1) H_0''(\hat{I}_1)|}. \tag{80}$$

In this harmonic approximation, the semiclassical quantization is known to be exact [7]. Thus, close to the stable equilibrium, the quasi-energy levels, labeled by the non-negative integer N, are given by the harmonic approximation. There are various cases which depend on the signs of $H_0''(\hat{I}_1)$, $V_1(\hat{I}_1)$, and λ, with the general result given by

$$\mathcal{E}_{N,k} = H_0(\hat{I}_1) - \omega \hat{I}_1 + \left(k + \frac{\mu}{4} \right) \hbar\omega - \ \text{sign}(H_0''(\hat{I}_1)) \left[|\lambda V_1(\hat{I}_1)| - \left(N + \frac{1}{2} \right) \hbar\omega_{\rm harm} \right]. \tag{81}$$

For $N = 0, k = 0$, this gives a fairly accurate estimate of the energy of the non-dispersive wave-packet with optimum localization. The EBK semiclassical scheme provides us also with some interesting information on the eigenstate. Indeed, the invariant tori considered here are tubes surrounding the resonant stable periodic orbit. They cover the $[0, 2\pi]$ range of the t variable but are well localized in the transverse $(\hat{I} = I, \hat{\theta} = \theta - \omega t)$ plane, with an approximately Gaussian phase space distribution. Hence, at any fixed time t, the Floquet

eigenstate will appear as a Gaussian distribution localized around the point $(I = \hat{I}_1, \theta = \omega t)$. As this point precisely defines the resonant, stable periodic orbit, one expects the $N = 0$ state to be a Gaussian wave-packet following the classical orbit. In the original (p, z) coordinates, the width of the wave-packet will depend on the system under consideration through the change of variables $(p, z) \rightarrow (I, \theta)$, but the Gaussian character is expected to be approximately valid for both the phase space density and the configuration space wave-function, as long as the change of variables is smooth.

Let us note that low-N states may be considered as excitations of the $N = 0$ "ground" state. Such states has been termed "flotons" in [42] where their wave-packet character was, however, not considered.

The number of eigenstates trapped within the resonance island – i.e. the number of non-dispersive wave-packets – is easily evaluated in the semiclassical limit, as it is the maximum N with librational motion. It is roughly the area of the resonance island, eq. (71), divided by $2\pi\hbar$:

$$\text{Number of trapped states} \simeq \frac{8}{\pi\hbar}\sqrt{\left|\frac{\lambda V_1(\hat{I}_1)}{H_0''(\hat{I}_1)}\right|}. \tag{82}$$

Near the unstable fixed point – that is at the energy which separates librational and rotational motion – the semiclassical quantization fails because of the critical slowing down in its vicinity [93]. The corresponding quantum states – known as separatrix states [84] – are expected to be dominantly localized near the unstable fixed point, simply because the classical motion there slows down, and the pendulum spends more time close to its upright position. This localization is once again of purely classical origin, but not perfect: some part of the wave-function must be also localized along the separatrix, which autointersects at the hyperbolic fixed point. Hence, the Floquet eigenstates associated with the unstable fixed points are not expected to form non-dispersive wave-packets with optimum localization (see also sec. 2.3).

3.1.4 The Mathieu approach

The pendulum approximation, eq. (66), for a resonantly driven system can also be found by a pure quantum description [39,42]. Let us consider a Floquet state of the system. Its spatial part can be expanded in the eigenbasis of the unperturbed Hamiltonian H_0,

$$H_0|\phi_n\rangle = E_n|\phi_n\rangle, \tag{83}$$

while the time-periodic wave-function can be expanded in a Fourier series. One obtains:

$$|\psi(t)\rangle = \sum_{n,k} c_{n,k} \ \exp(-ik\omega t) \ \ |\phi_n\rangle, \tag{84}$$

where the coefficients $c_{n,k}$ are to be determined. The Schrödinger equation for the Floquet states (eigenstates of $\mathcal{H}$), eq. (75), with quasi-energies $\mathcal{E}$ and time dependence (73), reads:

$$c_{n,k}(\mathcal{E} + k\hbar\omega - E_n) = \frac{\lambda}{2} \ \sum_p \langle\phi_n|V|\phi_{n+p}\rangle \ (c_{n+p,k+1} + c_{n+p,k-1}). \tag{85}$$

For $\lambda = 0$, the solutions of eq. (85) are trivial: $\mathcal{E} = E_n - k\hbar\omega$, which is nothing but the unperturbed energy spectrum modulo $\hbar\omega$. [11] In the presence of a small perturbation, only quasi-degenerate states with values close to $E_n - k\hbar\omega$ will be efficiently coupled. In the semiclassical limit, see section 2, eq. (40), the unperturbed eigenenergies E_n, labeled by a non-negative integer, are locally approximately spaced by $\hbar\Omega$, where Ω is the frequency of the unperturbed classical motion. Close to resonance, $\Omega \simeq \omega$ (eq. (65)), and thus:

$$E_n - k\hbar\omega \simeq E_{n+1} - (k+1)\hbar\omega \simeq E_{n+2} - (k+2)\hbar\omega \simeq ..., \tag{86}$$

so that only states with the same value of $n - k$ will be efficiently coupled.

The first approximation is thus to neglect the couplings which do not preserve $n - k$. This is just the quantum version of the secular approximation for the classical dynamics. Then, the set of equations (85) can be rearranged in independent blocks, each subset being characterized by $n - k$. The various subsets are in fact identical, except for a shift in energy by an integer multiple of $\hbar\omega$. This is nothing but the $\hbar\omega$-periodicity of the Floquet spectrum already encountered in secs. 3.1.2 and 3.1.3. As a consequence, we can consider the $n - k = 0$ block alone.

Consistently, since eq. (86) is valid close to the center of the resonance only, one can expand the quantities of interest in the vicinity of the center of the resonance, and use semiclassical approximations for matrix elements of V. Let n_0 denote the effective, resonant quantum number such that, with eqs. (40) and (65),

$$\left.\frac{dE_n}{dn}\right|_{n=n_0} = \hbar\omega. \tag{87}$$

[11] Note that, as a consequence of the negative sign of the argument of the exponential factor in eq. (84), the energy shift $k\hbar\omega$ appears here with a negative sign in the expression for $\mathcal{E}$ – in contrast to semiclassical expressions alike eq. (81), where we chose the more suggestive positive sign. Since $k = -\infty \ldots + \infty$, both conventions are strictly equivalent.

Note that, by this definition, n_0 is *not* necessarily an integer. In the semiclassical limit, where n_0 is large, the WKB approximation connects n_0 to the center of the classical resonance island, see eq. (39),

$$n_0 + \frac{\mu}{4} = \frac{\hat{I}_1}{\hbar}, \tag{88}$$

$$E_{n_0} = H_0(\hat{I}_1), \tag{89}$$

with μ being the Maslov index along the resonant trajectory. Furthermore, for n close to n_0, we can expand the unperturbed energy at second order in $(n - n_0)$,

$$E_n \simeq E_{n_0} + (n - n_0)\hbar\omega + \frac{1}{2} \left. \frac{d^2 E_n}{dn^2} \right|_{n_0} (n - n_0)^2, \tag{90}$$

where the second derivative d^2E_n/dn^2 is directly related to the classical quantity H_0'', see eq. (67), within the semiclassical WKB approximation, eq. (39). Similarly, the matrix elements of V are related to the classical Fourier components of the potential [7], eq. (55),

$$\langle \phi_n | V | \phi_{n+1} \rangle \simeq \langle \phi_{n+1} | V | \phi_{n+2} \rangle \simeq V_1(\hat{I}_1), \tag{91}$$

evaluated at the center $\hat{I} = \hat{I}_1$ – see eq. (65) – of the resonance zone.

With these ingredients and $r = n - n_0$, eq. (85) is transformed in the following set of approximate equations:

$$\left[\mathcal{E} - H_0(\hat{I}_1) + \omega \left(\hat{I}_1 - \frac{\mu\hbar}{4} \right) - \frac{\hbar^2}{2} H_0''(\hat{I}_1) r^2 \right] d_r = \lambda V_1 (d_{r+1} + d_{r-1}), \tag{92}$$

where

$$d_r \equiv c_{n_0+r, n_0+r}. \tag{93}$$

Note that, because of eq. (87), the r values are not necessarily integers, but all have the same fractional part.

The tridiagonal set of coupled equations (92) can be rewritten as a differential equation. Indeed, if one introduces the following function associated with the Fourier components d_r,

$$f(\phi) = \sum_r \exp(ir\phi) d_r, \tag{94}$$

eq. (92) can be written as

$$\left[-\frac{\hbar^2}{2} H_0''(\hat{I}_1) \frac{d^2}{d\phi^2} + H_0(\hat{I}_1) - \omega \left(\hat{I}_1 - \frac{\mu\hbar}{4} \right) + \lambda V_1 \cos\phi \right] f(\phi) = \mathcal{E} f(\phi), \tag{95}$$

which is nothing but the quantum version of the pendulum Hamiltonian, eq. (66). Thus, the present calculation is just the purely quantum description of the non-linear resonance phenomenon. The dummy variable ϕ introduced for convenience coincides with the classical angle variable $\hat{\theta}$. In general, r is not an integer, so that the various $\exp(ir\phi)$ in eq. (94) are not periodic functions of ϕ. However, as all r values have the same fractional part, if follows that $f(\phi)$ must satisfy "modified" periodic boundary conditions of the form

$$f(\phi + 2\pi) = \exp(-2i\pi n_0) f(\phi). \tag{96}$$

The reason for this surprising boundary condition is clear: $r = n - n_0$ is the quantum analog of $\hat{I} - \hat{I}_1$. In general, the resonant action $\hat{I}_1$ is *not* an integer or half-integer multiple of $\hbar$ – exactly as n_0 is not an integer. The semiclassical quantization, eq. (79), which expresses the $\hat{\theta}$ periodicity of the eigenstate, applies for the $\hat{I}$ variable. When expressed in terms of the variable $\hat{I} - \hat{I}_1$, it contains the additional phase shift present in eq. (96).

Few words of caution are in order: the equivalence of the semiclassical quantization with the pure quantum approach holds in the semiclassical limit only, when the quantum problem can be mapped on a pendulum problem. In the general case, it is not possible to define a quantum angle variable [94]. Hence, the quantum treatment presented here is no more general or more powerful than the semiclassical treatment. They both rely on the same approximations and have the same limitations: perturbative regime (no overlap of resonances) and semiclassical approximation.

Finally, eq. (95) can be written in its standard form, known as the "Mathieu equation" [95]:

$$\frac{d^2 y}{dv^2} + (a - 2q\cos 2v) y = 0. \tag{97}$$

The correspondence with eq. (95) is established via:

$$\phi = 2v, \tag{98}$$

$$a = \frac{8\left[\mathcal{E} - H_0(\hat{I}_1) + \omega\left(\hat{I}_1 - \frac{\mu\hbar}{4}\right)\right]}{\hbar^2 H_0''(\hat{I}_1)}, \tag{99}$$

$$q = \frac{4\lambda V_1}{\hbar^2 H_0''(\hat{I}_1)}. \tag{100}$$

The boundary condition, eq. (96), is fixed by the so-called "characteristic exponent" in the Mathieu equation,

$$\nu = -2n_0 \pmod 2. \tag{101}$$

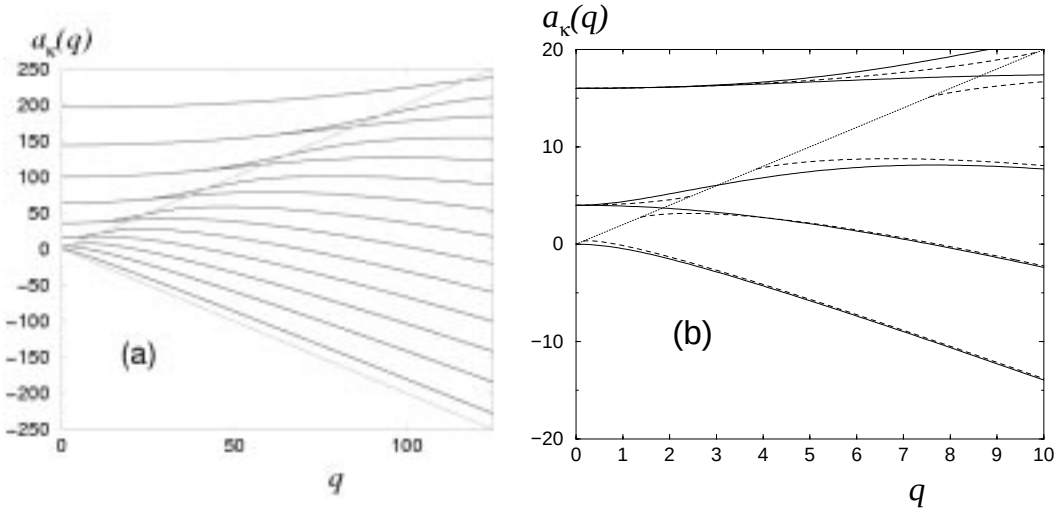

Fig. 9. Eigenvalues $a_\kappa(q)$ of the Mathieu equation, for a characteristic exponent $\nu = 0$. These represent the energy levels of a pendulum as a function of the gravitational field, see eqs. (66,95). (a): Eigenvalues in the range $[-2q, 2q]$ are associated with the librational bounded motion of the pendulum, while eigenvalues above $2q$ are associated with rotational modes. The dotted lines represent the energies of the stable equilibrium point (lower line) and of the unstable equilibrium point (separatrix, upper line). Near the separatrix, the classical motion slows down and the quantal energy levels get closer. (b): Details for the first excited states together with the semiclassical WKB prediction for the energy levels (dashed lines, eqs. (39)). The semiclassical prediction is very accurate, except in the vicinity of the separatrix.

The Mathieu equation has solutions (for a given characteristic exponent) for a discrete set of values of a only. That implies quantization of the quasi-energy levels, according to eq. (99). The quantized values $a_\kappa(\nu, q)$ depend on q and ν, and are labeled [12] by a non-negative integer κ. They are well known – especially asymptotic expansions are available both in the small and in the large q regime – and can be found in standard handbooks [95]. For example, fig. 9(a) shows the first $a_\kappa(q) \equiv a_\kappa(\nu = 0, q)$ curves for the case of "optimal" resonance (see below), where n_0 is an integer and thus the characteristic exponent ν vanishes. Equivalently, the figure can be interpreted as the evolution of the energy levels of a pendulum with the gravitational field.

The quasi-energy levels of the driven system can now be expressed as a function of $a_\kappa(\nu, q)$:

$$\mathcal{E}_\kappa = H_0(\hat{I}_1) - \omega \left(\hat{I}_1 - \frac{\mu\hbar}{4} \right) + \frac{\hbar^2}{8} H_0''(\hat{I}_1)\ a_\kappa(\nu, q). \tag{102}$$

[12] In the standard text books as [95], the various solutions of the Mathieu equation are divided in odd and even solutions, and furthermore in π- and 2π-periodic functions. In our case, only the "a_{2p}" and "b_{2p}" (in the language of [95]) are to be considered.

Together with eqs. (98)-(100), this equation gives the quasienergy levels of a periodically driven system in the vicinity of the resonance zone. The full, quasi-resonant part of the Floquet spectrum of the driven system is built from these quantized values through shifts $k\hbar\omega$, with arbitrary integer values of k.

A visual inspection of fig. 9 immediately shows the existence of two regions in the energy diagram: within the "inner region", $|a_\kappa(\nu, q)| \leq 2q$, the energy levels form a regular fan of curves and tend to decrease with q. On the contrary, for $a_\kappa(\nu, q) > 2q$, the energy levels increase with q. Around $a_\kappa(\nu, q) = 2q$, a transition region is visible with a series of apparent avoided crossings between the levels. This has a simple semiclassical explanation. The stable fixed point of the pendulum described by the Mathieu equation (97) lies at $v = 0$ with energy $-2q$, what explains why the $a_\kappa(\nu, q)$ values are always larger. The unstable fixed point has an energy $+2q$. Thus, in the range $a_\kappa(\nu, q) \in [-2q, 2q]$, the pendulum is trapped in a region of librational motion. The energy levels can be approximated using the standard WKB quantization in the $(\hat{I}, \hat{\theta})$ plane, as described in section 3.1.1. The number of such states is given by eq. (82) which can be rewritten, using eq. (100), as :

$$\text{Number of trapped states} \simeq \frac{4\sqrt{|q|}}{\pi}. \tag{103}$$

At the center of the island (states with small κ and/or large $|q|$), an approximate expression for $a_\kappa(\nu, q)$ reads [95]:

$$a_\kappa(\nu, q) \approx -2|q| + 4\left(\kappa + \frac{1}{2}\right)\sqrt{|q|}. \tag{104}$$

It does not depend on ν (what physically means in our case that the states deeply inside the resonance island are insensitive to the boundary condition). When inserted in eq. (102), it yields exactly the energy levels of eq. (78), with $\kappa = N$. Hence, the Mathieu approach agrees with the harmonic approximation within the resonance island, for sufficiently large islands.

For $a_\kappa(\nu, q) > 2q$, the pendulum undergoes a rotational, unbounded motion, which again can be quantized using WKB. For small $|q|$, $a_\kappa(\nu, q) \approx 4([(\kappa+1)/2] - \nu/2)^2$ (where [ ] stands for the integer part), see [95]. With this in eq. (102), one recovers the known Floquet spectrum, in the limit of a vanishingly weak perturbation. Note, however, that in this rotational mode, the eigenstates *are* sensitive to the boundary conditions (and the $a_\kappa(\nu, q)$ values depend on ν). This is essential for the correct $\lambda \to 0$ limit.

Around $a_\kappa(\nu, q) = 2q$, the pendulum is close to the separatrix between librational and rotational motion: the period of the classical motion tends to infinity (critical slowing down). That explains the locally enhanced density of states apparent in fig. 9(a).

In fig. 9(b), we also plot the semiclassical WKB prediction for the quantized $a_\kappa(q)$ values. Obviously, the agreement with the exact "quantum" Mathieu result is very good, even for weakly excited states, except in the vicinity of the separatrix. This is not unexpected because the semiclassical approximation is known to break down near the unstable fixed point, see sections 2 and 3.1.3 above.

The Mathieu equation yields accurate predictions for properties of non-dispersive wave-packets in periodically driven quantum systems. Indeed, in the range $a_\kappa(\nu, q) \in [-2q, 2q]$, the classical motion is trapped inside the resonance island, and the corresponding quantum eigenstates are expected to be non-dispersive wave-packets. In particular, the lowest state in the resonance island, associated with the ground state of the pendulum $\kappa = 0$, corresponds to the semiclassical eigenstate $N = 0$, see eq. (78), and represents the non-dispersive wave-packet with the best localization properties. As can be seen in fig. 9(b), the semiclassical quantization for this state is in excellent agreement with the exact Mathieu result. This signifies that eq. (81) can be used for *quantitative* predictions of the quasi-energy of this eigenstate.

As already mentioned, the characteristic exponent ν does not play a major role inside the resonance island, as the eigenvalues $a_\kappa(\nu, q)$ there depends very little on ν. However, it is an important parameter outside the resonance, close to the separatrix especially at small q. Indeed, at $q = 0$, the minimum eigenvalue is obtained for $\nu = 0 : a_0(\nu = 0, q = 0) = 0$. This implies that, even for very small q, the ground state enters most rapidly the resonance island. On the opposite, the worst case is $\nu = 1$ where the lowest eigenvalue is doubly degenerate: $a_0(\nu = 1, q = 0) = a_1(\nu = 1, q = 0) = 1$. As we are interested in the ground state of the pendulum (the one with maximum localization), the situation for $\nu = 0$ is preferable: not only the state enters rapidly the resonance island, but it is also separated from the other states by an energy gap and is thus more robust versus any perturbation. We will call this situation "optimal resonance". From eq. (101), it is associated with an integer value of n_0. On the contrary, a half-integer value of n_0 corresponds to $\nu = 1$ and the least optimal case.

3.2 Rydberg states in external fields

3.2.1 Rydberg atoms

In order to construct non-dispersive wave-packets, a quantum system subject to periodic driving with classically non-linear dynamics is needed. The latter requirement rules out the harmonic oscillator, and all its variants. The simplest periodic driving is certainly provided by an externally applied, monochromatic

electromagnetic field. Extremely stable, tunable and well controlled sources exist over a wide range of frequencies.

Furthermore, incoherent processes which destroy the phase coherence of the quantum wave-function have to be minimized. Otherwise, they will spoil the localization properties of the non-dispersive wave-packets and – in the worst case – destroy them completely. Therefore, the characteristic time scales of the incoherent processes should be at least much longer than the period of the driving field. In this respect, atomic electrons appear as very good candidates, since – given suitable experimental conditions – atoms can be considered as practically isolated from the external world, with spontaneous emission of photons as the only incoherent process. Spontaneous emission is usually a very slow mechanism, especially for highly excited states: the spontaneous life-time of typical atomic states is at least four or five orders of magnitude longer than the classical Kepler period (typically nanoseconds vs. femtoseconds for weakly excited states [22]).

The Coulomb interaction between the nucleus and the electrons is highly non-linear, which is very favourable. The efficiency of the coupling with an external electromagnetic field is known to increase rapidly with the degree of excitation of the atom [22]. As we have seen in the preceeding sections 3.1.1 and 3.1.2, non-dispersive wave-packets are the quantum mechanical counterparts of non-linear resonances in periodically driven Hamiltonian systems, where the period of the drive matches some intrinsic time scale of the unperturbed Hamiltonian dynamics. Due to the immediate correspondence between the classical Kepler problem and the hydrogen atom, the relevant time scale in this simplest atomic system is the unperturbed classical Kepler period, which – compare eq. (40) – coincides with the inverse level spacing between neighbouring eigenstates of the unperturbed atom, for large quantum numbers. Hence, the driving field frequency has to be chosen resonant with an atomic transition in the Rydberg regime, typically around the principal quantum number $n_0 = 60$. This is the microwave domain, where excellent sources exist. Thus, we believe that atomic Rydberg states are very well suited for the experimental preparation of non-dispersive wave-packets [13] .

In most cases, the energy scale involved in the dynamics of Rydberg electrons is so small that the inner electrons of the ionic core can be considered as frozen and ignored. Thus, we will consider mainly the hydrogen atom as the simplest prototype. Multi-electron effects are discussed in section 6.2. Alternative systems for observing non-dispersive wave-packets are considered in

[13] Note, however, that this is a specific choice. Any driven quantum system with a sufficiently high denisty of states and mixed regular-chaotic classical dynamics will exhibit nondispersive wave-packets. Since a mixed phase space structure is the generic scenario for dynamical systems, nondispersive wave-packets are expected to be a completely general and ubiquitous phenomenon.

section 5.2.

Compared to our simple one-dimensional model introduced in section 3.1 above, an *atom* displays a couple of additional features:

– A real hydrogen atom is a three-dimensional (3D) system. However, it is a degenerate system, because the energy depends on the principal quantum number n only, but not on the angular or magnetic quantum numbers L and M, respectively. Thus, the structure of the energy levels, which is crucial for the properties of the non-dispersive wave-packet, see section 3.1.2, is identical in the 1D and 3D cases. Before discussing the properties of 3D wave-packets in sections 3.3.2 to 4, we will consider a simplified 1D model of the hydrogen atom in section 3.3.1.
– Although spontaneous emission is a weak incoherent process, it nontheless limits the life time of the non-dispersive wave-packets which may decay to lower lying states, losing the phase coherence of the electronic wave-function. Non-dispersive wave-packets exhibit specific spontaneous decay properties which are studied in section 7.2;
– The electron in a hydrogen atom is not necessarily bound. It may ionize, especially when the atom is exposed to a microwave field. This is a *coherent* decay process where the ionized electron keeps its phase coherence. There are no exact bound states in the system, but rather resonances. From a quantum point of view, the Floquet spectrum is no longer discrete but continuous and we actually deal with an *open system*. In a more elementary language, the atom can successively absorb several photons so that its energy exceeds the ionization threshold. If initially prepared in a wave-packet eigenstate, this is a pure quantum phenomenon, since the classical dynamics remain trapped within the resonance island forever. The multi-photon ionization may then be considered as a tunneling process from inside the resonance island to the non-resonant part of phase space, where the Rydberg electron eventually escapes to infinity. This picture is elaborated in section 7.1.

3.2.2 Hamiltonian, basis sets and selection rules

In the presence of a microwave field, the dipole approximation [18,94] can be used to describe the atom-field interaction. Different gauges can be used, the physics being of course independent of the choice of gauge. The most common choices are the length and the velocity gauges. For simplicity, in our discussion, we shall use the length gauge, although actual quantum calculations are usually a bit easier in the velocity gauge [96–98]. The Hamiltonian reads:

$$H = \frac{\vec{p}^2}{2m} - \frac{q^2}{4\pi\epsilon_0 r} - q\vec{r}\cdot\vec{F}(t) \tag{105}$$

where q is the (negative) charge of the electron, m its mass, and $\vec{F}(t)$ the microwave electric field acting on the atom. We neglect here all relativistic, spin, QED effects, etc, and assume an infinitely massive nucleus. Later, unless specified otherwise, we shall use atomic units, where $|q| \equiv 4\pi\epsilon_0 \equiv m \equiv \hbar \equiv 1$, and the Hamiltonian reduces to

$$H = \frac{\vec{p}^2}{2} - \frac{1}{r} + \vec{r} \cdot \vec{F}(t). \tag{106}$$

Here,

$$H_0 = \frac{\vec{p}^2}{2} - \frac{1}{r} \tag{107}$$

describes the unperturbed atomic part, with bound energy spectrum:

$$E_n = -\frac{1}{2n^2}, \ n \geq 1. \tag{108}$$

The external driving

$$V = \vec{r} \cdot \vec{F}(t) \tag{109}$$

is characterized by the amplitude F of the microwave field, and by its frequency ω. We shall consider in detail the case of linear polarization,

$$V = Fz \cos \omega t, \tag{110}$$

in section 3.3, and that of circular polarization

$$V = F(x \cos \omega t + y \sin \omega t), \tag{111}$$

in section 3.4. The general case of elliptic polarization will be studied in section 3.5.

In the treatment of the perturbed Coulomb problem, eq. (106), there is an apparent difficulty with the singularity of the Coulomb potential at the origin, especially for the restricted one-dimensional model of the atom. This led several authors, see, e.g., [99–104], to consider unphysical potentials without singularity, for example of the type $(r^2 + a^2)^{-1/2}$. This is completely unnecessary and potentially dangerous. Indeed, such a potential breaks the Coulomb degeneracy which is responsible for the closed character of elliptical Kepler orbits (in the classical world), and for the degeneracy of the energy levels (in the quantum world). Such an unphysical symmetry breaking strongly modifies the structure of the non-linear resonance island, and affects the existence and properties of non-dispersive wave-packets outlined in section 3.3.2.

The Coulomb singularity can be rigorously regularized (in any dimension), both in classical and in quantum mechanics. In classical mechanics, this is

made possible through the well-known Kustaanheimo-Stiefel transformation [105], used by various authors for perturbed Coulomb problems, see, e.g., [106–110]. In quantum mechanics, one may use a basis set of non-orthogonal functions, known as the Sturmian functions. Ultimately, the whole analysis relies on the dynamical symmetry properties of the Coulomb interaction and the associated SO(4,2) group [111–114]. It not only allows to treat the Coulomb singularity properly, but also to define a basis set of Sturmian functions extremely efficient for numerical calculations. The most common set are "spherical" Sturmian functions characterized by three quantum numbers, L and M for the angular structure (the associated wave-functions are the usual spherical harmonics), and the positive integer n, for the radial part.

As discussed in section 3.1.2, the quantum properties of the non-dispersive wave-packets are encoded in the spectrum of the Floquet Hamiltonian (75), which acts in configuration space extended by the time axis. The temporal properties are completely independent of the spatial dimension, and any Floquet eigenstate can be expanded in a Fourier series indexed by the integer k, as in eq. (84). The Schrödinger equation for the Floquet Hamiltonian is tridiagonal in k, as in eq. (85). When the spatial part of the wave-function is expressed in a Sturmian basis, one finally obtains a generalized eigenvalue problem $(A - \mathcal{E}B)|\psi >= 0$, where both, A and B, are sparse matrices, the elements of which are known analytically and obey the following selection rules:

$$|\Delta M| \leq 1, \quad |\Delta L| \leq 1, \quad |\Delta n| \leq 2, \quad |\Delta k| \leq 1. \tag{112}$$

When a static electric or magnetic field is added, see section 4, some additional non-zero matrix elements exist, but sparsity is preserved. The eigenvalues can then be calculated using an efficient diagonalization routine such as the Lanczos algorithm [115–118].

Because – in the presence of a microwave field – the system is unbounded, there are in general no exact bound states but rather resonances. Using Sturmian functions, the properties of the resonances can be calculated *directly* using the complex rotation technique [119–125]. The price to pay is to diagonalize complex symmetric matrices, instead of real symmetric ones. The advantage is that the resonances are obtained as complex eigenvalues $E_n - i\Gamma_n/2$ of the complex rotated Hamiltonian, E_n being the position of the resonance, and Γ_n its width. All essential properties of resonances can be obtained from complex eigenstates [126].

3.2.3 Simplified 1D and 2D models

Because explicit calculations for the real 3D hydrogen atom may be rather complicated, it is fruitful to study also simplified 1D and 2D approximations

of the real world. Let us first consider the simplified restriction of the atomic motion to one single dimension of configuration space,

$$H_0 = \frac{p^2}{2} - \frac{1}{z}, \quad \text{with } z > 0, \tag{113}$$

with the external driving along z,

$$V = Fz\cos\omega t. \tag{114}$$

The energy spectrum of H_0 is identical to the spectrum in 3D [127]:

$$E_n^{(1D)} = -\frac{1}{2n^2}, \quad \text{with } n \geq 1. \tag{115}$$

Such a one-dimensional model allows to grasp essential features of the driven atomic dynamics, and provides the simplest example for the creation of non-dispersive wave-packets by a near-resonant microwave field. The classical dynamics live on a three-dimensional phase space, spanned by the single dimension of configuration space, the canonically conjugate momentum, and by time. This is the lowest dimensionality for a Hamiltonian system to display mixed regular-chaotic character [3].

For a circularly (or elliptically) polarized microwave, a 1D model is of course inadequate. One can use a two-dimensional model where the motion of the electron is restricted to the polarization plane. The energy spectrum in two dimensions is:

$$E_n^{(2D)} = -\frac{1}{2\left(n+\frac{1}{2}\right)^2}, \quad \text{with } n \geq 0. \tag{116}$$

It differs from the 3D (and 1D) energy spectrum by the additional 1/2 in the denominator, due to the specific Maslov indices induced by the Coulomb singularity.

3.2.4 Action-angle coordinates

In order to apply the general theory of nonlinear resonances and non-dispersive wave-packets derived in section 3.1, we need the action-angle coordinates for the hydrogen atom. For the simplified 1D model, the result is simple: the principal action I and the canonically conjugate angle θ are defined by [128,129]

$$I = \sqrt{\frac{a}{2}},$$
$$\theta = \begin{cases} \eta - \sin\eta, & p \geq 0, \\ 2\pi - \eta + \sin\eta, & p < 0, \end{cases}$$

$$\eta = 2\sin^{-1}\sqrt{\frac{z}{a}}, \quad a = -E^{-1}, \tag{117}$$

where a is the maximum distance. In celestial mechanics, θ and η are known as the *mean* and the *eccentric anomaly*, respectively [93]. The Hamilton function depends on the action through:

$$H_0 = -\frac{1}{2I^2}, \tag{118}$$

and the classical Kepler frequency reads:

$$\Omega = \frac{dH_0}{dI} = \frac{1}{I^3}. \tag{119}$$

Due to the Coulomb singularity at $z = 0$, the Maslov index of this system is $\mu = 0$ instead of $\mu = 2$, and the semiclassical energy spectrum, eq. (39) [14], matches the exact quantum spectrum, eq. (115).

The classical equations of motion can be solved exactly and it is easy to obtain the Fourier components of the dipole operator [130]:

$$z(\theta) = I^2\left(\frac{3}{2} - 2\sum_{m=1}^{\infty}\frac{J'_m(m)}{m}\cos(m\theta)\right), \tag{120}$$

where $J'_n(x)$ denotes the derivative of the usual Bessel function. The strongly non-linear character of the Coulomb interaction is responsible for the slow decrease of the Fourier components at high m.

For the 2D and 3D hydrogen atom, the action-angle variables are similar, but more complicated because of the existence of angular degrees of freedom. The classical trajectories are ellipses with focus at the nucleus. The fact that all bounded trajectories are periodic manifests the degeneracy of the classical dynamics. As a consequence, although phase space is six-dimensional with three angle and three action variables in 3D – four-dimensional with two angle and two action variables in 2D – the Hamilton function depends only on the total action I, precisely like the 1D hydrogen atom, i.e. through eq. (118). In 3D, the Maslov index is zero, so that the energy spectrum is again given by eq. (108), and the semiclassical approximation is exact. However, a different result holds for the 2D hydrogen atom, where the Maslov index is $\mu = 2$ (still yielding exact agreement between the semiclassical and the quantum spectrum, cf. eqs. (46,116)).

The action-angle variables which parametrize a general Kepler ellipse are well known [128]. In addition to the action-angle variables (I, θ) which determine

[14] As we are using atomic units, $\hbar$ is unity, and the principal quantum number just coincides with the action.

the total action and the angular position of the electron along the Kepler ellipse, respectively, the orientation of the ellipse in space is defined by two angles: ψ, canonically conjugate to the total angular momentum L, and the polar angle ϕ, canonically conjugate to M, the z-component of the angular momentum. The angle ψ conjugate to L has a direct physical meaning for $M = 0$: it represents the angle between the Runge-Lenz vector $\vec{A}$ (oriented along the major axis) of the Kepler ellipse, and the z-axis. For the 2D hydrogen atom (in the (x, y) plane), the orientation of the ellipse is defined by the angle ψ (canonically conjugate to the total angular momentum L) between the Runge-Lenz vector and the x-axis.

Also the Fourier components of the unperturbed classical position operator $\vec{r}(t)$ are well known [131]. In the local coordinate system of the Kepler ellipse (motion in the (x', y') plane, with major axis along x'), one gets:

$$x' = -\frac{3e}{2} I^2 + 2I^2 \sum_{m=1}^{\infty} \frac{J'_m(me)}{m} \cos m\theta \tag{121}$$

$$y' = 2I^2 \frac{\sqrt{1-e^2}}{e} \sum_{m=1}^{\infty} \frac{J_m(me)}{m} \sin m\theta \tag{122}$$

$$z' = 0 \tag{123}$$

where

$$e = \sqrt{1 - \frac{L^2}{I^2}} \tag{124}$$

denotes the eccentricity of the ellipse. $J_m(x)$ and $J'_m(x)$ are the ordinary Bessel function and its derivative, respectively.

In the laboratory frame, the various components can be found by combining these expressions with the usual Euler rotations [93,128]. The set of three Euler angles describes the successive rotations required for the transformation between the laboratory frame and the frame (x', y', z') linked to the classical Kepler ellipse. We choose to rotate successively by an angle ϕ around the z laboratory axis, an angle β around the y-axis [15], and an angle ψ around the z' axis. The physical interpretation of ϕ and ψ is simple: ϕ corresponds to a rotation around the z-axis, and is thus canonically conjugate to the z-component of the angular momentum, noted M. Similarly, ψ corresponds to a rotation around the axis of the total angular momentum $\vec{L}$, and is thus canonically conjugate to L. By construction, the third angle β is precisely the

[15] Some authors define the second Euler rotation with respect to the x-axis. The existence of the two definitions makes a cautious physicist's life much harder, but the physics does not – or at least should not – depend on such ugly details.

angle between the angular momentum $\vec{L}$ and the z-axis. Thus:

$$\cos\beta = \frac{M}{L}, \tag{125}$$

and $\beta = \pi/2$ for $M = 0$. Altogether, the coordinates in the laboratory frame are related to the local coordinates through

$$\begin{aligned} x &= (\cos\psi\cos\beta\cos\phi - \sin\psi\sin\phi)\ x' + (-\sin\psi\cos\beta\cos\phi - \cos\psi\sin\phi)\ y' + \sin\beta\cos\phi\ z', \\ y &= (\cos\psi\cos\beta\sin\phi + \sin\psi\cos\phi)\ x' + (-\sin\psi\cos\beta\sin\phi + \cos\psi\cos\phi)\ y' + \sin\beta\sin\phi\ z', \\ z &= -\cos\psi\sin\beta\ x' + \sin\psi\sin\beta\ y' + \cos\beta\ z', \end{aligned} \tag{126}$$

which, combined with eqs. (121-123), allows for a complete expansion of the classical trajectories in terms of action-angle coordinates.

The situation is somewhat simpler for the 2D model of the hydrogen atom. There, the angular momentum $\vec{L}$ is aligned along the z-axis, which means that $L = M$ and $\beta = 0$. Also, the rotation around $\vec{L}$ by an angle ψ can be absorbed in a rotation by an angle ϕ around the z-axis. Therefore, one is left with two pairs (I, θ) and (M, ϕ) of action-angle variables. The relation between the laboratory and the local coordinates reads:

$$\begin{aligned} x &= \cos\phi\ x' - \sin\phi\ y' \\ y &= \sin\phi\ x' + \cos\phi\ y', \end{aligned} \tag{127}$$

which is nothing but a rotation of angle ϕ in the plane of the trajectory. Formally, the 2D result, eq. (127), can be obtained from the 3D one, eq. (126), by specializing to $\beta = \psi = 0$. The eccentricity, eq. (124), of the trajectory now reads:

$$e = \sqrt{1 - \frac{M^2}{I^2}}. \tag{128}$$

3.2.5 Scaling laws

It is well known that the Coulomb interaction exhibits particular scaling properties: for example, all bounded trajectories are similar (ellipses), whatever the (negative) energy. Also, the classical period scales in a well-defined way with the size of the orbit (third Kepler law). This originates from the fact that the Coulomb potential is a homogeneous function – of degree -1 – of the radial distance r. Similarly, the dipole operator responsible for the coupling between the Kepler electron and the external driving field is a homogenous function – of degree 1 – of r. It follows that the classical equations of motion of the hydrogen atom exposed to an electromagnetic field are invariant under the following scaling transformation:

$$\begin{cases} \vec{r} \to \alpha^{-1}\vec{r}, \\ \vec{p} \to \alpha^{1/2}\vec{p}, \\ H_0 \to \alpha H_0, \\ t \to \alpha^{-3/2}t, \\ F \to \alpha^2 F, \\ \omega \to \alpha^{3/2}\omega, \\ V \to \alpha V. \end{cases} \tag{129}$$

where α is an arbitrary, positive real number. Accordingly, the action-angle variables transform as

$$\begin{cases} I \to \alpha^{-1/2} I, \\ L \to \alpha^{-1/2} L, \\ M \to \alpha^{-1/2} M, \\ \theta \to \theta, \\ \psi \to \psi, \\ \phi \to \phi. \end{cases} \tag{130}$$

It is therefore useful to introduce the "scaled" total angular momentum and its component along the z-axis, by chosing

$$\alpha = I^2, \tag{131}$$

what leads to

$$\begin{cases} L_0 = \frac{L}{I}, \\ M_0 = \frac{M}{I}. \end{cases} \tag{132}$$

The eccentricity of the classical ellipse then reads:

$$e = \sqrt{1 - L_0^2}, \tag{133}$$

and only depends – as it should – on scaled quantities. Similarly, the Euler angles describing the orientation of the ellipse are scaled quantities, by virtue of eq. (130).

When dealing with non-dispersive wave-packets, it will be useful to scale the amplitude and the frequency of the external field with respect of the action $\hat{I}_1$ of the resonant orbit. With the above choice of α, eq. (131), the scaling

relation (129) for ω defines the scaled frequency

$$\omega_0 = \omega I^3 \tag{134}$$

which turns into $\omega_0 = \Omega \hat{I}_1^3$ with the resonance condition, eq. (65), and enforces

$$\hat{I}_1 = \omega^{-1/3}, \tag{135}$$

by virtue of eq. (119). Correspondingly, the scaled external field is defined as

$$F_0 = F I^4, \tag{136}$$

which, with eq. (135), turns into $F_0 = F\omega^{-4/3}$ at resonance. Hence, except for a global multiplicative factor I^{-2}, the Hamiltonian of a hydrogen atom in an external field depends only on scaled quantities.

Finally, note that the *quantum* dynamics is not invariant with respect to the above scaling transformations. Indeed, the Planck constant $\hbar$ fixes an absolute scale for the various action variables. Thus, the spectrum of the Floquet Hamiltonian will not be scale invariant, while the underlying classical phase space structure is. This latter feature will be used to identify in the quantum spectrum the remarkable features we are interested in.

3.3 Rydberg states in linearly polarized microwave fields

We are now ready to consider specific examples of non-dispersive wave-packets. We consider first the simplest, one-dimensional, driven hydrogen atom, as defined by eqs. (113),(114).

For a real 3D atom, this corresponds to driving the electron initially prepared in a one-dimensional eccentricity one orbit along the polarization axis of the field. In fact, it turns out that the one-dimensionality of the dynamics is not stable under the external driving: the Kepler ellipse (with orientation fixed in configuration space by the Runge-Lenz vector) slowly precesses off the field polarization axis (see sections 3.3.2 and 4.1). Thus, the 1D presentation which follows has mostly pedagogical value – being closest to the general case discussed later. However, a one-dimensional model allows to grasp essential features of the driven atomic dynamics and provides the simplest example for the creation of non-dispersing wave-packets by a near-resonant microwave field. A subsequent section will describe the dynamics of the real 3D atom under linearly polarized driving, and amend on the flaws and drawbacks of the one-dimensional model.

3.3.1 One-dimensional model

From eqs. (113),(114), the Hamiltonian of the driven 1D atom reads

$$H = \frac{p^2}{2} - \frac{1}{z} + Fz\cos(\omega t),\ z > 0. \tag{137}$$

This has precisely the general form, eq. (54), and we can therefore easily derive explicit expressions for the secular Hamiltonian subject to the semiclassical quantization conditions, eqs. (76), (78),(79), as well as for the quantum mechanical eigenenergies, eq. (102), in the pendulum approximation. With the Fourier expansion, eq. (120), and identifying λ and $V(p,z)$ in eq. (54) with F and z in eq. (137), respectively, the Fourier coefficients in eq. (55) take the explicit form

$$V_0 = \frac{3}{2}I^2; \quad V_m = -I^2\frac{J'_m(m)}{m},\ m \neq 0. \tag{138}$$

The resonant action – which defines the position of the resonance island in fig. 8 – is given by eq. (135). In a quantum description, the resonant action coincides with the resonant principal quantum number:

$$n_0 = \hat{I}_1 = \omega^{-1/3}, \tag{139}$$

since the Maslov index vanishes in 1D, see section 3.2, and $\hbar \equiv 1$ in atomic units. The resonant coupling is then given by:

$$V_1 = -\hat{I}^2 J'_1(1), \tag{140}$$

and the secular Hamiltonian, eq. (64), reads:

$$\mathcal{H}_{\rm sec} = \hat{P}_t - \frac{1}{2\hat{I}^2} - \omega\hat{I} - J'_1(1)\hat{I}^2 F\cos\hat{\theta}. \tag{141}$$

This Hamiltonian has the standard form of a secular Hamiltonian with a resonance island centered around

$$\hat{I} = \hat{I}_1 = \omega^{-1/3} = n_0, \quad \hat{\theta} = \pi, \tag{142}$$

sustaining librational motion within its boundary.

Those energy values of $\mathcal{H}_{\rm sec}$ which define contour lines (see fig. 8) such that the contour integrals, eqs. (78),(79), lead to non-negative integer values of N, are the semiclassical quasienergies of the 1D hydrogen atom under external driving. The non-dispersive wave-packet eigenstate of this model atom in the electromagnetic field is represented by the ground state $N = 0$ of $\mathcal{H}_{\rm sec}$, localized (in phase space) near the center of the resonance island. A detailed comparison of the semiclassical energies to the exact quantum solution of our

problem will be provided in the next subsection, where we treat the three-dimensional atom in the field. There it will turn out that the spectrum of the 1D model is actually neatly embedded in the spectrum of the real 3D atom.

In the immediate vicinity of the resonance island, the secular Hamiltonian can be further simplified, leading to the pendulum approximation, see section 3.1.1 and eq. (66). The second derivative of the unperturbed Hamiltonian with respect to the action is:

$$H_0^{''} = -\frac{3}{n_0^4}, \tag{143}$$

and the pendulum Hamiltonian reads:

$$\mathcal{H}_{\text{pend}} = \hat{P}_t - \frac{3}{2n_0^2} - J_1'(1)n_0^2 F\cos\hat{\theta} - \frac{3}{2n_0^4}(\hat{I} - n_0)^2. \tag{144}$$

Remember that n_0 is the resonant action, not necessarily an integer. As we are interested in states deeply inside the resonance island, we can employ the harmonic approximation around the stable fixed point ($\hat{I} = n_0, \hat{\theta} = \pi$), and finally obtain the semiclassical energies of the non-dispersive wave-packets:

$$\mathcal{E}_{N,k} = k\omega - \frac{3}{2n_0^2} + J_1'(1)n_0^2 F - \left(N + \frac{1}{2}\right)\omega_{\text{harm}}, \tag{145}$$

where, in agreement with eq. (80)

$$\omega_{\text{harm}} = \sqrt{3J_1'(1)}\frac{\sqrt{F}}{n_0} = \omega\sqrt{3J_1'(1)F_0} \tag{146}$$

is the classical librational frequency in the resonance island. The quantum number k reflects the global ω periodicity of the Floquet spectrum, as a consequence of eq. (77).

As already noted in section 3.2.5, the semiclassical quantization breaks the scaling of the classical dynamics. Nontheless, the semiclassical energy levels can be written in terms of the scaled parameters introduced above, by virtue of eqs. (136,142):

$$\mathcal{E}_{N,k=0} = \frac{1}{n_0^2}\left[-\frac{3}{2} + J_1'(1)F_0 - \frac{N+1/2}{n_0}\sqrt{3J_1'(1)F_0}\right]. \tag{147}$$

Note that the term $(N + 1/2)/n_0$ highlights the role of $1/n_0$ as an effective Planck constant.

As discussed in section 3.1.4, the fully "quantum" quasienergies of the resonantly driven atom can be obtained using the very same pendulum approximation of the system, together with the solutions of the Mathieu equation.

In our case, the characteristic exponent in the Mathieu equation is given by eq. (101) and the Mathieu parameter is, according to eqs. (100),(140),(143):

$$q = \frac{4}{3} F n_0^6 J_1'(1) = \frac{4}{3} F_0 n_0^2 J_1'(1). \tag{148}$$

The quantum quasienergy levels are then given by eq. (102) which reads:

$$\mathcal{E}_{\kappa,k=0} = -\frac{3}{2n_0^2} - \frac{3}{8n_0^4}\, a_\kappa(\nu, q). \tag{149}$$

As discussed in section 3.1.2, the non-dispersive wave-packet with maximum localization is associated with $\kappa = 0$ and is well localized inside the non-linear resonance island between the internal coulombic motion and the external driving, provided the parameter q is of the order of unity (below this value, the resonance island is too small to support a localized state). The minimum scaled microwave amplitude is thus of the order of:

$$F_{0,\mathrm{trapping}} = F_{\mathrm{trapping}} n_0^4 \simeq \frac{1}{n_0^2} \tag{150}$$

which is thus *much smaller* – by a factor n_0^2, i.e. three orders of magnitude in typical experiments – than the electric field created by the nucleus. This illustrates that a well chosen weak perturbation may strongly influence the dynamics of a non-linear system. From the experimental point of view, this is good news, a limited microwave power is sufficient to create non-dispersive wave-packets.

We have so far given a complete description of the dynamics of the resonantly driven, one-dimensional Rydberg electron, from a semiclassical as well as from a quantum mechanical point of view, in the resonant approximation. These approximate treatments are now complemented by a numerical solution of the exact quantum mechanical eigenvalue problem described by the Floquet equation (75), with H_0 and V from eqs. (113),(114), as well as by the numerical integration of the classical equations of motion derived from eq. (137). Using this machinery, we illustrate some of the essential properties of nondispersive wave-packets associated with the principal resonance in this system, whereas we postpone the discussion of other primary resonances to section 5.3.

Fig. 10 compares the phase space structure of the exact classical dynamics generated by the Hamilton function (137), and the isovalue curves of the pendulum dynamics, eq. (144), for the case $n_0 = 60$, at scaled field strength $F_0 = F n_0^4 = 0.01$. The Poincaré surface of section is taken at phases $\omega t = 0 \pmod{2\pi}$ and plotted in (I, θ) variables which, for such times, coincide with the $(\hat{I}, \hat{\theta})$ variables, see eqs. (60),(61). Clearly, the pendulum approximation predicts the structure of the invariant curves very well, with the resonance island surrounding the stable periodic orbit at $(\hat{I} \approx 60, \hat{\theta} = \pi)$, the unstable

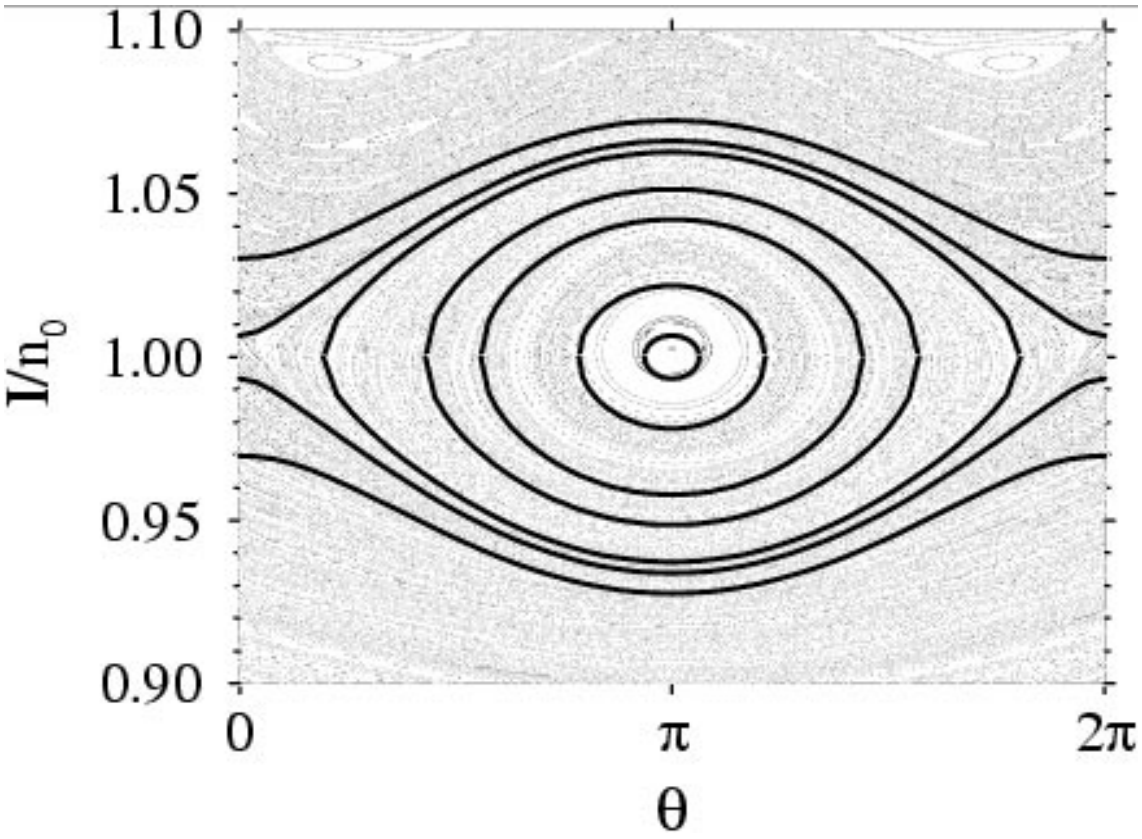

Fig. 10. Poincaré surface of section for the dynamics of a 1D hydrogen atom driven by an external oscillatory electric field, see eq. (137). The driving frequency is chosen as $\omega = 1/60^3$, such that the nonlinear resonance island is centered at principal action (or effective principal quantum number) $n_0 = 60$. The scaled external field amplitude is set to $F_0 = Fn_0^4 = 0.01$. Although the driving field is much weaker than the Coulomb field between the electron and the nucleus, it suffices to create a relatively large resonance island which supports several non-dispersive wave-packets.

fixed point at $(\hat{I} \approx 60, \hat{\theta} = 0)$, the separatrix, and the rotational motion outside the resonance island. Apparently, only tiny regions of stochastic motion invade the classical phase space, which hardly affects the quality of the pendulum approximation. It should be emphasized that – because of the scaling laws, see section 3.2.5 – the figure depends on the scaled field strength F_0 only. Choosing a different microwave frequency with the same scaled field leads, via eq. (139), to a change of n_0 and, hence, of the scale of I.

Fig. 11 compares the prediction of the Mathieu approach, eq. (149), for the quasienergy levels of the Floquet Hamiltonian to the exact numerical result obtained by diagonalization of the full Hamiltonian, see section 3.2. Because of the $\hbar\omega$ periodicity of the Floquet spectrum, the sets of energy levels of the pendulum, see fig. 9, are folded in one single Floquet zone. For states located inside or in the vicinity of the resonance island – the only ones plotted in fig. 9a – the agreement is very good for low and moderate field strengths. Stronger

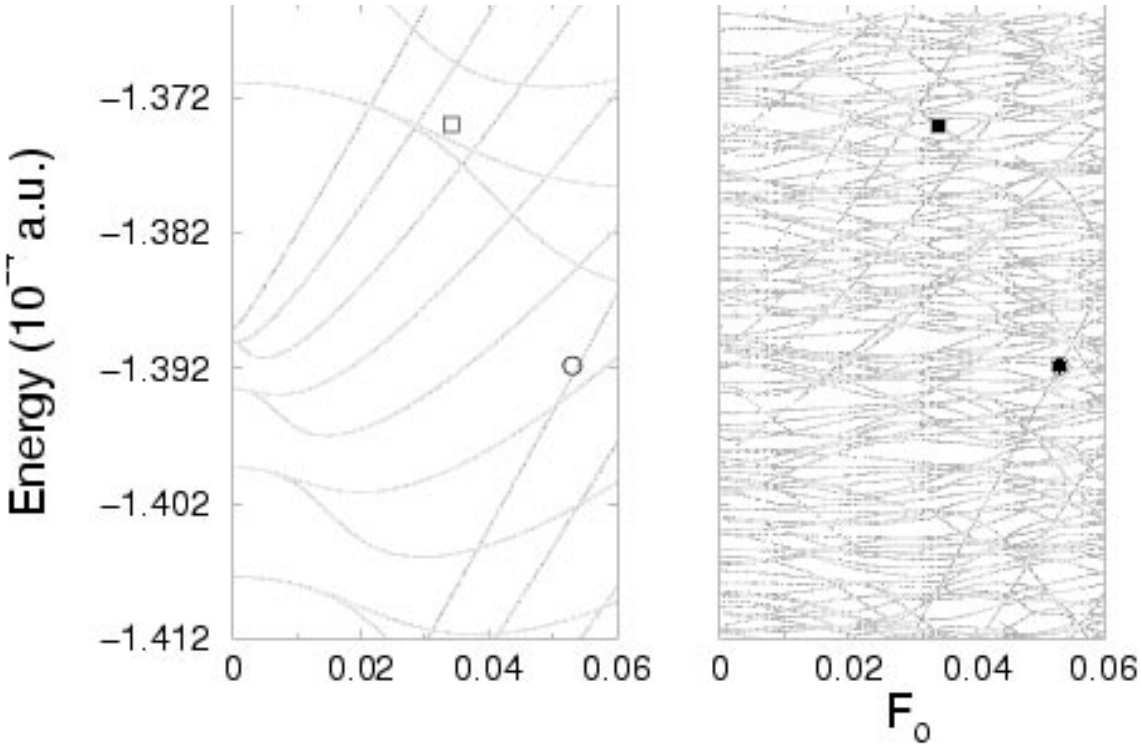

Fig. 11. Comparison of the exact quasienergy spectrum of the 1D hydrogen atom driven by a linearly polarized microwave field (right), eq. (137), with the prediction of the pendulum approximation (left), eq. (149). Because of the $\hbar\omega$ periodicity of the Floquet spectrum, the energy levels described by the pendulum approximation are folded inside one Floquet zone. The agreement between the exact quantum result and the pendulum approximation is very good. The filled circle shows the most localized non-dispersive wave-packet $N = 0$ shown in figs. 13-15, while the filled square represents the hyperbolic non-dispersive wave-packet partly localized in the vicinity of the unstable equilibrium point of the pendulum, shown in figs. 17 and 18. The open circle and square compare the exact location of the respective quasienergy values with the Mathieu prediction, which is considerably better for the ground state as compared to the separatrix state.

electromagnetic fields lead to deviations between the Mathieu and the exact result. This indicates higer order corrections to the pendulum approximation.

Fig. 12 shows a typical Poincaré surface of section of the classical dynamics of the driven Rydberg electron, at different values of the phase of the driving field. The field amplitude is chosen sufficiently high to induce largely chaotic dynamics, with the principal resonance as the only remnant of regular motion occupying an appreciable volume of phase space. The figure clearly illustrates the temporal evolution of the elliptic island with the phase of the driving field, i.e. the locking of the electronic motion on the external driving. The classical stability island follows the dynamics of the unperturbed electron along the

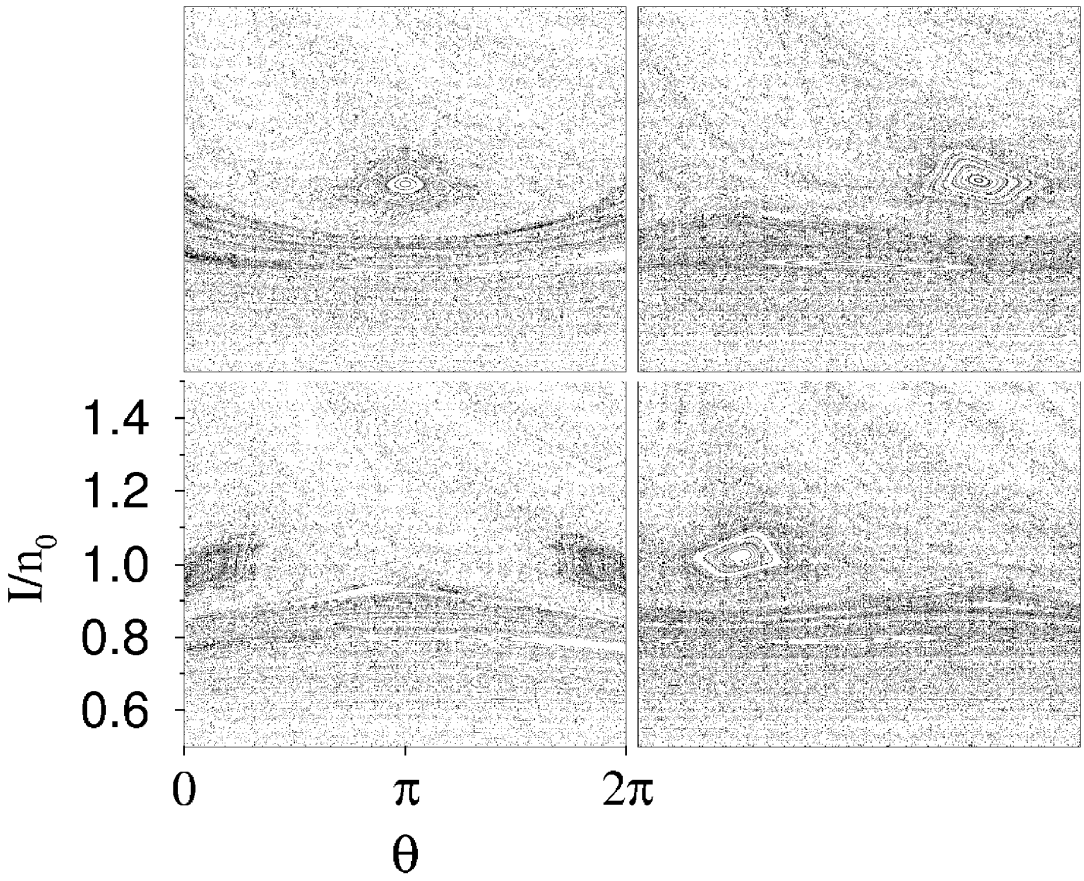

Fig. 12. Surface of section of the classical phase space of a 1D hydrogen atom, driven by a linearly polarized microwave field of amplitude $F_0 = 0.053$, for different values of the phase: $\omega t = 0$ (top left), $\omega t = \pi/2$ (top right), $\omega t = \pi$ (bottom left), $\omega t = 3\pi/2$ (bottom right). At this driving strength, the principal resonance remains as the only region of regular motion of appreciable size, in a globally chaotic phase space. The action-angle variables I, θ are defined by eq. (117), according to which a collision with the nucleus occurs at $\theta = 0$.

resonant trajectory. The distance from the nucleus is parametrized by the variable θ, see eq. (117). At $\omega t = \pi$, the classical electron hits the nucleus (at $\theta = 0$), its velocity diverges and changes sign discontinuously. This explains the distortion of the resonance island as it approaches $\theta = 0, \pi$.

Quantum mechanically, we expect a non-dispersive wave-packet eigenstate to be localized within the resonance island. The semiclassical prediction of its quasienergy, eq. (149), facilitates to identify the nondispersive wave-packet within the exact Floquet spectrum, after numerical diagonalization of the Floquet Hamiltonian (75). The wave-packet's configuration space representation is shown in fig. 13, for the same phases of the field as in the plots of the classical dynamics in fig. 12. Clearly, the wave-packet is very well localized at the outer turning point of the Kepler electron at phase $\omega t = 0$ of the driving

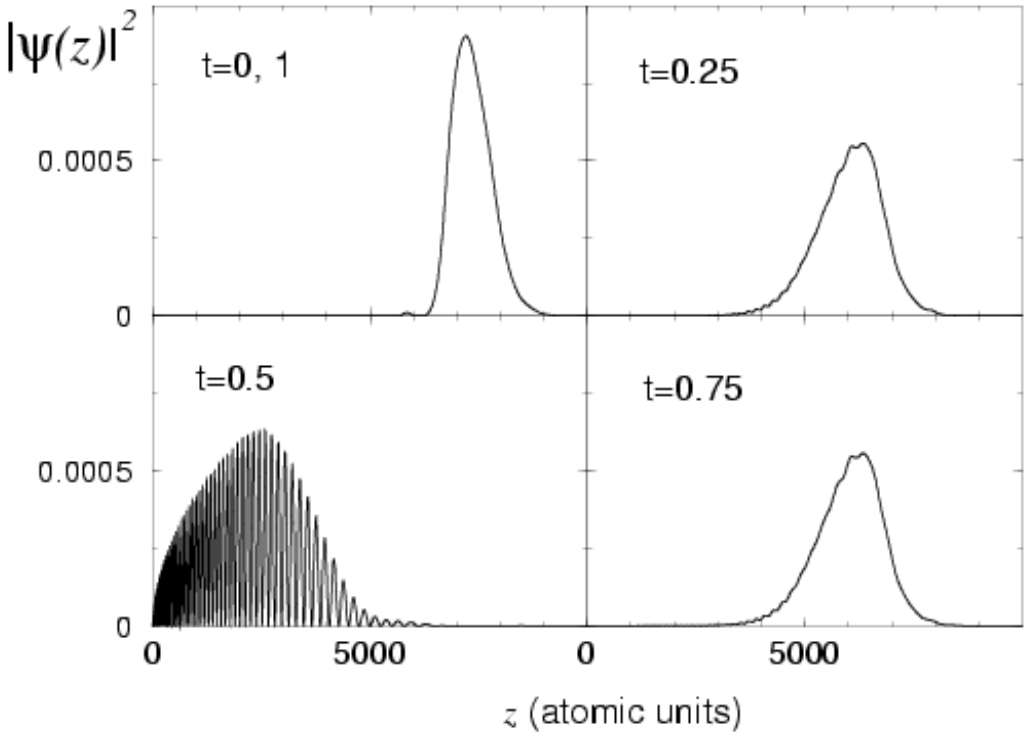

Fig. 13. Configuration space representation of the electronic density of the non-dispersive wave-packet eigenstate of a 1D hydrogen atom, driven by a linearly polarized microwave field, for the same field amplitude and phases as in fig. 12. The eigenstate is centered on the principal resonance of classical phase space, at action (principal quantum number) $n_0 = 60$. In configuration space, the wave-packet is localized at the outer turning point (with zero average velocity) at time $t = 0$, then propagates towards the nucleus which it hits at $t/T = 0.5$ (where $T = 2\pi/\omega$ is the microwave period). Afterwards, it propagates outward to the apocenter which is reached at time $t/T = 1$. After one period, the wave-packet recovers *exactly* its initial shape, and will therefore propagate along the classical trajectory forever, without spreading. The wave-packet has approximately Gaussian shape(with time-dependent width) except at $t/T \simeq 0.5$. At this instant, the head of the wave-packet, which already has been reflected off the nucleus, interferes with its tail, producing interference fringes.

field, and is reflected off the nucleus half a period of the driving field later. On reflection, the electronic density exhibits some interference structure, as well as some transient spreading. This is a signature of the quantum mechanical uncertainty in the angle θ: part of the wave-function, which still approaches the Coulomb singularity, interferes with the other part already reflected off the nucleus. The transient spreading is equally manifest in the temporal evolution of the uncertainty product $\Delta z \Delta p$ itself, which is plotted in fig. 14. Apart from this singularity at $\omega t = \pi$, the wave-packet is approximately Gaussian at any time, with a time-dependent width (compare $\omega t = 0$ and $\omega t = \pi/2$).

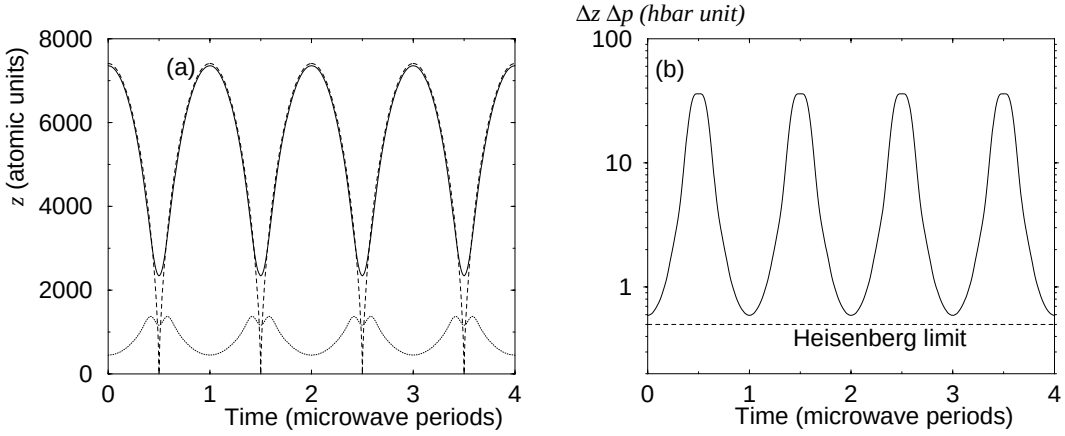

Fig. 14. (a) Dashed line: Classical temporal evolution of the position of the Rydberg electron resonantly driven by a linearly polarized microwave field, in the one dimensional model, eq. (137), of the hydrogen atom. ($n_0 = 60$; scaled field amplitude $F_0 = Fn_0^4 = 0.053$). Thick line: Expectation value $\langle z \rangle$ for the non-dispersive wave-packet shown in fig. 13, as a function of time. It follows the classical trajectory remarkably well (except for collisions with the nucleus). Dotted line: The position uncertainty $\Delta z = \sqrt{\langle z^2 \rangle - \langle z \rangle^2}$ of the wave-packet. Δz being much smaller than $\langle z \rangle$ (except near collisions with the nucleus) highlights the efficient localization of the wave-packet. (b) Uncertainty product $\Delta z \Delta p$ of the wave-packet. The periodically repeating maxima of this quantity indicate the collision of the electron with the atomic nucleus. Note that the minimum uncertainty at the outer turning point of the wave-packet is very close to the Heisenberg limit $\hbar/2$. Although the wave-packet is *never* a minimal one, it is nevertheless well localized and an excellent approximation of a classical particle.

To complete the analogy between classical and quantum motion, we finally calculate the Husimi distribution – the phase space representation of the wave-packet eigenstate defined in section 1.2, eq. (30) – in order to obtain a direct comparison between classical and quantum dynamics in phase space. Fig. 15 shows the resulting phase space picture, again for different phases of the driving field. The association of the quantum mechanical time evolution with the classical resonance island (see fig. 12) is unambiguous. The transient spreading at the collision with the nucleus ($\omega t = \pi$) is due to the divergence of the classical velocity upon reflection.

As discussed in section 3.1.1 and visible in fig. 10, there is an hyperbolic fixed point (i.e. an unstable equilibrium point) at $(\hat{I} = n_0, \hat{\theta} = 0)$: it corresponds to the unstable equilibrium position of the pendulum when it points "upwards". For the driven system, it corresponds to an unstable periodic orbit resonant with the driving frequency: it is somewhat similar to the stable orbit supporting the non-dispersive wave-packets, except that is is shifted in time by half a period.

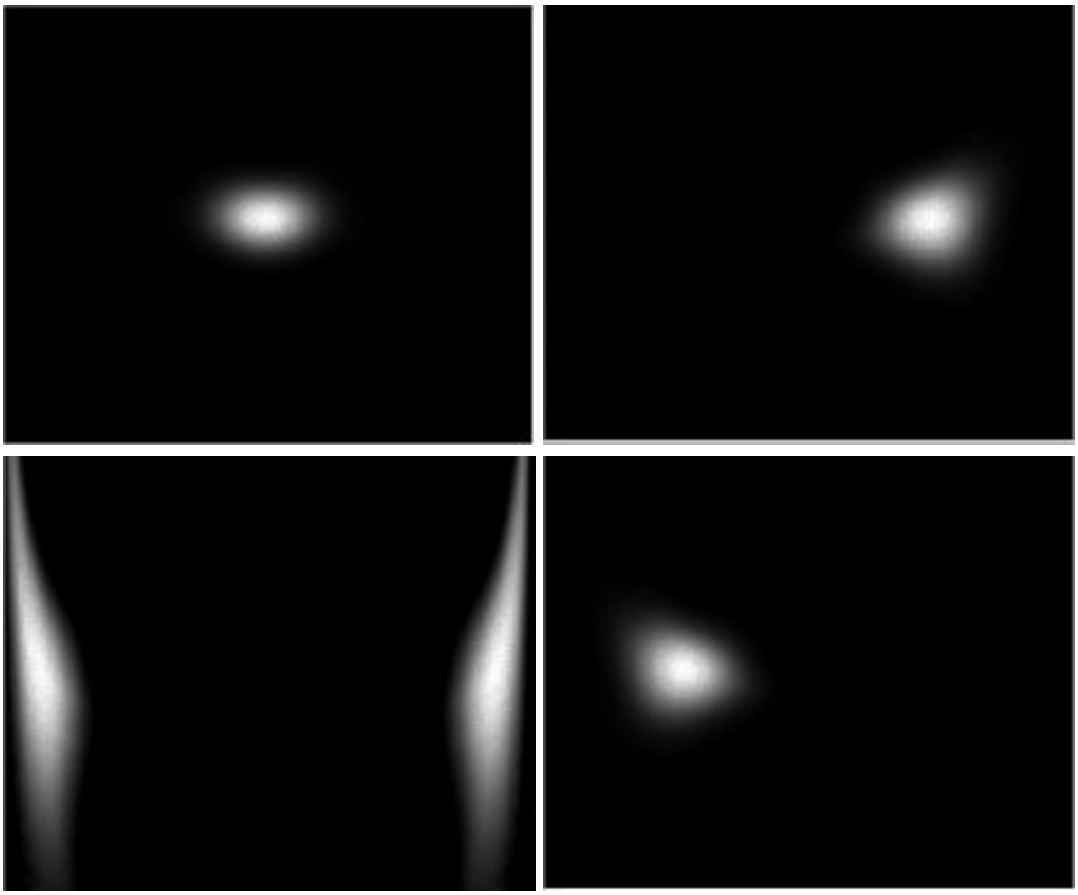

Fig. 15. Husimi representation of the wave-packet eigenstate of fig. 13 in classical phase space, for the same phases ωt and scales ($0 \leq \theta \leq 2\pi, 30 \leq I \leq 90$) as employed for the classical surface of section in fig. 12. Clearly, the quantum mechanical eigenstate of the atom in the field follows the classical evolution without dispersion, except for its transient spreading when reflected off the nucleus (at $\omega t = \pi$, bottom left), due to the divergence of the classical velocity at that position.

As discussed in section 2.3, the classical motion slows down at the hyperbolic fixed point (the time to reach the unstable equilibrium point with zero velocity diverges [93]), and the eigenfunction must exhibit a maximum of the electronic density at this position. In addition, due to the periodicity of the drive, the corresponding ("hyperbolic") wave-packet eigenstate necessarily follows the dynamics of a classical particle which evolves along the unstable periodic orbit. However, because the orbit is unstable, the quantum eigenstate cannot remain fully localized – some probability has to flow away along the unstable manifold of the classical flow in the vicinity of the hyperbolic fixed point. Consequently, such an eigenstate is partially localized along the separatrix between librational and rotational motion. For an illustration, first consider fig. 16, which shows classical surfaces of section of the driven (1D) hydrogen atom, at $F_0 = 0.034$, again for different phases ωt. Comparison with fig. 12 shows a larger elliptic island at this slightly lower field amplitude, as well as remnants of the $s = 2$ resonance island at slightly larger actions $I/n_0 \simeq 1.2 \ldots 1.3$. The

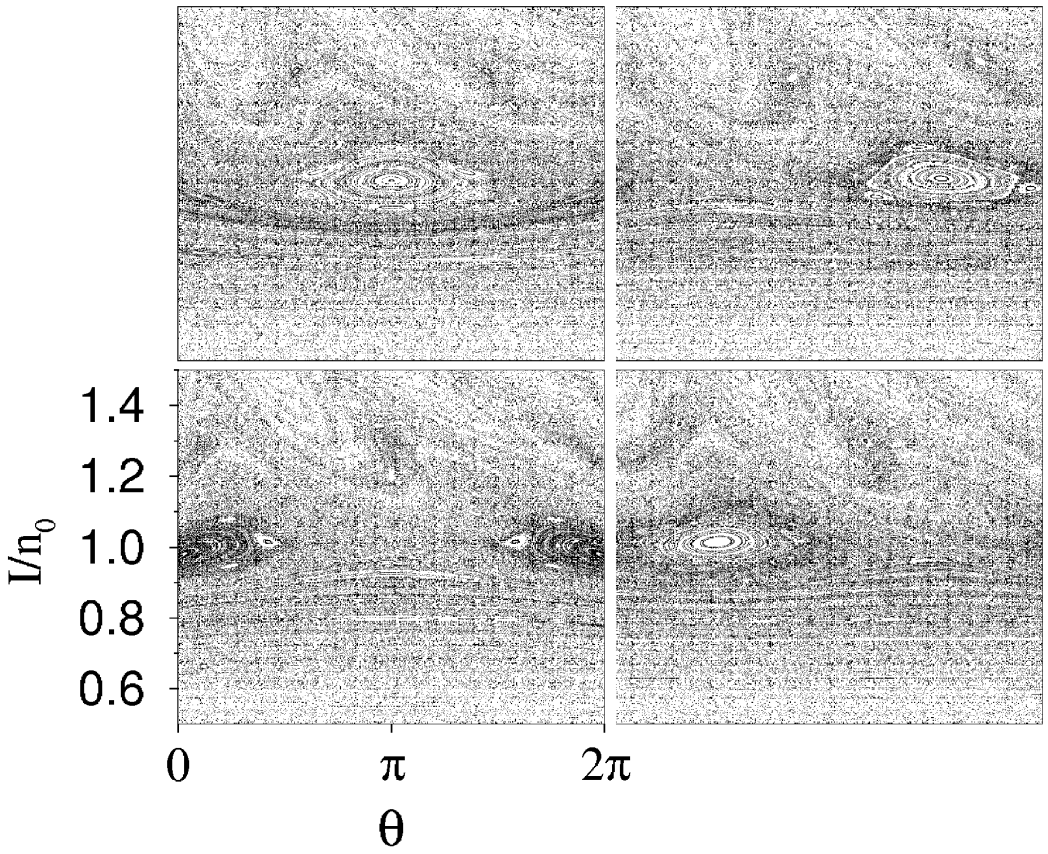

Fig. 16. Surface of section of the classical phase space of a 1D hydrogen atom driven by a linearly polarized microwave field, for different values of the phase: $\omega t = 0$ (top left), $\omega t = \pi/2$ (top right), $\omega t = \pi$ (bottom left), $\omega t = 3\pi/2$ (bottom right). The action angle variables I, θ are defined by eq. (117). At this value of the field amplitude, $F_0 = 0.034$, the principal resonance island (and a small remnant of the $s = 2$ resonance island) remain as the only regions of regular motion, in a globally chaotic phase space.

time evolution of the electronic density of the eigenstate localized near the hyperbolic fixed point is displayed in fig. 17, for different phases of the driving field. Clearly, as compared to fig. 13, the wave-packet moves in phase opposition to the driving field, and displays slightly irregular localization properties. Accordingly, the Husimi representation in fig. 18 exhibits reasonnably good localization on top of the hyperbolic point at phase $\omega t = \pi$, but the electronic probability spreads significantly along the separatrix layer at phase, as visible at $\omega t = 0$.

In the above discussion of the localization properties of the wave-packet eigenstate we represented the wave-function in the I-θ phase space of *classically bounded* motion (i.e., classical motion with negative energy). However, as we shall see in more detail in section 7.1, the microwave driving actually induces a nonvanishing overlap of *all* Floquet eigenstates [120,121], and, hence, of the wave-packet eigenstates, with the atomic continuum. It suffices to say here

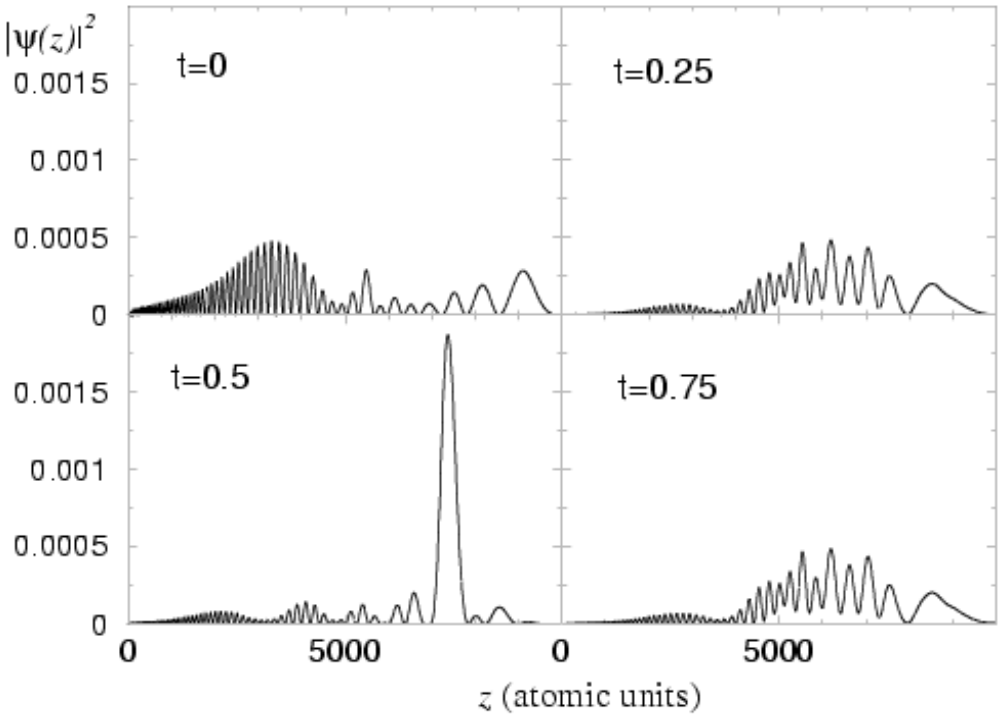

Fig. 17. Wave-packet eigenstate anchored to the hyperbolic fixed point of the principal resonance of the 1D hydrogen atom driven by a linearly polarized microwave field, in configuration space, for the same phases of the driving field as in fig. 16. The wave-function is partly localized, especially close to the outer turning point at $t = 0.5 \times 2\pi/\omega$, but the localization is far from being perfect. Comparison to figs. 12, 13 and 16 shows that the state evolves in phase opposition with the stable, non-dispersive wave-packet, with significantly worse localization properties.

that the associated finite decay rates induce finite life times of approx. 10^6 unperturbed Kepler orbits for the quantum objects considered in this chapter, and are therefore irrelevant on the present level of our discussion. In figs. 13, 15, 17, and 18, a finite decay rate would manifest as a slow reduction of the electronic density, without affecting its shape or localization properties, after 10^6 classical Kepler periods.

3.3.2 Realistic three-dimensional atom

Extending our previous analysis to the three-dimensional hydrogen atom driven by a linearly polarized microwave field, we essentially expand the accessible phase space. Since the Hamiltonian

$$H_{\rm LP} = \frac{\vec{p}^2}{2} - \frac{1}{r} + Fz\cos(\omega t) \tag{151}$$

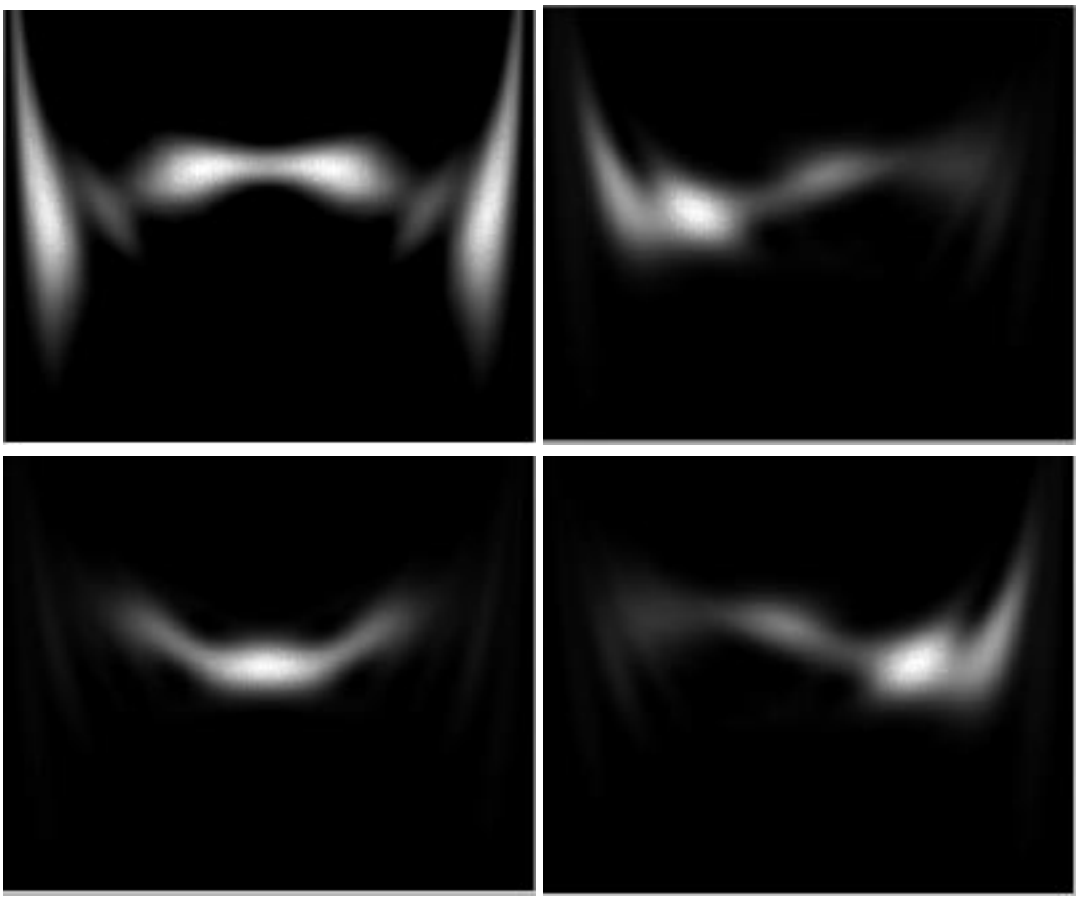

Fig. 18. Husimi representation of the "hyperbolic" wave-packet eigenstate of fig. 17, for the same phases (scales as in fig. 16). Clearly, the quantum mechanical eigenstate of the atom in the field follows the classical evolution. It is partly localized on top of the hyperbolic fixed point, but also spreads along the separatrix confining the principal resonance. The localization is more visible at $t = 0$ (top left), the spreading more visible at $t = 0.5 \times 2\pi/\omega$ (bottom left).

is invariant under rotations around the field polarization axis, the projection of the angular momentum is a conserved quantity and gives rise to a good quantum number M. Hence, only two dimensions of configuration space are left, which, together with the explicit, periodic time dependence, span a five-dimensional phase space.

In the 1D situation described previously, the key ingredient for the existence of non-dispersive wave-packets was the phase locking of the internal degree of freedom on the external drive. In the 3D situation, there remains one single drive, but there are several internal degrees of freedom. In the generic case, not all internal degrees of freedom can be simultaneously locked on the external drive, and one can expect only partial phase locking, i.e. only partially localized wave-packets. The non-trivial task is to understand how the phase locking of one degree of freedom modifies the dynamics along the other degrees of freedom. In atomic systems, the Coulomb degeneracy makes it possible to

gain a full understanding of this phenomenon.

The starting point is similar to the 1D analysis in sec. 3.3.1, that is the expression of the Floquet Hamiltonian – whose eigenstates are of interest – as a function of action-angle coordinates (I, θ), (L, ψ), (M, ϕ) introduced in section 3.2. Using eqs. (125,126) and the Fourier expansion, eq. (121-123), of the position operator, one obtains:

$$\mathcal{H} = P_t - \frac{1}{2I^2} + F\sqrt{1 - \frac{M^2}{L^2}} \sum_{m=-\infty}^{+\infty} [-X_m \cos\psi \cos(m\theta - \omega t) + Y_m \sin\psi \sin(m\theta - \omega t)], \quad (152)$$

with

$$X_m(I) = I^2 \frac{J'_m(me)}{m}, \qquad m \neq 0, \quad (153)$$

$$Y_m(I) = I^2 \frac{\sqrt{1-e^2} J_m(me)}{me}, \qquad m \neq 0, \quad (154)$$

$$X_0(I) = -\frac{3}{2} e I^2, \quad (155)$$

$$Y_0(I) = 0. \quad (156)$$

where $e = \sqrt{1 - L^2/I^2}$ is, as before, the eccentricity of the Kepler orbit (see eq. (124)). The absence of φ in the Hamiltonian reflects the azimuthal symmetry around the field axis and ensures the conservation of M.

Precisely as in the treatment of the one-dimensional problem, we now transform to slowly varying variables, given by eqs. (60)-(62):

$$\hat{\mathcal{H}} = \hat{P}_t - \frac{1}{2\hat{I}^2} - \omega \hat{I} + F\sqrt{1 - \frac{M^2}{L^2}} \times \sum_{m=-\infty}^{+\infty} \left[-X_m \cos\psi \cos(m\hat{\theta} + (m-1)\omega t) + Y_m \sin\psi \sin(m\hat{\theta} + (m-1)\omega t)\right] \quad (157)$$

Averaging over the fast variable t (over the driving field period T) gives the secular Hamiltonian of the three-dimensional problem

$$\mathcal{H}_{\text{sec}} = \hat{P}_t - \frac{1}{2\hat{I}^2} - \omega \hat{I} + F\sqrt{1 - \frac{M^2}{L^2}} (-X_1(\hat{I}) \cos\psi \cos\hat{\theta} + Y_1(\hat{I}) \sin\psi \sin\hat{\theta}). \quad (158)$$

Its physical interpretation is rather simple: the X_1 term represents the oscillating dipole (resonant with the frequency of the drive) along the major axis of the classical Kepler ellipse, while the Y_1 term represents the oscillating dipole along the minor axis. As these two components of the oscillating dipole are in quadrature, they interact with two orthogonal components of the external drive, hence the $\cos\hat{\theta}$ and $\sin\hat{\theta}$ terms. Finally, both components can be

combined to produce the compact form

$$\mathcal{H}_{\rm sec} = \hat{P}_t - \frac{1}{2\hat{I}^2} - \omega\hat{I} + F\chi_1 \cos(\hat{\theta} + \delta_1), \tag{159}$$

with

$$\chi_1(\hat{I}, L, \psi) := \sqrt{1 - \frac{M^2}{L^2}}\ \sqrt{X_1^2 \cos^2\psi + Y_1^2 \sin^2\psi}, \tag{160}$$

$$\tan\delta_1(L, \psi) := \frac{Y_1}{X_1}\tan\psi = \frac{J_1(e)\sqrt{1-e^2}}{J_1'(e)e}\tan\psi. \tag{161}$$

In this form, the secular Hamiltonian has the same structure as the general 1D expression, eq. (64), and its specialized version for the 1D hydrogen atom, eq. (141). The difference is that the additional action angle-variables (L, ψ), (M, ϕ) *only* enter in the amplitude and phase of the coupling defining the resonance island. This allows to separate various time scales in the system:

– The shortest time scale is associated with the Kepler motion, which is also the period of the external drive. In the resonant approximation discussed in detail in section 3.1.1, this time scale is eliminated by passing to the rotating frame.
– The time scale of the secular (or pendulum) motion in the $(\hat{I}, \hat{\theta})$ plane is significantly longer. It is the inverse of the classical pendulum frequency, eq. (80), of the order of $1/\sqrt{F_0}$ Kepler periods. In the regime of weak external driving we are interested in, $F_0 \ll 1$, it is thus much longer than the preceding time scale.
– The time scale of the "transverse" (or angular) motion along the (L, ψ), (M, ϕ) variables. Because these are constant for the unperturbed Coulomb system, the time derivatives like dL/dt and $d\psi/dt$ generated by eqs. (159)-(161) are proportional to F, and the resulting time scale is proportional to $1/F$. More precisely, it is of the order of $1/F_0$ Kepler periods, i.e., once again, significantly longer than the preceding time scale.

From this separation of time scales, it follows that we can use the following, additional secular approximation: for the motion in the $(\hat{I}, \hat{\theta})$ plane, χ_1 and δ_1 are adiabatic invariants, which can be considered as constant quantities. We then exactly recover the Hamiltonian discussed for the 1D model of the atom, with a resonance island confining trajectories with librational motion in the $(\hat{I}, \hat{\theta})$ plane, and rotational motion outside the resonance island. The center of the island is located at:

$$\hat{I} = \hat{I}_1 = \omega^{-1/3} = n_0, \qquad \hat{\theta} = -\delta_1. \tag{162}$$

As already pointed out in section 3.1.1, the size of the resonance island in phase space is determined by the strength of the resonant coupling $\chi_1(\hat{I}, L, \psi)$. In

the pendulum approximation, its extension in $\hat{I}$ scales as $\sqrt{\chi_1(\hat{I}_1, L, \psi)}$, i.e. with χ_1 evaluated at the center, eq. (162), of the island.

The last step is to consider the slow motion in the (L, ψ) plane. As usual, when a secular approximation is employed, the slow motion is due to an effective Hamiltonian which is obtained by averaging of the secular Hamiltonian over the fast motion. Because the coupling $\chi_1(\hat{I}, L, \psi)$ exhibits a simple scaling with $\hat{I}$ (apart from a global $\hat{I}^2$ dependence, it depends on the scaled angular variables L_0 and ψ only), the averaging over the fast motion results in an effective Hamiltonian for the (L_0,ψ) motion which depends on $\chi_1(\hat{I}, L, \psi)$ only. We deduce that the slow motion follows curves of constant $\chi_1(\hat{I}_1, L, \psi)$, at a velocity which depends on the average over the fast variables. $\chi_1(\hat{I}_1, L, \psi)$ is thus a constant of motion, both for the fast $(\hat{I}, \hat{\theta})$ and the slow (L, ψ) motion. This also implies that the order of the quantizations in the fast and slow variables can be interchanged: using the dependence of $\chi_1(\hat{I}_1, L, \psi)$ on (L, ψ), we obtain quantized values of χ_1 which in turn can be used as constant values to quantize the $(\hat{I}, \hat{\theta})$ fast motion. Note that the separation of time scales is here essential [16]. Finally, the dynamics in (M, ϕ) is trivial, since M is a constant of motion. In the following, we will consider the case $M = 0$ for simplity. Note that, when the eccentricity of the classical ellipse tends to 1 – i.e. $L \to 0$ – and when $\psi \to 0$, the Hamiltonian (158) coincides exactly with the Hamiltonian of the 1D atom, eq. (141). This is to be expected, as it corresponds to a degenerate classical Kepler ellipse along the z axis.

The adiabatic separation of the radial and of the angular motion allows the separate WKB quantization of the various degrees of freedom. In addition to the quantization conditions in $(\hat{P}_t, t)$ and $(\hat{I}, \hat{\theta})$, eqs. (76-79), already formulated in our general description of the semiclassical approach in section 3.1.3, we additionally need to quantize the angular motion, according to:

$$\frac{1}{2\pi} \oint_\gamma L d\psi = \left(p + \frac{1}{2}\right) \hbar, \tag{163}$$

along a loop γ of constant χ_1 in the (L, ψ) plane.

Importantly, the loops of constant χ_1 are independent of the microwave amplitude F and scale simply with $\hat{I}$. Thus, the whole quantization in the (L, ψ) plane has to be done only once. With this prescription we can unravel the semiclassical structure of the quasienergy spectrum induced by the additional degree of freedom spanned by (L, ψ), as an amendment to the spectral structure of the one-dimensional model discussed in section 3.3.1. Fig. 19 shows the equipotential curves of χ_1 in the (L, ψ) plane. For a comparison with quantal

[16] If one considers non-hydrogenic atoms – with a core potential in addition to the Coulomb potential – the classical unperturbed ellipse precesses, adding an additional time scale, and the separation of time scales is much less obvious. See also section 8.2.

data, the equipotential lines plotted correspond to the quantized values of χ_1 for $n_0 = 21$. Using the well-known properties of the Bessel functions [95], it is easy to show that $\chi_1(L, \psi)$ has the following fixed points:

- ($L = \hat{I}_1$, arbitrary ψ). This corresponds to a Kepler ellipse with maximum angular momentum, i.e. a circular orbit in a plane containing the microwave polarization axis along $\hat{z}$. As such a circle corresponds to a degenerate family of elliptical orbits with arbitrary orientation of the major axis, ψ is a dummy angle. This fixed point corresponds to a global maximum of $\chi_1(L = \hat{I}_1) = \hat{I}_1^2/2$, and is surrounded by "rotational" trajectories in the (L, ψ) plane. An alternative representation of the (L, ψ) motion on the unit sphere, spanned by L and the z and ρ-components of the Runge-Lenz vector, contracts the line representing this orbit in fig. 19 to an elliptic fixed point [87].
- ($L = 0, \psi = \pi/2, 3\pi/2$). This corresponds to a degenerate straight line trajectory perpendicular to the microwave field. Because of the azimuthal symmetry around the electric field axis, the two points actually correspond to the same physics. The oscillating dipole clearly vanishes there, resulting in a global minimum of $\chi_1(L = 0, \psi = \pi/2, 3\pi/2) = 0$. This stable fixed point is surrounded by "librational" trajectories in the (L, ψ) plane.
- ($L = 0, \psi = 0, \pi$). This corresponds to a degenerate, straight line trajectory along the microwave field, i.e. the situation already considered in the 1D model of the atom. $\psi = 0$ and π correspond to the two orbits pointing up and down, which are of course equivalent. This is a saddle point of $\chi_1(L = 0, \psi = 0, \pi) = J_1'(1)\hat{I}_1^2$. Hence, it is an unstable equilibrium point. As an implication, in the real 3D world, the motion along the microwave axis, with the phase of the radial motion locked on the external drive, is angularly unstable (see also section 4.1). This leads to a slow precession of the initially degenerate Kepler ellipse off the axis, and will manifest itself in the localization properties of the 3D analog of the nondispersive wavepacket displayed in fig. 13. This motion takes place along the separatrix between librational and rotational motion.

Once the quantized values of χ_1 (represented by the trajectories in fig. 19) have been determined, we can quantize the $(\hat{I}, \hat{\theta})$ motion with these values fixed. Fig. 20 shows the equipotential lines of $\mathcal{H}_{\rm sec}$, for the three values of χ_1 corresponding to the $p = 0$, 10 and 20 states, see eq. (163), of the $n_0 = 21$ manifold. In each case, the contour for the lowest state $N = 0$ has been drawn, together with the separatrix between the librational and rotational $(\hat{I}, \hat{\theta})$ modes. The separatrix determines the size of the principal resonance island for the different substates of the transverse motion. Note that the principal resonance is largest for the $p = 20$ state, localized closest to the stable circular orbit (hence associated with the maximum value of χ_1), whereas the smallest resonance island is obtained for the $p = 0$ state, localized in the vicinity of (though not precisely at) the straight line orbit perpendicular to the field axis (minimum value of χ_1). For the latter orbit itself, the first order coupling vanishes iden-

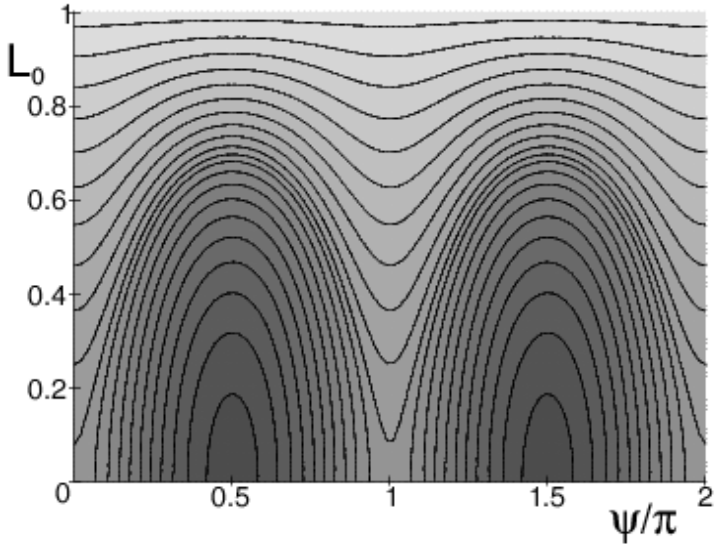

Fig. 19. Isovalue curves of the angular part χ_1, eq. (160), of the secular Hamiltonian $\mathcal{H}_{\rm sec}$ represented in the plane of the $L_0 = L/\hat{I}_1$ and ψ coordinates. The slow evolution of the Kepler ellipse of a Rydberg electron driven by a resonant, linearly polarized microwave field, takes place along such isovalue curves. $L_0 = L/\hat{I}$ represents the total angular momentum (a circular trajectory in a plane containing the field polarization axis has $L_0 = 1$), and ψ the [canonically conjugate] angle between the field polarization axis and the major axis of the Kepler ellipse. The separatrix emanating from the unstable fixed point $(L_0 = 0, \psi = 0)$ separates rotational and librational motion, both "centered" around their respective stable fixed points ($L_0 = 1$, ψ arbitrary) and ($L_0 = 0$, $\psi = \pi/2$). The former corresponds to a circular orbit centered around the nucleus. The latter represents a straight linear orbit perpendicular to the field axis. The unstable fixed point corresponds to linear motion along the polarization axis. However, this initially degenerate Kepler ellipse will slowly precess in the azimuthal plane. The equipotential curves shown here satisfy the quantization condition (163), for $n_0 = 21$ and $p = 0 \ldots 20$. At lowest order, the motion in the (L_0, ψ) plane is independent of the microwave field strength and of the resonant principal quantum number n_0.

tically ($\chi_1 = 0$), which shows that the semiclassical results obtained from our first order approximation (in F) for the Hamiltonian may be quite inaccurate in the vicinity of this orbit. Higher order corrections may become important.

As discussed above, the classical motion in the (L, ψ) plane is slower than in the $(\hat{I}, \hat{\theta})$ plane. In the semiclassical approximation, the spacing between consecutive states corresponds to the frequency of the classical motion (see also eq. (40)). Hence, it is to be expected that states with the same quantum number N, but with successive quantum numbers p, will lie at neighboring energies, building well-separated manifolds associated with a single value of N. The energy spacing between states in the same manifold should scale as F_0, while the spacing between manifolds should scale as $\sqrt{F_0}$ (remember that $F_0 \ll$

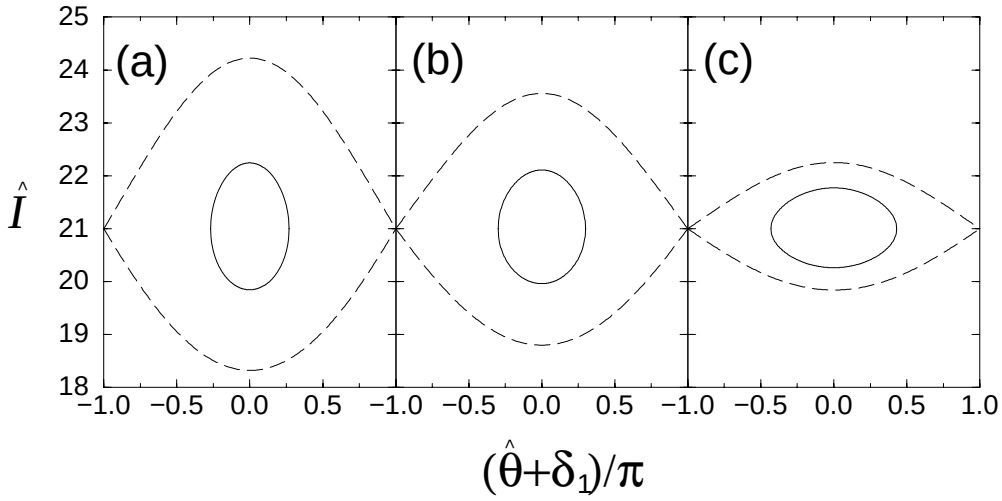

Fig. 20. Isovalue curves of the secular Hamiltonian $\mathcal{H}_{\rm sec}$, eq. (159), generating the $(\hat{I},\hat{\theta})$ motion of a Rydberg electron in a resonant microwave field. $\hat{I}$ and $\hat{\theta}$ correspond to the atomic principal quantum number, and to the polar angle of the electron on the Kepler ellipse, respectively. The scaled microwave amplitude is fixed at $F_0 = 0.03$. Since the isovalues of $\mathcal{H}_{\rm sec}$ depend on the transverse motion in (L,ψ) via the constant value of χ_1, eq. (160), contours (solid lines) are shown for three characteristic values of χ_1, corresponding to fixed quantum numbers $p = 0, 10, 20$, eq. (163), of the angular motion for the $n_0 = 21$ resonant manifold. Only the "ground state" orbit satisfying eq. (78) with $N = 0$ is shown, together with the separatrix (dashed lines) between librational and rotational motion in the $(\hat{I},\hat{\theta})$ plane. The separatrix encloses the principal resonance island in phase space, see also eqs. (66,71). Panel (a) corresponds to the orbit with $L_0 = L/n_0 \simeq 1$ (rotational orbit, $p = 20$), panel (b) to the orbit close to the separatrix of the angular motion ($p = 10$), panel (c) to the librational orbit close to the stable fixed point $L_0 = 0$, $\psi = \pi/2$. Note that the resonance island is smallest for librational, largest for rotational, and of intermediate size for separatrix modes of the angular motion.

1 in the case considered here). Accurate quantum calculations fully confirm this prediction, with manifolds originating from the degenerate hydrogenic energy levels at $F_0 = 0$, as we shall demonstrate now. We first concentrate on the $N = 0$ manifold, originating from $n_0 = 21$. Fig. 21 shows the comparison between the semiclassical and the quantum energies, for different values of the scaled driving field amplitude $F_0 = F n_0^4$. The agreement is excellent, except for the lowest lying states in the manifold for $F_0 = 0.02$. The lowest energy level ($p = 0$) corresponds to motion close to the stable fixed point $L = 0$, $\psi = \pi/2$ in fig. 19; the highest energy level ($p = 20$) corresponds to rotational motion $L/n_0 \simeq 1$. The levels with the smallest energy difference ($p = 10, 11$) correspond to the librational and the rotational trajectories closest to the separatrix, respectively. The narrowing of the level spacing in their vicinity is just a consequence of the slowing down of the classical motion [60]. In the same

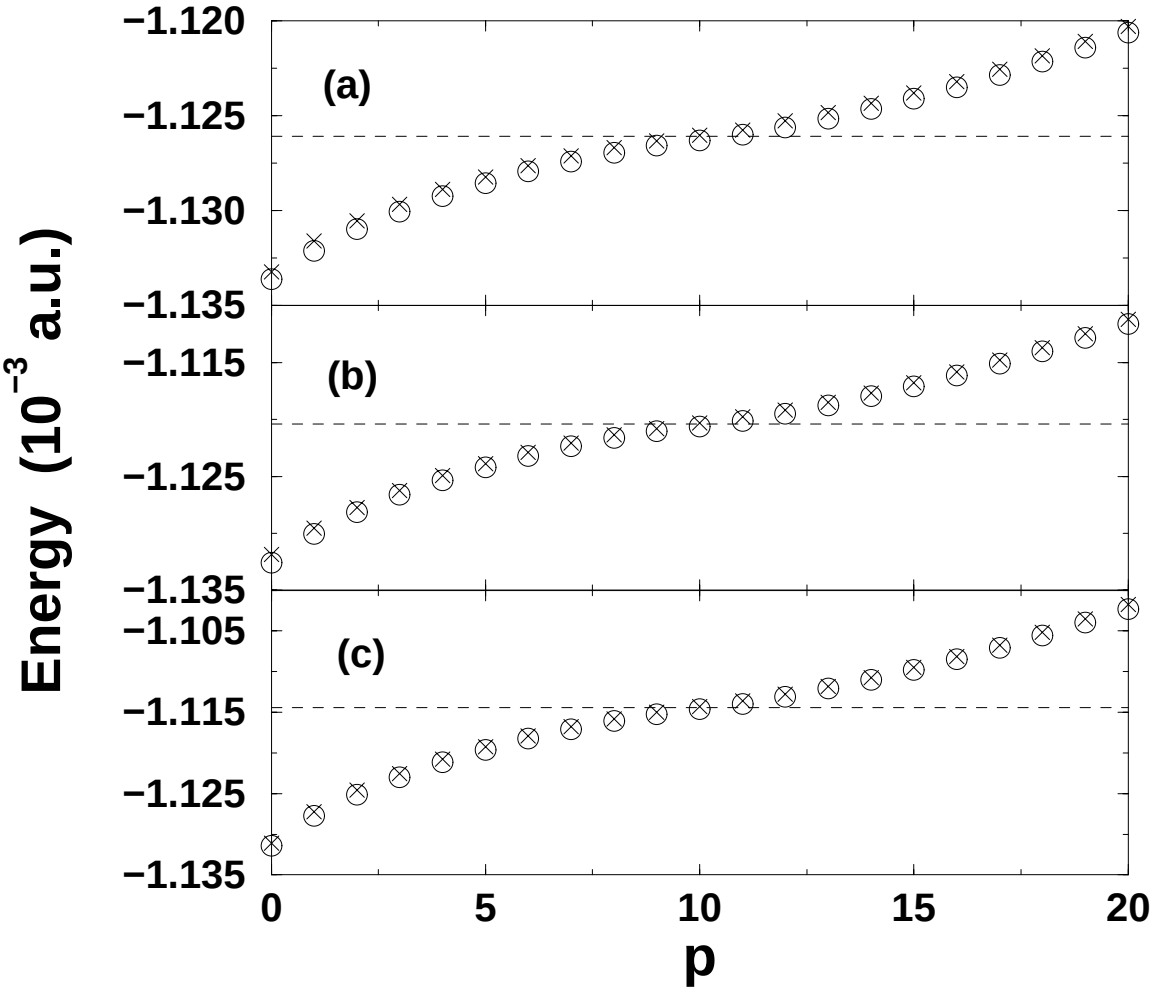

Fig. 21. Comparison of the semiclassical quasienergies (circles; with $N = 0$, see eq. (78)), originating from the unperturbed $n_0 = 21$ manifold, to the exact quantum result (crosses), at different values of the (scaled) driving field amplitude $F_0 = Fn_0^4 = 0.02$ (a), 0.03 (b), 0.04 (c). The agreement is excellent. The quantum number $p = 0 \ldots 20$ labels the quantized classical trajectories plotted in fig. 19, starting from the librational state $\mid p = 0\rangle$ at lowest energy, rising through the separatrix states $\mid p = 10\rangle$ and $\mid p = 11\rangle$, up to the rotational state $\mid p = 20\rangle$. The dashed line indicates the exact quasienergy of the corresponding wave-packet eigenstate of the 1D model discussed in section 3.3.1. The 1D dynamics is neatly embedded in the spectrum of the real, driven 3D atom.

figure, we also plot (as a dashed line) the corresponding exact quasienergy level for the 1D model of the atom (see section 3.3.1). As expected, it closely follows the separatrix state $p = 10$. Such good agreement is a direct proof of the validity of the adiabatic separation between the slow motion in (L, ψ), and the fast motion in $(\hat{I}, \hat{\theta})$.

Fig. 22 shows a global comparison of the semiclassical prediction with the exact level dynamics (energy levels vs. F_0), in a range from $F_0 = 0$ to $F_0 = 0.06$,

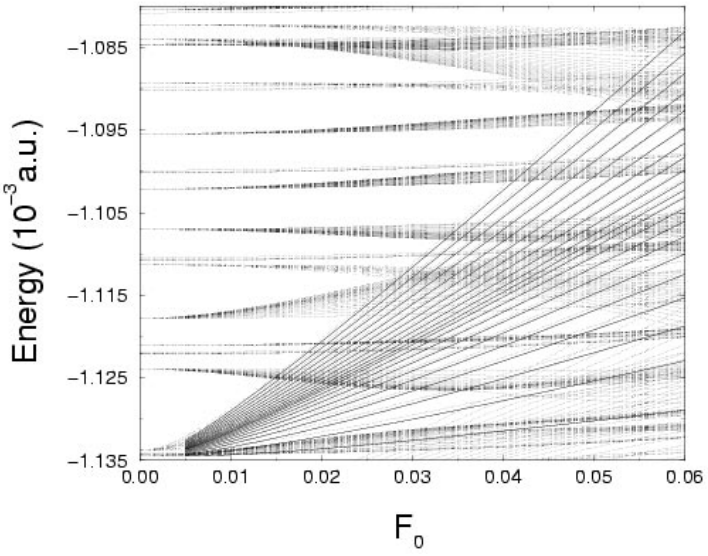

Fig. 22. Level dynamics of the numerically exact quasienergies (dotted lines) in the vicinity of the resonant manifold emerging from $n_0 = 21$ ($N = 0$), compared to the semiclassical prediction (full lines), for $F_0 = Fn_0^4 = 0 \ldots 0.06$. Note that the maximum field amplitude exceeds the typical ionization thresholds measured in current experiments for $\omega n_0^3 \simeq 1$ [132–134]. Nontheless, the semiclassical prediction accurately tracks the exact solution across a large number of avoided crossings with other Rydberg manifolds.

which exceeds the typical ionization threshold ($F_0 \simeq 0.05$) observed in current experiments [132–134]. We observe that the semiclassical prediction tracks the exact quasienergies quite accurately, even for large F_0-values, where the resonant $n_0 = 21$ manifold overlaps with other Rydberg manifolds, or with side bands of lower or higher lying Rydberg states. The agreement becomes unsatisfactory only in the region of very small F_0, where the size of the resonance island in $(\hat{I}, \hat{\theta})$ is very small. This is not unexpected, as semiclassics should fail when the area of the resonance island is comparable to $\hbar$, compare eq. (82). In this weak driving regime, the pendulum approximation can be used to produce more accurate estimates of the energy levels. The fast $(\hat{I}, \hat{\theta})$ motion is essentially identical to the one of the 1D driven hydrogen atom: thus, the Mathieu approach used in section 3.3.1 can be trivially extended to the 3D case. The only amendment is to replace the factor $J_1'(1)n_0^2$ in the expression of the Mathieu parameter q by the various quantized values of χ_1 for $0 \leq p \leq n_0 - 1$, and to use the same equation (149) for the energy levels.

The semiclassical construction of the energy levels from classical orbits is – necessarily – reflected in the localization properties of the associated eigenstates, as demonstrated by the electronic densities of the states $\mid p = 0\rangle$, $\mid p = 10\rangle$, and $\mid p = 20\rangle$ in fig. 23, for the same field amplitudes as in fig. 21. Note that, in this plot, the electronic densities are averaged over one field cycle, hence display only the angular localization properties of the eigenstates.

Their localization along the classical orbits defined by the stable or unstable fixed points of the (L, ψ) dynamics is obvious [64,67,87]. Note in particular the nodal structure of the state $\mid p = 10\rangle$, associated with the unstable fixed point: there are sharp nodal lines perpendicular to the z-axis, reflecting the dominant motion along the z-axis, but also nodal lines of low visibility in the angular direction. They are a manifestation of the slow classical precession of the Kepler ellipse, i.e. the slow secular evolution in the (L, ψ) plane. The quantum state, however, dominantly exhibits the motion along the z-axis, as a signature of the effective separation of time scales of radial and angular motion. Finally, it should be realized from a comparison of the top to the middle and bottom row of fig. 23 that the quasiclassical localization properties of the eigenstates are essentially unaffected as F rises, despite various avoided crossings which occur at intermediate field values, see fig. 22. Especially, the angular structure does not depend at all on F, as predicted by the secular approximation.

The eigenstates displayed here are localized along classical trajectories which are resonantly driven by the external field. Hence, we should expect them to exhibit wave-packet like motion along these trajectories, as the phase of the driving field is changed. This is indeed the case as illustrated in fig. 24 for the state $p = 20$ with maximal angular momentum $L/n_0 \simeq 1$ [48,64,67]. Due to the azimuthal symmetry of the problem, the actual 3D electronic density is obtained by rotating the figure around the vertical axis. Thus, the wave-packet is actually a doughnut moving periodically from the north to the south pole (and back) of a sphere, slightly deformed along the field direction. The interference resulting from the contraction of this doughnut to a compact wave-packet at the poles is clearly visible at phases $\omega t = 0$ and $\omega t = \pi$ in the plot. Note that the creation of unidirectional wave-packet eigenstates moving along a circle in the plane containing the field polarization axis is not possible for the real 3D atom [67], as opposed to the reduced 2D problem studied in [48], due to the abovementioned azimuthal symmetry (see also section 3.5). For other states in the $n_0 = 21$ resonant manifold, the longitudinal localization along the periodic orbit is less visible. The reason is that χ_1 is smaller than for the $p = 20$ state, leading to a smaller resonance island in $(\hat{I}, \hat{\theta})$ (see fig. 20) and, consequently, to less efficient localization. Proceeding to higher n_0-values should improve the situation.

Let us briefly discuss "excited" states in the resonance island, i.e. manifolds corresponding to $N > 0$ in eq. (78). Fig. 25 shows the exact level dynamics, with the semiclassical prediction for $N = 1$ superimposed [67]. The states in this manifold originate from $n_0 = 22$. We observe quite good agreement between the quantum and semiclassical results for *high* lying states in the manifold (for which the principal action island is large, see fig. 20). For lower lying states the agreement is improved for higher values of F_0. If F_0 is too low, the states are not fully localized inside the resonance island and, consequently,

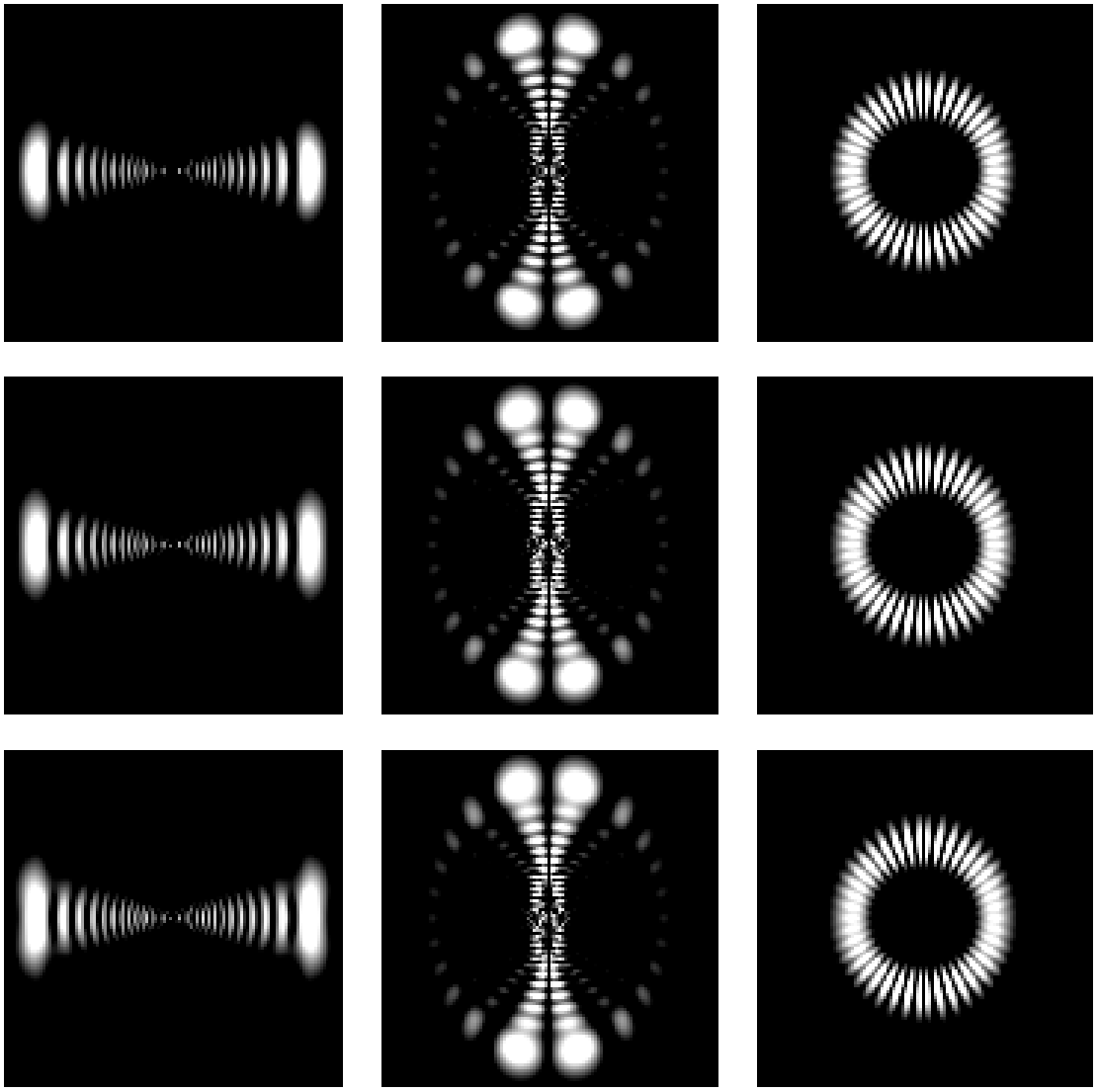

Fig. 23. Electronic densities of the extremal librational ($p = 0$, left), separatrix ($p = 10$, center), and extremal rotational ($p = 20$, right) quasienergy states of the $n_0 = 21$ manifold of a 3D hydrogen atom exposed to a resonant microwave field in cylindrical coordinates (ρ, z), at different values of the driving field amplitude $F_0 = Fn_0^4 = 0.02$ (top), 0.03 (middle), 0.04 (bottom), averaged over one period of the driving field. Note the clear localization along the classical orbits corresponding to the respective contours in fig. 19, for *all* field amplitudes. The nodal lines of the electronic densities clearly exhibit the direction of the underlying classical motion. The field-induced finite decay rate of the eigenstates (see section 7.1) is negligible on time scales shorter than approx. 10^6 Kepler periods. Each box extends over ± 1000 Bohr radii, in both ρ (horizontal) and z (vertical) directions, with the nucleus at the center of the plot. The microwave polarization axis is oriented vertically along z.

Fig. 24. Temporal evolution of the electronic density of the extremal rotational quasienergy state $|\ p = 20\rangle$ of the $n_0 = 21$ resonant manifold, for different phases $\omega t = 0$ (left), $\omega t = \pi/2$ (center), $\omega t = \pi$ (right) of the driving field, at amplitude $F_0 = 0.03$, in cylindrical coordinates. Each box extends over ± 700 Bohr radii, in both directions, ρ (horizontal) and z (vertical). The microwave polarization axis is oriented along z. Because of the azymuthal symmetry of the problem, the actual 3D electronic density is obtained by rotating the figure around the vertical axis. The state represents a non-dispersive wave-packet shaped like a doughnut, moving periodically from the north to the south pole (and back) of a sphere. For higher n_0, the angular localization on the circular orbit should improve.

are badly reproduced by the resonant semiclassical approximation. This is further exemplified in fig. 26, for $N = 2$. Here, the agreement is worse than for smaller values of N, and is observed only for large F_0 and large p. This confirms the picture that the validity of the semiclassical approach outlined here is directly related to the size, eqs. (71,82), of the resonance island in $(\hat{I}, \hat{\theta})$ space (see also the discussion in section 8.3).

Finally note that, as already mentioned at the end of section 3.3.1, all wave-packet eigenstates have a finite decay rate which induces a slow, global reduction of the electronic density localized on the resonantly driven classical periodic orbit. However, the time scale of this decay is of the order of thousands to millions of Kepler cycles, and therefore leaves our above conclusions unaffected. However, some very intriguing consequences of the nonvanishing continuum coupling will be discussed in section 7.1.

3.4 Rydberg states in circularly polarized microwave fields

As shown in the preceding section, the use of a linearly polarized microwave field is not sufficient to produce a non-dispersive wave-packet fully localized in all three dimensions, due to the azymuthal symmetry around the microwave polarization axis. To get more flexibility, one may consider the case of arbitrary polarization. It turns out that the results are especially simple in circular polarization. They are the subject of this section.

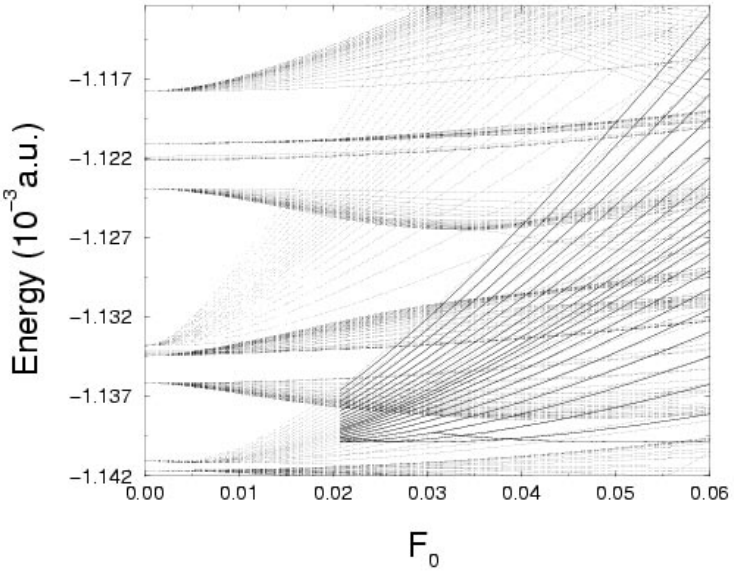

Fig. 25. Comparison of the numerically exact level dynamics (dotted lines) with the semiclassical prediction (solid lines), for the $n_0 = 22$ ($N = 1$) manifold of a 3D hydrogen atom exposed to a microwave field with frequency $\omega = 1/(21)^3$, resonant with the $n_0 = 21$ manifold. For sufficiently high F_0, the quantum states originating at $F_0 = 0$ from the unperturbed $n_0 = 22$ level are captured by the principal resonance island and then represent the first excited state of the motion in the $(\hat{I}, \hat{\theta})$ plane (i.e., $N = 1$ in eq. (78)). Since the island's size depends on the angular (L, ψ) motion (value of p in eq. (163), see also fig. 20), states with large p enter the resonance zone first. For these, the agreement between quantum and semiclassical quasienergies starts to be satisfactory at lower F_0 values than for low-p states.

In most experiments on microwave driven Rydberg atoms, linearly polarized (LP) microwaves have been used [132,133,135–137]. For circular polarization (CP), first experiments were performed for alkali atoms in the late eighties [138,139], with hydrogen atoms following only recently [134]. The latter experiments also studied the general case of elliptic polarization (EP). While, at least theoretically, different frequency regimes were considered for CP microwaves (for a review see [140]) – we shall restrict our discussion here to resonant driving. Given a different microwave polarization, and thus a different form of the interaction Hamiltonian, eq. (111), Kepler trajectories which are distinct from those considered in the LP case will be most efficiently locked on the external driving. Hence, in the sequal, we shall launch nondispersive wave-packets along periodic orbits which are distinct from those encountered above.

Historically, the creation of non-dispersive wave-packets in CP and LP microwave fields, respectively, has been considered quite independently. In particular, in the CP case, the notion of nondispersive wave-packets has been introduced [34] along quite different lines than the one adopted in this re-

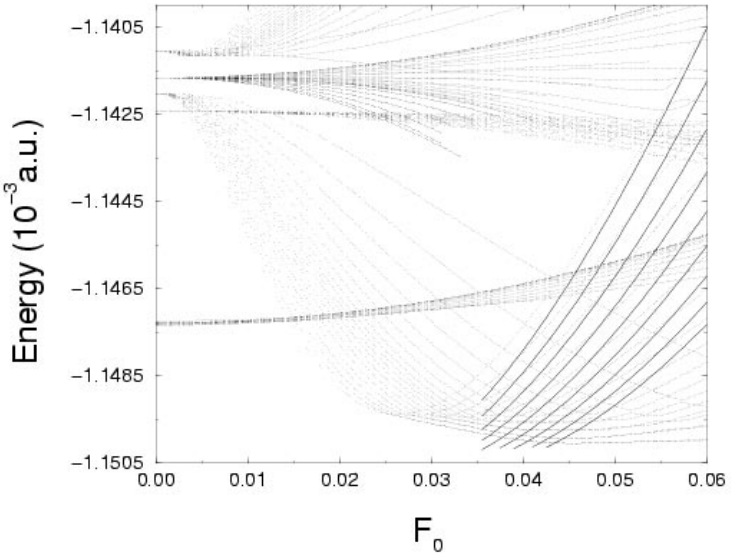

Fig. 26. Same as fig. 25, but for $N = 2$. The quantum states originate from the manifold $n_0 = 20$. The resonance island in the $(\hat{I}, \hat{\theta})$ coordinates is too small to support any $N = 2$ states for $F_0 < 0.03$, as seen from the negative slope of the quasienergy levels. The quantum states "cross" the separatrix as the amplitude is further increased, and successively enter the resonance zone, starting from the largest value of p in eq. (163) (the resonance island size increases with p). Even for $F_0 > 0.04$, only a minority of substates of the $n_0 = 20$ manifold is well represented by the resonant semiclassical dynamics (indicated by the solid lines).

view. The original work, as well as subsequent studies of the CP situation [44,45,47,49,50,55,61,63] used the fact that, in this specific case, the time-dependence of the Hamiltonian may be removed by a unitary transformation to the rotating frame (see below). Thus, the stable periodic orbit at the center of the island turns into a stable equilibrium point in the rotating frame. This allows the expansion of the Hamiltonian into a Taylor series in the vicinity of the fixed point, and in particular a standard harmonic treatment using normal modes. We shall review this line of reasoning in detail below. It is, however, instructive to first discuss the very same system using the general resonance approach exposed in section 3.1.

3.4.1 Hamiltonian

With $\hat{z}$ the propagation direction of the microwave, the electric field rotates in the $x - y$ plane, and the Hamiltonian (106) takes the following explicit form:

$$H_{\mathrm{CP}} = \frac{\vec{p}^2}{2} - \frac{1}{r} + F\left\{x\cos(\omega t) + y\sin(\omega t)\right\}. \tag{164}$$

In contrast to the LP situation, there is no simplified one-dimensional model in the CP case. However, a simplified two-dimensional model exists, where the

motion is restricted to the $x-y$ plane. As long as one is interested only in the dynamics of non-dispersive wave-packets, this motion is stable (see below), which means that a small deviation from the $z = 0$ plane does not affect the qualitative behavior. Hence, much physical insight can be obtained from the simplified 2D model. It will be discussed in section 3.4.3.

3.4.2 Resonance analysis

We follow the general treatment exposed in sections 3.1.1 and 3.3.1 for the 1D case, and express the external perturbation as a function of the action-angle variables (I, θ), (L, ψ) and (M, ϕ) introduced in section 3.2. By inserting equations (121,122) in eq.(164), after appropriate account for the projection of the body-fixed frame (x', y', z') onto the laboratory frame (x, y, z), eq. (126), we obtain for the Floquet Hamiltonian:

$$\mathcal{H} = P_t - \frac{1}{2I^2} + F \sum_{m=-\infty}^{\infty} \left[V_m \cos(m\theta + \phi - \omega t) - U_m \sin(m\theta + \phi - \omega t)\right], \quad (165)$$

where the Fourier coefficients are given by (see also eqs. (153-156)):

$$V_m(I, L, M, \psi) = \cos\psi \left(Y_m + \frac{M}{L} X_m\right), \quad (166)$$

$$U_m(I, L, M, \psi) = \sin\psi \left(X_m + \frac{M}{L} Y_m\right). \quad (167)$$

Once again, transformation to the "rotating frame", eqs. (60-62), and averaging over one field period $T = 2\pi/\omega$ (thereby neglecting all rapidly varying terms) leaves us with the explicit form of the secular Hamiltonian:

$$\mathcal{H}_{\text{sec}} = \hat{P}_t - \frac{1}{2\hat{I}^2} - \omega\hat{I} + F\left[V_1(\hat{I}, L, M, \psi)\cos(\hat{\theta} + \phi) - U_1(\hat{I}, L, M, \psi)\sin(\hat{\theta} + \phi)\right], \quad (168)$$

similar to eq. (158). This can be rewritten as:

$$\mathcal{H}_{\text{sec}} = \hat{P}_t - \frac{1}{2\hat{I}^2} - \omega\hat{I} + F\chi_1 \cos(\hat{\theta} + \phi + \delta_1), \quad (169)$$

with the effective perturbation

$$\chi_1(\hat{I}, L, M, \psi) = \sqrt{V_1^2 + U_1^2}, \quad (170)$$

and

$$\tan\delta_1(\hat{I}, L, M, \psi) = \frac{U_1}{V_1}. \quad (171)$$

This secular Hamiltonian, which has, once again, the same structure as the 1D secular Hamiltonian (64), governs the "slow" dynamics of the system in

the vicinity of the resonance. Similarly to the LP case, the various degrees of freedom evolve on different time scales:

– In the $(\hat{I}, \hat{\theta})$ plane, the situation is exactly like for a one-dimensional system. There is a resonance island around the resonant action, with a pendulum-like structure. Non-dispersive wave-packets are associated with eigenstates localized at the center of this island, at the point (see eqs. (135,169)):

$$\hat{I}_1 = \omega^{-1/3} = n_0, \qquad \hat{\theta} = -(\phi + \delta_1). \tag{172}$$

  The period of the secular classical motion close to the resonance center scales as $1/\sqrt{F}$. It defines an intermediate time scale, slower than the Kepler frequency, but faster than the transverse motion in the other coordinates (L, ψ) and (M, ϕ).
– In the subspace spanned by (L, M, ψ, ϕ), the motion is much slower, with a time scale proportional to $1/F$. The effective Hamiltonian describing this motion is obtained by averaging the fast motion in the perturbation which describes this motion $(\hat{I}, \hat{\theta})$ plane, which in turns implies that χ_1 itself is constant for both the motion in $(\hat{I}, \hat{\theta})$ and (L, M, ψ, ϕ) space.

Note that χ_1 does not depend on the angle ϕ. This, in turn, implies that M is a constant of the slow motion. This is because the circular polarization does not define any preferred direction in the $x - y$ polarization plane.

Once again, much alike our discussion in section 3.3.2, the well-known properties of Bessel functions [95], together with eqs. (166,170), imply that, for given M, the maximum of χ_1 occurs at $L = M$, corresponding to the situation when the electronic motion is restricted to the polarization plane. In this plane, the maximum $\chi_1 = \hat{I}^2$ is reached for the circular orbit defined by $M = L = \hat{I}$ (i.e. $L_0 = 1$). This defines a resonant periodic orbit locked on the external microwave driving, which maximizes the effective Hamiltonian in each coordinate and is, therefore, fully stable in all phase space directions. The orbit is a circular Kepler orbit in the polarization plane, where the electron rotates around the nucleus with exactly the angular velocity of the microwave. It is not really surprising that this orbit maximizes the interaction energy with the external field: indeed, along this orbit, the atomic dipole rotates exactly in phase with the polarization vector of the circularly polarized microwave field. As in the case of linear polarization discussed in section 3.3.2, the angular motion in the (L, ψ, M, ϕ) variables (which is trivial in (M, ϕ), since M is constant) could be studied in detail. For the sake of brevity, we will not repeat such an analysis here. We rather concentrate on the wave-packets which are best localized in the resonance island near the circular orbit. The simplest approximation to describe these states is to replace the largest quantized value of χ_1 by its maximum value $\hat{I}^2$ estimated at the center of the resonance island, eq. (172). Then, the situation is similar to the 1D model of the atom, eq. (141), except that the strength of the coupling is $\hat{I}^2$ instead of $-J_1'(1)\hat{I}^2$.

In complete analogy to the steps leading from eq. (141) to eqs. (145,146) we employ the pendulum approximation with a subsequent harmonic expansion around the pendulum's stable equilibrium point, deeply inside the resonance island. The harmonic frequency of the motion in the $(\hat{I}, \hat{\theta})$ plane is:

$$\omega_{\text{harm}} = \frac{\sqrt{3F}}{n_0} = \omega\sqrt{3F_0}, \tag{173}$$

and the quasi-energy levels are:

$$\mathcal{E}_{N,k} = k\omega - \frac{3}{2n_0^2} + n_0^2 F - \left(N + \frac{1}{2}\right)\omega_{\text{harm}}. \tag{174}$$

Note that, by construction, $-3/2n_0^2 + Fn_0^2$ is nothing but the energy at the center of the resonance island, i.e. the energy of the resonant circular orbit. For very small F, the resonance island shrinks and may support only a small number of states, or even no state at all. In this regime, the harmonic approximation, eq. (81), breaks down. Alternatively, one can apply a quantum treatment of the pendulum motion in the $(\hat{I}, \hat{\theta})$ plane, as explained in section 3.1.4 and discussed in section 3.3.1 for the 1D model of the atom exposed to a linearly polarized microwave. The analysis – essentially identical to the one in section 3.3.1 – yields the following expression for the energy levels:

$$\mathcal{E}_{k,N} = k\omega - \frac{3}{2n_0^2} - \frac{3a_N(\nu, q)}{8n_0^4}, \tag{175}$$

where $a_N(\nu, q)$ are the Mathieu eigenvalues (compare with eq. (99) for the general case), with

$$q = \frac{4}{3}Fn_0^6, \tag{176}$$

and

$$\nu = -2n_0 \pmod 2 \tag{177}$$

the characteristic exponent.

These expressions are valid for the states localized close to the resonant circular orbit. For the other states, the calculation is essentially identical, the only amendment being the use of the values of χ_1 following from the quantization of the secular motion, instead of the maximum value n_0^2.

Finally, as the center of the resonance island corresponds to a circular trajectory in the (x, y) plane, the Floquet states associated with the non-dispersive wave-packets will be essentially composed of combinations of circular states $|n,\ L = M = n-1\rangle$, with coefficients described by the solutions of the Mathieu equation, as explained in section 3.1.4. This Mathieu formalism has been

rediscovered in this particular CP situation via complicated approximations on the exact Schrödinger equation in [55]. We believe that the standard resonance analysis using the pendulum approximation leads, at the same time, to simpler calculations, and to a much more transparent physical picture.

3.4.3 The two-dimensional model

We shall now discuss the simplified 2D model of the CP problem, which amounts to restricting the motion to the (x, y) plane, but retains almost all the features of the full 3D problem. Instead of the six-dimensional phase space spanned by the action-angle variables (I, θ), (L, ψ), (M, ϕ), one is left with a four-dimensional submanifold with coordinates (I, θ), (M, ϕ), see section 3.2.4. The secular Hamiltonian then reads (compare eqs. (169,170)):

$$\mathcal{H}_{\rm sec} = \hat{P}_t - \frac{1}{2\hat{I}^2} - \omega\hat{I} + FV_1(\hat{I}, M)\cos(\hat{\theta} + \phi), \tag{178}$$

with (see eq. (166))

$$V_1(\hat{I}, M) = \hat{I}^2\left[J_1'(e) + \mathrm{sign}(M)\frac{\sqrt{1-e^2}}{e}J_1(e)\right], \tag{179}$$

where (as in eq. (124))

$$e = \sqrt{1 - \frac{M^2}{\hat{I}^2}}. \tag{180}$$

However, the Maslov index for the $(\hat{I}, \hat{\theta})$ motion is different. Indeed, the energy spectrum of the 2D atom is given by eq. (116). Thus, quantized values of the action are half-integer multiples of $\hbar$. The relation between the resonant action $\hat{I}_1 = \omega^{-1/3}$ and the corresponding principal quantum number now reads (with $\hbar = 1$):

$$n_0 = \hat{I}_1 - \frac{1}{2}. \tag{181}$$

As explained in section 3.1.4, the optimal case for the preparation of non-dispersive wave-packets – where the states are the most deeply bound inside the resonance island – is for integer values of n_0, i.e. frequencies (compare with eqs. (65,119))

$$\omega = \frac{1}{\left(n_0 + \frac{1}{2}\right)^3}. \tag{182}$$

For the energy levels of the non-dispersive wave-packets, this also implies that the characteristic exponents in the Mathieu equation – see section 3.1.4 – are

shifted by one unit:

$$\nu = -2n_0 \pmod 2 \quad = -2\hat{I}_1 + 1 \pmod 2. \tag{183}$$

3.4.4 Transformation to the rotating frame

The resonance analysis developed above is restricted to first order in the amplitude F of the external drive. Extensions to higher orders are possible, but tedious. For CP, an alternative approach is possible, which allows higher orders to be included quite easily. It is applicable to CP only and thus lacks the generality of the resonance approach we used so far. Still, it is rather simple and deserves an analysis.

In CP, one may remove the time dependence of the Hamiltonian (164) by a transformation to the noninertial frame rotating with the external frequency ω. The unitary fransformation $U = \exp(i\omega L_z t)$ leads to [141,142]

$$H_{\rm rot} = U\ H_{\rm CP}\ U^\dagger + iU\frac{\partial U^\dagger}{\partial t} = \frac{\vec{p}^2}{2} - \frac{1}{r} + Fx - \omega L_z. \tag{184}$$

Classically, such an operation corresponds to a time dependent rotation of the coordinate frame spanned by $\overline{x} = x\cos\omega t + y\sin\omega t$, $\overline{y} = y\cos\omega t - x\sin\omega t$ (and dropping the bar hereafter) [17]. The Hamiltonian (184), as a time-independent operator, has some energy levels and corresponding eigenstates. Its spectrum is not ω-periodic, although the unitary transformation assures that there is a one-to-one correspondence between its spectrum (eigenstates) and the Floquet spectrum of eq. (164) [18]. It was observed [143] that the Hamiltonian (184) allows for the existence of a stable fixed (equilibrium) point in a certain range of the microwave amplitude F. Later on, it was realized [34] that wave-packets initially localized in the vicinity of this fixed point will not disperse (being bound by the fact that the fixed point is stable) for at least several Kepler periods. In the laboratory frame, these wave-packets (also called "Trojan states" [44,45,34,47]) appear as wave-packets moving around the nucleus along the circular trajectory, which is nothing but the periodic orbit at the center of the resonance island discussed in section 3.4.2. In the original formulation [34]

[17] Passing to the rotating frame implies a change of ϕ to $\overline{\phi} = \phi - \omega t$ in eq. (165). That is definitely different from the change $\theta \to \hat{\theta} = \theta - \omega t$, eq. (60), used in the resonance analysis. Both transformations are unfortunately known under the same name of "passing to the rotating frame". This is quite confusing, but one has to live with it. Along the resonantly driven circular orbit we are considering here, it happens that the azimuthal angle ϕ and the polar angle θ actually coincide. It follows that the two approaches are equivalent *in the vicinity* of this orbit.

[18] In fact, if $|\phi_i\rangle$ is an eigenstate of $H_{\rm rot}$ with energy E_i, then $U^\dagger|\phi_i\rangle$ is a Floquet eigenstate with quasi-energy E_i, while states shifted in energy by $k\omega$ are of the form $\exp(ik\omega t)U^\dagger|\phi_i\rangle$. For a more detailed discussion of this point, see [68].

and the discussion which followed [44,45,47,55], great attention was paid to the accuracy of the harmonic approximation (see below). This was of utmost importance for the non-spreading character of *Gaussian-shaped* Trojan wave-packets considered in [44,45,34,47,55]. As soon pointed out in [49], however, the accuracy of this approximation is immaterial for the very existence of the wave-packets, which are to be identified, as shown above, with well-defined Floquet states.

Let us recapitulate the fixed point analysis of [34,143] in the rotating frame. Inspection of the classical version of the Hamiltonian $H_{\rm rot}$, eq. (184), shows that, due to symmetry, one may seek the fixed point at $z = y = 0$. The condition for an equilibrium (fixed) point, i.e., $d\vec{r}/dt = 0,\ d\vec{p}/dt = 0$, yields immediately that $p_{z,\rm eq} = p_{x,\rm eq} = 0$, $p_{y,\rm eq} = \omega x_{\rm eq}$, with the subscript "eq" for "equilibrium". The remaining equation for dp_x/dt gives the condition

$$-F + \omega^2 x_{\rm eq} - \frac{|x_{\rm eq}|}{x_{\rm eq}^3} = 0, \tag{185}$$

that defines the position of the fixed point as a function of F. Following [34] let us introduce the dimensionless parameter

$$q = \frac{1}{\omega^2 |x_{\rm eq}|^3}. \tag{186}$$

One may easily express the fixed point position, the microwave field amplitude, as well as the corresponding energy in terms of q and ω. Explicitly:

$$x_{\rm eq1} = \frac{1}{q^{1/3}\omega^{2/3}}, \qquad F = \frac{1-q}{q^{1/3}}\omega^{4/3}, \qquad E_{\rm eq} = \frac{1-4q}{2}\left(\frac{\omega}{q}\right)^{2/3}, \tag{187}$$

and

$$x_{\rm eq2} = -\frac{1}{q^{1/3}\omega^{2/3}}, \qquad F = \frac{q-1}{q^{1/3}}\omega^{4/3}, \qquad E_{\rm eq} = \frac{1-4q}{2}\left(\frac{\omega}{q}\right)^{2/3}. \tag{188}$$

For $F = 0$, $q = 1$ in eqs. (187,188). For $F < 0$, (i.e., $q > 1$ in eq. (187)), $x_{\rm eq1}$ is an unstable fixed point, while for moderately positive F (i.e., $8/9 < q < 1$ [34,143]) it is stable. Stability of the second equilibrium point $x_{\rm eq2}$ is achieved by changing the sign of F. For moderate fields (q close to unity), the stable and the unstable fixed points are located on opposite sides of the nucleus, and at almost the same distance from it. As the whole analysis is classical, it has to obey the scaling laws discussed in section 3.2.5. Hence, all quantities describing the equilibrium points in the preceding equations scale as powers of the microwave frequency. A consequence is that there is a very simple correspondence between the scaled microwave amplitude and the

dimensionless parameter q:

$$F_0 = F\omega^{4/3} = Fn_0^4 = \frac{1-q}{q^{1/3}}. \tag{189}$$

The parameter q can thus be thought of as a convenient parametrization (leading to simpler algebraic formula) of the scaled microwave amplitude.

A fixed point in the rotating frame corresponds to a periodic orbit with exactly the period $T = 2\pi/\omega$ of the microwave driving field in the original frame. The stable fixed point (periodic orbit) thus corresponds to the center of the resonance island, and to the stable equilibrium point of the pendulum in the secular approximation. Similarly, the unstable fixed point corresponds to the unstable equilibrium point of the pendulum. Note that the stable fixed point approaches $x_{\rm eq} = \omega^{-2/3} = \hat{I}_1^2$ when $F \to 0$, i.e. the radius of the circular classical Kepler trajectory with frequency ω. Thus, the stable fixed point smoothly reaches the location of the circular state of the hydrogen atom, with a classical Kepler frequency equal to the driving microwave frequency. Its energy $E_{\rm eq} = -3\omega^{2/3}/2$ is the energy of the circular orbit in the rotating frame.

Since the non-dispersive wave-packets are localized in the immediate vicinity of the stable fixed point in the rotating frame, an expansion of the Hamiltonian around that position is useful. Precisely at the fixed point, all first order terms (in position and momentum) vanish. At second order,

$$\begin{aligned} H_{\rm rot} \simeq H_{\rm harmonic} = E_{\rm eq} + \frac{\tilde{\vec{p}}^2}{2} - \omega(\tilde{x}\tilde{p}_y - \tilde{y}\tilde{p}_x) + \frac{\omega^2 q\tilde{y}^2}{2} \\ -\omega^2 q\tilde{x}^2 + \frac{\omega^2 q\tilde{z}^2}{2}, \end{aligned} \tag{190}$$

where $(\tilde{x}, \tilde{y}, \tilde{z}) = (x - x_{\rm eq}, y - y_{\rm eq}, z - z_{\rm eq})$ (and accordingly for the momenta) denotes the displacement with respect to the fixed point. Thus, in the harmonic approximation the motion in the z direction decouples from that in the $x-y$ plane and is an oscillation with frequency $\omega\sqrt{q}$. The Hamiltonian for the latter, up to the additive constant $E_{\rm eq}$, can be expressed in the standard form for a 2D, rotating anisotropic oscillator

$$H = \frac{\tilde{p}_x^2 + \tilde{p}_y^2}{2} + \frac{\omega^2(a\tilde{x}^2 + b\tilde{y}^2)}{2} - \omega(\tilde{x}\tilde{p}_y - \tilde{y}\tilde{p}_x), \tag{191}$$

where the two parameters a and b are equal to $-2q$ and q, respectively. This standard form has been studied in textbooks [93]. It may be used to describe the stability of the Lagrange equilibrium points in celestial mechanics (see [34,93] and references therein). Because this Hamiltonian mixes position and momentum coordinates, it is not straightforward to determine the stability at

the origin. The result is that there are two domains of stability:

$$a, b \geq 1 \tag{192}$$

and

$$-3 \leq a, b \leq 1, \quad \text{with} \;\; (a-b)^2 + 8(a+b) \geq 0 \tag{193}$$

For the specific CP case, where $a = -2q$ and $b = q$, only the second stability region is relevant, and the last inequality implies $8/9 \leq q \leq 1$ for the fixed point to be stable.

Alternatively, one can "diagonalize" the Hamiltonian (191) and construct its normal modes. The normal modes entangle position and momentum operators due to the presence of crossed position-momentum terms in the Hamiltonian. Only along the z-mode (which is decoupled from the rest), the creation and annihilation operators, $b_z^\dagger, b_z$ are the standard combinations of $\tilde{z}$ and $p_{\tilde{z}}$ operators. In the (x, y) plane, the creation and annihilation operators in the $\pm$ normal modes have complicated explicit formulae given in [68]. After some algebra, one ends up with the frequencies of the normal modes,

$$\omega_\pm = \omega \sqrt{\frac{2 - q \pm Q}{2}}, \tag{194}$$

$$\omega_z = \omega \sqrt{q}, \tag{195}$$

where

$$Q = \sqrt{9q^2 - 8q} \tag{196}$$

and $q \geq 8/9$ for Q to be real. In terms of creation/annihilation operators, the harmonic Hamiltonian, eq. (190), takes the form [34,49,50,68]

$$H_{\text{harmonic}} = E_{\text{eq}} + \left(b_+^\dagger b_+ + \frac{1}{2} \right) \omega_+ - \left(b_-^\dagger b_- + \frac{1}{2} \right) \omega_- + \left(b_z^\dagger b_z + \frac{1}{2} \right) \omega_z . \tag{197}$$

A minus sign appears in front of the ω_- term. This is because the fixed point is *not* a minimum of the Hamiltonian, although it is fully stable [19]. This is actually due to the momentum-position coupling, hence the Coriolis force. It is the same phenomenon which is responsible for the stability of the Trojan asteroids [34,75,93] and of an ion in a magnetic trap [144] (in the latter case, the position-momentum coupling is due to the magnetic field).

Finally, with $n_\pm, n_z$ counting the excitations in the corresponding modes, we obtain the harmonic prediction for the energies of the eigenstates in the vicin-

[19] In the first stability region, eq. (192), only + signs appear.

ity of the fixed point:

$$E(n_+, n_-, n_z) = E_{\rm eq} + \left(n_+ + \frac{1}{2}\right)\omega_+ - \left(n_- + \frac{1}{2}\right)\omega_- + \left(n_z + \frac{1}{2}\right)\omega_z. \quad (198)$$

In particular, for $n_\pm = 0,\ n_z = 0$, we get a prediction for the ground state of the oscillator, a Gaussian localized on top of the fixed point, i.e., a Trojan wave-packet. In the following, we denote eigenstates in the harmonic approximation as $|n_+, n_-, n_z\rangle$, thus the ground state non-dispersive wave-packet as $|0, 0, 0\rangle$. In a 2D model, the ω_z term is dropped, the corresponding eigenstates are denoted $|n_+, n_-\rangle$ and have energies:

$$E^{2D}(n_+, n_-) = E_{\rm eq} + \left(n_+ + \frac{1}{2}\right)\omega_+ - \left(n_- + \frac{1}{2}\right)\omega_-. \quad (199)$$

In fig. 27, we show the probability densities of the $|0, 0\rangle$ wave-packets obtained by exact numerical diagonalization of the 2D Hamiltonian (184), for various values of the microwave field amplitude. Clearly, for sufficiently strong microwave amplitudes, the wave-packets are well localized around the classical stable fixed point, with banana-like shapes. At very weak fields, the stability of the fixed point gets weaker and weaker; for a vanishing microwave field, all points on the circle with radius $\omega^{-2/3}$ are equivalent, and one has a ring of equilibrium points. Thus, when F tends to zero, the non-dispersive wave-packet progressively extends along the angular direction (with the radial extension almost unchanged), ending with a doughnut shape at vanishing field. This means that, if n_0 is chosen as an integer, the non-dispersive wave-packet smoothly evolves into a circular state $|n_0, M = n_0\rangle$ as $F \to 0$. The same is true for the 3D atom, where the non-dispersive wave-packet smoothly evolves into the circular state $|n_0, L = M = n_0 - 1\rangle$.

Provided the resonance island around the fixed point is large enough, the harmonic approximation can also be used for studying properties of "excited" states inside the resonance island. As an example, fig. 28 shows the $|n_+ = 1, n_- = 3\rangle$ state calculated from the harmonic approximation, compared to the state obtained by exact numerical diagonalization of the 2D Floquet Hamiltonian. Obviously, the structure of the exact state is very similar to the one obtained from its harmonic approximation. Because the creation and annihilation operators in the $\omega_\pm$ modes entangle position and momentum coordinates in a complicated way [68], and although the system is then completely integrable, the wave-function in the harmonic approximation is *not* separable in any coordinate system (in contrast with the usual harmonic oscillator). Actually, the wave-function can be written as a product of Gaussians and Hermite polynomials of the position coordinates, but the Hermite polynomials have to be evaluated for complex values. This results in the unusual pattern of the probability density displayed in fig. 28. An improvement over the harmonic approximation is possible, by bending the axis in the spirit of [47],

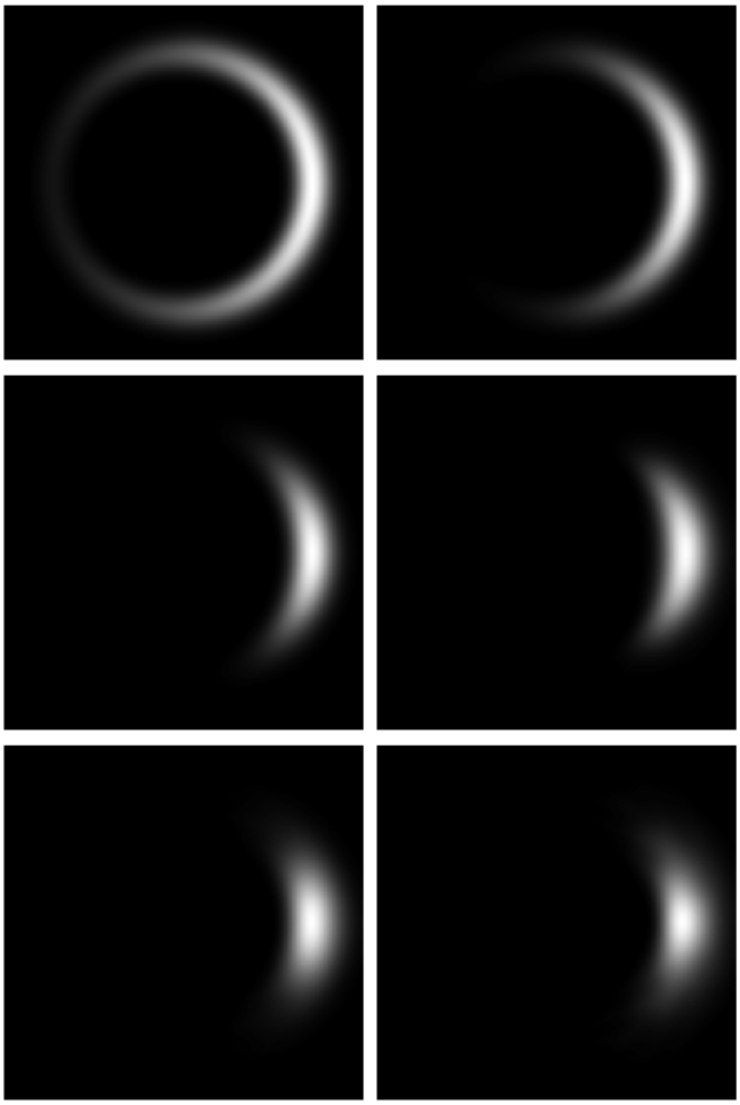

Fig. 27. Non-dispersive wave-packets of the two-dimensional hydrogen atom driven by a circularly polarized microwave field, for different values of the microwave amplitude F. The microwave frequency is fixed at $\omega = 1/(60.5)^3$, corresponding to a resonance island centered at $n_0 = 60$. With increasing microwave amplitude, more states are coupled and the wave-packet becomes better localized. The scaled microwave amplitude $F_0 = F\omega^{-4/3}$ is 0.0003, 0.0011, 0.0111, 0.0333, 0.0444, 0.0555, from top left to bottom right. The nucleus is at the center of the figure, which extends over ± 5000 Bohr radii in each direction. The microwave field is horizontal, pointing to the right.

in order to account for the spherical symmetry of the dominant Coulomb potential. With this improvement, the probability density, shown in the middle row of fig. 28, is almost indistinguishable from the exact result. Let us repeat that this bending – and consequently the deviation from Gaussian character of the wave-function – does not affect at all the non-dispersive character of the wave-packet.

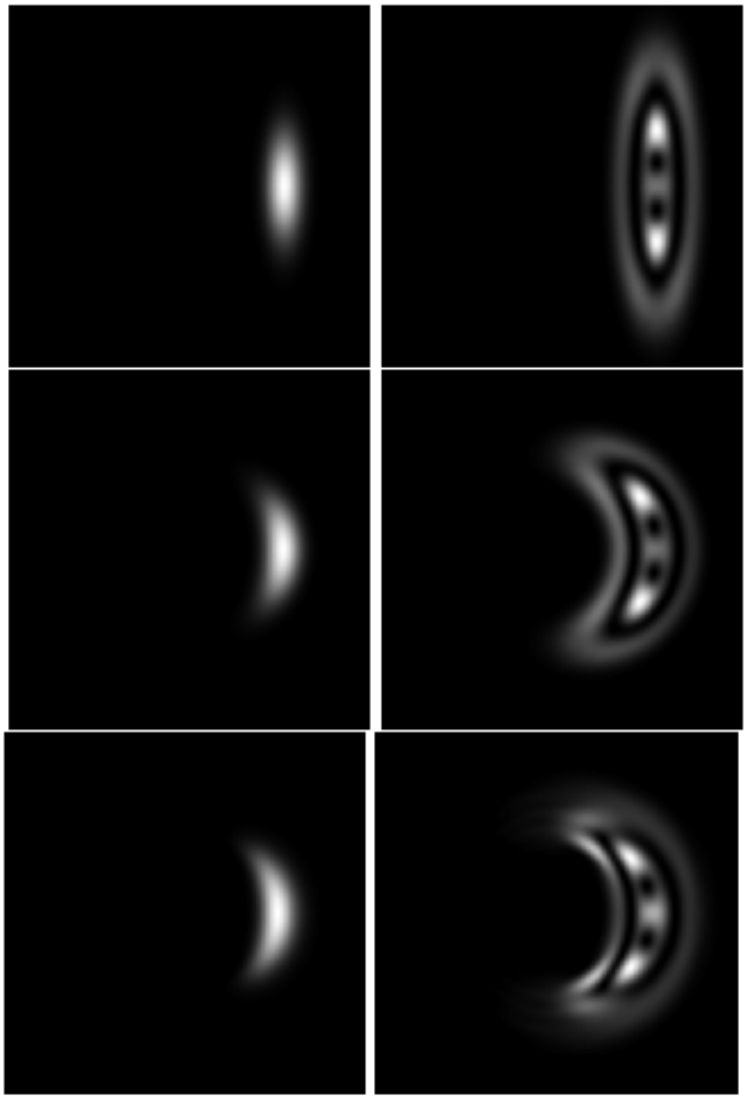

Fig. 28. Comparison of exact Floquet eigenstates (bottom row) and of their harmonic approximations, for the ground state wave-packet $|n_+ = 0, n_- = 0\rangle$ (left column), and for the $|n_+ = 1, n_- = 3\rangle$ excited state (right column), for the 2D hydrogen atom driven by a circularly polarized microwave (field pointing to the right of the figure), with amplitude $F_0 = 0.0333$ and resonant frequency corresponding to $n_0 = 60$. The nucleus is located at the center of each plot which extend over ± 5000 Bohr radii. The top row represents eigenfunctions in the harmonic approximation in $\tilde{x}, \tilde{y}$ coordinates, eq. (191). The eigenfunctions in the middle row are obtained from the harmonic approximation to eq. (184) in polar coordinates. They exhibit a clear bending of the electronic density along the circular trajectory. The excited wave-packet $|1, 3\rangle$ appears in fig. 30 as a straight line (modulo small avoided crossings) with a negative slope, meeting the state $|0, 0\rangle$ in a broad avoided crossing, around $F_0 \simeq 0.036$.

Let us now turn to the realistic 3D model of the atom. Fig. 29 shows an isovalue contour of several non-dispersive wave-packets for the hydrogen atom driven by a microwave field with frequency $\omega = 1/60^3$, i.e., roughly resonant with the $n_0 = 60 \to 59, 61$ transitions (see eqs. (40,65,119)). The best localized wave-packet is the ground state $|0, 0, 0\rangle$, while the three other states are excited by one quantum in either of the normal modes $\omega_{\pm,z}$, and are therefore significantly more extended in space. Again, as already mentioned in sections 3.3.1 and 3.3.2, these wave-packet eigenstates have finite, but extremely long lifetimes (several thousands to millions of Kepler orbits), due to the field induced ionization. For a detailed discussion of their decay properties see section 7.1.

As already demonstrated in the LP case (see figs. 21,22), the semiclassical prediction for the energies of the non-dispersive wave-packets is usually excellent. In order to stress the (small) differences, we plot in fig. 30 a part of the Floquet spectrum of the two-dimensional model atom, i.e. quasi-energy levels versus the (scaled) microwave amplitude, after substraction of the prediction of the harmonic approximation around the stable fixed point, eq. (198), for the ground state wave-packet $|0, 0\rangle$. The result is shown in units of the mean level spacing, estimated [20] to be roughly $2/n_0^4$. If the harmonic approximation was exact, the ground state wave-packet would be represented by a horizontal line at zero. The actual result is not very far from that, which proves that the semiclassical method predicts the correct energy with an accuracy mostly better than the mean level spacing. The other states of the system appear as energy levels which rapidly evolve with F_0, and which exhibit extremely small avoided crossings – hence extremely small couplings – with the wave-packet. In the vicinity of such avoided crossings, the energy levels are perturbed, the diabatic wave-functions mix (the wave-packet eigenstates get distorted), and, typically, the lifetime of the state decreases (induced by the coupling to the closest Floquet state [43,145], typically much less resistant against ionization, as we shall discuss in detail in sec. 7.1).

Thus, strictly speaking, when we speak of non-dispersive wave-packets as specific Floquet states, we really have in mind a generic situation, *far* from any avoided crossing. In particular, the examples of wave-packet states shown in the figures above correspond to such situations. The observed accuracy of the semiclassical approximation has important practical consequences: in order to obtain the "exact" wave-packets numerically, we do not need many eigenvalues for a given set of parameters. Using the Lanczos algorithm for the partial diagonalization of a matrix, it is enough to extract few (say five) eigenvalues only, centered on the semiclassical prediction. The accuracy of the latter (a fraction of the mean level spacing) is sufficient for a clear identification of

[20] This estimate follows from the local energy splitting, $\sim n_0^{-3}$, divided by the number $n_0/2$ of photons needed to ionize the initial atomic state by a resonant driving field.

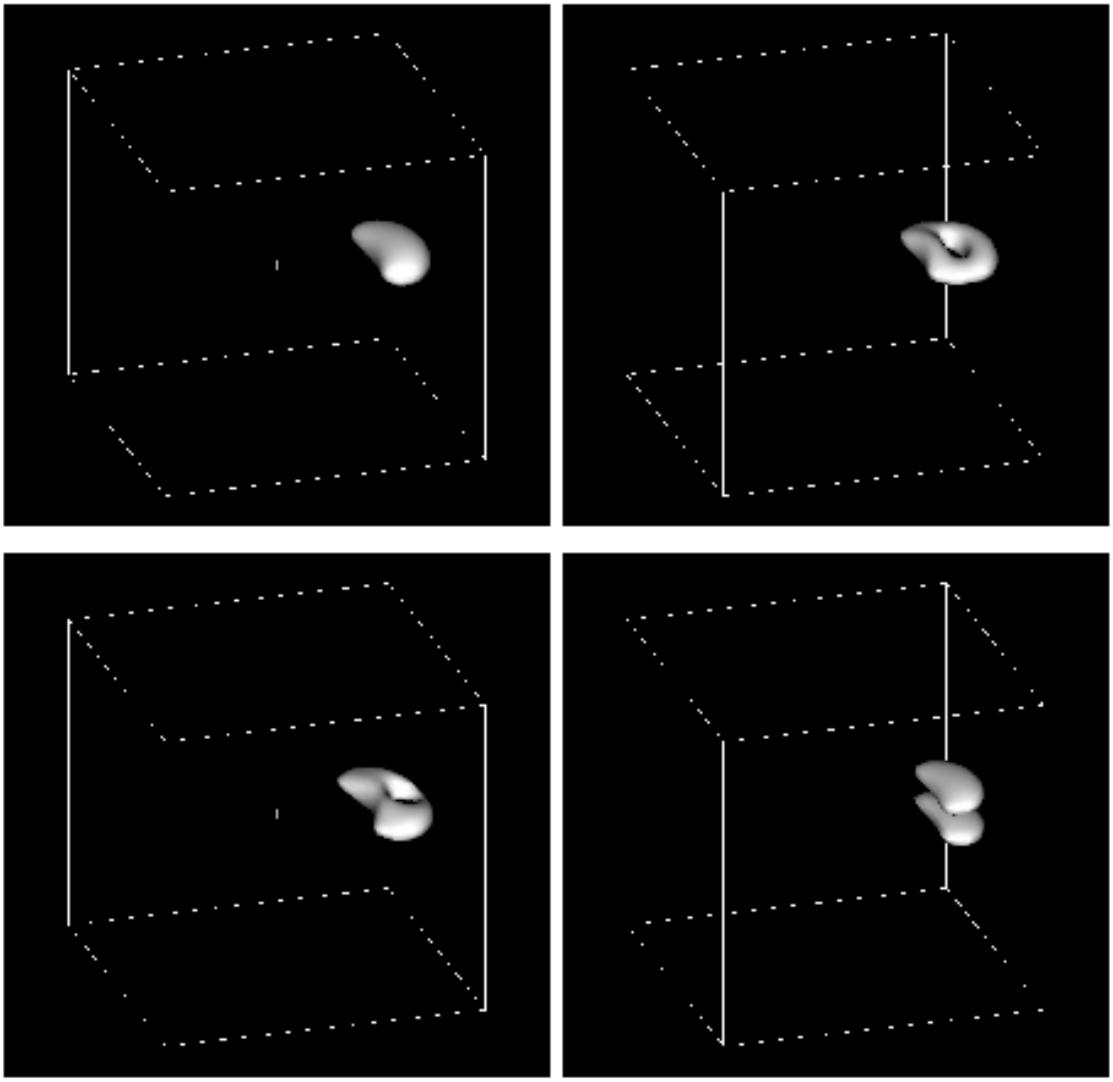

Fig. 29. Isovalue plots (at 30% of the maximum value) of non-dispersive wave-packets in the three-dimensional hydrogen atom driven by a circularly polarized microwave field. Frequency of the driving $\omega = 1/60^3$, amplitude $F_0 = 0.04442$. In the laboratory frame, the wave-packets propagate – without changing their shapes – along a circular trajectory centered around the nucleus indicated by a cross. The cube edges measure 10000 Bohr radii. The microwave polarization plane is horizontal with the field pointing to the right. The four wave-packets shown represent the ground state wave-packet $|0,0,0\rangle$ (top left), and the excited states $|1,0,0\rangle$ (bottom left), $|0,1,0\rangle$ (top right), and $|0,0,1\rangle$ (bottom right). Eventually, the microwave field will ionize such states, but their lifetimes are extremely long, of the order of thousands to millions of Kepler periods.

the appropriate quantum eigenvalue. Actually, in a real diagonalization of the Floquet Hamiltonian, we identify the wave-packet states by both their vicinity to the semiclassical prediction for the energy, and the large (modulus of the) slope of the level w.r.t. changes of F_0, induced by its large dipole mo-

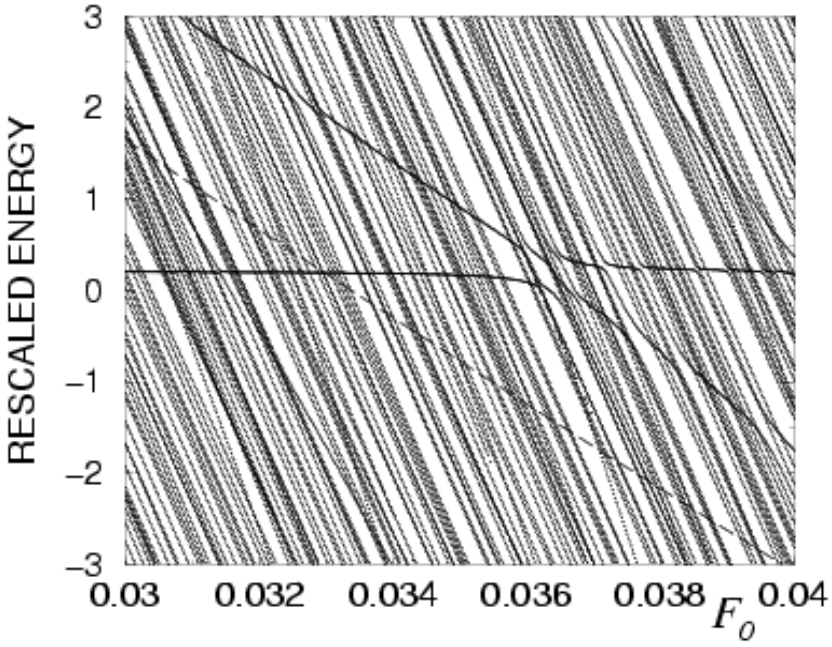

Fig. 30. Spectrum of the two-dimensional hydrogen atom in a circularly polarized microwave field of frequency $\omega = 1/(60.5)^3$, as a function of the scaled microwave amplitude $F_0 = F\omega^{-4/3}$. In order to test the accuracy of the harmonic prediction, we substract the semiclassical energy for the ground state $|0,0\rangle$ wave-packet, eq. (198), from the result of the exact numerical diagonalization, and rescale the energy axis in units of the mean level spacing. The almost horizontal line slightly above zero corresponds to the non-dispersive ground state wave-packet, which typically undergoes small avoided crossings with other Floquet states. A relatively large avoided crossing occurs when two wave-packet-like states meet, as here happens around $F_0 \simeq 0.036$. The other ("colliding") state is the excited wave-packet $|1,3\rangle$. The dashed line indicates the harmonic prediction, eq. (198), for this state, which is obviously less accurate. Note, however, that the slope is correctly predicted.

ment in the rotating frame (by virtue of the Hellman-Feynman theorem [18]). The latter criterion is actually also very useful for the identification of excited wave-packets in a numerically exact spectrum. The state $|1,3\rangle$ (in the harmonic approximation) presented in fig. 28 is precisely the excited wave-packet which appears in fig. 30 as a "line" with a negative slope, meeting the $|0,0\rangle$ state in a broad avoided crossing around $F_0 \simeq 0.036$. From that figure, it is apparent that the harmonic prediction for the energy is not excellent for the $|1,3\rangle$ state. On the other hand, the slope of the Floquet state almost matches the slope given by the harmonic approximation, which confirms that the exact wave-function is still well approximated by its harmonic counterpart. Note that also from the experimental point of view it is important to get accurate and simple semiclassical estimates of the energies of the non-dispersive wave-packets, since it may help in their preparation and unambiguous identification. For a more detailed discussion, see section 8.2.

It is interesting to compare the accuracy of the harmonic approximation to the pendulum description outlined previously in sec. 3.4.2. The latter results from lowest order perturbation theory in F. Taking the small F limit we get $\omega_+, \omega_z \to \omega$, and $\omega_- \to \omega\sqrt{3F_0}$, for the harmonic modes, see eqs. (194-196). The latter result coincides – as it should – with the pendulum prediction, eqs. (80,173). Similarly, the energy of the stable equilibrium point, eq. (187), becomes at first order in F:

$$E_{\rm eq} = -\frac{3}{2n_0^2} + n_0^2\ F + O(F^2) \tag{200}$$

which coincides with the energy of the center of the resonance island, see section 3.4.2. Thus, the prediction of the resonance analysis agrees with the harmonic approximation in the rotating frame. For a more accurate estimate of the validity of both approaches, we have calculated – for the 2D model of the atom, but similar conclusions are reached in 3D – the energy difference between the exact quantum result and the prediction using a semiclassical quantization of the secular motion in the (M, ϕ) plane together with the Mathieu method in the $(\hat{I}, \hat{\theta})$ plane on the one side, and the prediction of the harmonic approximation around the fixed point, eq. (198), on the other side. In fig. 31, we compare the results coming from both approaches. As expected, the semiclassical approach based on the Mathieu equation is clearly superior for very small microwave amplitudes, as it is "exact" at first order in F. On the other hand, for the harmonic approximation to work well, the island around the fixed point has to be sufficiently large. Since the size of the island increases as $\sqrt{F}$, the harmonic approximation may become valid only for sufficiently large microwave amplitudes, when there is at least one state trapped in the island. As seen, however, in fig. 31, the harmonic approximation yields a satisfactory prediction for the wave-packet energy (within few % of the mean spacing) almost everywhere. For increasing n_0, the harmonic approximation is better and better and the Mathieu approach is superior only over a smaller and smaller range of $F_0 = Fn_0^4$, close to 0. Still, both approaches give very good predictions for the typical values of F_0 used in the following, say $F_0 \simeq 0.03$. The spikes visible in the figure are due to the many small avoided crossings visible in fig. 30.

While we have shown some exemplary wave-packets for few values of n_0 and F only, they generally look very similar provided that

- n_0 is sufficiently large, say $n_0 > 30$. For smaller n_0, the wave-packet looks a bit distorted and one observes some deviations from the harmonic approximation (for a more detailed discussion of this point see secs. 7.1 and 7.2, where ionization and spontaneous emission of the wave-packets are discussed);
- F_0 is sufficiently large, say $F_0 > 0.001$, such that the resonance island can support at least one state. For smaller F_0, the wave-packet becomes more

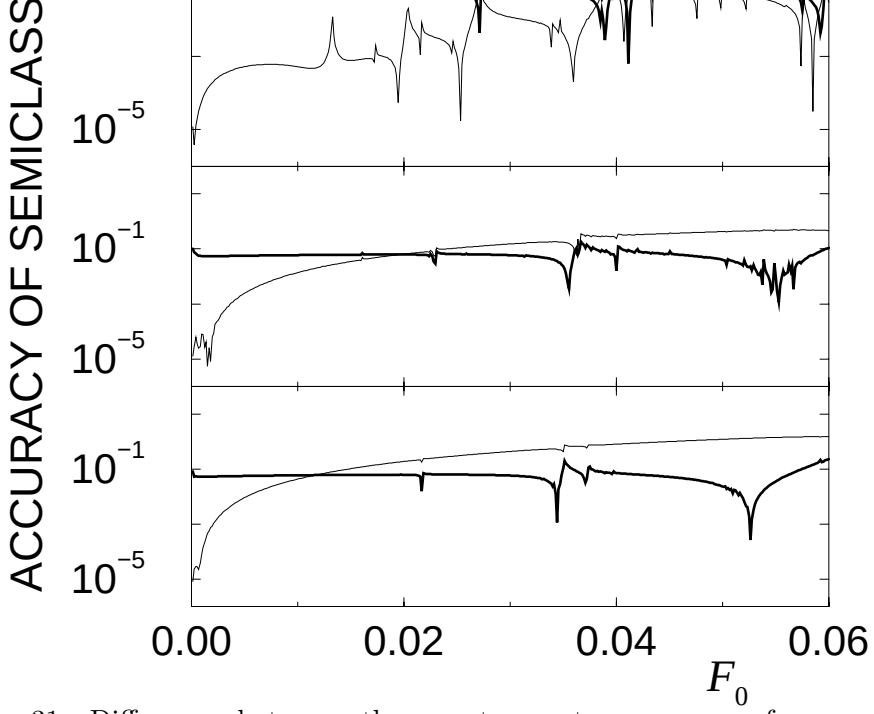

Fig. 31. Difference between the exact quantum energy of a non-dispersive wave-packet of a 2D hydrogen atom in a circularly polarized microwave field, and two different semiclassical predictions, as a function of the scaled microwave field amplitude, F_0. The thick lines are obtained from a harmonic approximation of the motion around the stable equilibrium point (in the rotating frame), eq. (199) and the thin lines use a quantum treatment (Mathieu approach, sec. 3.1.4) of the motion in the resonance island, combined with a semiclassical treatment of the secular motion. From top to bottom $\omega = 1/(30.5)^3,\ 1/(60.5)^3,\ 1/(90.5)^3$, corresponding to wave-packets associated with Rydberg states of principal quantum number $n_0 = 30, 60, 90$. The energy difference is expressed in units of the mean level spacing, estimated by $n_0^4/2$. The prediction of the Mathieu approach is consistently better for low F_0, and the harmonic approximation becomes clearly superior for larger F_0. For larger and larger n_0, the harmonic approximation is better and better. Note that both approximations make it possible to estimate the energy of the non-dispersive wave-packet with an accuracy better than the mean level spacing, allowing for its simple and unambiguous extraction from exact numerical data.

extended in the angular coordinate, since less atomic circular states are significantly coupled, see fig. 27;

– F_0 is not too large, say smaller than $F_0 \simeq 0.065$. Our numerical data suggest that the upper limit is not given by the limiting value of $q = 8/9$, for which the fixed point is still stable. The limiting value appears to be rather linked to the $1:2$ resonance between the ω_+ and ω_- modes, which occurs approx. at $F_0 \simeq 0.065$.
– In particular, the value $q = 0.9562$ (i.e. $F_0 \simeq 0.04442$), corresponding to optimal classical stability of the fixed point, advertised in [34] as the optimal one, is by no means favored. A much broader range of microwave amplitudes is available (and equivalent as far as the "quality" of the wave-packet is concerned). What is much more relevant, is the presence of some accidental

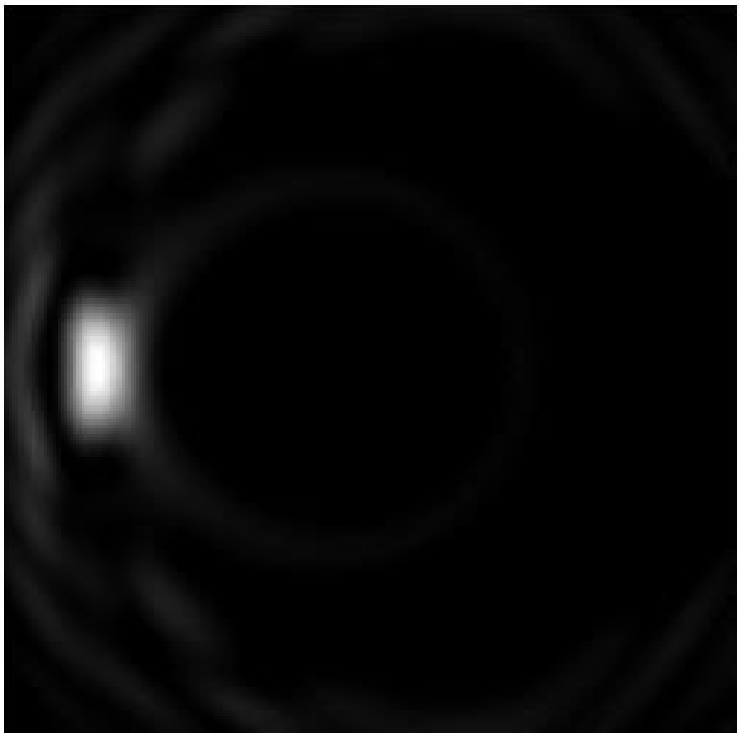

Fig. 32. Floquet eigenstate of the two-dimensional hydrogen atom in a circularly polarized microwave field. This state is partially localized on the unstable equilibrium point (in the rotating frame), see eqs. (185)-(188), for $F_0 = 0.057$ and $n_0 = 60$. This localization is of purely classical origin. The nucleus is at the center of the figure which extends over ± 5000 Bohr radii. The microwave field points to the right.

avoided crossings with other Floquet states.

Still, these are no very restrictive conditions, and we are left with a broad range of parameters favoring the existence of nondispersive wave-packets, a range which is experimentally fully accessible (see section 8 for a more elaborate discussion of experimental aspects).

Finally, in analogy with the LP case, we may consider Floquet states localized on the unstable fixed point associated with the principal resonance island. From the discussion following eq. (188), this point is located opposite to the stable fixed point, on the other side of the nucleus. An example of such a state is shown in fig. 32, for an amplitude of the microwave field that ensures that most of the nearby Floquet states ionize rather rapidly. The eigenstate displayed in the figure lives much longer (several thousands of Kepler periods). The localization in the vicinity of an unstable fixed point, in analogy to the LP case discussed previously, is of purely classical origin. As pointed out in [60], such a localization must not be confused with scarring [146] – a partial localization on an unstable periodic orbit embedded in a chaotic sea – which disappears in the semiclassical limit [146,147].

The origin of non-dispersive wave-packets being their localization inside the resonance island (locking the frequency of the electronic motion onto the external drive) suggests that such wave-packets are quite robust and should exist not only for CP and LP, but also for arbitrary elliptical polarization (EP).

The possible existence of nondispersive wave-packets for EP was mentioned in [30,148], using the classical "pulsating SOS" approach. The method, however, did not allow for quantitative predictions, and was restricted to elliptic polarisations very close to the CP case. However, the robustness of such wave-packets for arbitrary EP is obvious once the localization mechanism inside the resonance island is well understood [73,69].

Let us consider an elliptically polarized driving field of constant amplitude. With the ellipticity parameter $\alpha \in [0;1]$,

$$V = F(x\cos\omega t + \alpha y \sin\omega t) \tag{201}$$

establishes a continuous transition between linear ($\alpha = 0$) and circular ($\alpha = 1$) polarization treated in the two preceding chapters [21]. This general case is slightly more complicated than both limiting cases LP and CP. For LP microwaves (see section 3.3.2), the conservation of the angular momentum projection onto the polarization axis, M, makes the dynamics effectively two-dimensional. For the CP case, the transformation (184) to the frame rotating with the microwave frequency removes the explicit time-dependence (see section 3.4). None of these simplifications is possible in the general EP case, and the problem is truly three dimensional *and* time-dependent.

To illustrate the transition from LP to CP via EP, the two-dimensional model of the atom is sufficient, and we shall restrain our subsequent treatment to this computationally less involved case. The classical resonance analysis for EP microwave ionization has been described in detail in [149,150]. It follows closely the lines described in detail in sections 3.3 and 3.4. By expanding the perturbation, eq. (201), in the action-angle coordinates (I, M, θ, ϕ) of the two-dimensional atom (see sec. 3.2.4), one obtains the following secular Hamiltonian:

$$\mathcal{H}_{\rm sec} = \hat{P}_t - \frac{1}{2\hat{I}^2} - \omega\hat{I} + F\left[\mathcal{V}_1(\hat{I}, M, \phi; \alpha)\cos\hat{\theta} - \mathcal{U}_1(\hat{I}, M, \phi; \alpha)\sin\hat{\theta}\right], \tag{202}$$

[21] Note, however, that $\alpha = 0$ defines a linearly polarized field along the x-axis, i.e., *in* the plane of elliptical polarization for $\alpha > 0$. In sec. 3.3, the polarization vector was chosen along the z-axis. The physics is of course the same, but the algebraic expressions are slightly different, requiring a rotation by an angle $\beta = \pi/2$ around the y-axis.

with

$$\mathcal{V}_1(\hat{I}, M, \phi; \alpha) = \cos\phi\,(X_1 + \alpha Y_1)\,,$$
$$\mathcal{U}_1(\hat{I}, M, \phi; \alpha) = \sin\phi\,(Y_1 + \alpha X_1)\,. \tag{203}$$

This can be finally rewritten as:

$$\mathcal{H}_{\rm sec} = \hat{P}_t - \frac{1}{2\hat{I}^2} - \omega\hat{I} + F\chi_1(\hat{I}, M, \phi; \alpha)\cos(\hat{\theta} + \delta_1). \tag{204}$$

Both, χ_1 and δ_1, depend on the shape and orientation of the electronic elliptical trajectory, as well as on α, and are given by:

$$\chi_1(\hat{I}, M, \phi; \alpha) = \sqrt{\mathcal{V}_1^2 + \mathcal{U}_1^2}, \tag{205}$$

and

$$\tan\delta_1(M, \phi; \alpha) = \frac{\mathcal{U}_1}{\mathcal{V}_1}, \tag{206}$$

which is once more the familiar form of a system with a resonance island in the $(\hat{I}, \hat{\theta})$ plane. The expressions obtained are in fact very similar to the ones we obtained for the three-dimensional atom exposed to a circularly polarized microwave field, eqs. (169- 171), in section 3.4.2. This is actually not surprising: the relevant parameter for the transverse dynamics is the magnitude of the atomic dipole oscillating with the driving field, i.e. the scalar product of the oscillating atomic dipole with the polarization vector. The latter can be seen either as the projection of the oscillating atomic dipole onto the polarization plane or as the projection of the polarization vector on the plane of the atomic trajectory. If one considers a three-dimensional hydrogen atom in a circularly polarized field, the projection of the polarization vector onto the plane of the atomic trajectory is elliptically polarized with ellipticity $\alpha = L/M$. This is another method to rediscover the Hamiltonian (204) from Hamiltonian (169).

To obtain a semiclassical estimation of the energies of the nondispersive wave-packets we proceed precisely in the same way as for LP and CP. Since the radial motion in $(\hat{I}, \hat{\theta})$ is much faster than in the transverse/angular degree of freedom defined by (M, ϕ), we first quantize the effective perturbation $\chi_1(\hat{I}, M, \phi; \alpha)$ driving the angular motion. Fig. 33 shows $\chi_1/\hat{I}^2$, as a function of $M_0 = M/\hat{I}$ and ϕ, for two different values of the driving field ellipticity α. Note that χ_1 becomes more symmetric as $\alpha \to 0$, since this limit defines the LP case, where the dynamics cannot depend on the rotational sense of the electronic motion around the nucleus. The four extrema of χ_1 define the possible wave-packet eigenstates. Whereas the minima at $\phi = \pi/2, 3\pi/2$ correspond to elliptic orbits of intermediate eccentricity $0 < e < 1$ perpendicular to the driving field

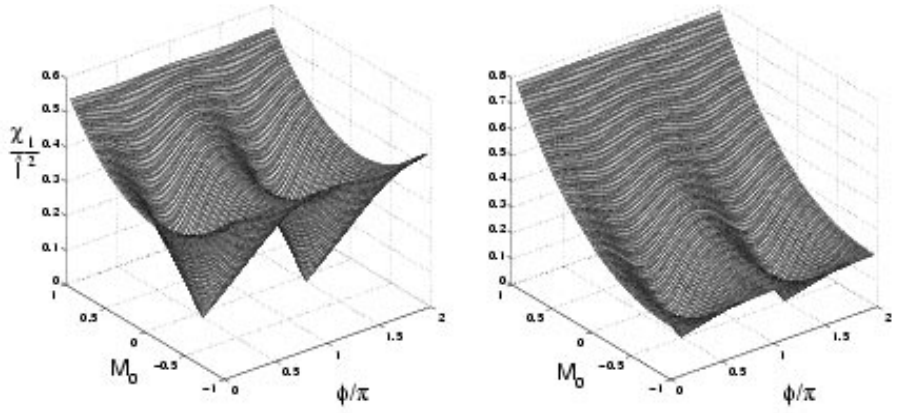

Fig. 33. The scaled effective perturbation $\chi_1/\hat{I}^2$ driving the transverse/angular motion of a two-dimensional hydrogen atom exposed to a resonant, elliptically polarized microwave field, plotted as a function of the scaled angular momentum, $M_0 = M/\hat{I}$, and of the angle ϕ between the Runge-Lenz vector and the major axis of the polarization ellipse. Left and right panels correspond to $\alpha = 0.1$ and $\alpha = 0.6$, respectively. Non-dispersive wave-packets are localized around the maxima of this effective potential, at $M_0 = \pm 1$, and are circularly co- and contra-rotating (with respect to the microwave field) around the nucleus (see fig. 35).

major axis, the (ϕ-independent) maxima at $M_0 = \pm 1$ define circular orbits which co- or contra-rotate with the driving field. In the limit $\alpha \to 0$, the $M_0 = \pm 1$ maxima are associated with the same value of χ_1. Hence, the actual Floquet eigenstates appear as tunneling doublets in the Floquet spectrum, each member of the doublet being a superposition of the co- and contra-rotating wave-packets.

The quantization of the fast motion in the $(\hat{I}, \hat{\theta})$ plane is similar to the one already performed in the LP and CP cases. As we already observed (see fig. 20), the size of the resonance island in the $(\hat{I}, \hat{\theta})$ plane is proportional to $\sqrt{\chi_1}$. Correspondingly, also the localization properties of the wave-packet along the classical trajectory improve with increasing χ_1. We therefore conclude from fig. 33 that the eigenstates corresponding to the minima of χ_1 cannot be expected to exhibit strong longitudinal localization, whereas the eigenstates localized along the circular orbits at the maxima of χ_1 can.

Fig. 34 compares the semiclassical prediction obtained by quantization of χ_1 and $\mathcal{H}_{\rm sec}$ (following the lines already described in section 3.3.2, for the ground state $N = 0$ in the resonance island) to the exact quasienergies (determined by numerical diagonalization of the Floquet Hamiltonian), for α varying from LP to CP. The agreement is excellent, with slightly larger discrepancies between the semiclassical and the exact results for the states with smallest energy. For those states the resonance island is very small (small χ_1), what explains the discrepancy.

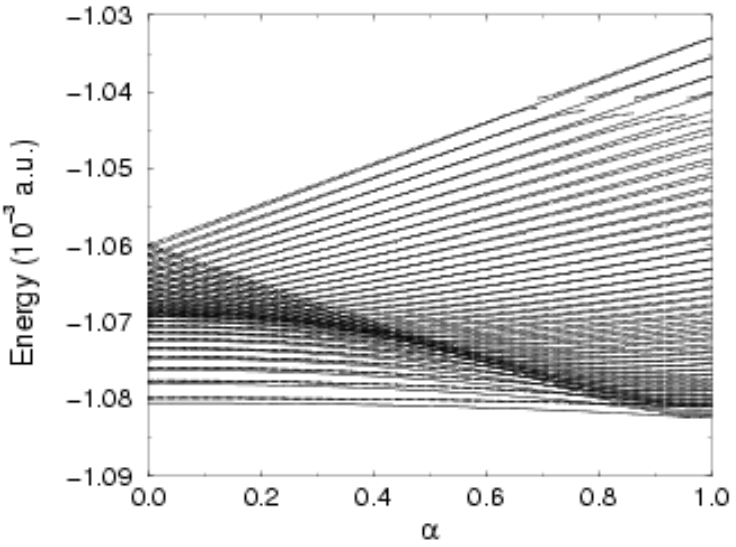

Fig. 34. Energy levels of the two dimensional hydrogen atom driven by a resonant, elliptically polarized microwave field of scaled amplitude $F_0 = 0.03$, for $n_0 = 21$, as a function of the field ellipticity α (the resonant frequency of the microwave is $\omega = 1/(21.5)^3$). Full lines: semiclassical prediction; dotted lines: exact numerical result for the states originating from the $n_0 = 21$ hydrogenic manifold. The non-dispersive wave-packets are the states originating from the upper doublet at $\alpha = 0$. The ascending (resp. descending) energy level is associated with the wave-packet co- (resp. contra-) rotating with the microwave field.

The highest lying state in fig. 34, ascending with α, is a non-dispersive wave-packet state located on the circular orbit and corotating with the EP field. It is shown in fig. 35 for $\alpha = 0.4$. As mentioned above, the corresponding counterrotating wave-packet is energetically degenerate with the co-rotating one for $\alpha = 0$. Its energy decreases with α (compare fig. 34). It is shown in the bottom row in fig. 35 for $\alpha = 0.4$. While the corotating wave-packet preserves its shape for all α values (except at isolated avoided crossings) the counter-rotating wave-packet undergoes a series of strong avoided crossings for $\alpha > 0.42$, progressively loosing its localized character. This is related to a strong decrease of the maximum of χ_1 at $M_0 = -1$ with α, clearly visible in fig. 33.

While we have discussed the 2-dimensional case only, the CP situation (compare section 3.4) indicates that for sufficiently large α, the important resonant motion occurs in the polarization plane, being stable versus small deviations in the z direction. Thus the calculations presented above are also relevant for the real three dimensional world, provided α is not far from unity [69,73]. For arbitrary α, a full 3D analysis is required. While this is clearly more involved, the general scenario of a wave-packet anchored to a resonance island will certainly prevail.

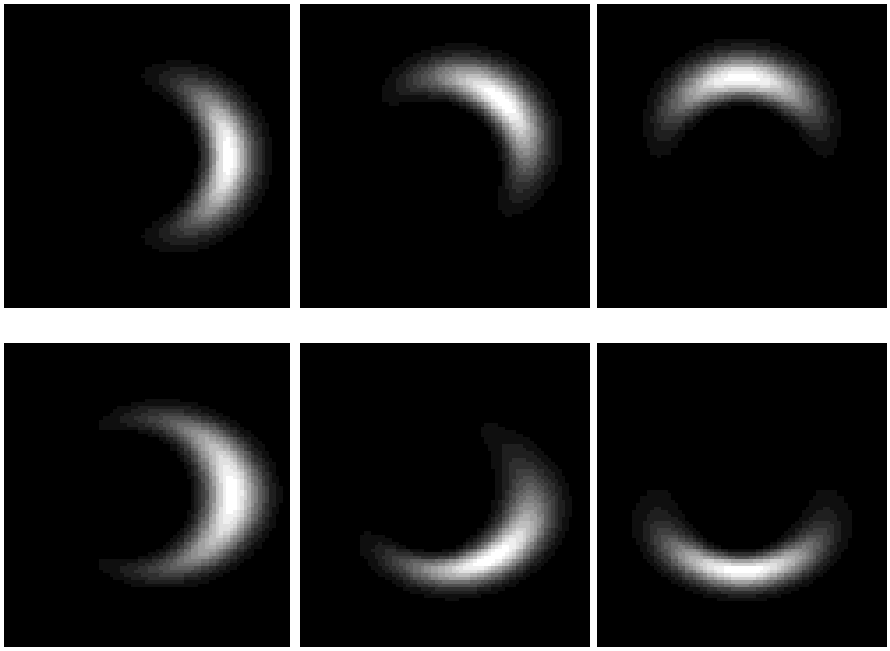

Fig. 35. Non-dispersive wave-packets of the two dimensional hydrogen atom exposed to an elliptically polarized, resonant microwave field. Scaled microwave amplitude $F_0 = 0.03$ (for resonant principal quantum number $n_0 = 21$), and ellipticity $\alpha = 0.4$. Top row: non-dispersive wave-packet moving on a circular orbit corotating with the microwave field, for phases $\omega t = 0, \pi/4, \pi/2$ (from left to right). This wave-packet evolves into the eigenstate represented in fig. 27, under continuous increase of the ellipticity to $\alpha = 1$. Bottom row: non-dispersive wave-packet launched along the same circular orbit, but contra-rotating with the driving field (for the same phases). Note that, while the co-rotating wave-packet almost preserves its shape during the temporal evolution, the contra-rotating one exhibits significant distortions during one field cycle, as a direct consequence of its complicated level dynamics shown in fig. 34. Still being an exactly time-periodic Floquet eigenstate, it regains its shape after every period of the microwave. The size of each box extends over ± 800 Bohr radii, in both x and y directions, with the nucleus in the middle. The major axis of the polarization ellipse is along the horizontal x axis and the microwave field points to the right at $t = 0$.

4 Manipulating the wave-packets

We have shown in the previous sections that non-dispersive wave-packets are genuine solutions of the Floquet eigenvalue problem, eq. (75), under resonant driving, for arbitrary polarization of the driving field. The semiclassical approximation used to guide our exact numerical approach directly demonstrates the localization of the electronic density in well defined regions of phase space, which protect the atom against ionization induced by the external field (see, however, sec. 7.1). We have also seen that classical phase space does not only undergo structural changes under changes of the driving field amplitude

(figs. 10, 12,16), but also under changes of the driving field ellipticity (fig. 33). Therefore, the creation of non-dispersive wave-packets can be conceived as an easy and efficient means of quantum control, which allows the manipulation and the controlled transfer of quantum population accross phase space. In particular, one may imagine the creation of a wave-packet moving along the polarization axis of a linearly polarized microwave field. A subsequent, smooth change through elliptical to finally circular polarization allows to transfer the electron to a circular orbit.

Adding additional static fields to the Hamiltonian (75) provides us with yet another handle to control the orientation and shape of highly excited Rydberg trajectories, and, hence, to manipulate the localization properties of nondispersive wave-packet eigenstates in configuration and phase space. The key point is that trapping inside the nonlinear resonance island is a robust mechanism which protects the non-dispersive wave-packet very efficiently from imperfections. This allows to adjust the wave-packet's properties at will, just by adiabatically changing the properties of the island itself. Moreover, when the strength of the external perturbation increases, chaos generically invades a large part of classical phase space, but the resonance islands most often survives. The reason is that the phase locking phenomenon introduces various time scales in the system, which have different orders of magnitude. That makes the system quasi-integrable (for example through some adiabatic approximation *à la Born-Oppenheimer*) and – locally – more resistant to chaos.

Hereafter, we discuss two possible alternatives of manipulating the wave-packets. One is realized by adding a static electric field to the LP microwave drive [72]. Alternatively, the addition of a static magnetic field to CP driving enhances the region of classical stability, and extends the range of applicability of the harmonic approximation [30,44,46,54,62,144,151].

4.1 Rydberg states in linearly polarized microwave and static electric fields

Let us first consider a Rydberg electron driven by a resonant, linearly polarized microwave, in the presence of a static electric field. We already realized (see the discussion in sec. 3.3.2) that the classical 3D motion of the driven Rydberg electron is angularly unstable in a LP microwave field. It turns out, however, that a stabilization of the angular motion is possible by the addition of a static electric field F_s parallel to the microwave polarization axis [72,152,153]. The corresponding Hamiltonian reads:

$$H = \frac{p_x^2 + p_y^2 + p_z^2}{2} - \frac{1}{r} + Fz\cos\omega t + F_s z, \tag{207}$$

which we examine in the vicinity of the $s = 1$ resonance. As in sec. 3.3.2, the angular momentum projection M on the z axis remains a constant of motion, and we shall assume $M = 0$ in the following. Compared to the situation of a pure microwave field, there is an additional time scale, directly related to the static field. Indeed, in the presence of a perturbative static field alone, it is known that the Coulomb degeneracy of the hydrogenic energy levels (in L) is lifted. The resulting eigenstates are combinations of the n_0 substates of the n_0 manifold (for $0leqL \leq n_0 - 1$) [22]. The associated energy levels are equally spaced by a quantity proportional to F_s ($3n_0F_s$ in atomic units). Classically, the trajectories are no longer closed but rather Kepler ellipses which slowly librate around the static field axis, periodically changing their shapes, at a (small) frequency $3n_0F_s \ll \omega_{\rm Kepler} = 1/n_0^3$. Thus, the new time scale associated with the static electric field is of the order of $1/F_{s,0}$ Kepler periods, where

$$F_{s,0} = F_s n_0^4 \tag{208}$$

is the scaled static field. This is to be compared to the time scales $1/F_0$ and $1/\sqrt{F_0}$, which characterize the secular time evolution in the (L, ψ) and $(\hat{I}, \hat{\theta})$ coordinates, respectively (see discussion in section 3.3.2), in the presence of the microwave field alone. To achieve confinement of the electronic trajectory in the close vicinity of the field polarization axis, we need $1/F_0 \simeq 1/F_{s,0}$, with both, F_s and F small enough to be treated at first order.

If we now consider the $s = 1$ resonance, we deduce the secular Hamiltonian by keeping only the term which does not vanish after averaging over one Kepler period. For the microwave field, this term was already identified in eq. (159). For the static field, only the static Fourier component of the atomic dipole, eqs. (155,156), has a non-vanishing average over one period. Altogether, this finally leads to

$$\mathcal{H}_{\rm sec} = \hat{P}_t - \frac{1}{2\hat{I}^2} - \omega\hat{I} + F_s X_0(\hat{I}, L)\cos\psi + F\chi_1(\hat{I}, L, \psi)\cos(\hat{\theta} + \delta_1). \tag{209}$$

Since the last two terms of this Hamiltonian depend differently on $\hat{\theta}$, it is no more possible, as it was in the pure LP case (see section 3.3.2), to perform the quantization of the slow LP motion first. Only the secular approximation [18] which consists in quantizing first the fast variables $(\hat{I}, \hat{\theta})$, and subsequently the slow variables (L, ψ), remains an option for the general treatment. However, since we are essentially interested in the wave-packet eigenstate with optimal localization properties, we shall focus on the ground state within a sufficiently large resonance island induced by a microwave field of an appropriate strength. This motivates the harmonic expansion of the secular Hamiltonian around the

[22] These states are called "parabolic" states, since the eigenfunctions are separable in parabolic coordinates [7].

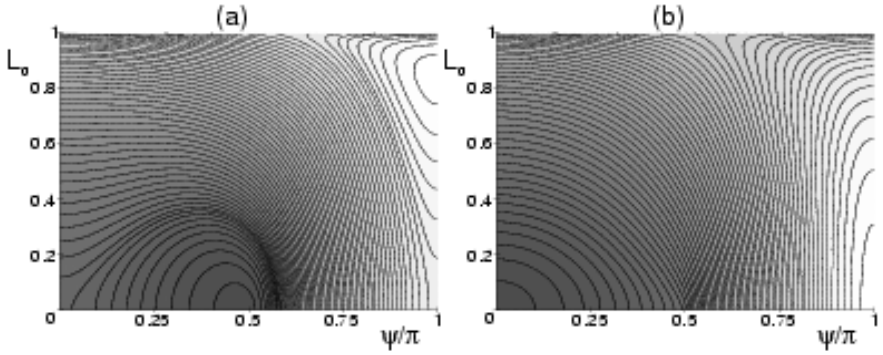

Fig. 36. Contours of the effective Hamiltonian, eq. (212), in the (L_0, ψ) plane (with $L_0 = L/n_0$ the scaled angular momentum, and ψ the angle between the major axis of the elliptical trajectory and the field axis). The potential surface generates the slow evolution of the angular coordinates of the Kepler trajectory of a Rydberg electron exposed to collinear, static and resonant microwave electric fields. Initial atomic principal quantum number $n_0 = 60$; scaled microwave amplitude $F_0 = F n_0^4 = 0.03$, and scaled static field amplitude $F_{s,0} = 0.12 F_0 < F_{s,c}$ (a), $F_{s,0} = 0.25 F_0 > F_{s,c}$ (b), with $F_{s,c}$ the critical static field amplitude defined in eq. (213). The lighter the background, the higher the effective energy. The contours are plotted at the semiclassical energies which quantize $H_{\rm eff}$ according to eq.(163), and thus represent the 60 eigenenergies shown in fig. 37. Observe the motion of the stable island along the $\psi = \pi$ line (corresponding to the energetically highest state in the manifold), under changes of F_s.

stable fixed point at

$$\hat{I} = \hat{I}_1 = \omega^{-1/3}, \qquad \hat{\theta} = -\delta_1. \tag{210}$$

with the characteristic frequency, see eq. (80):

$$\Omega(\hat{I}_1 L, \psi) = \frac{\sqrt{3F\chi_1(\hat{I}_1, L, \psi)}}{\hat{I}_1^2}. \tag{211}$$

Explicit evaluation of the ground state energy of the locally harmonic potential yields the effective Hamiltonian for the slow motion in the (L, ψ) plane:

$$H_{\rm eff} = -\frac{\Omega(L,\psi)}{2} + F\chi_1(L,\psi) + F_s X_0(L)\cos\psi, \tag{212}$$

where all quantities are evaluated at $\hat{I} = \hat{I}_1$. For the determination of the angular localization properties of the wave-packet it is now sufficient to inspect the extrema of $H_{\rm eff}$.

For $F_{s,0} = 0$, we recover the pure LP case with a maximum along the line $L_0 = 1$ (circular state), and a minimum at $L_0 = 0$, $\psi = \pi/2$ (see fig. 19), corresponding to a straight line orbit perpendicular to the field. For increasing $F_{s,0}$, the maximum moves towards lower values of L_0, and contracts in ψ,

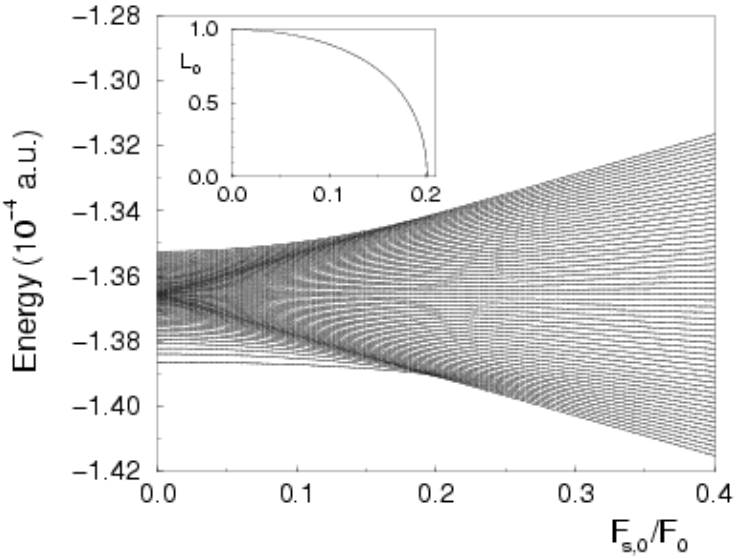

Fig. 37. Semiclassical energy levels of the resonantly driven manifold $n_0 = 60$ of the hydrogen atom, as a function of the ratio of the scaled static electric field strength F_s to the scaled microwave amplitude F_0, for fixed $F_0 = Fn_0^4 = 0.03$. The insert shows the scaled angular momentum $L_0 = L/n_0$ of the stable fixed point $(L_0, \psi = 0)$, see fig. 36, as a function of the same variable. The corresponding trajectory evolves from a circular orbit coplanar with the polarization axis to a straight line orbit stretched along this axis, via orbits of intermediate eccentricity. For $F_{s,0} > F_{s,c}$, eq. (213), the stable fixed point is stationary at $L_0 = 0$. The corresponding wave-packet state, localized in the vicinity of the fixed point, is the energetically highest state in the spectrum. For $F_{s,0} > F_{s,c}$, it is a completely localized wave-packet in the three dimensional space, propagating back and forth along the polarization axis, without spreading (see fig. 38).

whereas the minimum approaches $\psi = 0$ for constant $L_0 = 0$, see fig. 36. It is easy to show that there exists a critical value $F_{s,c}$ of the static field, depending on $\hat{I}_1$,

$$F_{s,c} = \frac{2}{3}\left| F_0 J_1'(1) - \frac{\sqrt{3F_0 J_1'(1)}}{4\hat{I}_1} \right| \simeq 0.217F_0 - 0.164\frac{\sqrt{F_0}}{\hat{I}_1}, \tag{213}$$

above which both fixed points reach $L_0 = 0$. Then, in particular, the maximum at $L_0 = 0$, $\psi = \pi$, corresponds to a straight line orbit *parallel* to $\vec{F}_s$. Note that in the classical limit, $\hat{I}_1 \to \infty$, eq. (213) recovers the purely classical value [153] for angular stability of the straight line orbit along the polarization axis, as it should. Therefore, by variation of $F_{s,0} \in [0, F_{s,c}]$, we are able to continuously tune the position of the maximum in the (L_0, ψ) plane. Consequently, application of an additional static electric field gives us control over the trajectory traced by the wave-packet. This is further illustrated in fig. 37, through the *semiclassical* level dynamics of the resonantly driven manifold originating from the $n_0 = 60$ energy shell, as a function of F_s. In the limit $F_s = 0$, the spectrum

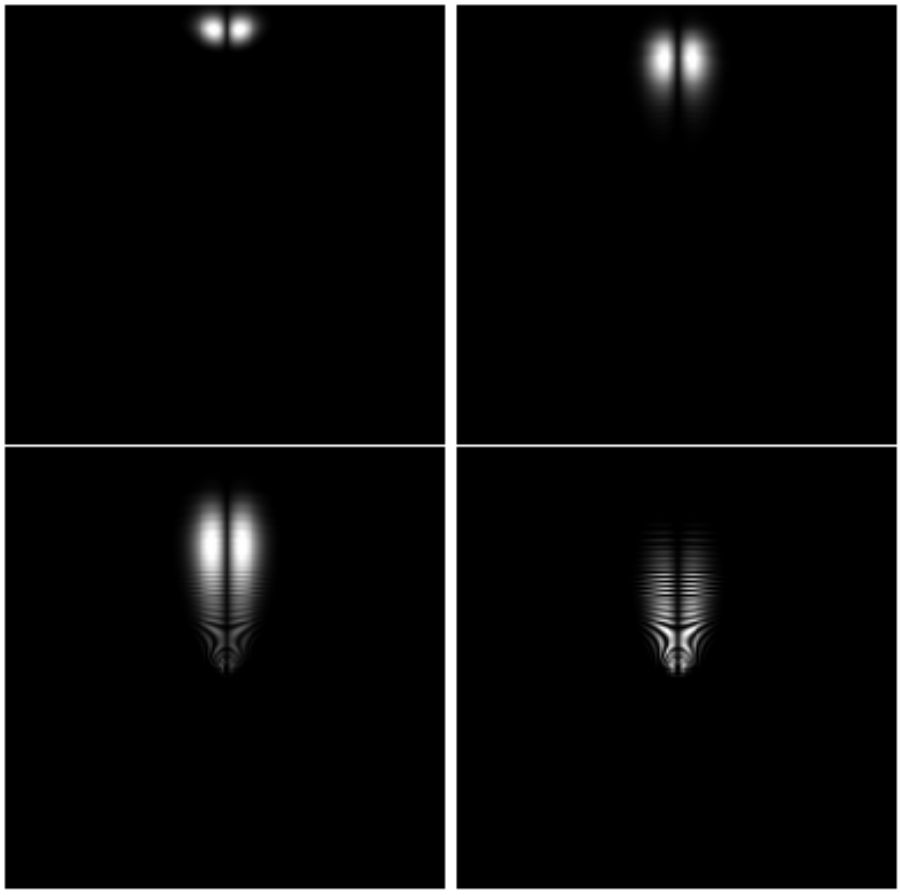

Fig. 38. Temporal dynamics of the non-dispersive wave-packet of a three-dimensional hydrogen atom exposed to a linearly polarized, resonant microwave field, in the presence of a parallel static electric field. $F_0 = 0.03$, $F_{s,0} = 0.009$, $F_{s,0}/F_0 = 0.3$, $n_0 = 60$. Driving field phases at the different stages of the wave-packet's evolution: $\omega t = 0$ (top left), $\pi/2$ (top right), $3\pi/4$ (bottom left), π (bottom right). It is well localized in the three dimensions of space and repeats its shape periodically (compare fig. 13 for the analogous dynamics in the restricted 1D model, where no additional static electric field is needed). The nucleus is at the center of the plot which extends over ± 8000 Bohr radii. The microwave polarization axis and the static field are oriented along the vertical axis.

is equivalent to the one plotted in fig. 21(b). As the static field is ramped up, the highest lying state (maximum value of the semiclassical quantum number p, for $F_s = 0$, see fig. 21, and the right column of fig. 23) gets stretched along the static field direction and finally, for $F_{s,0} > F_{s,c}$, collapses onto the quasi one dimensional wave-packet eigenstate bouncing off the nucleus along a straight line Kepler trajectory. Likewise, the energetically lowest state of the manifold (at $F_s = 0$, minimum value of the semiclassical quantum number p, left column of fig. 23) is equally rotated towards the direction defined by $\vec{F}_s$, but stretched in the opposite direction.

The existence of a non-dispersive wave-packet localized in all three dimensions of space is confirmed by a pure quantum calculation, using a numerically exact diagonalization of the Floquet Hamiltonian. Figure 38 shows the electronic density of a single Floquet eigenstate (the highest one in fig. 37, for $F_{s,0}/F_0 = 0.3$), at various phases of the driving field. The wave-packet is clearly localized along the field axis, and propagates along a straight line classical trajectory, repeating its shape periodically. Its dynamics precisely reproduces the dynamics of the 1D analogue illustrated in fig. 13. Once again, as for previous examples, the finite ionization rate (see section 7.1) of the 3D wave-packet is of the order of some million Kepler periods.

4.2 Wave-packets in the presence of a static magnetic field

Similarly to a static electric field which may stabilize an angularly unstable wave-packet, the properties of non-dispersive wave-packets under circularly polarized driving, in the presence of an additional static magnetic field normal to the polarization plane, has been studied in a series of papers [144,44,46,54,62,30,151]. The Hamiltonian of the system in the coordinate frame corotating with the CP field reads (compare with eq. (184), for the pure CP case)

$$H = \frac{p_x^2 + p_y^2 + p_z^2}{2} - \frac{1}{r} - (\omega - \omega_c/2)L_z + Fx + \frac{\omega_c^2}{8}(x^2 + y^2), \tag{214}$$

where ω_c is the cyclotron frequency. In atomic units, the cyclotron frequency $\omega_c = -qB/m$ equals the magnetic field value. It can be both positive or negative, depending on the direction of the magnetic field [23]. This additional parameter modifies the dynamical properties which characterize the equilibrium points, the analysis of which may be carried out alike the pure CP case treated in sec. 3.4. A detailed stability analysis can be found in [30,46,154] and we summarize here the main results only.

Since changing the sign of F in eq. (214) is equivalent to changing the sign of x from positive to negative, we only consider the equilibrium position at $x_{eq} > 0$ (compare eqs. (185-188)). For nonvanishing magnetic field, its position is given by

$$\omega(\omega - \omega_c)x_{eq} - \frac{1}{x_{eq}^2} - F = 0. \tag{215}$$

[23] A different convention is used (quantization axis defined by the orientation of the magnetic field) in many papers on this subject. It leads to unnecessarily complicated equations.

Redefining the dimensionless parameter q (see eq. (186)) via

$$q = \frac{1}{\omega(\omega - \omega_c)x_{eq}^3}, \tag{216}$$

we obtain for the microwave amplitude

$$F = [\omega(\omega - \omega_c)]^{2/3}(1-q)/q^{1/3}, \tag{217}$$

and

$$E_{eq} = [\omega(\omega - \omega_c)]^{1/3}(1-4q)/2q^{2/3} \tag{218}$$

for the equilibrium energy.

Harmonic expansion of eq. (214) around the equilibrium point ($x_{eq}, y_{eq} = 0, z_{eq} = 0$) allows for a linear stability analysis in its vicinity. Alike the pure CP case, the z motion decouples from the motion in the (x, y) plane. For the latter, we recover the generic harmonic Hamiltonian discussed in section 3.4, eq. (191), provided we substitute

$$\tilde{\omega} = \omega - \omega_c/2. \tag{219}$$

When expanded at second order around the equilibrium point, the Hamiltonian (214) takes the standard form of a rotating anisotropic oscillator, eq. (191), with $\tilde{\omega}$ replacing ω, and with the stability parameters:

$$\begin{aligned} a &= \frac{1}{\tilde{\omega}^2}\left(\frac{\omega_c^2}{4} - \frac{2}{x_{eq}^3}\right), \\ b &= \frac{1}{\tilde{\omega}^2}\left(\frac{\omega_c^2}{4} + \frac{1}{x_{eq}^3}\right). \end{aligned} \tag{220}$$

The regions of stability of the equilibrium point (x_{eq}, y_{eq}, z_{eq}) are thus obtained from the domains of stability of the 2D rotating anisotropic oscillator, given by eqs. (192,193). They are visualized in terms of the physical parameters F and ω_c, (using the standard scaled electric field $F_0 = Fn_0^4 = F\omega^{-4/3}$) in fig. 39, with the black region corresponding to eq. (192), and the grey region to eq. (193). Observe that the presence of the magnetic field tends to enlarge the region of stability in parameter space; for $\omega_c = 0$ (pure CP case, no magnetic field) the stability region is quite tiny, in comparison to large values of $|\omega_c|$ [24]. On the other hand, the stability diagram does not provide us any

[24] As long as we are interested in long-lived wave-packets, the region of small F_0 is of interest only. At higher F_0 and for $\omega_c < \omega$, the strong driving field will ionize the atom rather fast – see section 7.1. This makes the gray region $F_0 > 0.1$ of little practical interest.

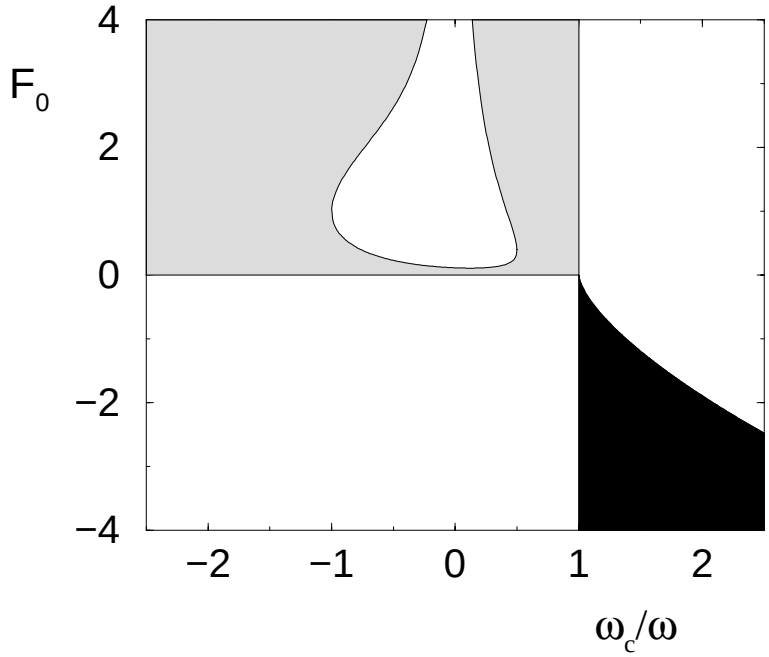

Fig. 39. (Shaded) Regions of stability of the equilibrium point $(x_{\rm eq}, y_{\rm eq}, z_{\rm eq})$ for circularly polarized driving (amplitude F, frequency ω) of a hydrogen atom, in the presence of a magnetic field (corresponding cyclotron frequency $\omega_{\rm c}$). The black and grey regions correspond to the two regions of stability, described by eqs. (192) and (193), respectively.

detailed information on the actual size of the resonance island surrounding the equilibrium point. However, it is precisely the size of the resonance island which is crucial for anchoring nondispersive quantum wave-packets close to the classical equilibrium point (see sec. 3.1.3).

An alternative approach to characterize the stability properties of the classical motion near $(x_{\rm eq}, y_{\rm eq}, z_{\rm eq})$ has been advertized in [30,44,46,54,62,144,151]: the concept of zero velocity surfaces (ZVS). In order to construct a ZVS, the Hamilton function is expressed in terms of velocities rather than canonical momenta. For the harmonic Hamiltonian (191), the calculation yields

$$H = \frac{v_x^2 + v_y^2}{2} + \frac{\omega^2}{2}\left[(a-1)x^2 + (b-1)y^2\right]. \tag{221}$$

Thus, the "kinetic energy" becomes a positive function of velocities, and one can define the ZVS as

$$S = H - \frac{v_x^2 + v_y^2}{2}, \tag{222}$$

the generalization of an effective potential for interactions which mix position and momentum coordinates. Note that, when the velocities coincide with the canonical momenta, S is nothing but the potential energy surface. We prefer to denote it S instead of V, to stress the difference. As discussed in detail in [30],

a ZVS may be used to locate the equilibrium points. However, their stability properties are not obvious (*contrary* to the potential surface, where minima define stable fixed points, while maxima and saddle points are unstable). For a ZVS, saddles are also unstable, but maxima may either be stable *or* unstable. For example, the first stability region, eq. (192), of the rotating 2D anistropic Hamiltonian is associated with a stable minimum of the ZVS. The second region of stability, eq. (193), corresponds to $a, b \leq 1$ and thus to a maximum of the ZVS. However, the ZVS does not show any qualitative change whether $(a-b)^2 + 8(a+b)$ is positive or negative, i.e. whether the equilibrium point is stable or unstable. Thus, a ZVS is clearly inappropriate, or at least potentially dangerous, for the discussion of the classical motion close to equilibrium. As a matter of fact, this difficulty with the ZVS is crucial in our case, even for the pure CP case, without additional magnetic field. Indeed, the ZVS becomes

$$S = \left(-\frac{2q+1}{2} x^2 + \frac{q-1}{2} y^2 \right) \omega^2, \tag{223}$$

where we use the single parameter q to parametrize S. At $q = 1$ (i.e. $F = 0$, see eq. (217)), the equilibrium point turns from a saddle (for $q > 1$) into a maximum. Consequently, the ZVS correctly reflects the change of the equilibrium point from unstable ($q > 1$) to stable ($q < 1$). However, for any $q \in (0, 1)$, the equilibrium remains a maximum of the ZVS, which completely misses the change of stability at $q = 8/9$. Thus, the very same maximum may change its stability (which fundamentally affects the classical motion in its vicinity) without being noticed by inspection of the ZVS. The latter evolves very smoothly around $q = 8/9$. Thus, the ZVS contours provide *no* information on the nature of the classical motion in the vicinity of the equilibrium point, in *disaccord* with [30,62,44,46,54,144,151]. Similarly, the isovalue contours of the ZVS (which are ellipses in the harmonic approximation) have no relation with the isovalue contours of the ground-state wave-packet localized around the equilibrium point (these contours are also ellipses in the harmonic approximation where the wave-packet is a Gaussian), contrary to what is stated in [30,44]. For example, the aspect ratio (major axis/minor axis) of the ZVS contour lines is $\sqrt{(2q+1)/(1-q)}$ which varies smoothly around $q = 8/9$, while the aspect ratio of the isocontours of the ground state wave-packet diverges when $q \to 8/9$. [25]

Nonwithstanding, a ZVS may be used for other purposes [144], e.g., to show the existence of an ionization threshold for the Hamiltonian (214), when $\omega_c > \omega$ (area coded in black in fig. 39). Clearly, due to the parabolic confinement in the $x-y$-plane, ionization is only possible along the z direction. The threshold

[25] While this argument has been presented here for the simplest case of the harmonic oscillator hamiltonian (191), it carries over to the full, nonlinear model, eq. (214).

is given by [144]

$$E_{\rm ion} = F^2/2\omega(\omega - \omega_{\rm c}), \tag{224}$$

which lies above the equilibrium energy $E_{\rm eq}$. Thus, for parameters in that region, the electron – initially placed close to the stable fixed point – cannot ionize. One may expect, therefore, that wave-packets built around the equilibrium point for $\omega_{\rm c} > \omega$ lead to *discrete* Floquet states. In other cases, e.g., for pure CP driving, non-dispersive wave-packets are rather represented by long-living resonances (see section 7.1).

Finally, it has been often argued [30,44,46,54,62,144,151] that the presence of the magnetic field is absolutely necessary for the construction of non-dispersive wave-packets. The authors consider non-dispersive wave-packets as equivalent to Gaussian shaped wave-functions (using equivalently the notion of coherent states). Then it is vital that the motion in the vicinity of the fixed point is locally harmonic within a region of size $\hbar$. This leads the authors to conclude that non-dispersive wave-packets may not exist for the pure CP case except in the extreme semiclassical regime. As opposed to that, the diamagnetic term in eq. (214) gives a stronger weight to the harmonic term, which is the basis of the above claim [26]. From our point of view, which, as already stated above, attributes the non-dispersive character of the wave-packet to a classical nonlinear resonance, the accuracy of the harmonic approximation (which, anyway, always remains an approximation) is irrelevant for the existence of non-dispersive wave-packets. The best proof is that [44] concludes, on the basis of the validity of the harmonic approximation, that non-dispersive wave-packets should not exist for $n_0 \simeq 60$ in CP field, in complete contradiction to numerically exact experiments showing their existence down to $n_0 = 15$ [49]. On the other hand, it is an interesting question how good the harmonic approximation actually is in the pure CP case. The interested reader may find a more quantitative discussion of this point in section 7.2.

5 Other resonances

5.1 General considerations

We have so far restricted our attention to nondispersive wave-packets anchored to the principal resonance of periodically driven Hamiltonian systems. In section 3.1, we already saw that *any* harmonic of the unperturbed classical

[26] Note that the non-harmonic terms, being entirely due to the Coulomb field, are not removed or decreased by the addition of a magnetic field. They are just hidden by a larger harmonic term.

motion can dominate the harmonic expansion (57) of the classical Hamilton function, provided it is resonantly driven by the external perturbation, i.e.

$$s\theta - \omega t \simeq \text{const}, \;\; s > 0 \text{ integer}. \tag{225}$$

This is the case when the s^{th} harmonic of the classical internal frequency Ω is resonant with the external driving ω. As Ω depends on the classical unperturbed action, the corresponding classical resonant action is defined by

$$\Omega(I_s) = \frac{\partial H_0}{\partial I}(I_s) = \frac{\omega}{s}. \tag{226}$$

At this action, the period of the classical motion is s times the period of the external drive. Precisely like in the $s = 1$ case (the principal resonance), for any integer $s > 1$, Floquet eigenstates of the driven system exist which are localized on the associated classical stability islands in phase space. The energy of these eigenstates can again be estimated through the semiclassical quantization of the secular dynamics. To do so, we start from eqs. (57,58) and transform to slowly varying variables (the "rotating frame") defined by

$$\begin{aligned} \hat{\theta} &= \theta - \frac{\omega t}{s}, \\ \hat{I} &= I, \\ \hat{P}_t &= P_t + \frac{\omega I}{s}. \end{aligned} \tag{227}$$

The Floquet Hamiltonian in this rotating frame now reads:

$$\hat{\mathcal{H}} = \hat{P}_t + H_0(\hat{I}) - \frac{\omega \hat{I}}{s} + \lambda \sum_{m=-\infty}^{+\infty} V_m(\hat{I}) \left\{ \cos\left(m\hat{\theta} + \left(\frac{m-s}{s} \right) \omega t \right) \right\}, \tag{228}$$

which is periodic with period $\tau = sT$ with $T = 2\pi/\omega$. Passing to the rotating frame apparently destroys the T-periodicity of the original Hamiltonian. This, however, is of little importance, the crucial point being to keep the periodicity sT of the internal motion. If we now impose the resonance condition (225), the major contribution to the sum in eq. (228) will come from the slowly evolving resonant term $m = s$, while the other terms vanish upon averaging the fast variable t over one period τ, leading to the secular Hamilton function

$$\mathcal{H}_{\text{sec}} = \hat{P}_t + H_0(\hat{I}) - \frac{\omega \hat{I}}{s} + \lambda V_s(\hat{I}) \cos(s\hat{\theta}). \tag{229}$$

This averaging procedure eliminates the explicit time dependence of $\hat{\mathcal{H}}$, and is tantamount to restricting the validity of $\mathcal{H}_{\text{sec}}$ to the description of those classical trajectories which comply with eq. (225) and, hence, exhibit a periodicity with period τ. This will have an unambiguous signature in the quasienergy spectrum, as we shall see further down. The structure of the secular Hamiltonian is simple and reminds us of the result for the principal $s = 1$ resonance,

eq. (64). However, due to the explicit appearance of the factor $s > 1$ in the argument of the cos term, a juxtaposition of s resonance islands close to the resonant action, eq. (226), is created. It should be emphasized that these s resonance islands are actually s clones of the same island. Indeed, a trajectory trapped inside a resonance island will successively visit all the islands: after one period of the drive, θ is approximately increased by $2\pi/s$, corresponding to a translation to the next island. At the center of the islands, there is a single, stable resonant trajectory whose period is exactly $\tau = sT$.

At lowest order in λ, all the quantities of interest can be expanded in the vicinity of I_s, exactly as for the principal resonance in section 3.1.1. V_s is consistently evaluated at the resonant action. The pendulum approximation of the secular Hamiltonian then reads:

$$\mathcal{H}_{\rm pend} = \hat{P}_t + H_0(\hat{I}_s) - \frac{\omega}{s}\hat{I}_s + \frac{1}{2}H_0''(\hat{I}_s)\ (\hat{I} - \hat{I}_s)^2 + \lambda V_s(\hat{I}_s)\cos s\hat{\theta}, \qquad (230)$$

with the centers of the islands located at:

$$\hat{I} = \hat{I}_s = I_s, \qquad (231)$$

$$\begin{cases} \hat{\theta} = k\dfrac{2\pi}{s}, & \text{if } \lambda V_s(\hat{I}_s)H_0''(\hat{I}_s) < 0, \\ \hat{\theta} = k\dfrac{2\pi}{s} + \dfrac{\pi}{s}, & \text{if } \lambda V_s(\hat{I}_s)H_0''(\hat{I}_s) > 0, \end{cases} \qquad (232)$$

where k is an integer running from 0 to $s-1$. For $H_0''(\hat{I}_s)$ – see eq. (67) – positive, these are minima of the secular Hamiltonian, otherwise they are maxima. The extension of each resonance island is, as a direct generalization of the results of section 3.1.1:

$$\Delta\hat{\theta} = \frac{2\pi}{s}, \qquad (233)$$

$$\Delta\hat{I} = 4\sqrt{\left|\frac{\lambda V_s(\hat{I}_s)}{H_0''(\hat{I}_s)}\right|}, \qquad (234)$$

and its area

$$A_s(\lambda) = \frac{16}{s}\sqrt{\left|\frac{\lambda V_s(\hat{I}_s)}{H_0''(\hat{I}_s)}\right|}. \qquad (235)$$

Again, the dependence of $A_s(\lambda)$ on $\sqrt{|\lambda|}$ implies that even small perturbations may induce significant changes in the phase space structure, provided the perturbation is resonant with a harmonic of the unperturbed classical motion [27].

[27] The situation is very different in the opposite case, when ω is the $s^{\rm th}$ SUBharmonic [93] of the internal frequency. A resonance island may then exist but it is

The construction of a non-dispersive wave-packet is simple once the s-resonance structure is understood: indeed, any set of initial conditions trapped in one of the s-resonance islands will classically remain trapped forever. Thus, a quantum wave-packet localized initially inside a resonance island is a good candidate for building a non-dispersive wave-packet. There remains, however, a difficulty: the wave-packet can be initially placed in any of the s resonance islands. After one period of the driving, it will have jumped to the next island, meaning that it will be far from its initial position. On the other hand, the Floquet theorem guarantees the existence of states which are strictly periodic with the period of the drive (not the period of the resonant internal motion). The solution to this difficulty is to build eigenstates which simultaneously occupy *all* s-resonance islands, that is, which are composed of s wave-packets each localized on a different resonance island. After one period of the drive, each individual wave-packet replaces the next one, resulting in globally T-periodic motion of this "composite" Floquet state. If the system has a macroscopic size (i.e. in the semiclassical limit), individual wave-packets will appear extremely well localized and lying far from the other ones while maintaining a well-defined phase coherence with them. For $s = 2$, the situation mimics a symmetric double well potential, where even and odd solutions are linear combinations of nonstationary states, each localized in either one well [7].

In order to get insight in the structure of the Floquet quasi-energy spectrum, it is useful to perform the semiclassical EBK quantization of the secular Hamiltonian (229). Quantization of the motion in $(\hat{I}, \hat{\theta})$, see section 3.1.3, provides states trapped within the resonance islands (librational motion), and states localized outside them (rotational motion). As usual, the number of trapped states is given by the size, eq. (235) of the resonance island:

$$\text{Number of trapped states} \simeq \frac{8}{\pi\hbar s}\sqrt{\left|\frac{\lambda V_s(\hat{I}_s)}{H_0''(\hat{I}_s)}\right|}. \tag{236}$$

The quantization can be performed along the contours of any of the s clones of the resonance island, giving of course the same result. However, this does *not* result in a s-degeneracy of the spectrum: indeed, the s clones belong to the same torus in phase space (see above) and do not generate s independent states.

If the number of trapped states is sufficiently large, the harmonic approximation to the pendulum (or secular) Hamiltonian can be used, with the frequency

typically much smaller as it comes into play only at order s in perturbation theory, with a size scaling as $|\lambda|^{s/2}$.

of the harmonic motion around the stable resonant orbit given by:

$$\omega_{\rm harm} = s\sqrt{|\lambda V_s(\hat{I}_s) H_0''(\hat{I}_s)|}. \tag{237}$$

In order to get the complete semiclassical Floquet spectrum, we additionally have to perform the semiclassical quantization in the $(t, \hat{P}_t)$ plane, giving:

$$\frac{1}{2\pi}\int_0^\tau \hat{P}_t dt = \frac{\hat{P}_t \tau}{2\pi} = \frac{s\hat{P}_t}{\omega} = \left(j + \frac{\mu}{4}\right)\hbar, \tag{238}$$

with j integer. This finally yields the semiclassical Floquet levels (in the harmonic approximation):

$$\mathcal{E}_{N,j} = H_0(\hat{I}_s) - \frac{\omega}{s}\hat{I}_s + \left(j + \frac{\mu}{4}\right)\hbar\frac{\omega}{s} - \ \text{sign}(H_0''(\hat{I}_s))\left[|\lambda V_s(\hat{I}_s)| - \left(N + \frac{1}{2}\right)\hbar\omega_{\rm harm}\right], \tag{239}$$

with N a non-negative integer. The wave-packet with optimum localization in the $(\hat{I}, \hat{\theta})$ plane, i.e. optimum localization along the classical unperturbed orbit, is the $N = 0$ state. According to eq. (239), the semiclassical quasi-energy spectrum has a periodicity $\hbar\omega/s$, whereas the "quantum" Floquet theory only enforces $\hbar\omega$ periodicity. Thus, inside a Floquet zone of width $\hbar\omega$, each state appears s times (for $0 \leq j < s$), at energies separated by $\hbar\omega/s$. Note that this property is a direct consequence of the possibility of eliminating the time dependence of $\mathcal{H}$ in eq. (228) by averaging over τ, leading to the time independent expression (229) for $\mathcal{H}_{\rm sec}$. Therefore, it will be only approximately valid for the exact quantum Floquet spectrum. In contrast, the $\hbar\omega$ periodicity holds exactly, as long as the system Hamiltonian is time-periodic.

We will now recover the $\hbar\omega/s$ periodicity in a quantum description of our problem, which will provide us with the formulation of an eigenvalue problem for the wave-packet eigenstates anchored to the s-resonance, in terms of a Mathieu equation. In doing so, we shall extend the general concepts outlined in section 3.1.4 above.

Our starting point is eq. (85), which we again consider in the regime where the eigenenergies E_n of the unperturbed Hamiltonian H_0 are locally approximately spaced by $\hbar\Omega$. The resonance condition (225) implies

$$\left.\frac{dE_n}{dn}\right|_{n=n_0} = \hbar\frac{\omega}{s}, \tag{240}$$

where, again, n_0 is not necessarily an integer, and is related to the resonant action and its associated Maslov index through:

$$\hat{I}_s = \left(n_0 + \frac{\mu}{4}\right)\hbar. \tag{241}$$

When the resonance condition is met, the only efficient coupling in eq. (85) connects states with the same value of $n - sk$. In other words, in the secular approximation, a given state (n, k) only couples to $(n + s, k + 1)$ and $(n - s, k - 1)$. We therefore consider a given ladder of coupled states labeled by $j = n - sk$. Because of the overall ω perodicity of the spectrum, changing j by s units (i.e., shifting all k-values by 1) is irrelevant, so that it is enough to consider the s independent ladders $0 \leq j \leq s - 1$. Furthermore, in analogy to section 3.1.4, eq. (91), we can replace the coupling matrix elements in eq. (228) by the resonantly driven Fourier coefficients of the classical motion,

$$\langle \phi_n | V | \phi_{n+s} \rangle \simeq \langle \phi_{n-s} | V | \phi_n \rangle \simeq V_s(\hat{I}_s). \tag{242}$$

With these approximations, and the shorthand notation $r = n - n_0$, eq. (85) takes the form of s independent sets of coupled equations, identified by the integer j:[28]

$$\left[\mathcal{E} - E_{n_0} + \frac{n_0 - j}{s} \hbar\omega - \frac{\hbar^2 r^2}{2} H_0''(\hat{I}_s) \right] d_r = \frac{\lambda}{2} V_s [d_{r+s} + d_{r-s}], \tag{243}$$

where

$$d_r = c_{n_0+r, \frac{n_0+r-j}{s}}, \tag{244}$$

as a generalization of the notation in eq. (93). Again, r is not necessarily an integer, but the various r values involved in eq. (243) are equal modulo s. Precisely as in the case of the principal resonance, eq. (243) can be mapped on its dual space expression, via eq. (94):

$$\left[-\frac{\hbar^2}{2} H_0''(\hat{I}_s) \frac{d^2}{d\phi^2} + E_{n_0} - \frac{n_0 - j}{s} \hbar\omega + \lambda V_s \cos(s\phi) \right] f(\phi) = \mathcal{E} f(\phi), \tag{245}$$

and identified with the Mathieu equation (97) through

$$\begin{aligned} s\phi &= 2v, \\ a &= \frac{8}{\hbar^2 s^2 H_0''(\hat{I}_s)} \left[\mathcal{E} - E_{n_0} + (n_0 - j)\hbar \frac{\omega}{s} \right], \ j = 0, \ldots, s - 1, \\ q &= \frac{4\lambda V_s(\hat{I}_s)}{s^2 \hbar^2 H_0''(\hat{I}_s)}. \end{aligned} \tag{246}$$

The quasienergies associated with the s resonance in the pendulum approximation then follow immediately as

$$\mathcal{E}_{\kappa,j} = E_{n_0} - (n_0 - j)\hbar \frac{\omega}{s} + \frac{\hbar^2 s^2}{8} H_0''(\hat{I}_s) a_\kappa(\nu, q), \tag{247}$$

[28] For $s = 1$, this equation reduces of course to eq. (92). We here use n_0 instead of $\hat{I}_s$; the two quantities differ only by the Maslov index, eq. (241).

where the index j runs from 0 to $s-1$, and κ labels the eigenvalues of the Mathieu equation [95]. Again, the boundary condition for the solution of the Mathieu equation is incorporated via the characteristic exponent, which reads

$$\nu = -2\frac{n_0 - j}{s} \pmod 2, \qquad j = 0, \ldots s-1. \tag{248}$$

The structure of this quasi-energy spectrum apparently displays the expected $\hbar\omega/s$ periodicity. However, the characteristic exponent ν – and consequently the $a_\kappa(\nu, q)$ eigenvalues – depend on j, what makes the periodicity approximate only. It is only far inside the resonance island that the $a_\kappa(\nu, q)$ eigenvalues are almost independent of ν and the periodicity is recovered. Deviations from this periodicity are further discussed in section 5.2. Finally, the asymptotic expansion of the $a_\kappa(\nu, q)$ for large q, eq. (104), gives again (compare section 3.1.4) the semiclassical estimate of the energy levels in the harmonic approximation, eq. (239), where the indices κ and N coincide.

5.2 A simple example in 1D: the gravitational bouncer

As a first example of non-dispersive wave-packets localized on $s > 1$ primary resonances, we consider the particularly simple 1D model of a particle moving vertically in the gravitational field, and bouncing off a periodically driven horizontal plane. This system is known as the Pustylnikov model [3] (or, alternatively, the "gravitational bouncer", or the "bubblon model" [42,155–157]) and represents a standard example of chaotic motion. Moreover, despite its simplicity, it may find possible applications in the dynamical manipulation of cold atoms [158]. A gauge transformation shows its equivalence to a periodically driven particle moving in a triangular potential well, with the Hamiltonian

$$H = \frac{p^2}{2} + V(z) + \lambda z \sin(\omega t), \tag{249}$$

where

$$V(z) = \begin{cases} z & \text{for } z \geq 0, \\ \infty & \text{for } z < 0. \end{cases} \tag{250}$$

The strength λ of the periodic driving is proportional to the maximum excursion of the oscillating surface. Classically, this system is well approximated by the standard map [3] (with the momentum and the phase of the driving at the moment of the bounce as variables), with kicking amplitude $K = 4\lambda$.

Apart from a (unimportant) phase shift $\pi/2$ in ωt, eq. (249) is of the general type of eq. (54) and the scenario for the creation of non-dispersive wave-packets described in sections 3.1.1 and 3.1.2 is applicable. As a matter of fact, a careful

analysis of the problem using the Mathieu approach described in sec. 3.1.4, as well as the semiclassical quantization of the Floquet Hamiltonian were already outlined in [42], where the associated Floquet eigenstates were baptized "flotons". We recommend [42,157] for a detailed discussion of the problem, reproducing here only the main results, with some minor modifications.

Solving the classical equations of motion for the unperturbed Hamiltonian is straightforward (piecewise uniformly accelerated motion alternating with bounces off the mirror) and it is easy to express the unperturbed Hamiltonian and the classical internal frequency in terms of action-angle variables:

$$H_0 = \frac{(3\pi I)^{2/3}}{2}, \tag{251}$$

$$\Omega = \frac{\pi^{2/3}}{(3I)^{1/3}}, \tag{252}$$

while the full, time-dependent Hamiltonian reads:

$$H = \frac{(3\pi I)^{2/3}}{2} + \frac{\lambda\pi I^{2/3}}{(3\pi)^{1/3}}\sin(\omega t) - \frac{2\lambda(3I)^{2/3}}{\pi^{4/3}}\sin(\omega t)\sum_{n=1}^{\infty}\frac{\cos(n\theta)}{n^2}. \tag{253}$$

Thus, the resonant action (226) is given by

$$\hat{I}_s = \frac{\pi^2 s^3}{3\omega^3}, \tag{254}$$

with the associated strength of the effective coupling

$$V_s = \frac{(3I)^{2/3}}{s^2\pi^{4/3}}. \tag{255}$$

Using the framework of sections 3.1.1, 3.1.2 (for $s = 1$), and 5.1 (for $s > 1$), the reader may easily compute the various properties of non-dispersive wave-packets in this system [29]. An example for $s = 1$ is presented in fig. 40, for the resonant principal quantum number $n_0 = 1000$, (i.e., $\hat{I}_1 = 1000.75$) where both, the (time-periodic) probability densities in configuration and phase space are shown. Note that such high n_0 values (or even higher) correspond to typical experimental falling heights (around 0.1 mm for $n_0 = 1000$) in experiments on cold atoms [158]. Therefore, the creation of an atomic wave-packet in such an experiment would allow to store the atom in a quasi classical "bouncing mode" over arbitrarily long times, and might find some application in the field of atom optics [159].

[29] There is, however, a tricky point: the Maslov index in this system is 3, with a contribution 1 coming from the outer turning point, and 2 from $z = 0$, since the oscillating plane acts as a hard wall. Hence, the relation between the principal quantum number and the action is $I_1 = n + 3/4$, see eq. (38).

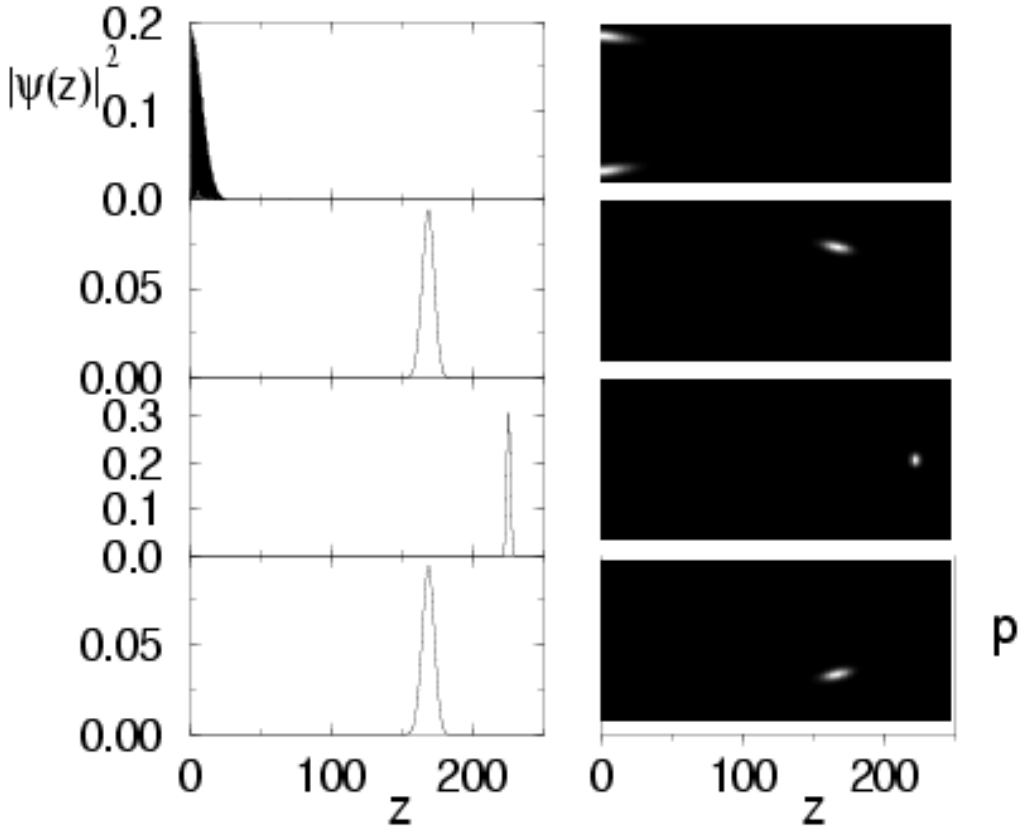

Fig. 40. A non-dispersive $s = 1$ wave-packet of the gravitational bouncer, eq. (249). The quantum number of the resonant state is chosen as $n_0 = 1000$, to match typical experimental dimensions [158]. The left column shows the time evolution of the wave-packet for $\omega t = 0, \pi/2, \pi, 3\pi/2$ (from top to bottom). The right column shows the corresponding phase space (Husimi, see eq. (30)) representation (z axis horizontal as in the left column, momentum p on the vertical axis). The parameters are $\omega \simeq 0.1487$, $\lambda = 0.025$. The periodic, nondispersive dynamics of the wave-packet bouncing off the mirror in the gravitational field is apparent.

For $s = 2$, we expect, following the general discussion in section 5.1, two quasi-energy levels, separated by $\omega/2$, according to the semiclassical result, eq. (239), which are *both* associated with the $s = 2$ resonance. As a matter of fact, such states are born out from an exact numerical diagonalization of the Floquet Hamiltonian derived from eq. (249). An exemplary situation is shown in fig. 41, for $n_0 = 1000$ (i.e., $\hat{I}_2 = 1000.75$, in eq. (254)). The tunneling coupling between the individual wave-packets shown in the right column of fig. 41 is given by the tunneling splitting Δ between the energies of both associated Floquet states (left column of fig. 41) modulo $\omega/2$. From the Mathieu approach – eqs. (247,248) – this tunneling coupling is directly related to the variations of the Mathieu eigenvalues when the characteristic exponent is changed. In the limit where the resonance island is big enough, $q \gg 1$ in

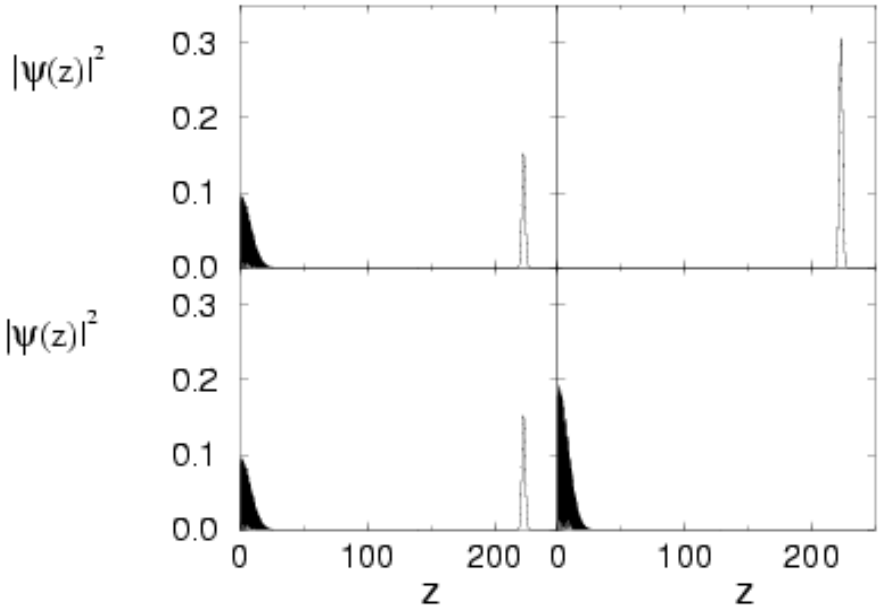

Fig. 41. Floquet eigenstates anchored to the $\omega = 2\Omega$ resonance in the gravitational bouncer (left column), in configuration space, at $\omega t = 0$. Each eigenstate exhibits two wave-packets shifted by a phase π along the classical trajectory, to abide the Floquet periodicity imposed by eq. (74). Symmetric and antisymmetric linear combinations of these states isolate either one of the wave-packets, which now evolves precisely like a classical particle (right column), periodically bouncing off the wall at $z = 0$. The parameters are $\omega \simeq 0.2974$, (corresponding to $n_0 = 1000$, for the $2:1$ resonance), $\lambda = 0.025$.

eq. (247), asymptotic expressions [95] allow for the following estimate [42]:

$$\Delta = \frac{8\sqrt{2}\lambda^{3/4}}{\pi\sqrt{\omega}} \exp\left(-\frac{16\pi\sqrt{\lambda}}{\omega^3}\right) = \frac{8[3(n_0+3/4)]^{1/6}\lambda^{3/4}}{\pi^{4/3}} \exp\left(-6(n_0+3/4)\sqrt{\lambda}/\pi\right), \quad (256)$$

which we can test with our numerically exact quantum treatment. The result is shown in fig. 42, for two different values of n_0.

Observe the excellent agreement for small λ, with an almost exponential decrease of the splitting with $\sqrt{\lambda}$, as expected from eq. (256). However, for larger values of λ (nontheless still in the regime of predominantly regular classical motion) the splitting saturates and then starts to fluctuate in an apparently random way. While the phenomenon has not been completely clarified so far, we are inclined to attribute it to tiny avoided crossings with Floquet states localized is some other resonance islands (for a discusion of related phenomena see [160,161]). Comparison of the two panels of fig. 42 additionally indicates that the region of λ values where avoided crossings become important increases in the semiclassical limit, and that eq. (256) remains valid for small λ only. This is easily understood: in the semiclassical limit $n_0 \to \infty$, the tunneling splitting decreases exponentially, while the density of states increases.

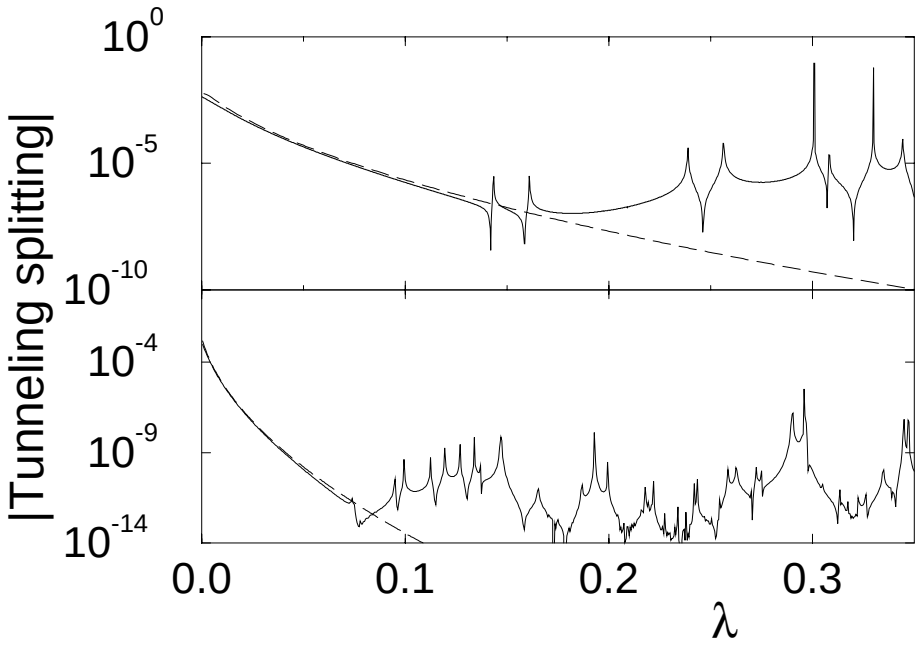

Fig. 42. Tunneling splitting between the energies (modulo $\omega/2$) of two Floquet states of the gravitational bouncer, anchored to the $s = 2$ resonance island, as a function of the driving amplitude λ. Driving frequency $\omega \simeq 1.0825$ (top) and $\omega \simeq 0.8034$ (bottom), corresponding to resonant states $n_0 = 20$ and $n_0 = 50$, respectively. The dashed line reproduces the prediction of Mathieu theory [42], eq. (256). Observe that the latter fits the exact numerical data only for small values of λ. At larger λ, small avoiding crossings between one member of the doublet and eigenstates originating from other manifolds dominate over the pure tunneling contribution and the Mathieu prediction is not accurate.

Finally, fig. 43 shows a Floquet eigenstate anchored to the $s = 11$ resonance island chain. It may be thought of as a linear combination of 11 non-dispersive wave-packets which, at a given time, may interfere with each other, or, at another time (bottom panel), are spatially well separated. For a Helium atom bouncing off an atom mirror in the earth's gravitational field (alike the setting in [158]), the z values for such a state reach 5 millimeters. This non-dispersive wave-packet is thus a macroscopic object composed of 11 individual components keeping a well-defined phase coherence.

5.3 The $s = 2$ resonance in atomic hydrogen under linearly polarized driving

Let us now return to the hydrogen atom driven by LP microwaves. The highly nonlinear character of the Coulomb interaction favours non-dispersive wave-packets anchored to the $s : 1$ resonance island, since the Fourier components V_s of the coupling between the atom and the microwave decay slowly [30] with

[30] The very same behavior characterizes the gravitational bouncer discussed in the previous section. For the bouncer the slow inverse square dependence of V_s on s is

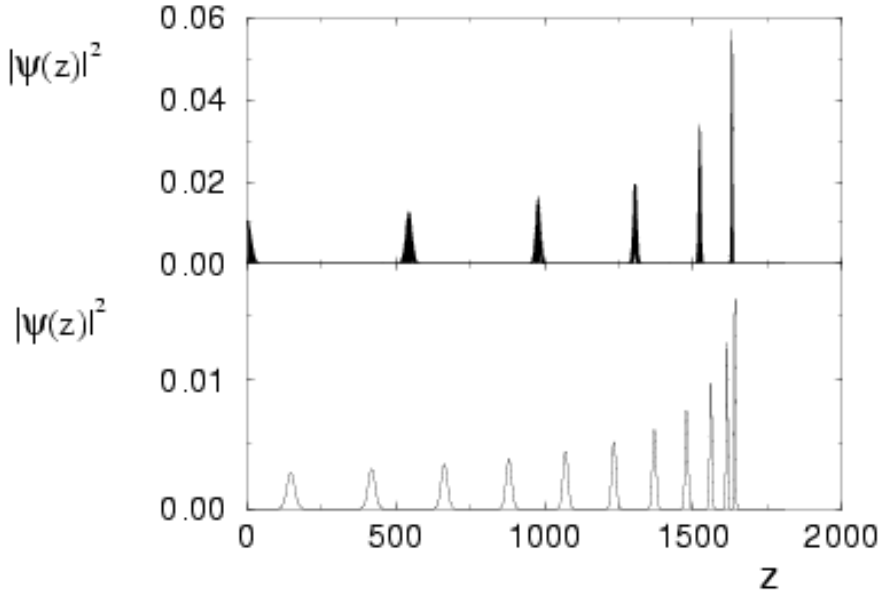

Fig. 43. Single Floquet state of the gravitational bouncer at phases $\omega t = 0$ (top) and $\omega t = \pi/2$ (bottom), anchored to the $11:1$ resonance island chain in classical phase space. Driving frequency $\omega = 11\Omega \simeq 0.6027$, $n_0 = 20000$, and $\lambda = 0.025$. In the upper plot, among 11 individual wave-packets which constitute the eigenstate, five pairs (with partners moving in opposite directions) interfere at distances $z > 0$ from the mirror, whereas the 11th wave-packet bounces off the wall and interferes with itself. At later times (bottom), the 11 wave-packets are well separated in space.

s – compare eqs. (120,121). Consider first the simpler 1D model of the atom. We discuss the $s = 2$ case only, since similar conclusions can be obtained for higher s values. The left panel in fig. 44 shows the classical phase space structure (Poincaré surface of section) for $F_0 = 0.03$, with the $s = 2$ resonance completely embedded in the chaotic sea, and well separated from the much larger principal resonance island. From our experience with the principal resonance, and from the general considerations on $s:1$ resonances above, we expect to find Floquet eigenstates which are localized on this classical phase space structure and mimic the temporal evolution of the corresponding classical trajectories. Indeed, the right plot in fig. 44 displays a Floquet eigenstate obtained by "exact" numerical diagonalization, which precisely exhibits the desired properties.

Again, this observation has its direct counterpart in the realistic 3D atom, where the $2:1$ resonance allows for the construction of non-dispersive wave-packets along elliptic trajectories, as we shall demonstrate now. We proceed as for the $s = 1$ case (sec. 3.3.2): the secular Hamiltonian is obtained by averaging the full Hamiltonian, eq. (152), after transformation to the "rotating frame",

due to a hard collision with the oscillating surface. For the Coulomb problem, the singularity at the origin is even stronger.

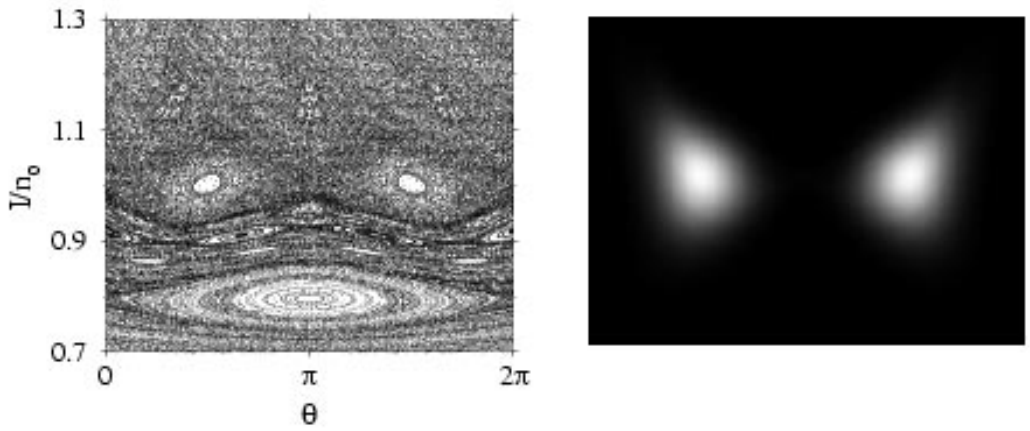

Fig. 44. Left: Poincaré surface of section of the one-dimensional hydrogen atom under linearly polarized driving, eq. (137), for resonant driving at twice the Kepler frequency. The scaled field strength is $F_0 = 0.03$, and the phase is fixed at $\omega t = 0$. The $s = 2$ resonance islands are apparent, embedded in the chaotic sea, and separated from the $s = 1$ resonance by invariant tori. Right: Husimi representation [145] of a Floquet eigenstate (for $n_0 = 60$) anchored to the $s = 2$ resonance displayed on the left.

eq. (228), over one period $\tau = sT$ of the resonantly driven classical trajectory:

$$\mathcal{H}_{\rm sec} = \hat{P}_t - \frac{1}{2\hat{I}^2} - \frac{\omega \hat{I}}{s} + F\sqrt{1-\frac{M^2}{L^2}}\left[-X_s(\hat{I})\cos\psi\cos\hat{\theta} + Y_s(\hat{I})\sin\psi\sin\hat{\theta}\right], \quad (257)$$

where X_s and Y_s are given by eqs. (153,154). This can be condensed into

$$\mathcal{H}_{\rm sec} = \hat{P}_t - \frac{1}{2\hat{I}^2} - \frac{\omega \hat{I}}{s} + F\chi_s\cos(s\hat{\theta} + \delta_s), \quad (258)$$

with

$$\chi_s(\hat{I}, L, \psi) := \sqrt{1-\frac{M^2}{L^2}}\sqrt{X_s^2\cos^2\psi + Y_s^2\sin^2\psi}, \quad (259)$$

$$\tan\delta_s(L,\psi) := \frac{Y_s}{X_s}\tan\psi = \frac{J_s(se)\sqrt{1-e^2}}{eJ_s'(se)}\tan\psi. \quad (260)$$

For simplicity, we will now discuss the case $M = 0, s = 2$. Fig. 45 shows the equipotential lines of χ_2 in the (L, ψ) plane, calculated from eqs. (258-260) [31]. For a comparison with quantum data, the equipotential lines represent the values of χ_2 for $n_0 = 42$, quantized from the WKB prescription in the (L, ψ) plane, exactly as done for the principal $s = 1$ resonance in section 3.3.2.

[31] Since χ_s scales globally as $\hat{I}^2$, the equipotential lines in fig. 45 do not depend on $\hat{I}$.

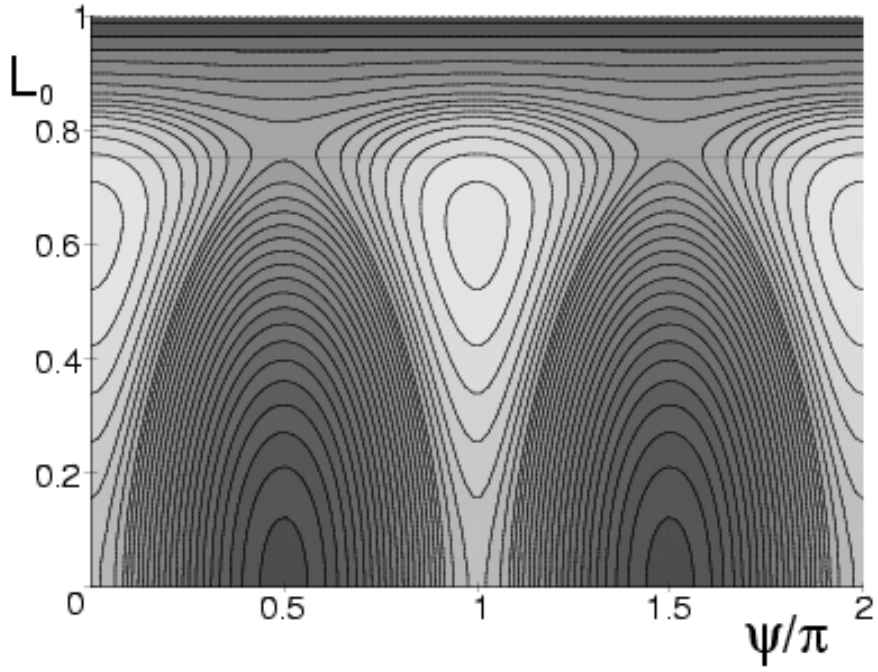

Fig. 45. Contour plot of the effective perturbation χ_2, eq. (259), generating the slow evolution of the electronic trajectory in the $(L_0 = L/\hat{I}, \psi)$ plane. The secular motion in this case is topologically different from that corresponding to the $s = 1$ resonance (compare with fig. 19). In particular, there appear new fixed points at $L_0 \simeq 0.77, \psi = \pi/2, 3\pi/2$ (unstable, corresponding to unstable elliptic orbits with major axis perpendicular to the polarization axis) and at $L_0 \simeq 0.65,\ \psi = 0, \pi$ (stable, corresponding to stable elliptic orbits with major axis parallel and antiparallel to the polarization axis). The resonance island in the $(\hat{I}, \hat{\theta})$ plane is quite large for the latter stable orbits, and the associated eigenstates are non-dispersive wave-packets localized both longitudinally along the orbit (locked on the microwave phase), and in the transverse direction, see figs. 48, 49, 50.

One immediately notices that the secular motion is in this case topologically different from that corresponding to the $s = 1$ resonance (compare to fig. 19), with the following features:

– three different types of motion coexist, with separatrices originating from the straight line orbits parallel $(L_0 = 0, \psi = 0, \pi)$ to the polarization axis.
– The straight line orbits perpendicular to the polarization axis $(L_0 = 0, \psi = \pi/2, 3\pi/2)$ lie at minima – actually zeros – of χ_2. At lowest order, they exhibit vanishing coupling to the external field, as for the $s = 1$ resonance. Hence, the resonance island in the $(\hat{I}, \hat{\theta})$ plane will be small, and the wave-packets localized along the corresponding orbits are not expected to exist for moderate excitations.
– The circular orbit (in the plane containing the polarization axis, $L_0 = 1$, arbitrary ψ) also exhibits vanishing coupling (since the circular motion is purely harmonic, no coupling is possible at $\omega = 2\Omega$).

– There are "new" fixed points at $L_0 \simeq 0.77, \psi = \pi/2, 3\pi/2$ (unstable), and at $L_0 \simeq 0.65, \psi = 0, \pi$ (stable), corresponding to elliptical orbits with major axis perpendicular and parallel to the polarization axis, respectively. The latter ones correspond to *maxima* of χ_2, and are associated with a large resonance island in the $(\hat{I}, \hat{\theta})$ plane. The motion in their vicinity is strongly confined, *both* in the angular (L_0, ψ) and in the $(\hat{I}, \hat{\theta})$ coordinates: the corresponding eigenstates can be characterized as non-dispersive wavepackets, localized both longitudinally along the orbit (locked on the microwave phase), and in the transverse direction.

In order to separate quantum states localized in different regions of the (L_0, ψ) space, we show in fig. 46 a comparison between the semiclassical prediction and the numerically exact Floquet energies (obtained as in section 3.3.2 for the $s = 1$ resonance) originating from this manifold, with $N = 0$ in eqs. (78,79), at $F_0 = 0.04$. Observe that the 16 upmost states appear in eight quasi-degenerate pairs differing by parity. Exact degeneracy does not happen because of tunneling effects: the lower the doublet in energy, the larger its tunneling splitting. The tunneling process involved here is a "transverse" tunneling in the (L, ψ) plane, where the electron jumps from the elliptic $(L_0 \simeq 0.65, \psi = 0)$ Kepler trajectory to its image under z-parity, the $(L_0 \simeq 0.65, \psi = \pi)$ trajectory (compare fig. 45). This tunneling process is entirely due to the specific form of χ_2, with two *distinct* maxima.

The energetically highest doublet in fig. 46 corresponds to states localized as close as possible to the fixed points $L_0 \simeq 0.65$, $\psi = 0, \pi$. For these states (large resonance island in the $(\hat{I}, \hat{\theta})$ plane), semiclassical quantization nicely agrees with the quantum results. On the other hand, the agreement between quantum and semiclassical results progressively degrades for lower energies, as the size of the island in the $(\hat{I}, \hat{\theta})$ plane becomes smaller. Still, the disagreement between semiclassical and quantum results is at most of the order of the spacing between adjacent levels [32] . Below the energy of the unstable fixed points at $L_0 \simeq 0.77, \psi = \pi/2, 3\pi/2$, there are no more pairs of classical trajectories in the (L, ψ) plane corresponding to distinct classical dynamics related by z-parity. Hence, the doublet structure has to disappear, as confirmed by the exact quantum results shown in fig. 46. On the other hand, there are two disconnected regions in the (L, ψ) plane which can give rise to quantized values of χ_2 (and, consequently, to quasienergies) within the same quasienergy range: the neighbourhood of the stable fixed points $(L_0 = 0, \psi = \pi/2, 3\pi/2)$, and the region close to $L_0 = 1$. In the semiclassical quantization scheme, these regions are completely decoupled and induce two independent, non-degenerate series of quasienergy levels. Consequently, the complete spectrum exhibits a rather complicated structure, caused by the interleaving of these two series.

[32] A quantum approach based on the pendulum approximation and the Mathieu equation would give a much better prediction for such states.

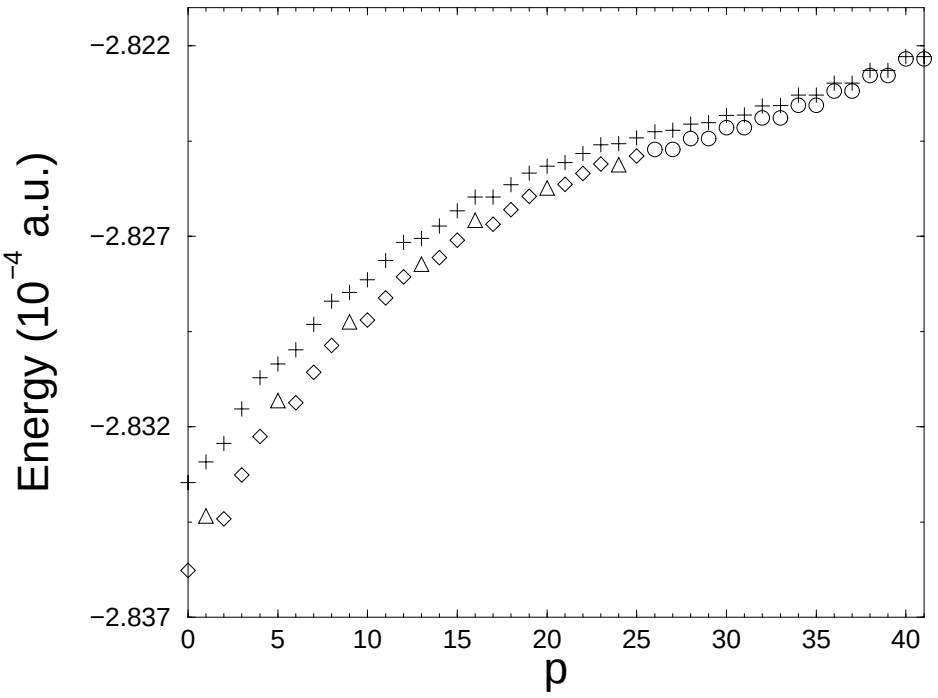

Fig. 46. Comparison of numerically exact quasienergies originating from the $n_0 = 42$ manifold (depicted by pluses) to the semiclassical prediction (open symbols) based on the quantization of the $s = 2$ resonance island (microwave frequency = 2× Kepler frequency), for scaled microwave field $F_0 = 0.04$. Circles correspond to doubly degenerate states localized in the vicinity of maxima of χ_2, around the elliptic fixed points at $(L_0 \simeq 0.65, \psi = 0, \pi)$ in fig. 45. Triangles correspond to almost circular states in the vicinity of the stable minimum at ($L_0 = 1, \psi$ arbitrary), while diamonds correspond to states localized around the stable minima at $L_0 = 0, \psi = \pi/2, 3\pi/2$. The agreement between the semiclassical and quantum energies is very good, provided the size of the resonance island in the $(\hat{I}, \hat{\theta})$ plane is sufficiently large (high lying states in the manifold). For low lying states in the manifold, the discrepancies between quantum and semiclassical results are significant, due to the insufficient size of the island.

As discussed in section 5.1, for a $s : 1$ resonance, in a Floquet zone of width $\omega = s\Omega$, there is not a single manifold of states, but rather a set of s different manifolds approximately identical and separated by Ω. Deviations from the exact ω/s periodicity are due to tunneling [42]. This tunneling process is however *completely* different from the "transverse" one in the (L, ψ) plane described above. It is a case of "longitudinal" tunneling, where the electron jumps from one location on a Kepler orbit to another, shifted along the *same* orbit. This longitudinal tunneling is similar in origin to the tunneling described in section 5.2. It has to be stressed that it represents a general phenomenon in the vicinity of a $s : 1$ resonance (with $s \geq 2$), due to the phase space structure in the $(\hat{I}, \hat{\theta})$ plane, see section 5.1, in contrast to the "transverse" quasi-degeneracy (discussed in fig. 46) due to the specific form of χ_2. Inspecting the numerically exact quantum quasienergy spectrum, we indeed find the manifold

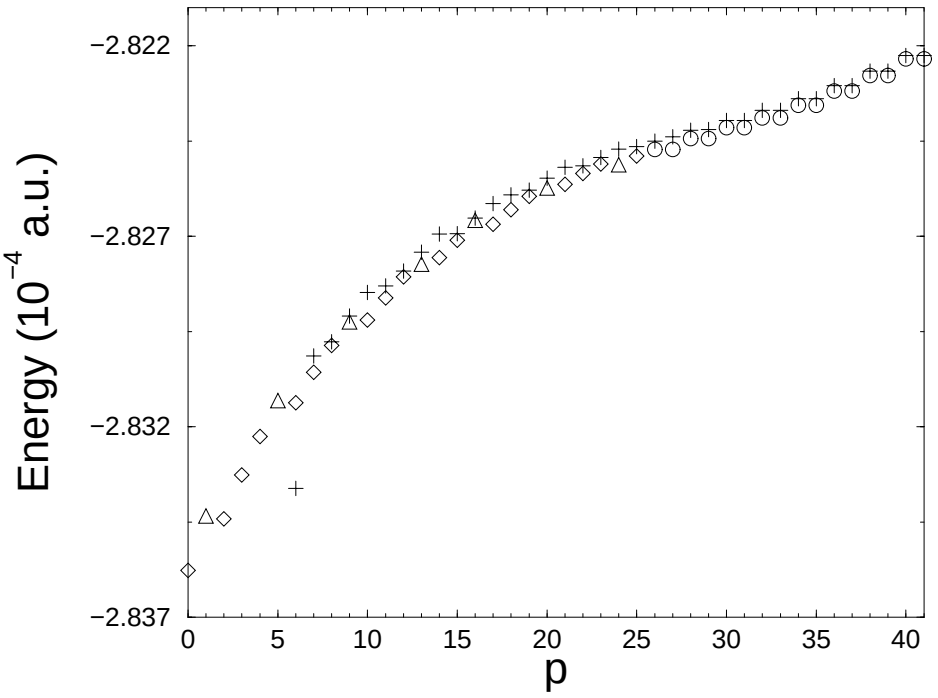

Fig. 47. Same as fig. 46, but for the mirror manifold shifted in energy by $\omega/2$. While, for most states, the agreement with semiclassics is of the same quality as in fig. 46, no quantum data are plotted at the bottom of the manifold. Indeed, at those energies, another Rydberg manifold strongly perturbs the spectrum due to close accidental degeneracy. Consequently, the unambiguous identification of individual states is very difficult.

shown in fig. 47 (compared to the semiclassical prediction). Observe that the agreement between quantum and semiclassical quasienergies is similar to that observed in fig. 46, except for the low lying states. Here, incidentally, the states anchored to the resonance island are strongly perturbed by another Rydberg manifold; proper identification of the individual quantum states is very difficult in this region, and therefore no quantum data are shown at low energies.

Finally, let us consider the localization properties of the wave-functions associated with the upmost states of the manifolds in figs. 46 and 47. These wave-functions should localize in the vicinity of stable trajectories of period 2, i.e. they should be strongly localized, both in angular and orbital coordinates, along an elliptic Kepler orbit of intermediate eccentricity. However, because of the longitudinal quasi-degeneracy, we expect the associated Floquet eigenstates to be composed of two wave-packets on the ellipse, exchanging their positions with period T. Furthermore, due to the transverse quasi-degeneracy, we should have combinations of the elliptic orbits labeled by $\psi = 0$ and $\psi = \pi$. Altogether, this makes four individual wave-packets represented by each Floquet state. Due to the azimuthal symmetry of the problem around the field po-

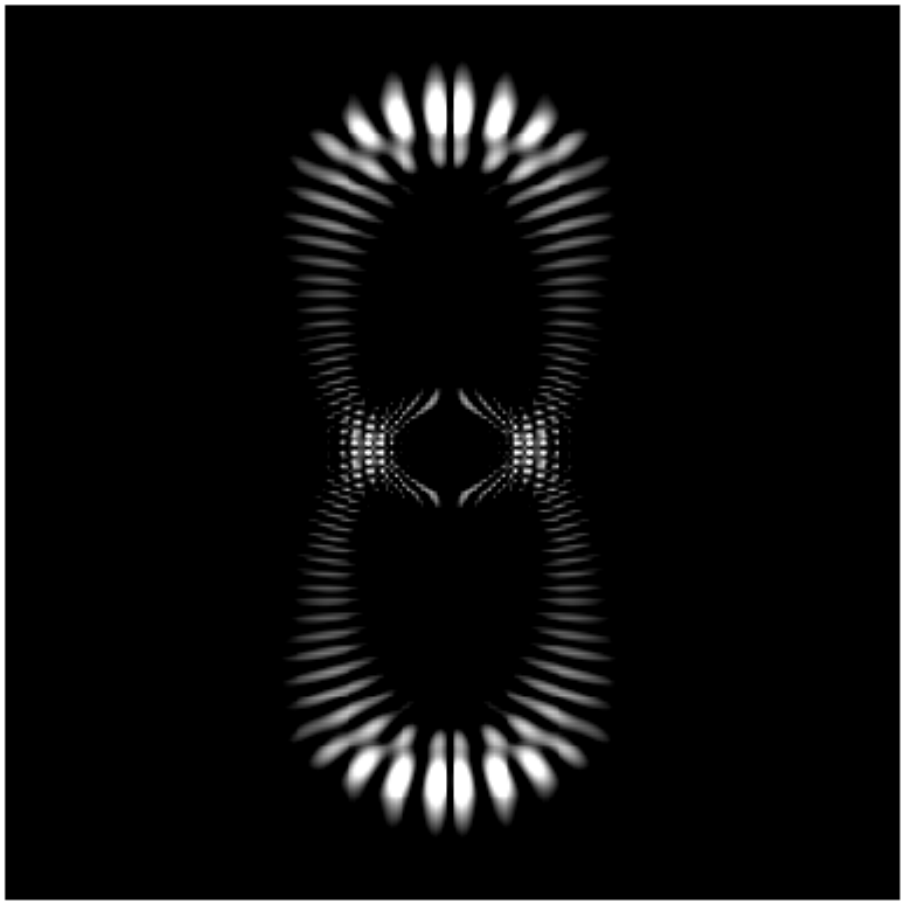

Fig. 48. Electronic density of the upmost eigenstate of the $n_0 = 42$ manifold of fig. 46, averaged over one microwave period. This state presents localization along a pair of Kepler ellipses oriented along the field polarization axis. The box measures ± 3500 Bohr radii in both ρ and z directions, with the nucleus at the center. The microwave polarization axis along z is parallel to the vertical axis of the figure. The orientation and eccentricity of the ellipse are well predicted by the classical resonance analysis.

larization axis, each wave-packet actually is doughnut-shaped (compare fig. 24 for the simpler $s = 1$ case).

Exact quantum calculations fully confirm this prediction. Fig. 48 shows the electronic density of the upmost Floquet state in the $n_0 = 42$ manifold (fig. 46), averaged over one field period. As expected, it is localized along two symmetric Kepler ellipses ($\psi = 0$ and $\psi = \pi$, respectively), but longitudinally delocalized because of the time average. In fact, there are four such Floquet states displaying very similar electronic densities. These are the energetically highest doublet in the $n_0 = 42$ manifold, and the upmost doublet in the "mirror" manifold displayed in fig. 47.

Fig. 49 shows the electronic densities of these four Floquet eigenstates at

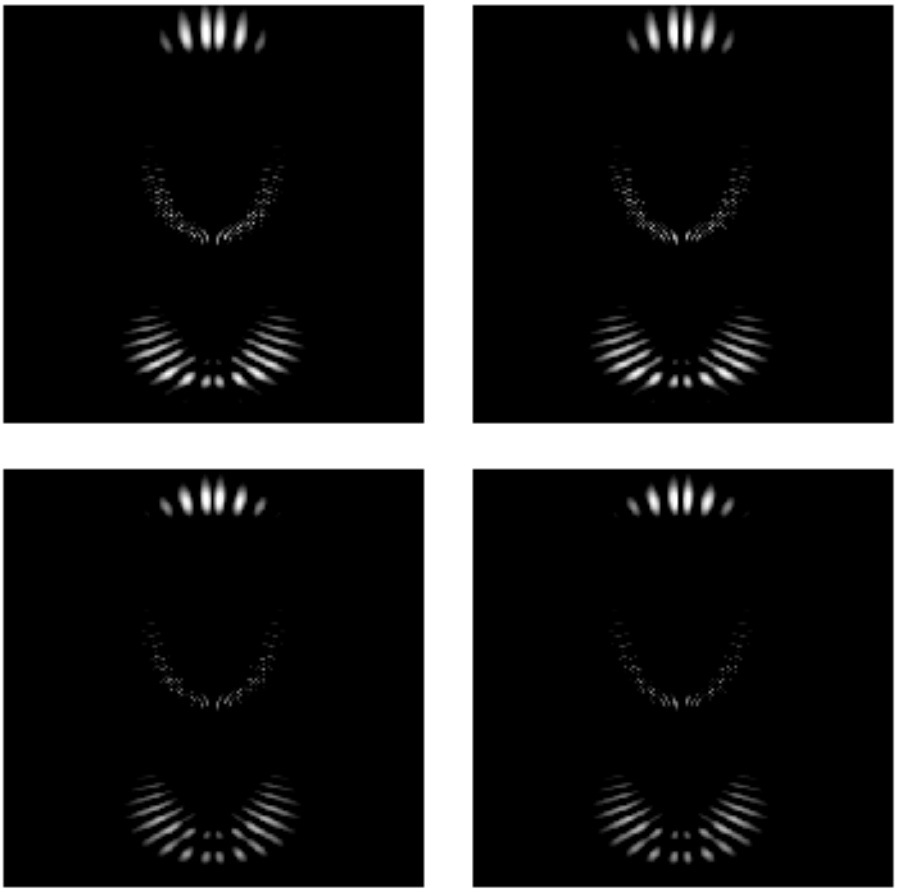

Fig. 49. Electronic densities of the eigenstates of the upmost doublet states (top) of the $n_0 = 42$ manifold of fig. 46, and of their mirror states (bottom), shifted in energy by $\omega/2$ (fig. 47), at driving field phase $\omega t = 0$. The longitudinal localization on the Kepler ellipses (similar for all states) is apparent. On each ellipse, four different individual wave-packets (or rather, due to azimuthal symmetry, two doughnut wave-packets) can be distinguished, propagating along the Kepler ellipse. Notice the phase shift of π in the temporal evolution on the two ellipses, implied by z-inversion. The microwave polarization axis along z is given by the vertical axis of the figure, with the nucleus at the center of the figure.

phase $\omega t = 0$ of the driving field: the four doughnuts are now clearly visible, as well as the orbital and radial localizations along the two elliptic trajectories. Very much in the same way as for a double well potential (or for the bouncer discussed in section 5.2, compare fig. 41), a linear combination of these four states allows for the selection of one single doughnut, localized along one single classical Kepler ellipse. This wave-packet then evolves along this trajectory without dispersion, as demonstrated in fig. 50. Note, however, that this single wave-packet is *not* a single Floquet state, and thus does not exactly repeat itself periodically. It slowly disappears at long times, for at least two reasons: firstly, because of longitudinal and transverse tunneling, the phases of the four Floquet eigenstates accumulate small differences as time evolves, what

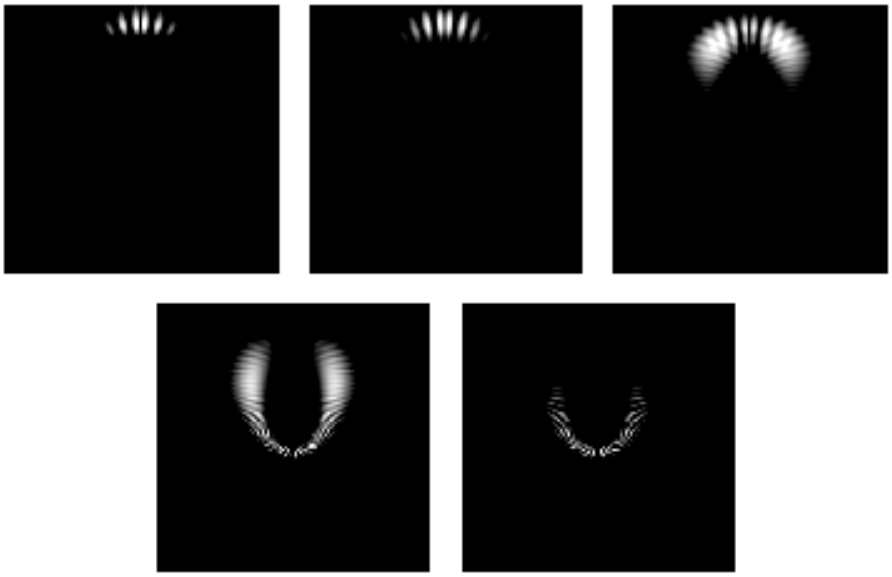

Fig. 50. Temporal evolution of a convenient linear combination of the four eigenstates of fig. 49, for phases $\omega t = 0$ (top left), $\pi/2$ (top center), π (top right), $3\pi/2$ (bottom left), 2π (bottom right) of the driving field. Clearly, a single doughnut propagating along a single trajectory has been selected by the linear combination. This wave-packet essentially repeats its periodic motion with period $2T = 4\pi/\omega$. It slowly disperses, because the four states it is composed of are not exactly degenerate (tunneling effect), and because it ionizes (see sec. 7.1). The microwave polarization axis along z is parallel to the vertical axis of the figure, with the nucleus at the center of the plot.

induces complicated oscillations between the four possible locations of the wave-packet, and secondly, the ionization rates of the individual Floquet states lead to ionization and loss of phase coherence, especially if the ionization rates (see sec. 7.1) of the four states are not equal.

6 Alternative perspectives

There are several known systems where an oscillating field is used to stabilize a specific mode of motion, such as particle accelerators [3], Paul traps [162] for ions, etc. In these cases, the stabilization is a completely classical phenomenon based on the notion of nonlinear resonances. What distinguishes our concept of non-dispersive wave-packets discussed in the preceding chapters from those situations is the necessity to use quantum (or semi-classical) mechanics to describe a given problem, due to relatively low quantum numbers. Still, the principle of localization remains the same, and consists in locking the motion of the system on the external drive. However, it is not essential that the drive be provided externally, it may well be supplied by a (large) part of the system to the (smaller) remainder. Note that, rather formally, also an atom exposed to

a microwave field can be understood as one large quantum system – a dressed atom, see sec. 2 – where the field-component provides the drive for the atomic part [18]. In the present section, we shall therefore briefly recollect a couple of related phase-locking phenomena in slightly more complicated quantum systems, which open additional perspectives for creating non-dispersive wave-packets in the microscopic world.

6.1 Non-dispersive wave-packets in rotating molecules

A situation closely related to atomic hydrogen exposed to CP microwaves (sec. 3.4) is met when considering the dynamics of a single, highly excited Rydberg electron in a rotating molecule [163]. In [51], the following model Hamiltonian has been proposed:

$$H = \frac{\vec{p}^2}{2} - \frac{1}{|\vec{r} + \vec{a}(t)|}, \tag{261}$$

where $\vec{a}(t)$ denotes the position of the center of the Coulomb field w.r.t. the molecular center of mass, and is assumed to rotate in the $x - y$ plane with constant frequency ω:

$$\vec{a}(t) = \begin{pmatrix} \cos\omega t & -\sin\omega t \\ \sin\omega t & \cos\omega t \end{pmatrix} \vec{a}. \tag{262}$$

In the rotating frame, one obtains the Hamiltonian [163]

$$H = \frac{p_x^2 + p_y^2 + p_z^2}{2} - \frac{1}{r} + a\omega^2 x - \omega L_z + \frac{a^2\omega^2}{2}, \tag{263}$$

which, apart from the constant term $a^2\omega^2/2$, is equivalent to the one describing an atom driven by a CP field (compare eq. 184)). Note that the role of the microwave amplitude (which can be arbitrarily tuned in the CP problem) is taken by $a\omega^2$, i.e., a combination of molecular parameters, what, of course, restricts the experimental realization of non-dispersive wave-packets in the molecule to properly selected molecular species [51].

With the help of the stability analysis outlined in sec. 3.4.4, eqs. (185-188), the equilibrium position $x_{\rm eq}$ of the molecular Rydberg electron is easily estimated according to (assuming a small value of a, limited by the size of the molecular core)

$$x_{\rm eq} \simeq (\mathcal{I}/\mathcal{J})^{2/3}, \tag{264}$$

with $\mathcal{I}$ the molecular momentum of inertia, $\mathcal{J} = \omega\mathcal{I}$ the rotational quantum number. To optimize the angular localization of the wave-packet, it is necessary

that $x_{\rm eq}$ be sufficiently large (from sec. 3.2, $x_{\rm eq} \sim n_0^2$, where n_0 is the electronic principal quantum number). Thus, for given $\mathcal{I}$, $\mathcal{J}$ should be small. In [51], a hydrogen-tritium molecule is considered, which yields $n_0 \simeq 18$ for $\mathcal{J} = 1$.

Note, however, that such reasoning is *not* justified. The effective Hamiltonian (261) implies a *classical* description of the molecular rotation (much as the *classical* treatment of the periodic drive in eq. (54), with a well-defined phase) defined by the position vector $\vec{a}(t)$. For such an approach to be valid, $\mathcal{J}$ must be sufficiently large. The molecular rotation plays the role of the microwave field in the analogous CP problem, the number of rotational quanta is just equivalent to the average number of photons defining the amplitude of the (classical) coherent state of the driving field. Clearly, if $\mathcal{J}$ is too small, the effect of an exchange of angular momentum between the Rydberg electron and the core on the *quantum state* of the core (and, hence, on $a\omega^2$ assumed to be constant in eq. (263)) cannot be neglected and, therefore, precludes any semiclassical treatment, see also [68,92]. In other words, if $\mathcal{J}$ is too small, the number of rotational states of the core which are coupled via the interaction is too small to mimic a quasi-classical evolution as suggested by eq. (262).

Nontheless, this caveat does not completely rule out the existence of molecular non-dispersive wave-packets, provided a fast rotation of a core with large momentum of inertia (to render $x_{\rm eq}$ sufficiently large, eq. (264), such that the electronic wave-packet gets localized far away from the molecular core) can be realized, as also suggested in [51].

6.2 Driven Helium in a frozen planet configuration

In the previous examples of non-dispersive wave-packets, the key point has been the generic appearance of a nonlinear resonance for periodically driven quantum systems whose unperturbed dynamics is integrable. A natural question to ask is whether the concept of non-dispersive wave-packets can be generalized to systems which exhibit mixed regular-chaotic dynamics even in the absence of the external perturbation. In the atomic realm, such a situation is realized for the helium atom, where electron-electron interactions provide an additional source of nonlinearity. The corresponding Hamiltonian writes in atomic units

$$H_{\rm He} = \frac{\vec{p}_1^{\,2}}{2} + \frac{\vec{p}_2^{\,2}}{2} - \frac{2}{r_1} - \frac{2}{r_2} + \frac{1}{|\vec{r}_1 - \vec{r}_2|}. \tag{265}$$

As a matter of fact, the classical and quantum dynamics of the three-body Coulomb problem generated by Hamiltonian (265) has been a largely unexplored "terra incognita" until very recently [164], since the dimensionality of the phase space dynamics increases from effectively two to effectively eight

dimensions when a second electron is added to the familiar Kepler problem. Furthermore, the exact quantum mechanical treatment of the helium atom remains a formidable task since the early days of quantum mechanics, and considerable advances could be achieved only very recently, with the advent of modern semiclassical and group theoretical methods [165–168]. Already the classical dynamics of this system exhibits a largely chaotic phase space structure, which typically leads to the rapid autoionization of the associated *doubly excited* quantum states of the atom. One of the major surprises in the analysis of the three body Coulomb problem during the last decades has therefore been the discovery of a new, highly correlated and classically globally stable electronic configuration, the "frozen planet" [169,170]. The appeal of this configuration resides in its counterintuitive, asymmetric character where both electrons are located on the same side of the nucleus. Furthermore, this configuration turns out to be the most robust of all known doubly excited two-electron configurations, in the sense that it occupies a large volume in phase space. Its stability is due to the strong coupling of the two electrons by the $1/|\vec{r}_1 - \vec{r}_2|$ term in the Hamiltonian (265), which enforces their highly correlated motion.

The frozen planet is an ideal candidate to test the prevailance of the concept of nondispersive wave-packets in systems with intrinsically mixed dynamics. In a recent study [171,110,172,173] the response of this highly correlated two-electron configuration to a periodic force has been investigated from a classical and from a quantum mechanical point of view. The Hamiltonian for the driven problem writes, in the length gauge,

$$H = H_{\mathrm{He}} + F\cos(\omega t)(z_1 + z_2). \tag{266}$$

Guided by the experience on non-dispersive wave-packets in one electron Rydberg states, the driving frequency ω was chosen near resonant with the natural frequency $\Omega_{\mathrm{FP}} \approx 0.3 n_i^{-3}$ of the frozen planet, where n_i denotes the principal quantum number of the inner electron. It was found that, for a suitably chosen driving field amplitude F, a nonlinear resonance between the correlated electronic motion and the external drive can be induced in the classical dynamics, at least for the collinear frozen planet where the three particles (two electrons and the nucleus) are aligned along the polarization axis of the driving field.

However, contrary to the situation for the driven hydrogen atom discussed in sections 3.3.1 and 3.3.2, there is a fundamental difference between the one dimensional model of the driven three body Coulomb problem and the full 3D problem. For the one-electron system, we have seen that the classical Kepler ellipse performs a slow precession in the angular variables, though remains bounded and does not ionize. In contrast, if one permits deviations from collinearity in the driven frozen planet dynamics, it is found that the transverse direction is generally unstable and leads to rapid ionization. This

transverse ionization is simply due to the fact that the external field destroys the intricate electron electron correlation which creates the unperturbed frozen planet. Notwithstanding, it has been shown that the application of an additional, weak static electric field allows to compensate for the transverse instability, and to establish a classically globally stable dynamical situation for the frozen planet. The transverse confinement through the static field again justifies the collinear model, and first quantum calculations performed for this restricted model show the existence of a wave-packet associated with the principal resonance between the frozen planet orbit and the driving field, which faithfully traces the classical trajectory at the period of the drive. As for driven one-electron systems, these nondispersive two-electron wave-packets exhibit life times of typically 10^6 driving field periods [33].

Hence, there is strong evidence that a resonant external forcing allows for the creation of quantum eigenstates with a quasi-classical temporal evolution, even in the presence of strong two-particle correlations.

6.3 Non-dispersive wave-packets in isolated core excitation of multielectron atoms

Another example of non-dispersive wave-packets in a two-component atomic system has recently been proposed for two-electron atoms [174–176]. The scheme uses an isolated-core excitation in which one of the electrons is transfered to a Rydberg trajectory by a *short* laser pulse, forming an initially well-localized wave-packet. A second source *continuously* drives a transition between two discrete states of the remaining atomic core. The latter induces Rabi oscillations (or a coherent superposition) between two Rydberg series to which the first electron is excited. If the Rabi frequency (controlled by the continuous drive of the core) is matched with the Kepler frequency of the orbit of the outer electron, the autoionization rate of the latter may be strongly suppressed, provided the respective phases are also matched properly: if the electron approaches its inner turning radius (where the configuration-interaction between Rydberg electron and core – leading to autoionization – is strongest) while the core is in its ground state, autoionization becomes impossible since the configuration-interaction does not compensate for the ionization potential of the Rydberg electron. On the other hand, when the electron is far from the nucleus (and electron-electron interaction is weak), the core may be in its excited state, without ejecting the Rydberg electron.

[33] Again, in contrast to the driven one electron problem, nothing guarantees that the life times obtained for the 1D model carry over to the real 3D object. On the contrary, first results on the bare 3D Coulomb problem [173] indicate a strong dependence of the life times on the dimension of the accessible configuration space.

Consequently, autoionization is supressed for the center of the Rydberg wave-packet. During time evolution, however, the wave-packet spreads, its head and its tail desynchronize with the Rabi evolution of the core, and eventually approach the region close to the nucleus (where configuration-interaction is most pronounced) when the core is not in its ground state. Then these parts of the wave-packet autoionize, and the remaining Rydberg population is reshaped into a localized wave-packet, since the spreading tails have been chopped off. Hence, these wave-packets exhibit a rather rapid "melting" (on a time scale of at most some hundred Kepler periods) – to be compared to hundreds of thousands or even more Kepler cycles performed by non-dispersive wave-packets in microwave driven hydrogen atoms studied above (which also ionize, however *very slowly*, see sec. 7.1).

The present scenario is in some sense reminiscent of the one in sec. 6.1, with a (quantum) two-level core replacing the rotating molecular core. As mentioned above, a two-level system alone can only exchange one quantum with the the outer electron and thus cannot provide an exact phase locking mechanism for the highly excited Rydberg electron. However, the two-level core is here *driven* by an external electromagnetic field and consequently gains an additional degree of freedom which can be used for the phase locking mechanism. The drawback is that this phase locking implies losses (through autoionization). Nevertheless, the quasi-classical evolution over ~ 100 Kepler cycles is still quite impressive, and presumably stems from the relatively sharp confinement of efficient configuration-interaction within a spatial region close to the inner turning point of the Rydberg wave-packet.

7 Characteristic properties of non-dispersive wave-packets

After presenting several examples of non-dispersive wave-packets in the previous chapters, we now study their specific properties in more detail. Especially, several important physical processes which may affect the existence of wave-packets have so far been hidden under the carpet [177]. The two most important ones, at least for driven atoms, are ionization and spontaneous emission, and they will be discussed in detail below. First, let us briefly discuss the general properties of wave-packet eigenstates under the variation of various parameters of the driven system (e.g., microwave amplitude and frequency, the strength of an external static field, etc.).

Atoms driven by microwaves will eventually ionize. Therefore, the non-dispersive wave-packet states discussed up till now cannot be, rigorously speaking, discrete states, they are rather resonances [23] with some finite life-times. Importantly, as we shall discuss in detail below, these life-times may be extremely long, of the order of millions of microwave periods. In that sense, they are comparable to those of highly excited atomic Rydberg states, which also decay, by spontaneous emission, on time scales of few millions of classical periods. Even more importantly, the life-times of the non-dispersive wave-packets are typically orders of magnitude larger than the life-times of other states in the Floquet spectrum: the wave-packets are particularly resistant to ionization. This is due to the classical confinement of the electron inside the regular island. To ionize, the electron has no other option but to tunnel out of the classically confining island, before gaining energy by diffusive excitation [131]. The resonance island is strictly confining only for a one-dimensional system. For multi-dimensional systems, the tori in the resonance islands are not fully isolating and a very slow classical diffusion process might eventually lead to ionization. This, however, takes place on extremely long time scales and is completely negligible in atomic systems. In practice, ionization of the wave-packet is essentially mediated by a pure quantum process, exponentially unlikely in the semiclassical limit. As we shall see below, this tunneling process has quite interesting properties which may be quantitatively described for microwave driven atoms. More details can be found in [50,65,66].

Due to the initial tunneling step, the life-times of non-dispersive wave-packets will typically be much longer than those of Floquet states localized in the chaotic sea surrounding the island [145]. Moreover, since the ionization mechanism involves chaotic diffusion, many quantum mechanical paths link the initial wave-packet to the final continuum. Thus, the life-time of the wave-packet will reflect the interferences between those different possible paths, and will sensitively depend on parameters such as the microwave frequency or amplitude, that affect the interfering paths through the chaotic sea. These fluctuations, reported first in [50], are perfectly deterministic and resemble the conductance fluctuations observed in mesoscopic systems [178] . In fig. 51, we show the fluctuations of the ionization rate (width) of the non-dispersive wave-packet of the two dimensional hydrogen atom in a circularly polarized microwave field. The energy levels and widths are obtained as explained in sec. 3.2, by numerical diagonalization of the complex rotated Hamiltonian. All the data presented in this section have been obtained in the regime where the typical ionization rate is smaller than the mean energy spacing between consecutive levels, so that the ionization can be thought as a small perturbation acting on bound states. The width (although very small) displays strong fluctuations over several orders of magnitude. Similarly, the real part of the

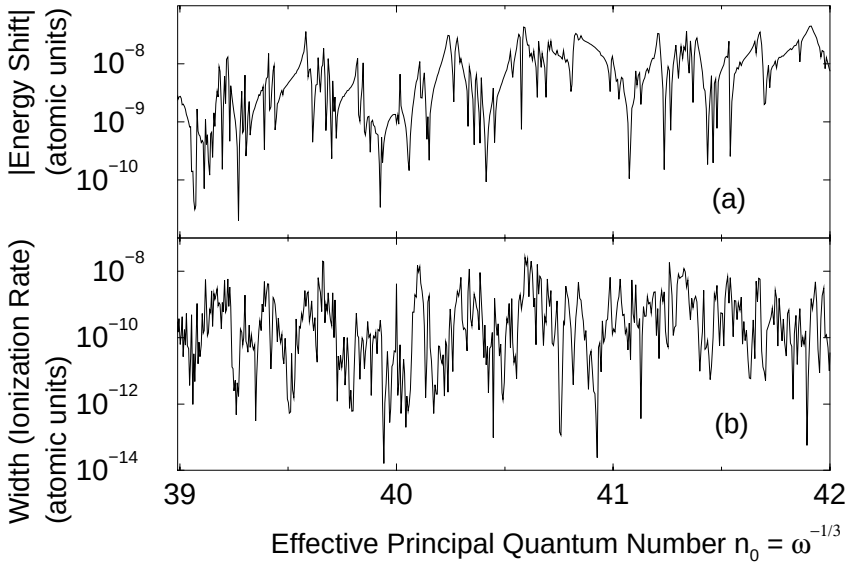

Fig. 51. Typical fluctuations of the width (ionization rate) and of the energy (with respect to its averaged, smooth behavior) of the non-dispersive wave-packet of a two-dimensional hydrogen atom in a circularly polarized microwave field. The data presented are obtained for small variations of the effective principal quantum number $n_0 = \omega^{-1/3}$ around 40, and a scaled microwave electric field $F_0 = 0.0426$. To show that the fluctuations cover several orders of magnitude, we use a logarithmic vertical scale, and plot the absolute value of the shift.

energy (i.e., the center of the atomic resonance) displays wild fluctuations. The latter can be observed only if the smooth variation of the energy level with the control parameter (following approximately the semiclassical prediction given by eq. (174)) is substracted. Therefore, we fitted the numerically obtained energies by a smooth function and substracted this fit to obtain the displayed fluctuations. Note that these fluctuations are so small that an accurate fit is needed [34]. This can be easily seen in fig. 30 where, on the scale of the mean level spacing, these fluctuations are invisible by eye (the level appears as a straight horizontal line).

The explanation for the fluctuations is the following: in a quantum language, they are due to the coupling between the localized wave-packet and states localized in the chaotic sea surrounding the resonance island. While the energy of the wave-packet is a smooth function of the parameters F and ω, the energies of the chaotic states display a complicated behavior characterized by level repulsion and large avoided crossings. It happens often that – for some parameter values – there is a quasi-degeneracy between the wave-packet eigenstate and a chaotic state, see the numerous tiny avoided crossings in fig. 30. There, the two states are efficiently mixed, the wave-packet captures some part of the coupling of the chaotic state to the continuum and its ionization

[34] In particular, the semiclassical expression is not sufficiently accurate for such a fit.

width increases (see also [145]). This is the very origin of the observed fluctuations. Simultaneously, the chaotic state repels the wave-packet state leading to a deviation of the energy from its smooth behavior, and thus to the observed fluctuations. This mechanism is similar to "chaos assisted tunneling", described in the literature [179–189] for both, driven one-dimensional and two-dimensional autonomous systems. There, the tunneling rate between two symmetric islands – which manifests itself through the splitting between the symmetric and antisymmetric states of a doublet – may be strongly enhanced by the chaotic transport between the islands. We have then a "regular" tunneling escape from one island, a chaotic diffusive transport from the vicinity of one island to the other (many paths, leading to interferences and resulting in large fluctuations of the splitting), and another "regular" tunneling penetration into the second island. In our case, the situation is even simpler – we have a "regular" tunneling escape supplemented by a chaotic diffusion and eventual ionization. Thus, instead of the level splitting, we observe a shift of the energy level and a finite width.

Since these fluctuations stem from the coupling between the regular wave-packet state and a set of chaotic states, it is quite natural to model such a situation via a Random Matrix model [65], the approach being directly motivated by a similar treatment of the tunneling splitting in [187]. For details, we refer the reader to the original work [65]. It suffices to say here that the model is characterized by three real parameters: σ – which characterizes the mean strength of the coupling between the regular state and the chaotic levels, γ – which measures the decay of the chaotic states (due to ionization; direct ionization transitions from the wave-packet state to the continuum are negligible), and Δ – which is the mean level spacing of chaotic levels. The two physically relevant, dimensionless parameters are γ/Δ and σ/Δ. In the perturbative regime ($\gamma/\Delta, \sigma/\Delta \ll 1$) it is possible to obtain analytical [65] predictions for the statistical distribution of the energy shifts $P(s)$ (of the wave-packet's energy from its unperturbed value) and for the distribution of its widths $P(\Gamma)$. $P(s)$ turns out to be a Cauchy distribution (Lorentzian), similarly to the tunneling splitting distribution found in [187]. The distribution of the widths is a bit more complicated (it is the square root of Γ which is approximately Lorentzian distributed). The perturbative approach fails for the asymptotic behavior of the tails of the distributions, where an exponential cut-off is expected and observed in numerical studies [65,187]. By fitting the predictions of the Random Matrix model to the numerical data of fig. 51, we may finally extract the values of γ/Δ, the strength of the decay, and of σ/Δ, the coupling between the regular and the chaotic states. An example of such a fit is shown in fig. 52. The numerical data are collected around some mean values of n_0 and F_0, typically 1000 data points were used for a single fit [65]. This allowed us to study the dependence of the parameters $\gamma/\Delta, \sigma/\Delta$ on n_0 and F_0. The dependence on n_0 is shown in fig. 53. Clearly, the tunneling rate σ/Δ decreases *exponentially* with n_0. Since n_0 is the inverse of the effective Planck

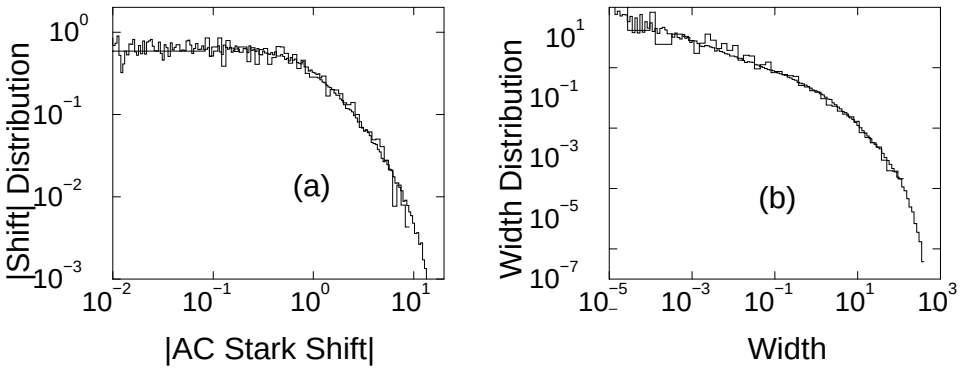

Fig. 52. The distribution of energy shifts (a) and ionization widths (b) for the non-dispersive wave-packet of a two-dimensional hydrogen atom in a circularly polarized field, obtained by numerical diagonalization of the Hamiltonian (large bins), compared to the random matrix model (small bins). Both distributions are shown on a double logarithmic scale to better visualize the behavior over a large range of shift and width values. Since the energy shift may be positive or negative, we show the distribution of its modulus. The random matrix model fits very well the numerical results, with both distributions showing regions of algebraic behavior followed by an exponential cut-off.

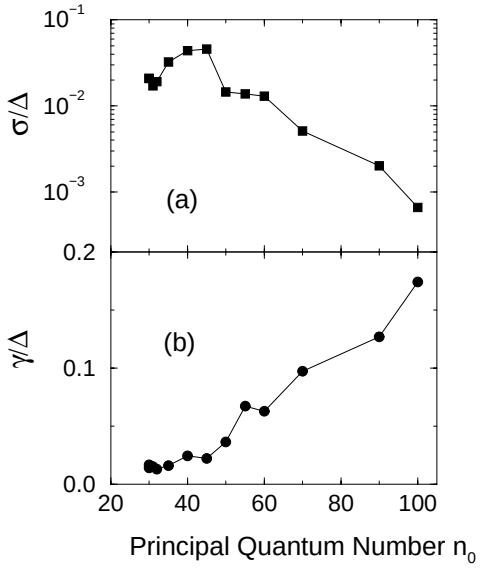

Fig. 53. Effective tunneling rate σ/Δ of the wave-packet (a), as a function of the effective quantum number $n_0 = \omega^{-1/3}$ (the inverse of the effective Planck constant), for fixed classical dynamics, $F_0 = 0.0426$. Note the exponential decrease for sufficiently high n_0 (the vertical scale is logarithmic). The corresponding effective chaotic ionization rate γ/Δ (b) smoothly increases with n_0, approximately as n_0^2.

constant in our problem (see the discussion in section 3.3.1 and eq. (147)), this shows that

$$\sigma/\Delta \propto \exp\left(-\frac{S}{\hbar_{\text{eff}}}\right), \tag{267}$$

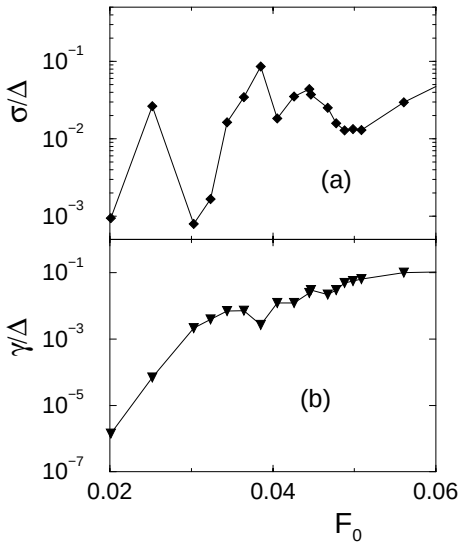

Fig. 54. The tunneling rate σ/Δ (panel (a)) and the chaotic ionization rate γ/Δ (panel (b)), as a function of the scaled microwave amplitude F_0, for wave-packet eigenstates of a two-dimensional hydrogen atom in a circularly polarized microwave field. Observe the oscillatory behavior of the tunneling rate. The bumps are due to secondary nonlinear resonances in the classical dynamics of the system.

where S, corresponding to some effective imaginary action [188], is found to be given for our specific choice of parameters by $S \simeq 0.06 \pm 0.01$ (as fitted from the plot). Such an exponential dependence is a hallmark of a tunneling process, thus confirming that the wave-packets are strongly localized in the island and communicate with the outside world via tunneling. The n_0 dependence of the dimensionless chaotic ionization rate γ/Δ is very different: it shows a slow, algebraic increase with n_0. A simple analysis based on a Kepler map [131] description would yield a linear increase with n_0, whereas our data seem to suggest a quadratic function of n_0. This discrepancy is not very surprising, bearing in mind the simplicity of the Kepler map approach.

Similarly, we may study, for fixed n_0, the dependence of γ/Δ and σ/Δ on F_0, i.e. on the microwave field strength. Such studies, performed for both linear and circular polarizations, have indicated that, not very surprisingly, the chaotic ionization rate γ/Δ increases rather smoothly with the microwave amplitude F_0. On the other hand, the tunneling rate σ/Δ shows pronounced non-monotonic variations with F_0, see fig. 54. This unexpected behavior can nontheless be explained [65]. The bumps in σ/Δ occur at microwave field strengths where secondary nonlinear resonances emerge within the resonance island in classical phase space. For circular polarization, this corresponds to some resonance between two eigenfrequencies ω_+ and ω_- (see sec. 3.4 and figs. 30,59) of the dynamics in the classical resonance island. Such resonances strongly perturb the classical dynamics and necessarily affect the quantum transport from the island.

Let us stress finally that, even for rather strong microwave fields (say $F_0 = 0.05$), where most of the other Floquet states have life-times of few tens or hundreds of microwave periods, and irrespective of the polarization of the driving field or of the dimension of the accessible configuration space (1D, 2D or 3D), the life-time (modulo fluctuations) of a non-dispersive wave-packet is typically of the order of 10^5 Kepler periods, for $n_0 \simeq 60$. This may be used for their possible experimental detection, see section 8.4.

7.2 Radiative properties

So far, we have considered the interaction of the atom with the coherent driving field only. However, this is not the full story. Since the driving field couples excited atomic states, it remains to be seen to which extent spontaneous emission (or, more precisely, the coupling to other, initially unoccupied modes of the electromagnetic field) affects the wave-packet properties. This is very important, since the non-dispersive wave-packets are supposed to be long living objects, and spontaneous emission obviously limits their life-time. Furthermore, we have here an example of decoherence effects due to interaction with the environment. More generally, the interaction of non-dispersive wave-packets with an additional weak external electromagnetic field may provide a useful tool to probe their properties. In particular, their localization within the resonance island implies that an external probe will couple them efficiently only to neighboring states within the island. In turn, that should make their experimental characterization easy and unambiguous. Of course, external drive (microwave field) and probe must not be treated on the same footing. One should rather consider the atom dressed by the external drive as a strongly coupled system, or use the Floquet picture described above, and treat the additional mode(s) of the probe (environment) as a perturbation. We first start with the simplest situation, where a single mode of the environment is taken into account.

7.2.1 Interaction of a non-dispersive wave-packet with a monochromatic probe field

Let us first consider the addition of a monochromatic probe field of frequency ω_p. The situation is very similar to the probing of a time-independent system by a weak monochromatic field, with the only difference that the Floquet Hamiltonian replaces the usual time-independent Hamiltonian. Thus, the weak probe field may induce a transition between two Floquet states if it is *resonant* with this transition, i.e. if $\hbar\omega_p$ is equal to the quasi-energy difference between the two Floquet states. According to Fermi's Golden Rule, the transition probability is proportional to the square of the matrix element coupling the initial

Floquet state $|\mathcal{E}_i\rangle$ to the final one $|\mathcal{E}_f\rangle$.

Using the Fourier representation of Floquet states,

$$|\mathcal{E}(t)\rangle = \sum_k \exp(-ik\omega t)|\mathcal{E}^k\rangle, \tag{268}$$

and averaging over one driving field cycle $2\pi/\omega$ we get

$$\langle\mathcal{E}_f|\mathcal{T}|\mathcal{E}_i\rangle = \sum_{k=-\infty}^{\infty} \langle\mathcal{E}_f^k|\mathcal{T}|\mathcal{E}_i^k\rangle. \tag{269}$$

$\mathcal{T}$ denotes the transition operator, usually some component of the dipole operator depending on the polarization of the probe beam. If the quasi-energy levels are not bound states but resonances with finite life-time (for example because of multiphoton transition amplitudes to the continuum) this approach is easily extended [18], yielding the following expression for the photoabsorption cross-section of the probe field at frequency ω_p:

$$\sigma(\omega_p) = \frac{4\pi\omega_p\alpha}{c}\mathrm{Im}\sum_f |\langle\mathcal{E}_f|\mathcal{T}|\mathcal{E}_i\rangle|^2 \left[\frac{1}{\mathcal{E}_f - \mathcal{E}_i - \omega_p} + \frac{1}{\mathcal{E}_f - \mathcal{E}_i + \omega_p}\right] \tag{270}$$

where α is the fine structure constant, and where $\mathcal{E}_f$ and $\mathcal{E}_i$ are the complex energies of the initial and final Floquet states. The sum extends over all the Floquet states of the system. Although the Floquet energy spectrum is itself ω-periodic (see sec. 3.1.2), this is *not* the case for the photoabsorption cross-section. Indeed, the Floquet states at energies $\mathcal{E}_f$ and $\mathcal{E}_f + \omega$ have the same Fourier components, but shifted by one unit in k, resulting in different matrix elements. The photoabsorption spectrum is thus composed of series of lines separated by ω with unequal intensities. When the driving is weak, each Floquet state has a dominant Fourier component. The series then appears as a dominant peak accompanied by side bands shifted in energy by an integer multiple of the driving frequency ω. In the language of the scattering theory [18,23,24], these side bands can be seen as the scattering of the probe photon assisted by one or several photons of the drive. In any case, the Floquet formalism is well suited, since it contains this weak driving regime as a limiting case, as well as the strong driving regime needed to generate a non-dispersive wave-packet.

7.2.2 Spontaneous emission from a non-dispersive wave-packet

We now address the situation where no probe field is added to the microwave field. Still, photons of the driving field can be scattered in the (initially empty) remaining modes of the electromagnetic field. This is thus some kind of spontaneous emission or rather resonance fluorescence of the atom under coherent driving. It can be seen as spontaneous emission of the dressed atom, where

an initial Floquet state decays spontaneously to another Floquet state with a lower quasi-energy, the energy difference being carried by the spontaneous photon. As an immediate consequence, the spectrum of the emitted photons is composed of the resonance frequencies of the Floquet system, the same that are involved in eq. (270). The decay rate along a transition depends on the dipole matrix element connecting the initial and the final states, but also on the density of modes for the emitted photons. If we consider, for simplicity, the case of free atoms, one obtains:

$$\Gamma_{if} = \frac{4\alpha^3(\mathcal{E}_i - \mathcal{E}_f)^3}{3}|\langle\mathcal{E}_f|\mathcal{T}|\mathcal{E}_i\rangle|^2 \tag{271}$$

where $\mathcal{E}_i - \mathcal{E}_f$ is the positive energy difference between the initial and final Floquet states. As the matrix element of the dipole operator $\mathcal{T}$ is involved, clearly the localization properties of the Floquet states will be of primordial importance for the spontaneous emission process.

The total decay rate (inverse of the life-time) of a state $|\mathcal{E}_i\rangle$ is obtained by summing the partial rates Γ_{if} connecting the initial state to all states with lower energy. It is not straightforward to determine which Floquet states contribute most to the decay rate – the two factors in eq. (271) compete: while $|\langle\mathcal{E}_f|\mathcal{T}|\mathcal{E}_i\rangle|^2$ tends to favor states localized close to the initial state (maximum overlap), the factor $(\mathcal{E}_i - \mathcal{E}_f)^3$ (due to the density of modes in free space) favors transitions to much less excited states. Which factor wins depends on the polarization of the driving field.

7.2.3 Circular Polarization

Consider first a circularly polarized microwave field. A first analysis of spontaneous emission has been given in [59], where the rotating frame (see sec. 3.4) approach was used. The driven problem becomes then time-independent, and the analysis of spontaneous emission appears to be simple. This is, however, misleading, and it is quite easy to omit some transitions with considerable rate. The full and correct analysis, both in the rotating and in the standard frame [68], discusses this problem extensively. The reader should consult the original papers for details.

A crucial point is to realize that the Floquet spectrum of the Hamiltonian in CP splits into separate blocks, all of them being identical, except for a shift by an integer multiple of the driving frequency ω. Each block corresponds to a fixed quantum number $\kappa = k + M$ where k labels the photon block (Fourier component) in the Floquet approach, while M is the azimutal quantum number. This merely signifies that the absorption of a driving photon of circular polarization σ^+ increases M by one unit. In other words, κ is nothing but the total angular momentum (along the direction of propagation of the mi-

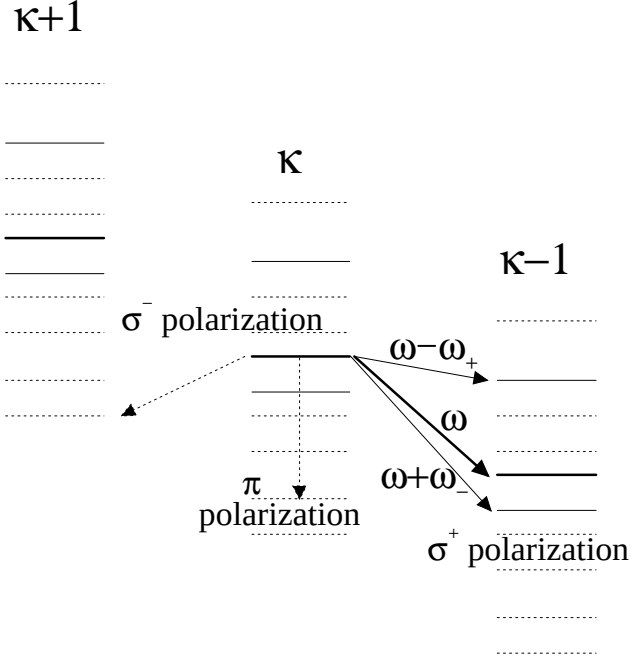

Fig. 55. Spontaneous emission transitions for the non-dispersive wave-packet of an atom in a circularly polarized microwave field. The quasi-energy levels of the Floquet Hamiltonian can be split in series labelled by κ (total angular momentum of the atom and of the microwave field). The various series are identical, except for an energy shift equal to an integer multiple of the microwave frequency ω. The arrows indicate possible spontaneous transitions leaving the initial state $|0,0,0\rangle$. Only arrows drawn with solid lines are allowed in the harmonic approximation. The position of the $|0,0,0\rangle$ wave-packet in each Floquet ladder is indicated by the fat lines.

crowave field) of the entire system comprising the atom and the driving field. The separate κ blocks are coupled by spontaneous emission. Since, again, the spontaneously emitted photon carries one quantum of angular momentum, spontaneous emission couples states within the same κ-block (for π polarization of the emitted photon w.r.t. the z axis, which leaves M invariant) or in neighboring κ-blocks $\kappa' = \kappa \pm 1$ (see fig. 55). σ^+ polarization of the emitted photon gives rise to higher frequency photons since – for the same initial and final Floquet states – the energy difference in the σ^+ channel is larger by $\hbar\omega$ than in the π channel (and by $2\hbar\omega$ than in the σ^- channel), as immediately observed in fig. 55. As the emission rate, eq. (271), changes with the cubic power of the energy difference, spontaneous photons with σ^+ polarization are expected to be dominant.

In the absence of any further approximation, the spontaneous emission spectrum is fairly complicated - it consists of three series with different polarizations, $\sigma^\pm$ and π. We may use, however, the harmonic approximation, discussed in detail in sec. 3.4. The Floquet states localized in the vicinity of the stable fixed point may be labelled by three quantum numbers $|n_+, n_-, n_z\rangle$, corresponding to the various excitations in the normal modes. The non-dispersive

wave-packet we are most interested in corresponds to the ground state $|0,0,0\rangle$. The dipole operator (responsible for the spontaneous transition) may be expressed as a linear combination of the creation and annihilation operators in these normal modes. Consequently, we obtain strong selection rules for dipole transitions between $|n_+, n_-, n_z\rangle$ states belonging to different ladders (at most $\Delta n_i = 0, \pm 1$ with not all possibilities allowed – for details see [68]). The situation is even simpler for $|0,0,0\rangle$, which may decay only via three transitions, all σ^+ polarized (i.e., from the κ block to the $\kappa - 1$ block):

– a transition to the $|0,0,0\rangle$ state in the $\kappa-1$ block. By definition, this occurs precisely at the microwave frequency of the drive. One can view this process as elastic scattering of the microwave photon;
– a transition to the state $|1,0,0\rangle$, at frequency $\omega - \omega_+$;
– a transition to the state $|0,1,0\rangle$, at frequency $\omega + \omega_-$.

In the harmonic approximation, explicit analytic expressions can be obtained for the corresponding transition rates [68]. It suffices to say here that in the semiclassical limit the elastic component becomes dominant, since its intensity scales as $\omega^{5/3}$, while the intensities of the other two components are proportional to ω^2, i.e., are typically weaker by a factor $n_0 = \omega^{-1/3}$. This implies that the non-dispersive wave-packet decays exclusively (in the harmonic approximation) to its immediate neighbor states, emitting a photon with frequency in the microwave range, comparable to the driving frequency. Direct decay to the atomic $|n = 1, L = M = 0\rangle$ ground state or to weakly excited states of the system is forbidden by the selection rules of the dipole operator. This is easily understood: the CP nondispersive ground state wave-packet $|0,0,0\rangle$ is built essentially from states with large angular momentum (of the order of n_0), and as it can lose only one unit of angular momentum per spontaneous emission event, it can decay only to similar states. When the harmonic approximation breaks down, additional lines may appear, but, for the same reason, in the microwave range only. Another important observation is that the inelastic component at $\omega+\omega_-$ is by far stronger than the one at $\omega-\omega_+$. This is entirely due to the cubic power of the transition frequency entering the expression for the rate (271). Note the sign difference, due to the sign difference between $\pm$ modes in the harmonic hamiltonian, eq. (197).

In the semiclassical limit $\omega = n_0^{-3} \to 0$, the decay is dominated by the elastic component, and the total decay rate is [68]:

$$\Gamma = \frac{2\alpha^3 \omega^{5/3} q^{-2/3}}{3}, \tag{272}$$

what, multiplied by the energy ω of the spontaneous photon, gives the energy

loss due to spontaneous emission:

$$\frac{dE}{dt} = \frac{2\alpha^3\omega^{8/3}q^{-2/3}}{3} = \frac{2\alpha^3\omega^4|x_{\rm eq}|^2}{3}, \tag{273}$$

where we used eq. (186). This is nothing but the result obtained from classical electrodynamics [190] for a point charge moving on a circular orbit of radius $|x_{\rm eq}|$ with frequency ω. Since the charge loses energy, it cannot survive on a circular orbit and would eventually fall onto the nucleus following a spiral trajectory. This model stimulated Bohr's original formulation of quantum mechanics. Let us notice that the non-dispersive wave-packet is the first physical realization of the Bohr model. There is no net loss of energy since, in our case, the electron is driven by the microwave field and an emission at frequency ω occurs in fact as an elastic scattering of a microwave photon. Thus the non-dispersive wave-packet is a cure of the long-lasting Bohr paradox.

Figure 56 shows the square of the dipole matrix elements connecting the non-dispersive wave-packet, for $n_0 = 60$ (i.e., microwave frequency $\omega = 1/60^3$) and scaled microwave field $F_0 = 0.04446$, to other Floquet states with lower energy. These are the results of an exact numerical diagonalization of the full Floquet Hamiltonian. They are presented as a stick spectrum because the widths of the important lines are very narrow on the scale of the figure, which is given as a function of the energy difference between the initial and the final state, that is the frequency of the scattered photon. Thus, this figure shows the lines that could be observed when recording the photoabsorption of a weak microwave probe field. As expected, there is a dominant line at the frequency ω of the microwave, and two other lines at frequencies $\omega-\omega_-$ and $\omega+\omega_+$ with comparable intensities, while all other lines are at least 10 times weaker. This means that the harmonic approximation works here very well; its predictions, indicated by the crosses in the figure, are in good quantitative agreement with the exact result (apart from tiny shifts recognizable in the figure, which correspond to the mismatch between the exact and the semiclassical energies observed in figs. 30 and 59). This is not completely surprising as the energy levels themselves are well reproduced by this harmonic approximation, see sec. 3.4.4. However, the photoabsorption spectrum probes the *wave-functions* themselves (through the overlaps) which are well known to be much more sensitive than the energy levels. The good agreement for both the energy spectrum and the matrix elements is a clear-cut proof of the reliability of the harmonic approximation for physically accessible principal quantum numbers, say $n_0 < 100$; in fact, it is good down to $n_0 \simeq 30$, and the non-dispersive wave-packet exists even for lower n_0 values (e.g. $n_0 = 15$ in [49]) although the harmonic approximation is not too good at such low quantum numbers. There were repeated claims in the literature [30,44,46,54,62,144] that the stability island as well as the effective potential are necessarily unharmonic in the vicinity of the equilibrium point, and that the unharmonic terms will destroy the stability of the non-dispersive wave-packets. The present results prove that

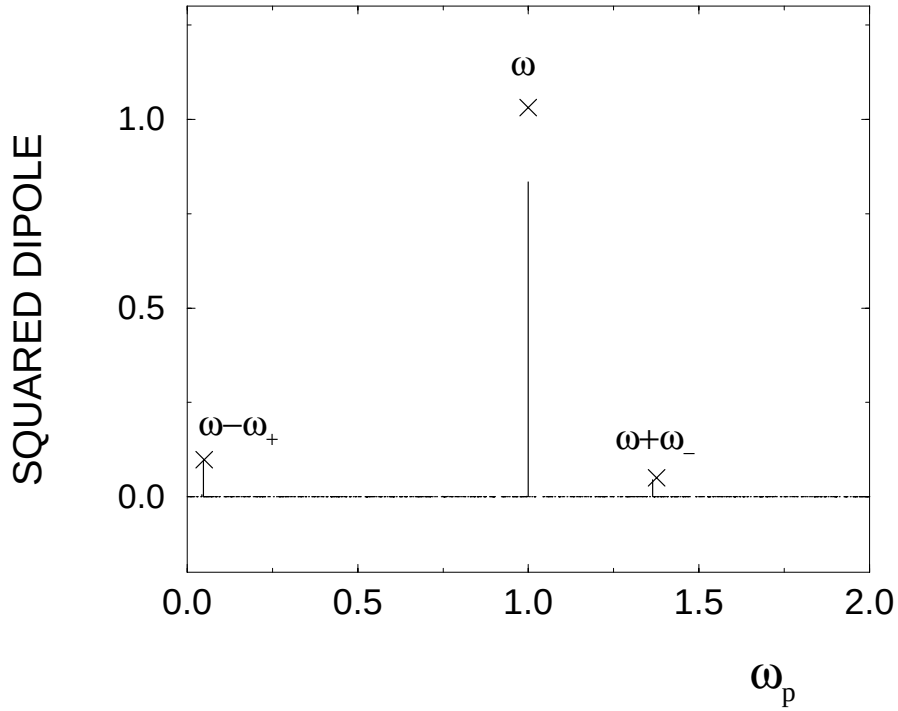

Fig. 56. Square of the dipole matrix element (scaled w.r.t. n_0, i.e. divided by n_0^2) connecting the $|0,0,0\rangle$ non-dispersive wave-packet of a three-dimensional hydrogen atom in a circularly polarized microwave field with other Floquet states, as a function of the energy difference between the two states. The stick spectrum is the exact result obtained from a numerical diagonalization with $\omega = 1/60^3$, corresponding to a principal quantum number $n_0 = 60$, and scaled amplitude $F_0 = 0.04446$; in natural units, the microwave frequency $\omega/2\pi$ is 30.48 GHz, and the microwave amplitude 17.6 V/cm. The crosses represent the analytic prediction within the harmonic approximation [68]. There are three dominant lines (σ^+ polarized) discussed in the text, other transitions (as well as transitions with σ^- or π polarizations) are negligible, what proves the validity of the harmonic approximation. If a weak probe field (in the microwave domain) is applied to the system in addition to the driving field, its absorption spectrum should therefore show the three dominant lines, allowing an unambiguous characterization of the non-dispersive wave-packet.

these claims are doubly wrong: firstly, as explained in sec. 3.4.4, harmonicity is *not* a requirement for non-dispersive wave-packets to exist (the only condition is the existence of a sufficiently large resonance island); secondly, the harmonic approximation is clearly a very good approximation even for moderate values of n_0.

Multiplication by the free space density of states transforms fig. 56 in fig. 57, which shows that the corresponding spontaneous decay rates are very low, of the order of 100 Hz at most. They are few orders of magnitude smaller than the ionization rates and thus may be difficult to observe. With increasing n_0, the spontaneous rate decreases algebraically while the ionization rate decreases *exponentially*, see sec. 7.2.4. Thus for large n_0, the spontaneous emission may be the dominant process. For $F_0 \simeq 0.05$ the cross-over may be expected around

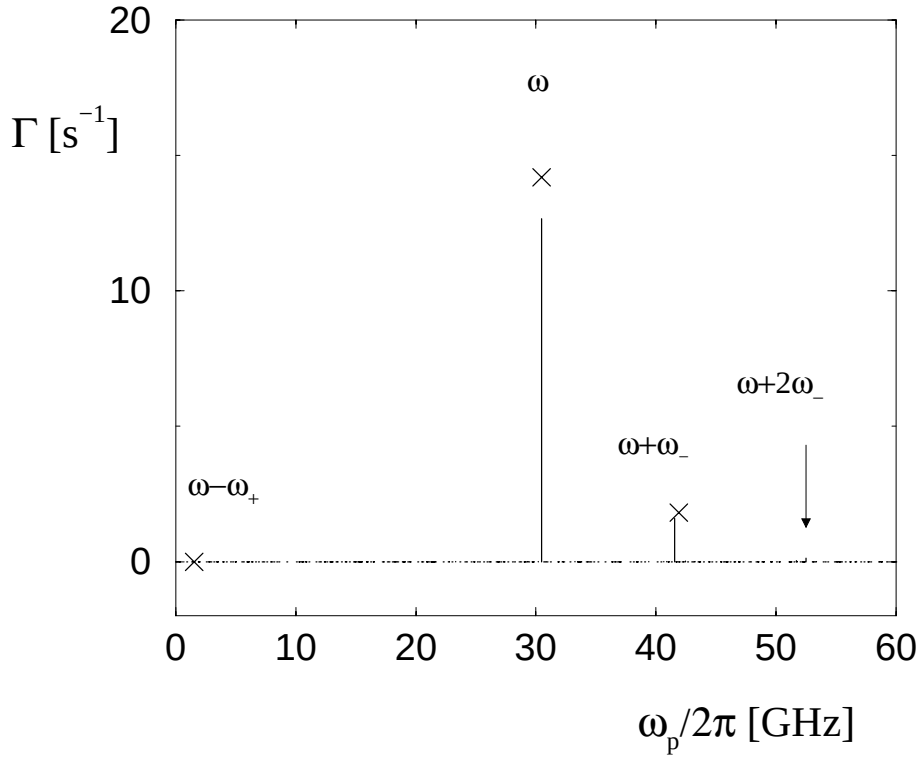

Fig. 57. Same as figure 56, but for the decay rates along the different transitions and in natural units. The density of modes of the electromagnetic field completely kills the transition at frequency $\omega - \omega_+$, invisible in the figure. One can see a small line at frequency approximately $\omega + 2\omega_-$ (see arrow), an indication of a weak breakdown of the harmonic approximation.

$n_0 = 200$. However, for smaller F_0, the ionization rate decreases considerably, and for $F_0 \simeq 0.03$ both rates become comparable around $n_0 = 60$. Still, a rate of few tens of photons (or electrons in the case of ionization) per second may be quite hard to observe experimentally.

To summarize, resonance fluorescence of non-dispersive wave-packets in circularly polarized microwave occurs only in the microwave range (close to the driving frequency). In particular, the elastic component (dominant in the semiclassical limit) does not destroy the wave-packet, the wave-packet merely converts the microwave photon into a photon emitted with the same polarization, but in a different direction. Let us stress that we assumed the free space density of modes in this discussion. Since the microwave field may be also supplied to the atom by putting the latter in a microwave cavity, it should be interesting to investigate how the density of modes in such a cavity affects the spontaneous emission rate either by increasing or decreasing it (see [191] for a review) or, for special cavities (waveguides), even invalidates the concept of a decay rate [192,193].

7.2.4 Linearly polarized microwave

Let us now discuss the spontaneous emission of non-dispersive wave-packets driven by a linearly polarized microwave field. The situation becomes complicated since we should consider different wave-packets corresponding to (see fig. 23) extreme librational states ($p = 0$, located perpendicularly to the polarization axis), separatrix states elongated along the polarization axis, and extreme rotational (maximal p, doughnut shaped) states of the resonantly driven manifold. Clearly, all these wave-packet states have different localization properties and spontaneous emission will couple them to different final states. No systematic analysis of the effect has been presented until now, only results based on the simplified one-dimensional model are available [71]. Those are of relevance for the spontaneous emission of the separatrix based wave-packet and are reviewed below. Quantitatively we may, however, expect that the spontaneous emission properties of the extreme rotational wave-packet will resemble those of the non-dispersive wave-packet in circular polarization. Indeed, the linearly polarized wave can be decomposed into two circularly polarized waves, and the extreme rotational state (fig. 24) is a coherent superposition of two circular wave-packets – each locked on one circularly polarized component – moving in the opposite sense. The decay of each component can then be obtained from the preceding discussion.

A completely different picture emerges for other wave-packets. Their electronic densities averaged over one period are concentrated along either the ρ (extreme librational) or z axes and do not vanish close to the nucleus (fig. 23). They have non-negligible dipole elements with Floquet states built on low lying atomic states (i.e. states practically unaffected by the driving field). Because of the cubic power dependence of the decay rate, eq. (271), on the energy of the emitted photon, these will dominate the spontaneous emission. Thus, in contrast to the CP case, spontaneous decay will lead to the destruction of the wave-packet. A quantitative analysis confirms this qualitative picture. To this end, a general master equation formalism can be developed [71], which allows to treat the ionization process induced by the driving field exactly, while the spontaneous emission is treated perturbatively, as in the preceding section. Applied to the one-dimensional model of the atom (sec. 3.3.1), with the density of field modes of the real three-dimensional world, it is possible to approximately model the behaviour of the separatrix states of the three-dimensional atom.

A non-dispersive wave-packet may decay either by ionization or by spontaneous emission, the total decay rate being the sum of the two rates [71]. Like in the CP case, the decay rate to the atomic continuum decreases exponentially with n_0 (since it is essentially a tunneling process, see sec. 7.1, eq. (267)) while the spontaneous decay rate depends algebraically on n_0 [22]. The wave-packet is a coherent superposition of atomic states with principal quantum number

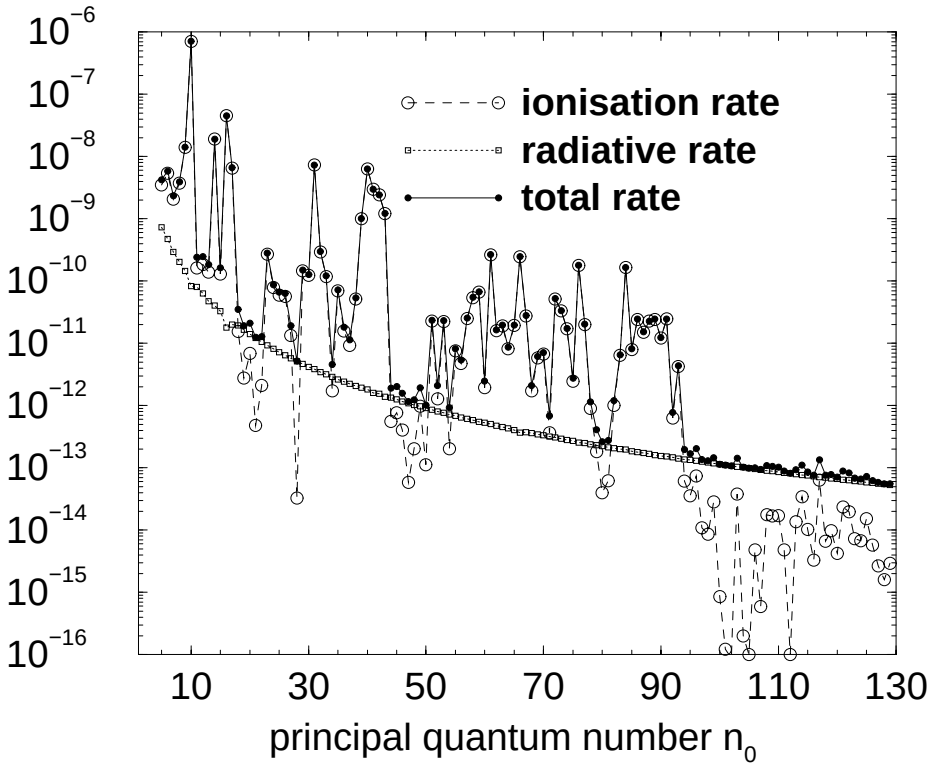

Fig. 58. Comparison of the spontaneous decay rate, the ionization rate, and their sum, for a non-dispersive wave-packet in a linearly polarized microwave field, as a function of the principal quantum number n_0. Microwave amplitude $F_0 = 0.04442$, decay rates in atomic units. The full decay rate exhibits a cross-over from a dominantly coherent (ionization) to a dominantly incoherent (spontaneous emission) regime. The fluctuations of the rate present in the coherent regime are suppressed in the incoherent regime. The data presented here are obtained by an exact numerical calculation on the one-dimensional model of the atom [71], see sec. 3.3.1.

close to $n_0 = \omega^{-1/3}$, and the dipole matrix element between an atomic state n and a weakly excited state scales as $n^{-3/2}$[22]. Since the energy of the emitted photon is of order one (in atomic units), eq. (271) shows that the spontaneous emission rate should decrease like α^3/n_0^3. The numerical results, presented in fig. 58, fully confirm this $1/n_0^3$ prediction. However, the spontaneous decay of real, 3D wave-packets with near 1D localization properties (see fig. 23, middle column, and fig. 38) is certainly slower. Indeed, these states are combinations of atomic states with various total angular momenta L; among them, only the low-L values decay rapidly to weakly excited states, the higher L components being coupled only to higher excited states. In other words, they are dominantly composed by extremal parabolic Rydberg states, which have well-known decay properties [22]. Altogether, their decay rate is decreased by a factor of the order of n_0, yielding a n_0^{-4} law instead of n_0^{-3}.

On the other hand, since the ionization process is dominated by tunneling in the direction of the microwave polarization axis [43,67,87,194], the ionization

rate in 3D remains globally comparable to the ionization rate in 1D, for the wave-packet launched along straight line orbits. This remains true even if the generic fluctuations of the ionization rate (see section 7.1) may induce locally (in some control parameter) large deviations between individual 3D and 1D decay rates [35]. Therefore, the transition from dominant ionization to dominant spontaneous decay will shift to slightly higher values of n_0 in 3D. As in the CP case studied above, this cross-over may be moved to smaller values of n_0 by reducing the ionization rate, i.e., by decreasing F_0.

7.3 Non-dispersive wave-packet as a soliton

The non-dispersive character of the wave-packets discussed in this review brings to mind solitons, i.e. solutions of *nonlinear* wave equations that propagate without deformation: the non-linearity is there essential to overcome the spreading of the solution. The non-dispersive wave-packets discussed by us are, on the other hand, solutions of the *linear* Schrödinger wave equation, and it is not some non-linearity of the wave equation which protects them from spreading, but rather the periodic driving. Thus, at first glance, there seems to be no link between both phenomena. This is not fully correct. One may conceive non-dispersive wave-packets as solitonic solutions of particular nonlinear equations, propagating not in time, but in parameter space [63]. The evolution of energy levels in such a space, called "parametric level dynamics", has been extensively studied (see [15,195] for reviews), both for time-independent and for periodically time-dependent systems. In the latter case, the energy levels are the quasi-energies of the Floquet Hamiltonian (see sec. 3.1.2).

For the sake of simplicity, we consider here the two-dimensional hydrogen atom exposed to a circularly polarized microwave (sec. 3.4.3), where the explicit time dependence can be removed by transforming to the rotating frame (see sec. 3.4.4), but completely similar results are obtained for the Floquet Hamiltonian of any periodically time-dependent system. The Hamiltonian, given by eq. (184),

$$H = \frac{\vec{p}^2}{2} - \frac{1}{r} + Fx - \omega L_z, \tag{274}$$

may be thought of as an example of a generic system of the form

$$H(\lambda) = H_0 + \lambda V, \tag{275}$$

where λ is a parameter. In our case, for example, the microwave amplitude

[35] A similar behaviour is observed in circular polarization for the 2D and 3D non-dispersive wave-packets: they exhibit comparable ionization rates, but distinct fluctuations [50].

may be tuned, leading to $V = x$ and $\lambda = F$. The interesting quantities are then the eigenvalues $E_i(\lambda)$ and the eigenfunctions $|\psi_i(\lambda)\rangle$ of eq. (275). Differenciating the Schrödinger equation with respect to λ, one shows (with some algebra) [15] that the behavior of $E_i(\lambda)$ with λ may be viewed as the motion of N fictitious classical particles (where N is the dimension of the Hilbert space) with positions E_i and momenta $p_i = V_{ii} = \langle\psi_i|V|\psi_i\rangle$, governed by the Hamiltonian

$$\mathcal{H}_{\rm cl} = \sum_{i=1}^{N} \frac{p_i^2}{2} + \frac{1}{2}\sum_{i=1}^{N}\sum_{j=1,j\neq i}^{N} \frac{|\ \mathcal{L}_{ij}\ |^2}{(E_j - E_i)^2}, \tag{276}$$

where $\mathcal{L}_{ij} = (E_i - E_j)\langle\psi_i|V|\psi_j\rangle$ are additional independent variables obeying the general Poisson brackets for angular momenta. The resulting dynamics, although nonlinear, is integrable [15].

Let us now consider the parametric motion of some eigenstate $|\ n_+, n_-\rangle$, for example of the ground state wave-packet $|0,0\rangle$. Its coupling to other states is quite weak – because of its localization in a well defined region of phase space – and the corresponding $\mathcal{L}_{ij}$ are consequently very small. If we first suppose that the wave-packet state is well isolated (in energy) from other wave-packets (i.e., states with low values of n_+, n_-), the fictitious particle associated with $|0,0\rangle$ basically ignores the other particles and propagates freely at constant velocity. It preserves its properties across the successive interactions with neighboring states, in particular its shape: in that sense, it is a solitonic solution of the equations of motion generated by Hamiltonian (276).

Suppose that, in the vicinity of some F values, another wave-packet state (with low n_+, n_- quantum numbers) becomes quasi-degenerate with $|0,0\rangle$. In the harmonic approximation, see sec. 3.4.4, the two states are completely uncoupled; it implies that the corresponding $\mathcal{L}_{ij}$ vanishes and the two levels cross. The coupling between the two solitons stems from the *difference* between the exact hamiltonian and its harmonic approximation, i.e. from third order or higher terms, beyond the harmonic approximation. Other $|n_+, n_-\rangle$ states having different slopes w.r.t. F induce "solitonic collisions" at some other values of F. To illustrate the effect, part of the spectrum of the two-dimensional hydrogen atom in a CP microwave is shown in fig. 59, as a function of the scaled microwave amplitude F_0. For the sake of clarity, the energy of the ground state wave-packet $|0,0\rangle$ calculated in the harmonic approximation, eq. (174) is substracted, such that it appears as an almost horizontal line. Around $F_0 = 0.023$, it is crossed by another solitonic solution, corresponding to the $|1,4\rangle$ wave-packet [36] , what represents the collision of two solitons. Since this avoided crossing is narrow and well isolated from other avoided crossings,

[36] Similarly to the wave-packet $|1,3\rangle$ discussed in fig. 30, the semiclassical harmonic prediction for the energy of $|1,4\rangle$ is not satisfactory. However, the slope of the energy level is well reproduced as a function of F_0.

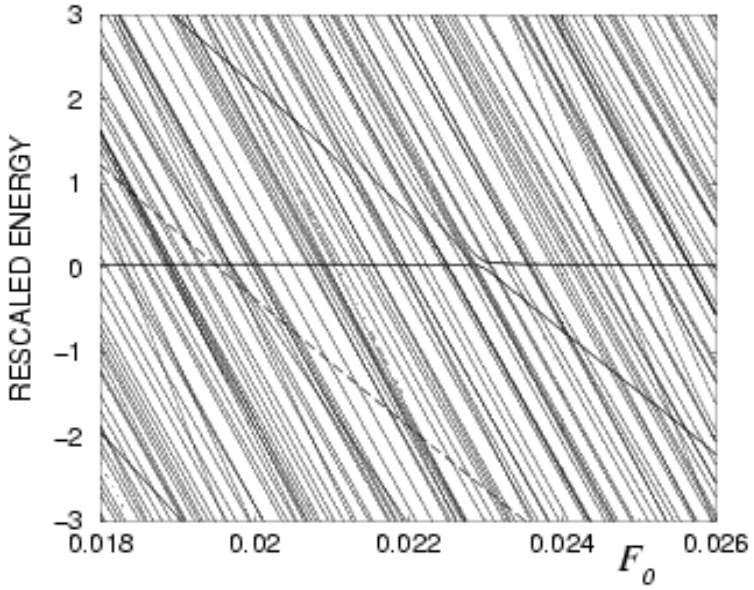

Fig. 59. The quasi-energy spectrum of a two-dimensional hydrogen atom in a circularly polarized microwave field, as a function of the scaled microwave amplitude F_0 (for $n_0 = 60$). In order to emphasize the dynamics of wave-packet states, the semiclassical prediction, eq. (174) for the ground state wave-packet energy is substracted from the numerically calculated energies. Consequently, the ground state wave-packet $|0,0\rangle$ is represented by the almost horizontal line. The dashed line represents the semiclassical prediction for the $|1,4\rangle$ wave-packet. Although it is rather far from the exact result, the slope of the energy level is well reproduced. The size of the avoided crossing between the "solitonic" levels $|0,0\rangle$ and $|1,4\rangle$ is a direct measure of the failure of the harmonic approximation.

the wave-functions before and after the crossing preserve their shape and character, as typical for an isolated two-level system. This may be further verified by wave-function plots before and after the collision (see [63] for more details). The avoided crossings become larger (compare fig. 30) with increasing F_0. In fact, as mentioned in sec. 3.4.4, we have numerically verified that the solitonic character of the ground state wave-packet practically disappears at the $1:2$ resonance, close to $F_0 \simeq 0.065$ [63]. For larger F_0, while one may still find nicely localized wave-packets for *isolated* values of F_0, the increased size of the avoided crossings makes it difficult to follow the wave-packet when sweeping F_0. For such strong fields, the ionization rate of wave-packet states becomes appreciable, comparable to the level spacing between consecutive states and the simple solitonic model breaks down. In order to understand the variations of the (complex) energies of the resonances with F, a slightly more complicated model – level dynamics in the complex plane – should be used [15].

8 Experimental preparation and detection of non-dispersive wave-packets

In the preceding chapters, we have given an extensive theoretical description of the characteristic properties of non-dispersive wave-packets in driven Rydberg systems. We have seen that these surprisingly robust "quantum particles" are ubiquitous in the interaction of electromagnetic radiation with matter. However, any theoretical analysis needs to be confronted with reality, and we have to deal with the question of creating and identifying non-dispersive wave-packets in a laboratory experiment. In our opinion, none of the currently operational experiments on the interaction of Rydberg atoms with microwave fields allows for an unambiguous identification of non-dispersive wave-packets, although some of them [133] certainly have already populated such states. In the following, we shall therefore start out with a brief description of the typical approach of state of the art experiments, and subsequently extend on various alternatives to create and to probe non-dispersive wave-packets in a real experiment. We do not aim at a comprehensive review on the interaction of Rydberg atoms with microwave fields, but rather refer to [43,32,69,133,196] for a detailed treatment of various aspects of this intricate problem. Here, we strictly focus on issues pertinent to our specific purpose.

8.1 Experimental status

The theoretical interest in the interaction of Rydberg states of atomic hydrogen with low frequency electromagnetic fields has been triggered by early experiments [135] which showed a surprisingly efficient excitation and subsequent ionization of the atoms by the field. More precisely, a microwave field of frequency ω comparable to the energy difference between the initial atomic state and its nearest neighbor was observed to induce appreciable ionization, for atom-field interaction times of approx. 100 driving field cycles, and for field amplitudes beyond a certain threshold value (of the order of $5-10\%$ of the Coulomb field experienced by the Rydberg electron on its unperturbed Kepler orbit). This threshold behavior of the ionization probability as a function of the driving field amplitude rather than of the driving frequency – in apparent contradiction to the photoeffect – motivated a theoretical analysis of the classical dynamics of the Rydberg electron under external driving. It turned out that the ionization threshold marks the transition from regular to chaotic *classical dynamics* of the driven electron [197].

The microwave ionization of atomic Rydberg states was thus identified as an experimental testing ground for quantum transport under the conditions of classically mixed regular chaotic dynamics, where the transport was simply

measured by the experimentally observed ionization yield, or – with some additional experimental effort – by the time dependent redistribution of the atomic population over the bound states [198–201]. Depending on the precise value of the scaled frequency ω_0 – the ratio of the microwave frequency ω to the Kepler frequency $\Omega_{\rm Kepler}$ of the initially excited Rydberg atom, eq. (134) – of the driving field, theory soon predicted essentially "classical" ionization yields ($\omega_0 < 1.0$), or some quantum suppression of chaotic ionization ($\omega_0 > 1.0$) [202], mediated by the quantum mechanical interference effect known as *dynamical localization*, analogous to Anderson localization in the electronic transport through disordered solids [203–208]. The physical process involved in chaotic ionization is classically deterministic diffusion, therefore essentially statistical in nature, and insensitive to the details of the transport process. Correspondingly, the mere ionization probability condenses all details of the ionization process in one single number, without revealing details on individual local structures in phase space. It reflects the statistical characteristics of the excitation process, rather than the population of some well defined individual atomic states in its course [43,145]. Hence, state of the art experiments are "blind" for the details of the atomic excitation process on the way to ionization, and therefore not suitable for the unambiguous identification of individual eigenstates of the atom in the field, notably of non-dispersive wave-packets. The case is getting worse with additional complications which are unavoidable in a real experiment, such as the unprecise definition of the initial state the atoms are prepared in [133,137,209–216], the experimental uncertainty on the envelope of the amplitude of the driving field experienced by the atoms as they enter the interaction region with the microwave (typically a microwave cavity or wave guide) [200,211,217], stray electric fields due to contact potentials in the interaction region, and finally uncontrolled noise sources which may affect the coherence effects involved in the quantum mechanical transport process [218]. On the other hand, independent experiments on the microwave ionization of Rydberg states of atomic hydrogen [132,137], as well as on hydrogenic initial states of lithium [217], did indeed provide hard evidence for the relative stability of the atom against ionization when driven by a resonant field of scaled frequency $\omega_0 \simeq 1.0$. Furthermore, in the hydrogen experiments, this stability was observed to be insensitive to the polarization of the driving field, be it linear, circular or elliptical [134]. These experimental findings suggest that some atomic dressed states anchored to the principal resonance island in the classical phase space are populated by switching on the microwave field, since these states tend to be more stable against ionization than states localized in the chaotic sea [145], see section 7.1.

Consequently, for an unambiguous preparation and identification of non-dispersive wave-packets launched along well defined classical trajectories the experimental strategy has to be refined. We suggest two techniques for their preparation:

– The direct, selective optical excitation from a low lying state *in the presence*

of the microwave field. This approach actually realizes some kind of "Floquet state absorption spectroscopy" [64].
– The preparation of the appropriate atomic initial state – optionally in the presence of a static field – followed by switching the microwave field on the appropriate time scale to the desired maximum field amplitude [219].

Two, possibly complementary methods should allow for an efficient detection of such wave-packets:

– Floquet spectroscopy – this time involving either microwave or optical transitions between states dressed by the microwave field;
– Measurements of the time-dependence of the ionization yield of the non-dispersive wave-packet. This requires the ability to vary the interaction time between the atoms and the microwave by more than one order of magnitude [43,145,217,220–222].

All these techniques are experimentally well-developed and actually realized in different, currently operational experimental settings [217,220,223]. The only prerequisite for an unambiguous identification of non-dispersive wave-packets therefore remains an experimental set-up which allows to follow these complementary strategies simultaneously.

8.2 Direct preparation

The most straightforward way to populate a non-dispersive wave-packet state is its direct optical excitation in the presence of the driving field, from a weakly excited state of the system at energy E_0. In section 7.2.1, we have discussed how a weak electromagnetic probe field can induce transitions between Floquet states. This is particularly easy if one of the states involved is in an energetically low lying state. Such a state is practically unaffected by the driving microwave field (which is weak as compared to the Coulomb field experienced by a deeply bound state, and very far from any resonance), such that the corresponding Floquet state is almost exactly identical with the time-independent atomic state. In other words, all the Fourier components of the Floquet state vanish, except the $k = 0$ component, which represents the unperturbed atomic state $|\phi_0\rangle$. In such a case, the photoexcitation cross-section (270) becomes (neglecting the anti-resonant term):

$$\sigma(\omega_p) = \frac{4\pi\omega_p\alpha}{c}\mathrm{Im}\sum_f |\langle\mathcal{E}_f^0|\mathcal{T}|\phi_0\rangle|^2\frac{1}{\mathcal{E}_f - E_0 - \omega_p}, \tag{277}$$

where the sum extends over all Floquet states with energy $\mathcal{E}_f$ and involves only their $k = 0$ Fourier component [37].

Eq. (277) shows that the excitation probability exhibits a maximum any time the laser is scanned across a frequency which is resonant with the transition from the 1s ground state $|\phi_0\rangle$ to a specific dressed state of the atom in the field. Fig. 60 shows an example for the photoabsorption probability from the ground state of atomic hydrogen in the presence of a microwave field and a parallel static electric field. The microwave frequency is resonant with atomic transitions in the region of $n_0 \simeq 60$. Clearly, the cross-section shows extremely narrow peaks each of which corresponds to a Floquet eigenstate of the atom in the field. As a matter of fact, the state marked by the arrow is similar to the dressed state of the 3D atom displayed in fig. 38, a wave-packet periodically moving along the field polarization axis. As obvious from the figure, this state can be efficiently reached by direct excitation from the ground state. Furthermore, due to its sharp signature in $\sigma(\omega_p)$, it is easily and unambiguously identified. On the other hand, this kind of preparation of the wave-packet is obviously reserved to those dressed states which have nonvanishing overlap with the deeply bound atomic states. For wave-packets tracing circular or elliptical orbits far from the nucleus, another strategy is needed, that is discussed below.

A slightly adapted spectroscopic approach should be equally useful for the unambiguous identification of wave-packet eigenstates. Instead of probing the dressed spectrum from a weakly excited state using a laser field, one may equally well probe the local structure of the dressed spectrum in the vicinity of the wave-packet eigenstate by inducing transitions from the wave-packet to neighboring states by a second, weak microwave field of linear or circular polarization [224]. Such stimulated transitions will be mediated by the dipole matrix elements given in equation (269), and allow to measure the energy spacings in the immediate vicinity of the wave-packet state directly. Hence, microwave probe spectroscopy should be an extremely sensitive probe, since it allows for the unambiguous identification of the wave-packet via the characterization of its local spectral environment.

Given the spectroscopic resolution which is nowadays available in the optical as well as in the microwave domain, the spectroscopic approach outlined above seems to be the method of choice for an unambiguous identification, and – where possible – for an efficient launch of nondispersive wave-packets along a periodic orbit of the classical dynamics. What it requires, however, is a precise determination of Floquet spectra from the accompanying quantum calculation.

[37] Alternatively, the sum could be rewritten as a sum over one Floquet zone only, with all the Fourier components $|\phi_f^k\rangle$ involved, with the denominator replaced by $\mathcal{E}_f + k\omega - E_0 - \omega_p$.

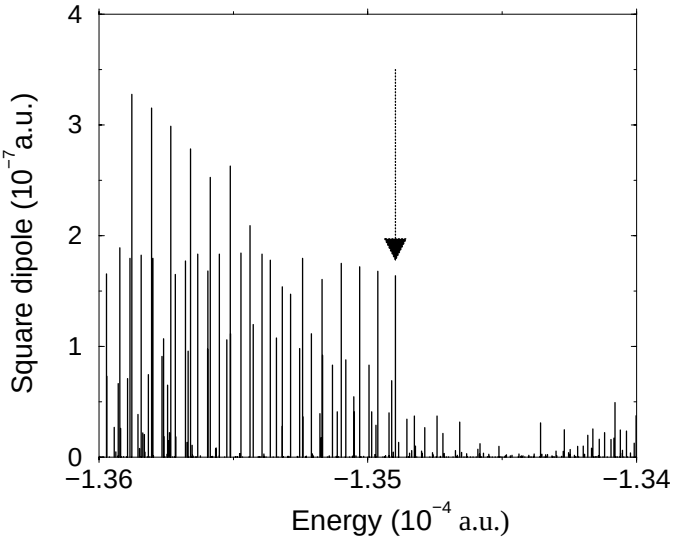

Fig. 60. Photo-excitation of highly excited Rydberg states of the hydrogen atom in the presence of a linearly polarized microwave field of frequency $\omega/2\pi = 30.48$ GHz and amplitude $F = 7.93$ V/cm and a parallel static electric field $F_s = 2.38$ V/cm. The initial state is the ground state of the atom, and the polarization of the probe beam is parallel to the static and microwave fields. The spectrum is displayed in the region where Floquet states are mainly composed of Rydberg states with principal quantum number around $n_0 = 60$, while the microwave driving is resonant with the Kepler frequency of such states. Hence, some of the Floquet states are trapped in the non-linear resonance island and behave as non-dispersive wave-packets. Of special interest is the state marked with an arrow, which is similar to the non-dispersive wave-packet displayed in fig. 38, localized in all three dimensions of space (the field amplitude is slightly different). Its large photo-excitation probability should make a direct experimental preparation possible. At the scale of the figure, the width of the various lines is very small, and the spectrum is almost a pure stick spectrum.

Fortunately, both for hydrogen and for alkali atoms, the necessary theoretical quantum data may be obtained from already existing software [225,226].

Although we elaborated in this review paper only the case of the hydrogen atom, the general concepts are also fruitful for non-hydrogenic atoms. Indeed, the major difference between the Rydberg electron in a hydrogen atom and in a non-hydrogenic atom is the existence in the latter case of an ionic core which affects the classical and quantum dynamics of the Rydberg electron. On the scale of a Rydberg atom, the ionic core is a extremely small object which will thus induce a very local perturbation. As long as the Rydberg electron does not approach the ionic core, it behaves completely similarly in hydrogen or non-hydrogenic atoms. Thus, the properties of non-dispersive wave-packets tracing circular or elliptical classical orbits are essentially independent of the ionic core, and the hydrogenic analysis holds. For orbits which come close to the nucleus, the ionic core may scatter the Rydberg electron. Thus, instead of being indefinitely trapped on a torus inside a resonance island, it may happen that the Rydberg electron hops from a torus to another one when it gets close

to the nucleus. This of course will affect the long time classical and quantum dynamics. Nevertheless, it remains true that most of the time the classical dynamics – and consequently the phase locking phenomenon responsible for the existence of non-dispersive wave-packets – is identical to the hydrogenic dynamics. From the quantum point of view, the ionic core is responsible for the existence of non-zero quantum defects in the low angular momentum channels. The energy levels, mixed by the microwave driving, will thus be significantly shifted from their hydrogenic positions. However, the *structure* of the energy levels – grouped in manifolds – will essentially survive, see [225]. It is likely that some non-dispersive wave-packets also exist in non-hydrogenic atomic species.

8.3 Preparation through tailored pulses

Another, indirect method for preparing non-dispersive wave-packets is also available. This will be the method of choice for wave-packets moving along classical orbits of large angular momentum (small eccentricity). Such states, obviously, are not accessible to a direct optical excitation from weakly excited, low angular momentum states. The same general scheme may be also applicable to high eccentricity wave-packets although in that case we expect that the direct excitation may be more efficient and flexible. The method to be discussed here consists of two stages. We first prepare the atom in a well chosen and well defined initial highly excited state, and then turn the microwave field on relatively slowly, from zero amplitude to its plateau value $F_{\max}$.

A non-dispersive wave-packet is a single eigenstate $|\mathcal{E}\rangle$ of the Floquet Hamiltonian describing the driven system at fixed driving field amplitude F. As shown in sections 3.3.2, 3.4 and 7.3, the evolution of the quasienergies of the driven atom with an external control parameter like the driving field amplitude is rather complicated. It reflects the dramatic transformation of the structure of classical phase space, manifesting in an abundance of avoided crossings of various sizes in the level dynamics. Still, as exemplified in figs. 9, 30, and 59, the wave-packet states may be followed rather easily under changes of F (parametrized by t, during the switching of the pulse) in the level dynamics, in agreement with their "solitonic" character (see section 7.3). Nontheless, the very same figures illustrate clearly that the targeted wave-packet state undergoes many avoided crossings as the microwave amplitude is swept. To remain in a single eigenstate, the avoided crossings should be passed either adiabatically or diabatically, with a branching ratio at an individual crossing being described by the well known Landau-Zener scenario [7,227]. Consequently, if we want to populate an individual wave-packet eigenstate from a field free atomic state $|\psi_0\rangle$, we need some knowledge of the energy level dynamics. Then it is possible to identify those field free states which are connected to

the wave-packet via adiabatic and/or diabatic transitions in the network of energy levels, and subsequently to design $F(t)$ such as to transfer population from $|\psi_0\rangle$ to $|\mathcal{E}\rangle$ most efficiently. A precise experimental preparation of $|\psi_0\rangle$ is the prerequisite of any such approach.

When the driving field is increased from zero, the major modification in the classical phase space is the emergence of the resonance island (see figs. 22, 25, 26). Quantum mechanically, the states with initial principal quantum number close to $n_0 = \omega^{-1/3}$ will enter progressively inside the resonance island. For a one-dimensional system, the Mathieu equation, discussed in section 3.1.4, fully describes the evolution of the energy levels in this regime. As shown for example in figure 9, the non-dispersive wave-packet with the best localization, i.e. $N = 0$, is – in this simple situation – adiabatically connected to the field-free state with principal quantum number closest to n_0, i.e. the eigenstate $\kappa = 0$ of the Mathieu equation. When the Mathieu parameter q, eq. (100), is of the order of unity, the state of interest is trapped in the resonance island, which happens at field amplitudes given by eq. (150) for the one-dimensional atom, and for linear polarization of the microwave field. A similar scaling is expected for other polarizations, too. In the interval $F \leq F_{\text{trapping}}$, the field has to be increased slowly enough such as to avoid losses from the ground state to the excited states of the Mathieu equation, at an energy separation of the order of n_0^{-4}. The most favorable situation is then the case of "optimal" resonance (see section 3.1.2), when n_0 is an integer, the situation in figure 9. The wave-packet state is always separated from the other states by an energy gap comparable to its value at $F = 0$, i.e. of the order of $3/(2n_0^4)$. The situation is less favorable if n_0 is not an integer, because the energy gap between the wave-packet of interest and the other states is smaller when $F \to 0$. The worst case is met when n_0 is half-integer: the free states $n_0 + 1/2$ and $n_0 - 1/2$ are quasi-degenerate, and selective excitation of a single wave-packet is thus more difficult.

The appropriate time scale for switching on the field is given by the inverse of the energy splitting, i. e. for "optimal" resonance

$$\tau_{\text{trapping}} \sim n_0^4 = n_0 \times 2\pi/\omega, \tag{278}$$

or n_0 driving field periods.

Once trapped in the resonance island, the coupling to states localized outside the island will be residual – mediated by quantum mechanical tunneling, see section 7.1 – and the size of the avoided crossings between the trapped and the untrapped states is exponentially small. After adiabatic switching into the resonance island on a time scale of n_0 Kepler orbits, we now have to switch diabatically from F_{trapping} to some final F value, in order to avoid adiabatic losses from the wave-packet into other states while passing through the avoided crossings.

The preceding discussion is based on a one-dimensional model and the Mathieu equation. Taking into account the other "transverse" degrees of freedom is not too difficult. Indeed, as noticed in sections 3.3.2, 3.4, the various time scales of the problem are well separated. The transverse motion is slow and can be adiabatically separated from the fast motion in $(\hat{I}, \hat{\theta})$. Instead of getting a single set of energy levels, one gets a family of sets, the various families being essentially uncoupled. An example for the 3D atom in a linearly polarized microwave field is shown in fig. 22. It follows that the estimate for the trapping field and the switching time are essentially the same as for 1D systems. Inside the resonance island, the situation becomes slightly more complicated, because there is not a single frequency for the secular motion, but several frequencies along the transverse degrees of freedom. For example, in CP, it has been shown that there are three eigenfrequencies, eqs. (194,195), in the harmonic approximation – see section 3.4.4. This results in a large number of excited energy levels which may have avoided crossings with the "ground state", i.e. the nondispersive wave-packet we want to prepare. As shown in section 7.3, most of these avoided crossings are extremely small and can be easily crossed diabatically. However, some of them are rather large, especially when there is an internal resonance between two eigenfrequencies. Examples are given in figs. 30 and 59, where $\omega_+ = 3\omega_-$ and $\omega_+ = 4\omega_-$, respectively.

These avoided crossings are large and dangerous, because the states involved lie *inside* the resonance island, which thus loses its protective character. They are mainly due to the unharmonic character of the Coulomb potential. Their size may be qualitatively analyzed as we do below on the CP example, expecting similar sizes of the avoided crossings for any polarization.

The unharmonic corrections to the harmonic approximation around the stable fixed point x_e, p_e in the center of the nonlinear resonance – as outlined in section 3.4 – are due to the higher order terms $(-1)^j \tilde{x}^j / j! x_e^{j+1}$ in the Taylor series of the Coulomb potential, where $\tilde{x}, \tilde{y}$ are excursions from the equilibrium position. $\tilde{x}$ and $\tilde{y}$ can be expressed as linear combinations of $a_\pm^\dagger$ and $a_\pm$ operators [68] giving $\tilde{x}, \tilde{y} \sim \omega^{-1/2} \sim n_0^{3/2}$. Furthermore, the equilibrium distance from the nucleus scales as the size of the atom, $x_e \sim n_0^2$, and, therefore,

$$\tilde{x}^j / x_e^{j+1} \sim n_0^{\left(-2-\frac{j}{2}\right)}. \tag{279}$$

A state $|n_+, n_-\rangle$ is obtained by the excitation of N_+ quanta in the ω_+-mode and of N_- quanta in the ω_--mode, respectively, i. e. by the application of the operator product $(a_+^\dagger)^{n_+}(a_-^\dagger)^{n_-}$ on the wave-packet state $|0,0\rangle$, which – by virtue of eq. (279) – will be subject to an unharmonic correction scaling like

$$\Delta E_{\text{unharmonic}} \sim n_0^{\left(-2-\frac{n_+ + n_-}{2}\right)}. \tag{280}$$

Hence, the size of the avoided crossings between the wave-packet eigenstate

and excited states of the local potential around the stable fixed point decreases with the number of quanta in the excited modes.

In addition, we can determine the width $\Delta F_{\text{unharmonic}}$ of such avoided crossings in the driving field amplitude F, by differentiation of the energy (198) of $|n_+, n_-\rangle$ with respect to F. Then, the difference between the energies of two eigenstates localized in the resonance island is found to scale like Fn_0. Defining $\Delta F_{\text{unharmonic}}$ by the requirement that Fn_0 be of the order of $\Delta E_{\text{unharmonic}}$, we find

$$\Delta F_{\text{unharmonic}} \sim n_0^{\left(-3-\frac{n_+ + n_-}{2}\right)}. \tag{281}$$

Since we want to switch the field to a maximum value $F_{\max} \sim n_0^{-4}$, the Landau-Zener formula

$$\tau \sim \frac{F_{\max}}{\Delta E \Delta F} \tag{282}$$

yields

$$\tau_{\text{unharmonic}} \sim n_0^{n_- + n_+ + 1} \sim n_0^{n_- + n_+ - 2} \quad \text{microwave periods} \tag{283}$$

for the scaling behavior of the time scale which guarantees diabatic switching through avoided crossings of the wave-packet eigenstate with excited states of the elliptic island. Let us stress that this is only a very rough estimate of the switching time, some numerical factors (not necessarily close to unity) are not taken into account.

The above predictions can be checked, e.g., by a numerical integration of the time dependent Schrödinger equation for a microwave-driven atom, taking into account the time-dependent amplitude of the field. An exemplary calculation on the two-dimensional model atom (see sec. 3.4.3) can be found in [61], for CP driving. Fig. 61 shows the evolution of the electronic density of the atomic wave-function (initially prepared in the circular Rydberg state $n = M = 60$) during the rising part of the driving field envelope, modeled by

$$F(t) = F_{\max} \sin^2\left(\frac{\pi t}{2T_{\text{switch}}}\right). \tag{284}$$

The driving field frequency was chosen according to the resonance condition with the $n_0 = 60$ state, with a maximum scaled amplitude $F_{0,\max} = 0.03$. Inspection of fig. 59 shows that, for this value of $F_{\max}$, the crossing between the wave-packet eigenstate and the state $|n_+ = 1, n_- = 4\rangle$ has to be passed diabatically after adiabatic trapping within the principal resonance. By virtue of the above estimations of the adiabatic and the diabatic time scales, the switching time (measured in driving field cycles) has to be chosen such that $n_0 < T_{\text{switch}} < n_0^3$ (in microwave periods). Clearly, the pulse populates the desired wave-packet once the driving field amplitude reaches its maximum value.

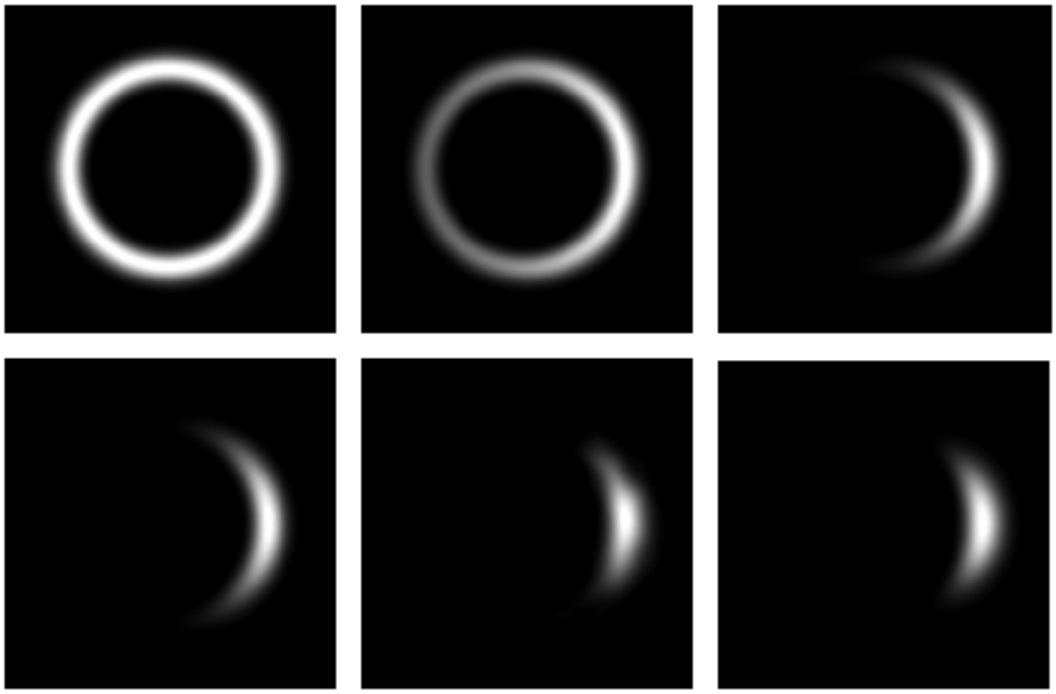

Fig. 61. Snapshots of the electronic density for a two-dimensional hydrogen atom exposed to a circularly polarized microwave field with increasing amplitude. The microwave field amplitude is switched on according to eq. (284), with maximum scaled field $F_{0,\max} = 0.03$ and $T_{\rm switch} = 400 \times 2\pi/\omega$, where ω is resonant with $n_0 = 60$ (frequency $\omega = 1/(60.5)^3$). The evolution of the initial circular state $n = M = 60$ is numerically computed by solving the time dependent Schrödinger equation in a convenient Sturmian basis. Top-left – $t = 0$ (initial circular state); top-middle – $t = 20$ microwave periods; top-right – $t = 60$ periods, bottom-left – $t = 100$ periods; bottom-middle – the final state, $t = 400$ periods; bottom-right – the non-dispersive wave-packet (exact Floquet eigenstate): it is almost indistinguishable from the previous wave-function, what proves that the excitation process efficiently and almost exclusively populates the state of interest. The box extends over 10000 Bohr radii in both directions, with the nucleus at the center. The microwave field is along the horizontal axis, pointing to the right.

More quantitatively, the overlap of the final state after propagation of the time-dependent Schrödinger equation with the wave-packet eigenstate of the driven atom in the field (bottom-right panel) amounts to 94%. Since losses of atomic population due to ionization are negligible on the time scales considered in the figure, 6% of the initial atomic population is lost during the switching process. The same calculation, done for the realistic three-dimensional atom with $n_0 = 60$ gives the same result, proving that the z-direction (which is neglected in the 2D model) is essentially irrelevant in this problem. Figure 62 shows the efficiency of the proposed switching scheme as a function of the switching time $T_{\rm switch}$, expressed in units of microwave periods. Observe that too long switching times tend to be less effective, since the avoided crossings passed during the switching stage are not traversed diabatically. The rough

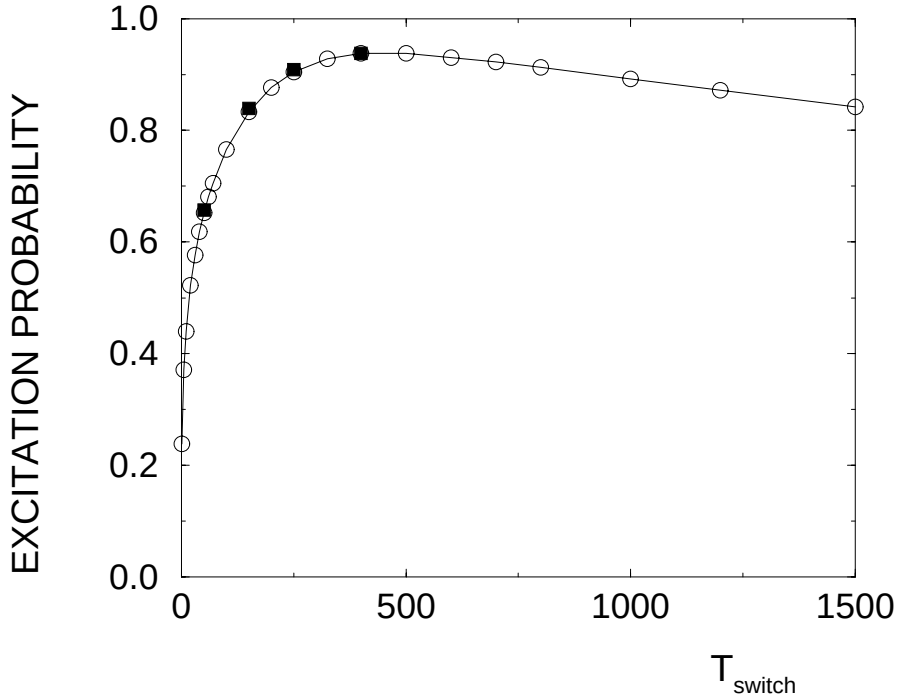

Fig. 62. Overlap between the wave-function obtained at the end of the microwave turn-on and the exact target state representing the non-dispersive wave-packet, as a function of the switching time $T_{\rm switch}$, for the two-dimensional hydrogen atom (circles). The filled squares indicate the results obtained for a fully three-dimensional atom. $F_{\rm max}$, ω, and n_0 as in fig. 61.

estimate, eq. (283), overestimates the maximum switching time by one order of magnitude. On the other hand, too short switching times do not allow the wave-packet to localize inside the resonance island. However, a wide range of switching times remains where good efficiency is achieved.

For a given initial state $|\psi_0\rangle$ of the atom, only the resonance condition defining the driving field frequency is to some extent restrictive, as depicted in fig. 63. It is crucial that the initially excited field-free state is adiabatically connected (through the Mathieu equation) to the ground state wave-packet. The best choice is "optimal resonance", but the adiabaticity is preserved if n_0 is changed by less than one half, see section 3.1.2. This corresponds to a relative change of ω of the order of $3/2n_0$. Given the spectral resolution of presently available microwave generators, the definition of the frequency with an accuracy of less than 1% is not a limitation. The exact numerical calculation displayed in fig. 63 fully confirms that efficient excitation is possible as long as $n_0 = \omega^{-1/3} - 1/2$ matches the effective principal quantum number of the initially excited field-free state within a margin of $\pm 1/2$ (in the range [59.5,60.5]).

In conclusion, the preparation of non-dispersive wave-packets by excitation of a Rydberg state followed by careful switching of the microwave field can be considered as an efficient method, provided a clean experimental preparation

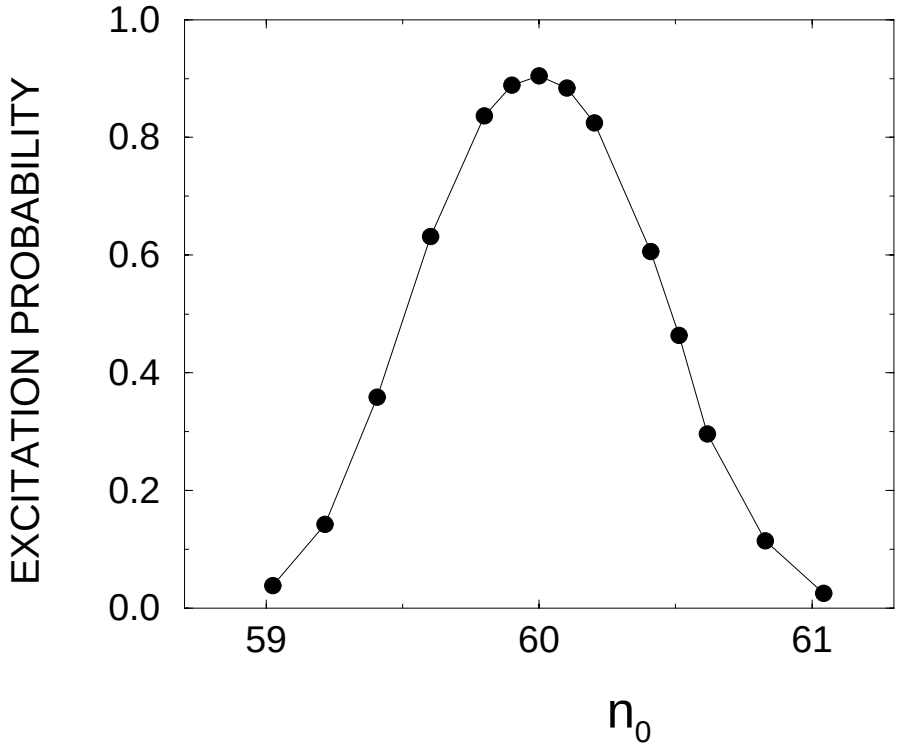

Fig. 63. Overlap between the wave-function obtained at the end of the microwave turn-on and the exact target state representing the non-dispersive wave-packet as a function of n_0, obtained for the two-dimensional hydrogen atom (circles). $F_{\max}$ is as in fig. 61, and the switching time is $T_{\rm switch} = 250$ microwave periods. The initial state corresponds to a circular $n = 60$ state of a 2D hydrogen atom.

of the atomic initial state can be achieved. Furthermore, the boundaries – eqs. (278) and (283) – imposed on the time scale for the switching process leave a sufficient flexibility for the experimentalist to efficiently prepare the wave-packet. A final word is in place on the homogeneity of the driving field amplitude experienced by the atoms in the "flat top region" of the interaction, i.e. after the switching from the field free state into the wave-packet state at $F(t) = F_{\max}$. In any laboratory experiment, a slow drift of the amplitude will be unavoidable over the interaction volume. Hence, slightly different non–dispersive wave-packets will coexist at various spatial positions. Since the ionization rate of nondispersive wave-packets is rather sensitive with respect to detailed values of the parameters, see section 7.1, this should manifest itself by a deviation of the time dependence of the ionization yield from purely exponential decay.

8.4 Life time measurements

Given the above, rather efficient experimental schemes for the population of non-dispersive wave-packet eigenstates – either via direct optical Floquet ab-

sorption or through an appropriate switching procedure – we still need some means to prove that we really *did* populate the wave-packet. As a matter of fact, to provide unambiguous experimental evidence, one has to test various characteristic properties of the wave-packet, so as to exclude accidental coincidences. A natural way is Floquet spectroscopy (see sec. 8.2), i.e. probing the structure of the Floquet quasi-energy levels, in either the optical or the microwave regime (via absorption, stimulated emission, Raman spectroscopy etc.). Another possibility is to explore unique properties of wave-packet Floquet states. For example, as discussed in sec. 7.1, these states exhibit extremely small ionization rates. Hence, an experimentally accessible quantity to identify these states is the time-dependence of their survival probability, i.e. of the probability not to ionize during an interaction time t. It is given by [43,97]

$$P(t) = \sum_{\epsilon} |c_\epsilon|^2 \exp(-\Gamma_\epsilon t), \tag{285}$$

where the c_ϵ denote the expansion coefficients of the initial field-free state in the Floquet basis, at a given value of microwave amplitude F.

If the selective population of the wave-packet is successful, only one Floquet state contributes to $P(t)$, and the decay of the population to the atomic continuum should manifest in its exponential decrease, as opposed to a multiexponential decrease in the case of a broad distribution of the c_ϵ over the Floquet states [43,145,206–208,220]. Of course, the distinction between an exponential and an algebraic decay law requires the variability of the experimental interaction time over more than one order of magnitude. This is a nontrivial task in experiments on atomic Rydberg states of hydrogen, since the typical velocities of the atomic beam are of the order of 1000 m/s. That significantly restricts the interval on which the interaction time may be changed, taking into account the typical size (in the cm-range) of the atom-field interaction region [133,228]. However, the feasibility of such measurements has already been demonstrated in microwave experiments on rubidium Rydberg states, where the interaction time has been scanned from approx. 100 to approx. 100000 field cycles, i.e., over three orders of magnitude [220,221]. Note that, whereas the dynamics of the driven Rydberg electron along a Kepler ellipse of large eccentricity will certainly be affected by the presence of a non-hydrogenic core, non-dispersive wave-packets as the ones discussed in sections 3.4 and 3.5 can certainly be launched along circular trajectories, since the Rydberg electron of the rubidium atom essentially experiences a Coulomb field on such a circular orbit.

To use the character of the decay as a means to identify the wave-packet, the microwave field amplitude should be sufficiently large to guarantee that other Floquet states localized in the chaotic sea (see sec. 7.1) decay rapidly. Otherwise, the observation of a mono-exponential decay simply suggests that we succeeded in populating a single Floquet state - not necessarily a wave-

packet [220]. The appropriate choice of the driving field amplitude F, such that appreciable ionization is achieved for the longer experimentally accessible interaction times, should therefore allow for the experimental identification of the mono-exponential decay from the wave-packet to the atomic continuum, but also – by varying F – of the variations of the decay rate with F, which is predicted to fluctuate wildly over several orders of magnitude, see section 7.1. Note, however, that this requires an excellent homogeneity of the microwave field (e.g., provided by a high quality microwave cavity), as the fluctuations take place over rather small intervals of F.

9 Conclusions

In this report, we have shown that novel and highly robust eigenstates of periodically driven quantum systems – non-dispersive wave-packets – are born out of classically mixed regular-chaotic dynamics. As much as a mixed phase space is generic for classical Hamiltonian systems, non-dispersive wave-packets are a generic manifestation thereof on the quantum level, given a sufficiently high density of states (needed to resolve finite-size phase space structures). While we described their semiclassical properties and their experimental preparation, manipulation, and identification during the largest part of this report for a specific system – atomic Rydberg states driven by a microwave field – it is clear from our approach that such "quantum particles" can be anchored to any nonlinear resonance between a periodic drive and a periodic trajectory of a Hamiltonian system. As an alternative example, we have briefly touched upon the atomic realization of the gravitational bouncer, though many other realizations in simple quantum optical or atomic and molecular systems can be thought of. Let us only mention unharmonic traps for ions, atoms, or BEC condensates, periodically kicked atoms [229], as well as molecular dynamics [230,231] on adiabatic potential surfaces (the driven frozen planet briefly discussed in section 6.2 may be conceived as opening a perspective in this direction). Nontheless, atomic Rydberg states remain arguably the best objects to study the fundamental properties of non-dispersive wave-packets as the realization of Schrödinger's dream [2]. On one hand, they are microscopic realizations of the Keplerian motion and of Bohr's orbitals using a well understood non-linear dynamical system. On the other hand, they possess the essential complication which open quantum systems add to bounded Hamiltonian dynamics – the driving-induced, coherent coupling to the atomic continuum of free electronic states. On top of that, all these features can be controlled in real laboratory experiments, and we might actually dream of probing the characteristic properties of nondispersive wave-packets on single, trapped atoms or ions, using novel experimental approaches yet to come. Let us finally dare to speculate on the potential use of non-dispersive wave-packets in coherent

control: given their spectacular robustness – which we abundantly illustrated in this report – it is clear that they provide a means to store and to "ship" quantum probability densities in and across phase space, e.g., under adiabatic changes of the driving field polarization and/or of the strength or orientation of additional static fields. Given the recent advances in coherent control of molecular reactions employing laser fields [230] – which so far do not explore the unique perspectives of nonlinear dynamics – it looks like a promising (and challenging) program to systematically study non-dispersive wave-packets in molecular reaction dynamics.

10 Acknowledgments

It is a pleasure to acknowledge a longstanding and fruitful collaboration with Robert Gębarowski, Benoît Grémaud, Klaus Hornberger, Andreas Krug, Romek Marcinek, Krzysiek Sacha, Peter Schlagheck, and Sandro Wimberger on non-dispersive wave-packets and related topics over the past five years.

We acknowledge support of bilateral collaborations via programmes Procope (German-French) and Polonium (Polish-French). J.Z. acknowledges support by Polish Committee for Scientific Research under grant 2P03B00915. Laboratoire Kastler Brossel is laboratoire de l'Université Pierre et Marie Curie et de l'Ecole Normale Supérieure, unité mixte de recherche 8552 du CNRS. CPU time on various computers has been provided by IDRIS (Orsay) and RZG (Garching).

References

[1] J. A. Bergou and B. G. Englert, J. Mod. Opt. **45**, 701 (1998).

[2] E. Schrödinger, Die Naturwissenschaften **14**, 664 (1926).

[3] A. J. Lichtenberg and M. A. Lieberman, *Regular and Stochastic Motion*, Vol. 38 of *Applied Mathematical Sciences* (Springer, Berlin, 1983).

[4] C. Raman, T. C. Weinacht, and P. H. Bucksbaum, Phys. Rev. A **55**, R3995 (1997).

[5] J. A. Yeazell, M. Mallalieu, and J. C. R. Stroud, Phys. Rev. Lett. **64**, 2007 (1990).

[6] G. Alber and P. Zoller, Phys. Rep. **199**, 231 (1991).

[7] L. D. Landau and E. M. Lifschitz, *Quantum Mechanics* (Pergamon, Oxford, 1977).

[8] J. Parker and J. C. R. Stroud, Phys. Rev. Lett. **56**, 716 (1986).

[9] G. Alber, H. Ritsch, and P. Zoller, Phys. Rev. **34**, 1058 (1986).

[10] I. S. Averbukh and N. F. Perelman, Physics Letters A **139**, 449 (1989).

[11] J. A. Yeazell and J. C. R. Stroud, Phys. Rev. **43**, 5153 (1991).

[12] M. Hillery, R. F. O'Connell, M. O. Scully, and E. P. Wigner, Phys. Rep. **106**, 12 (1984).

[13] J. E. Moyal, Proc. Camb. Phil. Soc. Math. Phys. Sci. **45**, 99 (1949).

[14] L. D. Landau and E. M. Lifschitz, *Mechanics* (Pergamon, Oxford, 1994).

[15] F. Haake, *Quantum Signatures of Chaos*, Vol. 54 of *Springer Series in Synergetics* (Springer, Berlin, 1991).

[16] R. J. Glauber, Phys. Rev. **131**, 2766 (1963).

[17] L. Mandel and E. Wolf, *Coherence and Quantum Optics* (Cambridge University Press, Cambridge, 1995).

[18] C. Cohen-Tannoudji, J. Dupont-Roc, and G. Grynberg, *Atom-Photon Interactions: Basic Processes and Applications* (John Wiley and Sons, New York, 1992).

[19] C. Cohen-Tannoudji, B. Diu, and F. Laloë, *Mécanique quantique* (Hermann, Paris, 1973).

[20] R. L. Liboff, *Introductory Quantum Mechanics* (Holden-Day, San Francisco, 1980).

[21] K. Husimi, Proc. Phys. Math. Soc. Japan **22**, 264 (1940).

[22] H. A. Bethe and E. E. Salpeter, *Quantum Mechanics of One- and Two-Electron Atoms* (Plenum Publishing Corp., New York, 1977).

[23] M. S. Goldberger and K. M. Watson, *Collision Theory* (Wiley, New York, 1964).

[24] F. H. M. Faisal, *Theory of Multiphoton Processes* (Plenum Press, New York, 1987).

[25] J. A. Yeazell and J. C. R. Stroud, Phys. Rev. Lett. **60**, 1494 (1988).

[26] L. Marmet *et al.*, Phys. Rev. Lett. **72**, 3779 (1994).

[27] M. Mallalieu and J. C. R. Stroud, Phys. Rev. **A49**, 2329 (1994).

[28] T. C. Weinacht, J. Ahn, and P. H. Bucksbaum, Nature **397**, 233 (1999).

[29] E. Ott, *Chaos in Dynamical Systems* (Cambridge University Press, Cambridge, 1993).

[30] E. Lee, A. F. Brunello, and D. Farrelly, Phys. Rev. A **55**, 2203 (1997).

[31] E. Schrödinger, in *Sources of Quantum Mechanics*, edited by B. L. van der Waerden (Dover, New York, 1968).

[32] D. Delande and A. Buchleitner, Adv. At. Mol. Opt. Phys. **35**, 85 (1994).

[33] A. Buchleitner and D. Delande, Phys. Rev. Lett. **75**, 1487 (1995).

[34] I. Białynicki-Birula, M. Kalinski, and J. H. Eberly, Phys. Rev. Lett. **73**, 1777 (1994).

[35] J. Ahn, T. C. Weinacht, and P. H. Bucksbaum, Science **287**, 463 (2000).

[36] D. A. Meyer, Science **289**, 1431a (2000).

[37] P. G. Kwiat and R. J. Hughes, Science **289**, 1431a (2000).

[38] P. H. Bucksbaum, J. Ahn, and T. C. Weinacht, Science **289**, 1431a (2000).

[39] G. P. Berman and G. M. Zaslavsky, Phys. Lett. **61A**, 295 (1977).

[40] J. Henkel and M. Holthaus, Phys. Rev. **A45**, 1978 (1992).

[41] M. Holthaus, Prog. Theor. Phys. Supplement **116**, 417 (1994).

[42] M. Holthaus, Chaos, Solitons and Fractals **5**, 1143 (1995).

[43] A. Buchleitner, Ph.D. thesis, Université Pierre et Marie Curie, Paris, 1993.

[44] D. Farrelly, E. Lee, and T. Uzer, Phys. Rev. Lett. **75**, 972 (1995).

[45] I. Białynicki-Birula, M. Kalinski, and J. H. Eberly, Phys. Rev. Lett. **75**, 973 (1995).

[46] D. Farrelly, E. Lee, and T. Uzer, Physics Letters A **204**, 359 (1995).

[47] M. Kalinski, J. H. Eberly, and I. Białynicki-Birula, Phys. Rev. **A52**, 2460 (1995).

[48] M. Kalinski and J. H. Eberly, Phys. Rev. **A52**, 4285 (1995).

[49] D. Delande, J. Zakrzewski, and A. Buchleitner, Europhys. Lett. **32**, 107 (1995).

[50] J. Zakrzewski, D. Delande, and A. Buchleitner, Phys. Rev. Lett. **75**, 4015 (1995).

[51] I. Białynicki-Birula and Z. Białynicka-Birula, Phys. Rev. Lett. **77**, 4298 (1996).

[52] J. H. Eberly and M. Kalinski, in *Multiphoton Processes 1996, Proceedings of the 7th International Conference on Multiphoton Processes, Garmisch-Partenkirchen, Germany, October 1996*, Vol. 154 of *Institute of Physics Conference Series*, edited by P. Lambropoulos and H. Walther (Institute of Physics, Bristol and Philadelphia, 1997), pp. 29–36.

[53] M. Kalinski and J. H. Eberly, Phys. Rev. Lett. **77**, 2420 (1996).

[54] A. F. Brunello, T. Uzer, and D. Farrelly, Phys. Rev. Lett. **76**, 2874 (1996).

[55] M. Kalinski and J. H. Eberly, Phys. Rev. **A53**, 1715 (1996).

[56] M. Kalinski and J. H. Eberly, Phys. Rev. Lett. **79**, 3542 (1997).

[57] M. Kalinski, Phys. Rev. **57**, 2239 (1998).

[58] I. Białynicki-Birula and Z. Białynicka-Birula, Phys. Rev. Lett. **78**, 2539 (1997).

[59] Z. Białynicka-Birula and I. Białynicki-Birula, Phys. Rev. **A56**, 3629 (1997).

[60] D. Delande, J. Zakrzewski, and A. Buchleitner, Phys. Rev. Lett. **79**, 3541 (1997).

[61] J. Zakrzewski and D. Delande, J. Phys. B: Atom. Mol. Opt. Phys.**30**, L87 (1997).

[62] C. Cerjan, E. Lee, D. Farrelly, and T. Uzer, Phys. Rev. **A55**, 2222 (1997).

[63] J. Zakrzewski, A. Buchleitner, and D. Delande, Z. Phys. **B103**, 115 (1997).

[64] A. Buchleitner, D. Delande, and J. Zakrzewski, in *Multiphoton Processes 1996, Proceedings of the 7th International Conference on Multiphoton Processes, Garmisch-Partenkirchen, Germany, October 1996*, Vol. 154 of *Institute of Physics Conference Series*, edited by P. Lambropoulos and H. Walther (Institute of Physics, Bristol and Philadelphia, 1997), pp. 19–28.

[65] J. Zakrzewski, D. Delande, and A. Buchleitner, Phys. Rev. **E57**, 1458 (1998).

[66] J. Zakrzewski, D. Delande, and A. Buchleitner, Acta Physica Polon. **A 93**, 179 (1998).

[67] A. Buchleitner, K. Sacha, D. Delande, and J. Zakrzewski, Eur. Phys. J. D **5**, 145 (1999).

[68] D. Delande and J. Zakrzewski, Phys. Rev. A **58**, 466 (1998).

[69] K. Sacha, Ph.D. thesis, Jagellonian University, Kraków, 1998, unpublished.

[70] K. Hornberger, Master's thesis, Ludwig-Maximilians-Universität, München, 1998.

[71] K. Hornberger and A. Buchleitner, Europhys. Lett. **41**, 383 (1998).

[72] K. Sacha, J. Zakrzewski, and D. Delande, Eur. Phys. J. **D1**, 231 (1998).

[73] K. Sacha and J. Zakrzewski, Phys. Rev. A **58**, 3974 (1998).

[74] K. Sacha and J. Zakrzewski, Phys. Rev. A **59**, 1707 (1999).

[75] D. Farrelly, in *Physics and Chemistry of Wave Packets*, edited by J. A. Yeazell and T. Uzer (John Wiley & Sons, New York, 2000).

[76] M. V. Berry and K. E. Mount, Rep. Prog. Phys. **35**, 315 (1972).

[77] A. M. O. de Almeida, *Hamiltonian Systems: Chaos and Quantization* (Cambridge University Press, Cambridge, 1988).

[78] A. Einstein, Verh. d. Dtsch. Phys. Ges. 82 (1917).

[79] M. Born and E. Wolf, *Principles of Optics* (Academic Press, Oxford, 1999).

[80] H. P. Breuer and M. Holthaus, Ann. Phys. **211**, 249 (1991).

[81] E. J. Heller, in *Chaos and Quantum Physics*, Vol. Session LII of *Les Houches* (North-Holland, Amsterdam, 1991), p. 547.

[82] H. J. Stöckmann, *Quantum Chaos: An Introduction* (Cambridge University Press, Cambridge, 1999).

[83] R. V. Jensen, M. M. Sanders, M. Saraceno, and B. Sundaram, Phys. Rev. Lett. **63**, 2771 (1989).

[84] J. G. Leopold and D. Richards, J. Phys. B: Atom. Mol. Opt. Phys.**27**, 2169 (1994).

[85] G. M. Zaslavsky, Phys. Rep. **80**, 157 (1981).

[86] J. Ringot, P. Szriftgiser, J. C. Garreau, and D. Delande, Phys. Rev. Lett. **85**, 2741 (2000).

[87] A. Buchleitner and D. Delande, Phys. Rev. **A55**, R1585 (1997).

[88] B. V. Chirikov, Doc. Ac. Sci. USSR **125**, 1015 (1959).

[89] B. V. Chirikov, Phys. Rep. **52**, 263 (1979).

[90] M. G. Floquet, Ann. École Norm. Sup. **12**, 47 (1883).

[91] N. W. Ashcroft and N. D. Mermin, *Solid State Physics* (Saunders College Publishing, Fort Worth, 1976), college edition.

[92] J. H. Shirley, Phys. Rev. **138**, B979 (1965).

[93] J. B. Marion, *Classical Dynamics of Particles and Systems*, 2nd ed. (Academic Press, New York, 1970).

[94] R. Loudon, *The Quantum Theory of Light*, 2nd ed. (Clarendon Press, Oxford, 1986).

[95] in *Handbook of Mathematical Functions*, edited by M. Abrammowitz and I. A. Stegun (Dover, New York, 1972).

[96] R. Shakeshaft, Z. Phys. D **8**, 47 (1988).

[97] A. Buchleitner, D. Delande, and J. C. Gay, J. Opt. Soc. Am. B **12**, 505 (1995).

[98] E. Cormier and P. Lambropoulos, J. Phys. B **29**, 1667 (1996).

[99] J. Javanainen, J. H. Eberly, and Q. Su, Phys. Rev. **A38**, 3430 (1988).

[100] Q. Su and J. H. Eberly, Phys. Rev. **A44**, 5997 (1991).

[101] V. C. Reed, P. L. Knight, and K. Burnett, Phys. Rev. Lett. **67**, 1415 (1991).

[102] K. Burnett, V. C. Reed, J. Cooper, and P. L. Knight, Phys. Rev. **A45**, 3347 (1992).

[103] R. Grobe and J. H. Eberly, Phys. Rev. **A47**, R1605 (1993).

[104] R. Grobe, K. Rzążewski, and J. H. Eberly, J. Phys. B **27**, L503 (1994).

[105] P. Kustaanheimo and E. Stiefel, J. Reine Angew. Math. **218**, 204 (1965).

[106] D. Delande and J.-C. Gay, J. Phys. B: Atom. Mol. Opt. Phys.**17**, 335 (1984).

[107] O. Rath and D. Richards, J. Phys. B: Atom. Mol. Opt. Phys.**21**, 555 (1988).

[108] J. A. Griffiths and D. Farrelly, Phys. Rev. **A45**, R2678 (1992).

[109] R. Gębarowski and J. Zakrzewski, Phys. Rev. **A51**, 1508 (1995).

[110] P. Schlagheck and A. Buchleitner, Physica D **131**, 110 (1999).

[111] A. O. Barut, C. K. E. Schneider, and R. Wilson, J. Math. Phys. **20**, 2244 (1979).

[112] A. C. Chen, Phys. Rev. **A 22**, 333 (1980).

[113] A. C. Chen, Phys. Rev. **A 23**, 1655 (1981).

[114] D. Delande, Ph.D. thesis, Université de Paris, Paris, 1988, thèse de doctorat d'etat.

[115] C. Lanczos, J. Res. Nat. Bur. Standards, Sect B **45**, 225 (1950).

[116] D. Delande, A. Bommier, and J.-C. Gay, Phys. Rev. Lett. **66**, 141 (1991).

[117] T. Ericsson and A. Ruhe, Math. Comput. **35**, 1251 (1980).

[118] R. G. Grimes, J. G. Lewis, and H. D. Simon, SIAM J. Matrix Anal. Appl. **15**, 228 (1994).

[119] E. Balslev and J. M. Combes, Commun. math. Phys. **22**, 280 (1971).

[120] S. Graffi, V. Grecchi, and H. J. Silverstone, Ann. Inst. Henri Poincaré **42**, 215 (1985).

[121] K. Yajima, Comm. Math. Phys. **87**, 331 (1982).

[122] C. A. Nicolaides and D. R. Beck, Int. J. Quant. Chem. **XIV**, 457 (1978).

[123] B. R. Johnson and W. P. Reinhardt, Phys. Rev. A **28**, 1930 (1983).

[124] Y. K. Ho, Phys. Rep. **99**, 1 (1983).

[125] N. Moiseyev, Phys. Rep. **302**, 211 (1998).

[126] A. Buchleitner, B. Grémaud, and D. Delande, J. Phys. B: Atom. Mol. Opt. Phys.**27**, 2663 (1994).

[127] M. J. Englefield, *Group Theory and the Coulomb Problem* (Wiley, New-York, 1972).

[128] H. Goldstein, *Classical Dynamics* (Addison-Wesley, Reading, Ma., 1980), p.146.

[129] R. V. Jensen, Phys. Rev. **A30**, 386 (1984).

[130] B. I. Meerson, E. A. Oks, and P. V. Sasorov, J. Phys. B: Atom. Mol. Opt. Phys.**15**, 3599 (1982).

[131] G. Casati, I. Guarneri, and D. L. Shepelyansky, IEEE J. Quantum Electron. **24**, 1420 (1988).

[132] J. E. Bayfield, G. Casati, I. Guarneri, and D. W. Sokol, Phys. Rev. Lett. **63**, 364 (1989).

[133] P. M. Koch and K. A. H. van Leeuwen, Phys. Rep. **255**, 289 (1995).

[134] M. R. W. Bellermann, P. M. Koch, D. Mariani, and D. Richards, Phys. Rev. Lett. **76**, 892 (1996).

[135] J. E. Bayfield and P. M. Koch, Phys. Rev. Lett. **33**, 258 (1974).

[136] J. E. Bayfield, S. Y. Luie, L. C. Perotti, and M. P. Skrzypkowski, Phys. Rev. **A53**, R12 (1996).

[137] E. J. Galvez *et al.*, Phys. Rev. Lett. **61**, 2011 (1988).

[138] P. Fu, T. J. Scholz, J. M. Hettema, and T. F. Gallagher, Phys. Rev. Lett. **64**, 511 (1990).

[139] C. H. Cheng, C. Y. Lee, and T. F. Gallagher, Phys. Rev. **A54**, 3303 (1996).

[140] D. Delande and J. Zakrzewski, in *Classical, Semiclassical and Quantum Dynamics in Atoms*, No. 485 in *Lecture Notes in Physics*, edited by H. Friedrich and B. Eckhardt (Springer, New York, 1997), p. 205.

[141] F. V. Bunkin and A. M. Prokhorov, Sov. Phys. JETP **19**, 739 (1964).

[142] T. P. Grozdanov, M. J. Raković, and E. A. Solovev, J. Phys. B: Atom. Mol. Opt. Phys.**25**, 4455 (1992).

[143] H. Klar, Z. Phys. D **11**, 45 (1989).

[144] E. Lee, A. F. Brunello, and D. Farrelly, Phys. Rev. Lett. **75**, 3641 (1995).

[145] A. Buchleitner and D. Delande, Chaos, Solitons and Fractals **5**, 1125 (1995).

[146] E. J. Heller, in *Classical and Quantum Chaos*, edited by A. Voros, M. Giannoni, and A. Zinn-Justin (Elsevier, Amsterdam, 1991), Chap. Scars.

[147] E. B. Bogomolny, Physica D **31**, 169 (1988).

[148] A. Brunello, Ph.D. thesis, State University of New York at Stony Brook, Stony Brook, 1997, unpublished.

[149] K. Sacha and J. Zakrzewski, Phys. Rev. **A56**, 719 (1997).

[150] K. Sacha and J. Zakrzewski, Phys. Rev. A **58**, 488 (1998).

[151] A. F. Brunello, T. Uzer, and D. Farrelly, Phys. Rev. A **55**, 3730 (1997).

[152] J. G. Leopold and D. Richards, J. Phys. B: Atom. Mol. Opt. Phys.**19**, 1125 (1986).

[153] J. G. Leopold and D. Richards, J. Phys. B: Atom. Mol. Opt. Phys.**20**, 2369 (1987).

[154] M. J. Raković, T. Uzer, and D. Farrelly, Phys. Rev. A **57**, 2814 (1998).

[155] F. Benvenuto, G. Casati, I. Guarneri, and D. L. Shepelyansky, Z. Phys. B **84**, 159 (1991).

[156] C. R. de Oliveira, G. Casati, and I. Guarneri, Europhys. Lett. **27**, 187 (1994).

[157] M. E. Flatté and M. Holthaus, Ann. Phys. **245**, 113 (1996).

[158] A. Steane, P. Szriftgiser, P. Desbiolles, and J. Dalibard, Phys. Rev. Lett. **74**, 4972 (1995).

[159] M. K. Oberthaler *et al.*, Phys. Rev. Lett. 4447 (1999).

[160] L. Bonci, A. Farusi, P. Grigilini, and R. Roncaglia, Phys. Rev. E **58**, 5689 (1998).

[161] O. Brodier, P. Schlagheck, and D. Ullmo, Phys. Rev. Lett. **87**, 64101 (2001).

[162] W. Paul, Rev. Mod. Phys. **62**, 531 (1992).

[163] F. Benvenuto, G. Casati, and D. L. Shepelyansky, Phys. Rev. Lett. **72**, 1818 (1994).

[164] G. Tanner, K. Richter, and J. M. Rost, Rev. Mod. Phys. **72**, 497 (2000).

[165] D. Wintgen and D. Delande, J. Phys. B: Atom. Mol. Opt. Phys.**26**, L399 (1993).

[166] B. Grémaud and D. Delande, Europhys. Lett. **40**, 363 (1997).

[167] B. Grémaud, Ph.D. thesis, Université Paris 6, 1997.

[168] R. Püttner *et al.*, Phys. Rev. Lett. **86**, 3747 (2001).

[169] U. Eichmann, V. Lange, and W. Sandner, Phys. Rev. Lett. **64**, 274 (1990).

[170] K. Richter and D. Wintgen, Phys. Rev. Lett. **65**, 1965 (1990).

[171] P. Schlagheck and A. Buchleitner, J. Phys. B: Atom. Mol. Opt. Phys.**31**, L489 (1998).

[172] P. Schlagheck and A. Buchleitner, Europhys. Lett. **46**, 24 (1999).

[173] P. Schlagheck, Ph.D. thesis, Technische Universität, München, 1999, published by Herbert Utz Verlag.

[174] L. G. Hanson and P. Lambropoulos, Phys. Rev. Lett. **74**, 5009 (1995).

[175] O. Zobay and G. Alber, Phys. Rev. **54**, 5361 (1996).

[176] B. Mecking and P. Lambropoulos, Phys. Rev. **A57**, 2014 (1998).

[177] M. Berry, I. Marzoli, and W. P. Schleich, Physics World **14**, (2001).

[178] P. A. Lee and A. D. Stone, Phys. Rev. Lett. **55**, 1622 (1985).

[179] W. A. Lin and L. E. Ballentine, Phys. Rev. Lett. **65**, 2927 (1990).

[180] W. A. Lin and L. E. Ballentine, Phys. Rev. **45**, 3637 (1992).

[181] F. Grossmann, T. Dittrich, P. Jung, and P. Hänggi, Phys. Rev. Lett. **67**, 516 (1991).

[182] F. Grossmann, T. Dittrich, P. Jung, and P. Hänggi, Z. Phys. B **84**, 315 (1991).

[183] F. Grossmann *et al.*, J. Stat. Phys. **70**, 229 (1993).

[184] J. Plata and J. M. G. Llorente, J. Phys. A **25**, L303 (1992).

[185] O. Bohigas, S. Tomsovic, and D. Ullmo, Phys. Rep. **223**, 43 (1993).

[186] O. Bohigas, D. Boosé, R. E. de Carvalho, and V. Marvulle, Nucl. Phys. **A560**, 197 (1993).

[187] S. Tomsovic and D. Ullmo, Phys. Rev. **E50**, 145 (1994).

[188] A. Shudo and K. S. Ikeda, Phys. Rev. Lett. **74**, 682 (1995).

[189] F. Leyvraz and D. Ullmo, J. Phys. A **29**, 2529 (1996).

[190] J. D. Jackson, *Classical Electrodynamics* (Wiley, New York, 1975).

[191] S. Haroche, in *Fundamental Systems in Quantum Optics, Le Houches, Session LIII,1990*, edited by J. Dalibard, J. M. Raimond, and J. Zinn-Justin (Elsevier, New York, 1992).

[192] M. Lewenstein, J. Zakrzewski, T. W. Mossberg, and J. Mostowski, J. Phys. B: Atom. Mol. Opt. Phys.**21**, L9 (1988).

[193] M. Lewenstein, J. Zakrzewski, and T. W. Mossberg, Phys. Rev. **A38**, 808 (1988).

[194] D. D. R. Buchleitner, D. Delande, and J. Zakrzewski, in *Non-spreading Knödel-packets in Microsoft fields, Proceedings of the Third International Bavarian Conference on Knödel-Packets*, No. 007 in *Food, physics and politics*, edited by H. Schalther and W. Weich (Stoiber Comp., Aidling, 1997), p. 294561.

[195] K. Nakamura, *Quantum chaos, a new paradigm of nonlinear dynamics*, *Cambridge Nonlinear Science Series 3* (Cambridge University Press, Cambridge, 1993).

[196] G. Casati, I. Guarneri, and D. L. Shepelyansky, Phys. Rev. **A36**, 3501 (1987).

[197] J. G. Leopold and I. C. Percival, Phys. Rev. Lett. **41**, 944 (1978).

[198] J. E. Bayfield and D. W. Sokol, Phys. Rev. Lett. **61**, 2007 (1988).

[199] R. Blümel *et al.*, Phys. Rev. Lett. **62**, 341 (1989).

[200] R. Blümel *et al.*, Phys. Rev. **A44**, 4521 (1991).

[201] A. Buchleitner, L. Sirko, and H. Walther, Europhys. Lett. **16**, 35 (1991).

[202] G. Casati, B. V. Chirikov, and D. L. Shepelyansky, Phys. Rev. Lett. **53**, 2525 (1984).

[203] S. Fishman, D. R. Grempel, and R. E. Prange, Phys. Rev. Lett. **49**, 509 (1982).

[204] D. R. Grempel, R. E. Prange, and S. Fishman, Phys. Rev. **A29**, 1639 (1984).

[205] N. Brenner and S. Fishman, Phys. Rev. Lett. **77**, 3763 (1996).

[206] A. Buchleitner, I. Guarneri, and J. Zakrzewski, Europhys. Lett. **44**, 162 (1998).

[207] S. Wimberger, Master's thesis, Ludwig-Maximilians-Universität München, 2000.

[208] S. Wimberger and A. Buchleitner, J. Phys. A **34**, 7181 (2001).

[209] L. Sirko, A. Haffmans, M. R. W. Bellermann, and P. M. Koch, Europhys. Lett. **33**, 181 (1996).

[210] L. Sirko *et al.*, Phys. Rev. Lett. **71**, 2895 (1993).

[211] B. E. Sauer, M. R. W. Bellermann, and P. M. Koch, Phys. Rev. Lett. **68**, 1633 (1992).

[212] K. A. H. van Leeuwen *et al.*, Phys. Rev. Lett. **55**, 2231 (1985).

[213] P. M. Koch, Physica D **83**, 178 (1995).

[214] P. M. Koch, in *Chaos and Quantum Chaos*, Vol. 411 of *Lecture Notes in Physics*, edited by W. D. Heiss (Springer, Berlin, 1992).

[215] P. M. Koch, CHAOS **2**, 131 (1992).

[216] P. M. Koch *et al.*, Physica Scripta **T26**, 51 (1989).

[217] M. W. Noël, M. W. Griffith, and T. F. Gallagher, Phys. Rev. **A62**, 063401 (2000).

[218] J. E. Bayfield, CHAOS **1**, 110 (1991).

[219] J. Zakrzewski and D. Delande, J. Phys. B **28**, L667 (1995).

[220] A. Buchleitner *et al.*, Phys. Rev. Lett. **75**, 3818 (1995).

[221] M. Arndt, A. Buchleitner, R. N. Mantegna, and H. Walther, Phys. Rev. Lett. **67**, 2435 (1991).

[222] O. Benson *et al.*, Phys. Rev. **A51**, 4862 (1995).

[223] M. W. Noël, M. W. Griffith, and T. F. Gallagher, Phys. Rev. Lett. **87**, 043001 (2001).

[224] R. Blümel and U. Smilansky, J. Opt. Soc. Am. B **7**, 664 (1990).

[225] A. Krug and A. Buchleitner, Europhys. Lett. **49**, 176 (2000).

[226] A. Krug and A. Buchleitner, Phys. Rev. Lett. **86**, 3538 (2001).

[227] H. P. Breuer and M. Holthaus, Physics Letters A **140**, 507 (1989).

[228] J. E. Bayfield and L. A. Pinnaduwage, Phys. Rev. Lett. **54**, 313 (1985).

[229] C. O. Reinhold *et al.*, J. Phys. B: Atom. Mol. Opt. Phys.**34**, L551 (2001).

[230] A. Assion *et al.*, Science **282**, 919 (1998).

[231] T. Brixner, N. H. Damrauer, P. Niklaus, and G. Gerber, Nature **414**, 57 (2001).